2016

From Model Systems To Real Catalysts: Bridging The Pressure And Materials Gaps

Audrey S. Duke
University of South Carolina

FROM MODEL SYSTEMS TO REAL CATALYSTS: BRIDGING THE PRESSURE AND MATERIALS GAPS

by

Audrey S. Duke

Bachelor of Science
Auburn University, 2011

Submitted in Partial Fulfillment of the Requirements

For the Degree of Doctor of Philosophy in

Chemistry

College of Arts and Sciences

University of South Carolina

2016

Accepted by:

Donna A. Chen, Major Professor

Michael L. Myrick, Committee Member

Hans-Conrad zur Loye, Committee Member

Christopher T. Williams, Committee Member

Lacy Ford, Senior Vice Provost and Dean of Graduate Studies

DEDICATION

To the love of my life, Daniel, whose endless love and support are a daily source of inspiration and motivation for me, and to my cat, Princess Buttercup, for being my companion throughout my graduate school years.

ACKNOWLEDGEMENTS

I extend my deepest gratitude to the innumerable list of people who made this arduous journey a success in spite of its many seemingly insurmountable obstacles. First, I thank my mentor and advisor, Dr. Donna Chen, whose challenging yet supportive guidance has been invaluable to me. I thank the members of my doctoral committee: Dr. Micky Myrick, Dr. Hanno zur Loye, Dr. Chris Williams, and Dr. John Weidner. Thanks also to the faculty and staff of the Department of Chemistry and Biochemistry as well as the University of South Carolina for honoring me with the elite Presidential Fellowship.

I am grateful for the diligent and industrious fellow members of my lab group, both past and present, most especially: Dr. Samuel Tenney, Dr. Randima Galhenage, Dr. Hui Yan, Dr. Brett Cagg, Mara Levine, Kangmin Xie, Grant Seuser, Amy Brandt, Thathsara Maddumapatabandi, and Tyler Hernandez. I also acknowledge all of my collaborators, most especially: Dr. Ali Ahsen, Dr. Ye Lin, and Ekaterina Dolgopolova. I thank the knowledgeable individuals at SPECS GmbH and Duniway Stockroom, who patiently endured my badgering questions about troubleshooting. Most especially, I am deeply indebted to Fred Waldeck, Arthur Illingworth, and Allen Frye who were absolutely indispensable to me for all of the miracles they worked throughout the years!

Words fail to express the gratitude and love I feel for all of my friends, especially my fellow USC graduate students, for my family, and for Daniel.

Above all, I thank God, whose grace has always proven sufficient for me, as His power is made perfect in my weakness.

ABSTRACT

For decades a fundamental understanding of heterogeneous catalysts has been pursued for rational catalyst design using model systems under ultrahigh vacuum (UHV) conditions; however, there exist stark differences between the simplified models investigated under UHV and the industrial catalysts used at high pressures. To bridge these gaps, it becomes essential to utilize progressively more complex materials and to correlate their surface structure and activity using incrementally higher pressure techniques. In this work, both model Pt-Re catalysts and powdered metal-organic frameworks (MOFs) were studied using a suite of traditional UHV surface science techniques in addition to ambient pressure X-ray photoelectron spectroscopy (APXPS) and UHV-coupled ambient pressure cells. CO oxidation and methanol oxidation were investigated by APXPS on Pt(111), Re films on Pt(111), and on Pt−Re alloy model surfaces. Pt-Re alloy surfaces were found to dissociate oxygen more readily than Pt surfaces, and CO was found to desorb at lower temperatures from Pt−Re alloy surfaces than from Pt. Pt and Pt-Re surfaces were found to have similar product formation with Pt-Re alloys having higher activity and maintaining greater selectivity than Pt to CO_2 formation. Model Pt-Re systems were also studied for methanol oxidation in a UHV-coupled microreactor where products were determined via GC-TCD, and pre- and post-reaction surfaces were characterized by XPS without exposure to air. The Pt-Re alloy surface initially showed less activity than Pt; but over extended time periods, the alloy maintained higher activity than Pt, which deactivated due to accumulation of atomic

carbon. Re films were unstable since they form volatile Re_2O_7, but alloying Re with Pt made it less susceptible to sublimation. Water-gas shift was also performed in the microreactor on TiO_2(110)-supported Pt, Re, and Pt-Re bimetallic clusters. Surface ReO_x appears to block Pt active sites, but Re underneath Pt shows higher activity than Pt alone as Re modifies Pt. A separate UHV XPS-coupled high pressure cell was used to study the generation of mixed valence $Cu^{+1}/^{+2}$ sites in a powdered MOF before and after extensive heating and exposure to H_2, O_2, CO, and air, which corresponded to changes in the valence band, indicating tunability of the MOF's electronic properties.

Table of Contents

LIST OF TABLES

.

LIST OF FIGURES

List of Abbreviations

AES ..... Auger electron spectroscopy

APR ..... aqueous phase reforming

APXPS ..... ambient pressure X-ray photoelectron spectroscopy

ESCA ..... electron spectroscopy for chemical analysis

DFT ..... density functional theory

IRAS ..... infrared reflection absorption spectroscopy

LEED ..... low energy electron diffraction

LEIS/ISS ..... low energy ion scattering spectroscopy

ML ..... monolayer

MOF ..... metal-organic framework

QCM ..... quartz crystal microbalance

sccm ..... standard cubic centimeters per minute

STM ..... scanning tunneling microscopy

TPD ..... temperature programmed desorption

UHV ..... ultra-high vacuum

VLE ..... vapor-liquid equilibrator

XPS ..... X-ray photoelectron spectroscopy

CHAPTER 1

INTRODUCTION

1.1 THE SIGNIFICANCE OF CATALYSIS

Over the past century, catalysis in its various forms has grown to become a multi-billion-dollar industry, partially due to the fact that it is responsible for over 90% of the world's chemical production.[1] Additionally, this ability of a regenerable chemical or biological substance to improve the rate or selectivity of a desirable reaction is essential to most biological processes and also plays a vital role in food, fuel, and energy production. The use of heterogeneous catalysts in particular has become paramount in the global chemical industry where solid-state catalysts are used in many of the top manufacturing processes, such as the oxidation of SO_2 to SO_3 and the generation of ammonia from H_2 and N_2, with zeolites being the most widely used catalysts in industry.[2-6] As the global economy shifts towards green and sustainable energy chemistry, an intense effort has been made to reduce the carbon footprint of fuels and chemicals by removing the petrochemical industry's dependence on natural gas through renewable resources like biomass derivatives, such as alcohols, for oxidation reactions or as organic hydrogen donors.[7,8] Concomitantly, a need for new and different kinds of heterogeneous catalysts has arisen.

Recent attention has turned to the development of new catalysts for a variety of applications, including generation of fuel sources, such as H_2 from alcohols, that promise to be cleaner than their predecessor, fossil fuels. Ni-based catalysts in particular have shown the most promising activity for steam reforming of ethanol at 100% conversion and better than 90% selectivity towards H_2; however, over relatively short time intervals these Ni-based catalysts suffer decreased selectivity due to a methanation side-reaction as well as undergo deactivation by coking and CO poisoning.[9-14] Furthermore, as an

endothermic process, steam reforming requires high temperatures (600-1100 K) and pressures (15-30 atm) to drive it forward.[9,13,15,16] As an alternative, Pt based catalysts have been recently studied for aqueous phase reforming (APR) of alcohols and other biomass derivatives to H_2, and multiple studies have demonstrated that the addition of Re to supported Pt catalysts increases the catalyst's activity, stability, and lifetime on stream for a variety of reactions.[15,17,18] The improvements have been attributed to an assortment of causes including the ability of Re to form a range of oxidation states and weaker binding of CO to Pt on the bimetallic surfaces that leads to decreased CO poisoning of Pt active sites, but the exact means by which Re enhances the activity of Pt catalysts are still not agreed upon.[19-34]

Despite the ubiquitous and manifold use of catalysts in the world today, much is still unknown about the operational principles that drive the behavior of even some of the most common catalysts currently in use. The discovery of new catalysts most often comes about through inefficient "trial-and-error" processes because of the inherent difficulties in identifying the cause of a catalyst's activity.[35,36] In many cases, a clear understanding of the relationship between a catalyst's physicochemical properties and its activity or selectivity for a particular reaction is still lacking. Attempting to address this problem is one of the primary pursuits of modern surface science, as it seeks to discover and control the geometry and composition of active sites on heterogeneous catalysts so that they will yield enhanced activity, selectivity, and catalyst lifetime. Catalysts fashioned from such rational design would not only improve the efficiency of existent industries, but could also lead to the development of new technologies. Thus, it is important to gain a fundamental understanding of how catalysts operate.

1.2 THE APPLICATION OF SURFACE SCIENCE

The trouble with characterizing the sort of catalysts actually used in real-world applications lies in the complexity of the environment and of the materials. Industrial processes generally operate on a massive scale within high temperature and pressure regimes. Moreover, the catalysts employed are typically metallic or bimetallic nanoparticles inhomogeneously dispersed on powdered porous oxide supports, partly because the porosity of the material provides a large surface area and consequently the potential for a greater number of catalytic active sites.[37] While this increases product yield, the nonuniformity of the catalyst's structure and morphology makes it problematic to map, and it can be challenging to separate the effects of metal-metal interactions from metal-support interactions. To fully understand the relationship between the physical properties and the chemical activity of a surface requires information about the physical topography, the chemical composition and structure, the atomic and electronic structures, and the bonding of molecular species at the surface.[38]

A simple solution to the aforementioned problems is the use of well-defined, reproducible model systems.[39] Model catalysts typically consist of nanoparticles of at least one metal controllably dispersed over single crystal metal or metal-oxide samples with long-range order, hosting active sites of known quantity, composition, and structure. The model system as a whole is generally comprised of a model catalyst contained within a highly-controlled ultra-high vacuum (UHV) environment (pressures < $1x10^{-9}$ Torr). Ultra-high vacuum is a necessity for maintaining atomic scale cleanliness, given that it can take only one second for a room temperature surface to become covered by a complete layer of contamination from atmospheric gases at $1x10^{-6}$ Torr. At pressures

below $1x10^{-9}$ Torr, this timescale can be extended to several hours. Furthermore, the high inelastic scattering cross section of electrons with matter prevents them from being able to traverse very far unhindered in a gas.[40] Under ultra-high vacuum, the mean free path of an electron is long enough to allow the use of highly surface sensitive ion- and electron-based microscopic and spectroscopic techniques for surface characterization. Such techniques include low energy electron diffraction (LEED), scanning tunneling microscopy (STM), low energy ion scattering spectroscopy (LEIS), X-ray photoelectron spectroscopy (XPS), Auger electron spectroscopy (AES), and temperature programmed desorption (TPD). Many of these techniques require UHV conditions not only so that the electrons and ions involved in the technique can travel from source to detector without colliding with atmospheric gas particles, but also because most of them require the use of high voltages, which would discharge and destroy the sensitive equipment if operated at pressures above UHV.

1.3 MOTIVATION: BRIDGING THE PRESSURE AND MATERIALS GAPS

With this suite of UHV surface science techniques, one can obtain atomic level information about a variety of surface properties, including surface composition and morphology, electronic states, surface reactivity, and binding sites, which can be used to generate an extensive and careful correlation between catalyst surface characteristics and reactivity. However, as discussed, these techniques require pressures far below the working pressures of real catalytic processes. Moreover, the well-defined model catalysts employed in such highly controlled environments may not be truly effective representations of real catalysts.

Known as the "pressure gap" and "materials gap," these divergences between the pressures and materials used in the model studies and those used in an industrial reactor imply that the results and conclusions obtained from traditional UHV surface science techniques may not always apply to actual industrial conditions. Surfaces at ambient pressure conditions are not pristine as under UHV conditions, but rather are regularly covered by thick layers of physisorbed molecules such as water even at room temperature. Metal surfaces are different in air than in vacuum, too, since many form thick oxide films when in oxygenated environments.[41] CO oxidation over Ru catalysts is the classic example of a reaction that sparked concern over discrepancies between analysis conducted under UHV and ambient pressure conditions.[36,42] Studies showed that under UHV conditions, supported Ru and Ru(0001) single crystal catalysts had the lowest activity for CO oxidation among a series of late transition metals, but at much higher pressures, they had the best activity.[43,44] Though this was initially quite a mystery, it was later realized that the increased activity at high pressures was due to a surface layer of RuO_2 that forms under highly oxygen-rich reaction environments.[36,42] Since then, a great deal of attention has been focused on developing methods such as ambient pressure X-ray photoelectron spectroscopy and UHV-coupled reaction cells which combine the atomic-level control and understanding of the UHV environment with more catalytically realistic in situ measurements.

Transitioning from well-defined single-crystal surfaces to real powdered porous oxide catalysts is a difficult task; however, a relatively new class of materials called "metal-organic frameworks," or "MOFs" provide a sort of bridge between the two material extremes. Traditional zeolite catalysts have long dominated gas phase reactions

in the petroleum industry due to their high thermal stability and high surface area, but their pore sizes are limited and can be unstable under reaction conditions where they can clog or collapse.[45] Furthermore, metal particles dispersed on porous oxide supports often undergo metal redistribution within clusters or else suffer a loss of active surface area due to sintering under reaction conditions, so it can be difficult to tune the catalyst's active sites in a way that survives catalytic processes. In contrast, MOFs consist of metal nodes, or clusters of metal ions, which are connected by organic linkers in a crystalline structure. MOFs can be manufactured as powders or as films with a variety of rigid pore sizes depending on the linkers used, which translates to controllably sized active surface areas and larger pore volumes than conventional zeolites.[46] Additionally, the metal nodes in the framework are structurally resistant to sintering and can be tailored to incorporate a variety of catalytically relevant metals including Co, Ni, Cu, Zn, and Ru in several different configurations, and many of these same metals have already been investigated as supported catalysts for generating H_2 from alcohols like ethanol.[9-14] Thus far, MOFs have been considered for a wide variety of applications from gas sensing, selective capturing, and purification to photocatalysts and conductive membranes and films.[47,48] Encouraged by the catalytic relevance of the available metal nodes and by the fact that several MOFs have shown activity for a variety of liquid phase organic reactions including oxidation and reduction, researchers have also considered them very recently for their potential in catalyzing gas phase reactions.[48] MOFs appear promising as heterogeneous catalysts because of their high degree of tunability, very large surface areas, decent thermal stability, and the existence of coordinatively unsaturated metal sites (UMS) in the metal nodes. However, the exact nature of these various UMS and how

they interact with different adsorbate species is still largely unknown, meriting a careful and controlled study, which is facilitated by the MOFs' well-defined crystalline structure.

In order to bridge the pressure and materials gaps, it is necessary to take advantage of approaches that can be used at higher pressures on more catalytically relevant materials. Thus, the motivation of the work presented in this dissertation was to study the catalytic behavior of both well-defined Pt-Re model catalysts and powdered metal-organic frameworks using a battery of traditional UHV surface science techniques in tandem with technological innovations like ambient pressure X-ray photoelectron spectroscopy (APXPS), a high-pressure cell within a UHV chamber capable of handling powdered materials, and a UHV-coupled ambient pressure microreactor, all of which are described in Chapter 2.

1.4 REFERENCES

(1) "Recognizing the Best in Innovation: Breakthrough Catalyst". *R&D Magazine*, September 2005, pg 20.

(2) Facts & Figures Of The Chemical Industry. *Chem. Eng. News* 2013.

(3) Schlögl, R., Heterogeneous Catalysis. *Angew. Chem.-Int. Edit.* **2015,** *54* (11), 3465-520.

(4) Krämer, M.; Schubert, M.; Lautensack, T.; Hill, T.; Körner, R.; Rosowski, F.; Zühlke, J. Catalyst for the oxidation of SO_2 to SO_3. US8323610 B2, 2012.

(5) Corma, A., Inorganic Solid Acids and Their Use in Acid-Catalyzed Hydrocarbon Reactions. *Chem. Rev.* **1995,** *95*, 559-414.

(6) Corma, A., From Microporous to Mesoporous Molecular Sieve Materials and Their Use in Catalysis. *Chem. Rev.* **1997,** *97*, 2373-2419.

(7) Guo, Z.; Liu, B.; Zhang, Q.; Deng, W.; Wang, Y.; Yang, Y., Recent advances in heterogeneous selective oxidation catalysis for sustainable chemistry. *Chem. Soc. Rev.* **2014,** *43* (10), 3480-524.

(8) Gilkey, M. J.; Xu, B., Heterogeneous Catalytic Transfer Hydrogenation as an Effective Pathway in Biomass Upgrading. *ACS Catal.* **2016**, 1420-1436.

(9) Haryanto, A.; Fernando, S.; Murali, N.; Adhikari, S., Current status of hydrogen production techniques by steam reforming of ethanol: A review. *Energy Fuels* **2005,** *19* (5), 2098-2106.

(10) Rostrup-Nielsen, J. R., Conversion of hydrocarbons and alcohols for fuel cells. *Phys. Chem. Chem. Phys.* **2001,** *3*, 283.

(11) Cortright, R. D.; Davda, R. R.; Dumesic, J. A., Hydrogen from catalytic reforming of biomass-derived hydrocarbons in liquid water. *Nature* **2002,** *418* (6901), 964-967.

(12) V. Fierro, V. K., O. Akdim, C. Mirodatos, Oxidative reforming of biomass derived ethanol for hydrogen production in fuel cell applications. *Catal. Today* **2002,** *75*, 141-144.

(13) Deluga, G. A.; Salge, J. R.; Schmidt, L. D.; Verykios, X. E., Renewable hydrogen from ethanol by autothermal reforming. *Science* **2004,** *303* (5660), 993-997.

(14) Chheda, J. N.; Huber, G. W.; Dumesic, J. A., Liquid-phase catalytic processing of biomass-derived oxygenated hydrocarbons to fuels and chemicals. *Angew. Chem.-Int. Edit.* **2007,** *46* (38), 7164-7183.

(15) Shabaker, J. W.; Davda, R. R.; Huber, G. W.; Cortright, R. D.; Dumesic, J. A., Aqueous-phase reforming of methanol and ethylene glycol over alumina-supported platinum catalysts. *J. Catal.* **2003,** *215* (2), 344-352.

(16) Sun, J.; Qiu, X. P.; Wu, F.; Zhu, W. T., H_2 from steam reforming of ethanol at low temperature over Ni/Y_2O_3, Ni/La_2O_3 and Ni/Al_2O_3 catalysts for fuel-cell application. *Int. J. Hydrog. Energy* **2005,** *30* (4), 437-445.

(17) Huber, G. W.; Shabaker, J. W.; Evans, S. T.; Dumesic, J. A., Aqueous-phase reforming of ethylene glycol over supported Pt and Pd bimetallic catalysts. *Appl. Catal. B-Environ.* **2006,** *62* (3-4), 226-235.

(18) Shabaker, J. W.; Huber, G. W.; Davda, R. R.; Cortright, R. D.; Dumesic, J. A., Aqueous-phase reforming of ethylene glycol over supported platinum catalysts. *Catal. Lett.* **2003,** *88* (1-2), 1-8.

(19) Kunkes, E. L.; Simonetti, D. A.; Dumesic, J. A.; Pyrz, W. D.; Murillo, L. E.; Chen, J. G. G.; Buttrey, D. J. The Role of Rhenium in the Conversion of Glycerol to Synthesis Gas over Carbon Supported Platinum-Rhenium Catalysts. *J. Catal.*, **2008**, *260*, 164-177.

(20) Simonetti, D. A.; Kunkes, E. L.; Dumesic, J. A. Gas-Phase Conversion of Glycerol to Synthesis Gas over Carbon-Supported Platinum and Platinum-Rhenium Catalysts. *J. Catal.*, **2007**, *247*, 298-306.

(21) Soares, R. R.; Simonetti, D. A.; Dumesic, J. A. Glycerol as a Source for Fuels and Chemicals by Low-Temperature Catalytic Processing. *Angew. Chem.-Int. Edit.*, **2006**, *45*, 3982-3985.

(22) Zhang, L.; Karim, A. M.; Engelhard, M. H.; Wei, Z. H.; King, D. L.; Wang, Y. Correlation of Pt-Re Surface Properties with Reaction Pathways for the Aqueous-Phase Reforming of Glycerol. *J. Catal.*, **2012**, *287*, 37-43.

(23) King, D. L.; Zhang, L. A.; Xia, G.; Karim, A. M.; Heldebrant, D. J.; Wang, X. Q.; Peterson, T.; Wang, Y. Aqueous Phase Reforming of Glycerol for Hydrogen Production over Pt-Re Supported on Carbon. *Appl. Catal. B-Environ.*, **2010**, *99*, 206-213.

(24) Daniel, O. M.; DeLaRiva, A.; Kunkes, E. L.; Datye, A. K.; Dumesic, J. A.; Davis, R. J. X-Ray Absorption Spectroscopy of Bimetallic Pt-Re Catalysts for Hydrogenolysis of Glycerol to Propanediols. *ChemCatChem*, **2010**, *2*, 1107-1114.

(25) Ciftci, A.; Ligthart, D.; Hensen, E. J. M. Aqueous Phase Reforming of Glycerol over Re-Promoted Pt and Rh Catalysts. *Green Chem.*, **2014**, *16*, 853-863.

(26) Ciftci, A.; Ligthart, D.; Sen, A. O.; van Hoof, A. J. F.; Friedrich, H.; Hensen, E. J. M. Pt-Re Synergy in Aqueous-Phase Reforming of Glycerol and the Water-Gas Shift Reaction. *J. Catal.*, **2014**, *311*, 88-101.

(27) Ciftci, A.; Eren, S.; Ligthart, D.; Hensen, E. J. M. Platinum-Rhenium Synergy on Reducible Oxide Supports in Aqueous-Phase Glycerol Reforming. *ChemCatChem*, **2014**, *6*, 1260-1269.

(28) Kirilin, A. V.; Tokarev, A. V.; Manyar, H.; Hardacre, C.; Salmi, T.; Mikkola, J. P.; Murzin, D. Y. Aqueous Phase Reforming of Xylitol over Pt-Re Bimetallic Catalyst: Effect of the Re Addition. *Catal. Today*, **2014**, *223*, 97-107.

(29) Azzam, K. G.; Babich, I. V.; Seshan, K.; Mojet, B. L.; Lefferts, L. Stable and Efficient Pt-Re/TiO_2 Catalysts for Water-Gas-Shift: On the Effect of Rhenium. *ChemCatChem*, **2013**, *5*, 557-564.

(30) Azzam, K. G.; Babich, I. V.; Seshan, K.; Lefferts, L. Role of Re in Pt-Re/TiO_2 Catalyst for Water Gas Shift Reaction: A Mechanistic and Kinetic Study. *Appl. Catal. B-Environ.*, **2008**, *80*, 129-140.

(31) Iida, H.; Igarashi, A. Difference in the Reaction Behavior between Pt-Re/TiO_2 (Rutile) and Pt-Re/ZrO_2 Catalysts for Low-Temperature Water Gas Shift Reactions. *Appl. Catal. A*, **2006**, *303*, 48-55.

(32) Iida, H.; Yonezawa, K.; Kosaka, M.; Igarashi, A. Low-Temperature Water Gas Shift Reaction over Pt-Re/TiO_2 Catalysts Prepared by a Sub-Critical Drying Method. *Catal. Commun.*, **2009**, *10*, 627-630.

(33) Azzam, K. G.; Babich, I. V.; Seshan, K.; Lefferts, L. A Bifunctional Catalyst for the Single-Stage Water-Gas Shift Reaction in Fuel Cell Applications. Part 2. Roles of the Support and Promoter on Catalyst Activity and Stability. *J. Catal.*, **2007**, *251*, 163-171.

(34) Carrasquillo-Flores, R.; Gallo, J. M. R.; Hahn, K.; Dumesic, J. A.; Mavrikakis, M. Density Functional Theory and Reaction Kinetics Studies of the Water-Gas Shift Reaction on Pt-Re Catalysts. *ChemCatChem*, **2013**, *5*, 3690-3699.

(35) Senkan, S. M., High-throughput screening of solid state catalyst libraries. *Nature* **1998,** *394*, 350-353.

(36) Reuter, K., Insight into a Pressure and Materials Gap: CO Oxidation at "Ruthenium" Catalysts. *Oil & Gas Science and Technology - Rev. IFP* **2006,** *61* (4), 471-477.

(37) Bäumer, M.; Freund, H. J., Metal Deposits on Well-Ordered Oxide Films. *Prog. Surf. Sci.* **1999,** *61* (7-8), 127-198.

(38) Vickerman, J. C. and Gilmore, I. S., Ed. *Surface Analysis: The Principal Techniques*. 2nd ed.; John Wiley & Sons: Chichester, UK, 2009.

(39) Goodman, D. W., Correlations Between Surface Science Models and "Real World" Catalysts. *Journal of Physical Chemistry* **1996,** *100*, 13090–13102.

(40) Schnadt, J.; Knudsen, J.; Andersen, J. N.; Siegbahn, H.; Pietzsch, A.; Hennies, F.; Johansson, N.; Martensson, N.; Ohrwall, G.; Bahr, S.; Mahl, S.; Schaff, O., The new ambient-pressure X-ray photoelectron spectroscopy instrument at MAX-lab. *Journal of synchrotron radiation* **2012,** *19* (Pt 5), 701-4.

(41) Salmeron, M.; Schlögl, R., Ambient pressure photoelectron spectroscopy: A new tool for surface science and nanotechnology. *Surface Science Reports* **2008,** *63* (4), 169-199.

(42) Over, H.; Muhler, M., Catalytic CO oxidation over ruthenium—bridging the pressure gap. *Progress in Surface Science* **2003,** *72* (1-4), 3-17.

(43) C. H. F. Peden, D. W. G., Kinetics of CO Oxidation over Ru(0001). *J. Phys. Chem.* **1986,** *90* (7), 1360-1365.

(44) Cant, N.W.; Hicks, P.C.; Lennon, B.S. Steady-state oxidation of carbon monoxide over supported noble metals with particular reference to platinum. *J. Catal.* **1978**, *54*, 372-383.

(45) Dhakshinamoorthy, A.; Opanasenko, M.; Čejka, J.; Garcia, H., Metal organic frameworks as heterogeneous catalysts for the production of fine chemicals. *Catal. Sci. Tech.* **2013,** *3* (10), 2509.

(46) Furukawa, H.; Cordova, K. E.; O'Keeffe, M.; Yaghi, O. M., The chemistry and applications of metal-organic frameworks. *Science* **2013,** *341* (6149), 1230444.

(47) Chaemchuen, S.; Kabir, N. A.; Zhou, K.; Verpoort, F., Metal-organic frameworks for upgrading biogas *via* CO_2 adsorption to biogas green energy. *Chem. Soc. Rev.* **2013**, *42*, 9304-9332.

(48) Chughtai, A. H.; Ahmad, N.; Younus, H. A.; Laypkov, A.; Verpoort, F., Metal-organic frameworks: versatile heterogeneous catalysts for efficient catalytic organic transformations. *Chem. Soc. Rev.* **2015**, *44*, 6804.

CHAPTER 2

EXPERIMENTAL TECHNIQUES

2.1 X-RAY PHOTOELECTRON SPECTROSCOPY (XPS)

XPS provides elemental identification and chemical environment information about the top several monolayers of a sample surface. Developed by Kai Siegbahn, who won the Nobel Prize in Physics in 1981 for his work, the technique was originally dubbed "electron spectroscopy for chemical analysis," or ESCA, but is now more commonly referred to as XPS.[1] A schematic of a typical lab-based XPS experimental setup is shown in Figure 2.1. XPS takes advantage of the photoelectric effect; in an XPS experiment, a sample is irradiated with X-ray photons, which eject electrons from the core levels of the material into vacuum as shown in the left panel of Figure 2.2. Once the photoelectron has been ejected, a higher level electron can fill the hole left behind in the core shell, thereby lowering the energy of the system; and, the extra energy is then emitted from the

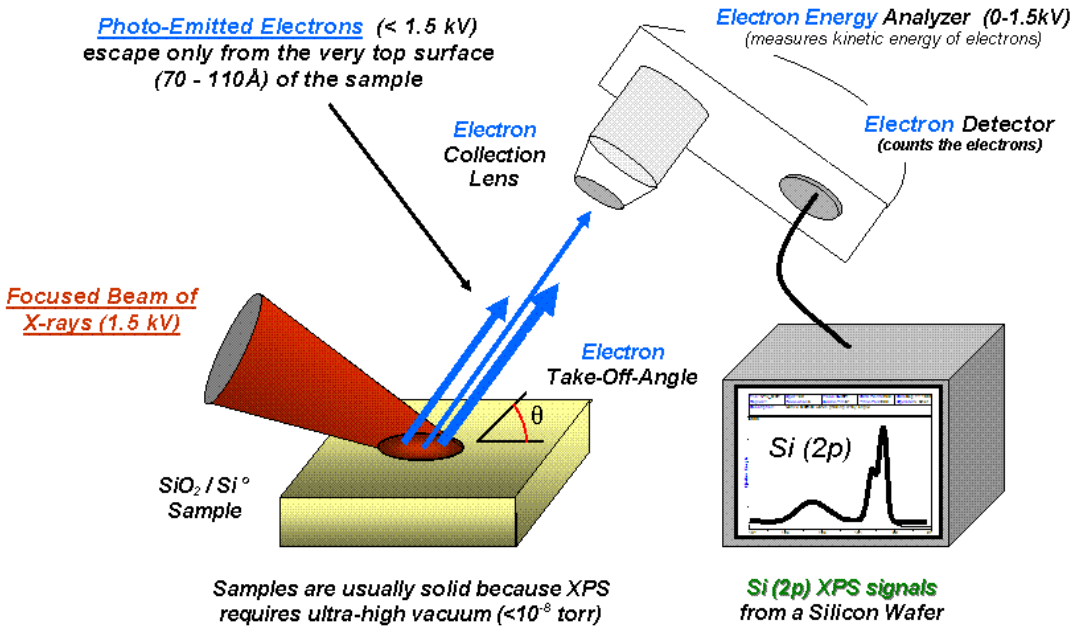

Figure 2.1: Schematic diagram of a typical XPS experimental setup.[2]

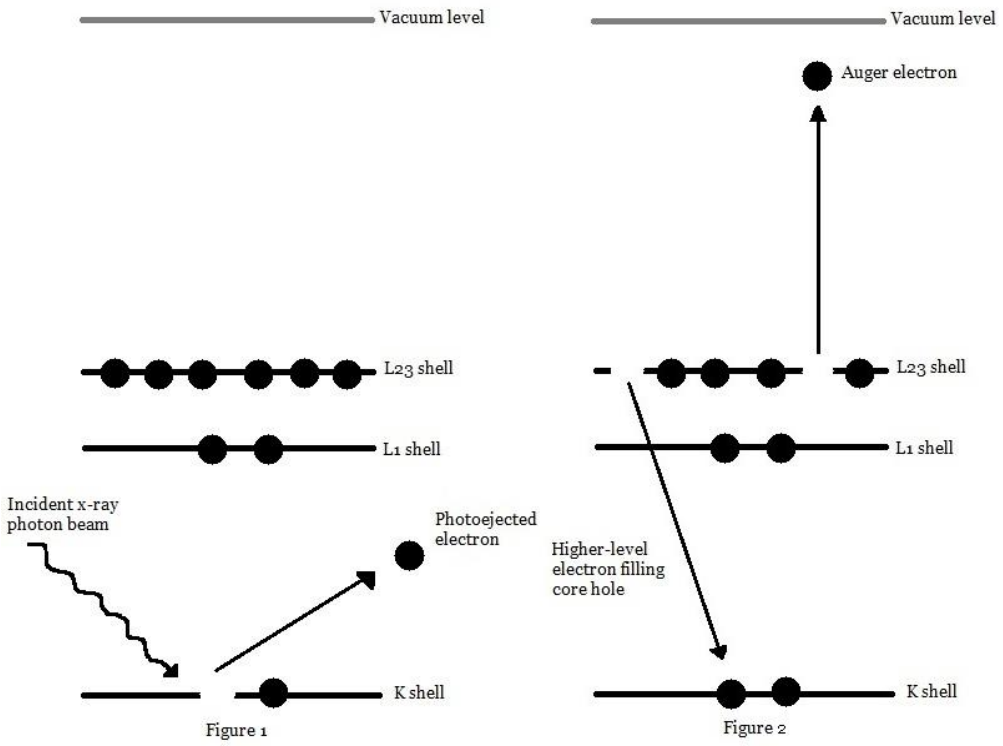

Figure 2.2: Energy level diagram illustrating the generation of X-ray-induced photoelectrons (left) and Auger electrons (right).[3]

system in the form of another electron, in what is known as the Auger process (Figure 2.2, right panel), or as an X-ray photon in a process known as X-ray fluorescence. A series of electrostatic or magnetic lenses collects and focuses both the photoelectrons and Auger electrons into a hemispherical analyzer that separates them based on their kinetic energies before they arrive at a detector. The measured kinetic energies of the photo-ejected electrons are directly related to their binding energies, which are characteristic of the atoms from which they were emitted since core-level electrons do not participate in chemical bonding but are sensitive to changes in the electronic structure of the material, thus providing elemental identification as well as information about the oxidation state of

the material. The number of electrons counted by the detector can be used to quantify the composition of the sample. The kinetic energy of the Auger electron is not related to its binding energy; however, when Auger electrons are present, they can be useful. For example, they can be used to distinguish Cu(0) from Cu(I) even though the two species have virtually inseparable binding energies.

For X-ray induced photoelectrons, the original binding energy, E_B, of the core-level electron in the atom can be calculated using the equation:

$$E_B = h\nu - E_K - \theta \qquad \text{Equation 1}$$

where $h\nu$ is the incident photon energy, E_K is the measured kinetic energy of the photoelectrons, and θ is the work function of the spectrometer, which denotes the minimum energy necessary to eject an electron from the valence band into vacuum. For typical lab-based X-ray sources, $h\nu$ is 1253.6 eV for a Mg anode or 1486.6 eV for an Al anode. Though these X-rays are able to penetrate rather deeply into a material, the sampling depth of this technique is limited by the mean free path of the photoelectron as it travels out through the layers of the sample towards vacuum and is therefore no more than ~10 nm deep, which makes XPS a surface characterization technique.

2.2 AMBIENT PRESSURE X-RAY PHOTOELECTRON SPECTROSCOPY (APXPS)

The fundamental concept of APXPS is the same as the UHV-based forerunner, but it can provide elemental identification and chemical environment information under much higher pressure conditions with current technology reportedly able to operate under pressures at or below ~22 Torr, or about 10 orders of magnitude higher than traditional UHV XPS systems.[4] APXPS has an additional advantage in that it can also identify gas phase reactant and product molecules between the surface and the analyzer, which can be

used to complement simultaneous mass spectrometry analysis of the reaction environment.[5]

APXPS overcomes the traditional pressure limitations previously discussed in two ways: one, by using a differentially-pumped analyzer, and two, by enclosing a synchotron or monochromated X-ray source behind an X-ray transparent window. As illustrated in Figure 2.3, in an APXPS experiment, the sample is brought extremely close (~150-500 μm) to a conical aperture on the analyzer with a very small diameter (~0.3-1.0 mm). The hemispherical analyzer is divided into 4 stages, each with its own oil-less pump to progressively drop the pressure from the Torr regime. Along the neck of the analyzer, electrostatic lenses guide the photoelectrons through small apertures between each stage to the detector, which is able to operate because the differential pumping system brings the pressure down to UHV levels.[4] The X-ray sources used in APXPS are

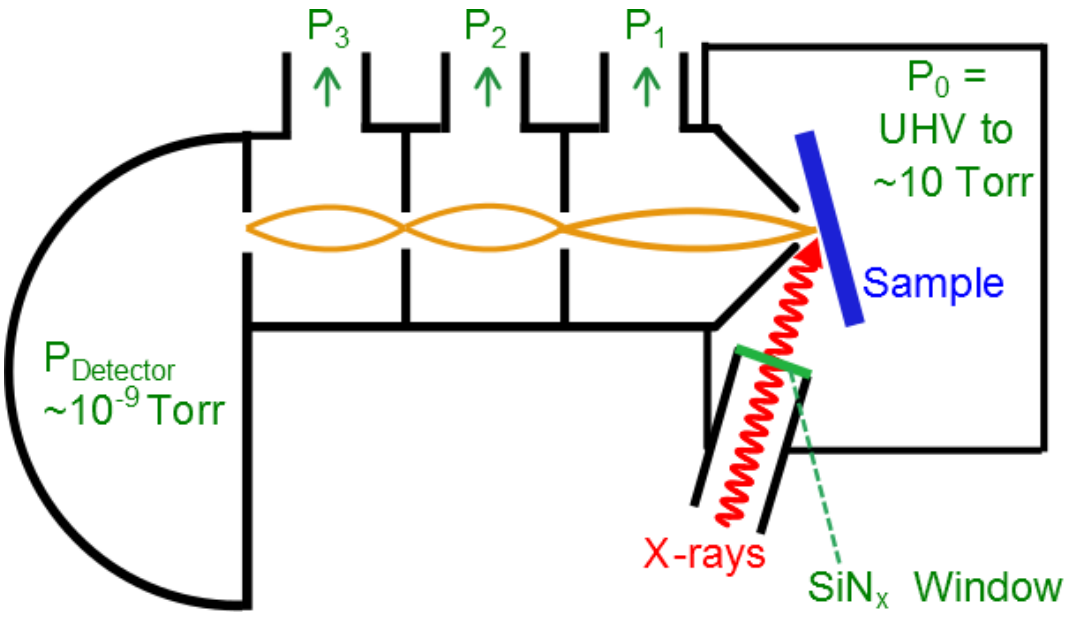

Figure 2.3:. Schematic diagram of a typical APXPS experiment.

often synchrotron based; however, lab-based APXPS units which use monochromated sources also exist. In either case, vacuum is still a necessity for operation, so for APXPS experiments, the source must be separated from the Torr level pressures in the chamber. This is achieved by enclosing the source behind an ultrathin silicon nitride window, which is X-ray transparent. A 100 nm thick window can maintain UHV on the source side and greater than 1 atm of pressure on the chamber side.[4]

2.3 HIGH PRESSURE CELLS

A relatively simple approach to merging the benefits of vacuum with the relevance of high pressure studies is the use of high pressure cells, which allow samples to be temporarily exposed to high pressures and temperatures within the confines of a UHV chamber so that they can be characterized by traditional UHV techniques before and after exposure to reaction gases without exposure to air. While these can be homemade, the one used for the work described herein is a "catalytic cell" commercially produced by Kratos Analytical. Small quantities of powdered samples as well as other materials can be introduced to the chamber via a loadlock system without breaking the main chamber vacuum. Samples can be characterized by XPS in vacuum using a monochromated Al source with a 1 mm^2 spot size, which is necessary for looking at small quantities of powders. Both conductive and insulating samples can be analyzed since the chamber is equipped with a charge neutralizer. The samples can then be transferred in vacuum to a small cell which can be valved off to the rest of the chamber and filled with gas, and a boron nitride heating element along with a type K thermocouple positioned underneath the sample stub allow the sample to be heated in the gas.

Afterwards, the gas can be pumped out of the cell and the sample transferred back in vacuum to the analysis chamber for post-reaction XPS.

2.4 UHV-COUPLED REACTORS

Though high pressure cells like the one described above are convenient ways to investigate the surface effects of high pressures of gases, in this case, particularly on powdered materials instead of model catalysts, they do not always allow for in situ characterization like APXPS, nor do they usually allow for kinetic studies. Instead, the kinetic studies referred to in this work were performed on a novel recirculating loop microreactor, which is coupled to a UHV chamber for full characterization by UHV techniques before and after reaction without exposure to air as shown in Figures 2.4 and 2.5.[6] Thus, this setup allows the user to study the oxidation states of air-sensitive materials such as Re in a semi-*in situ* fashion. Designed for use with model, planar catalysts which have a low number of active sites compared to commercial catalysts, the

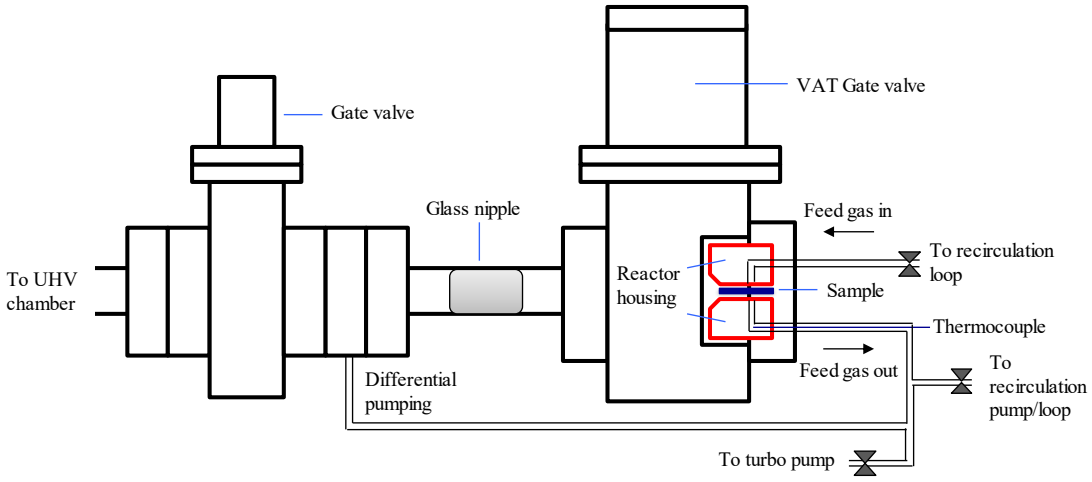

Figure 2.4:. Schematic diagram of the recirculation loop reactor used in this work.[6]

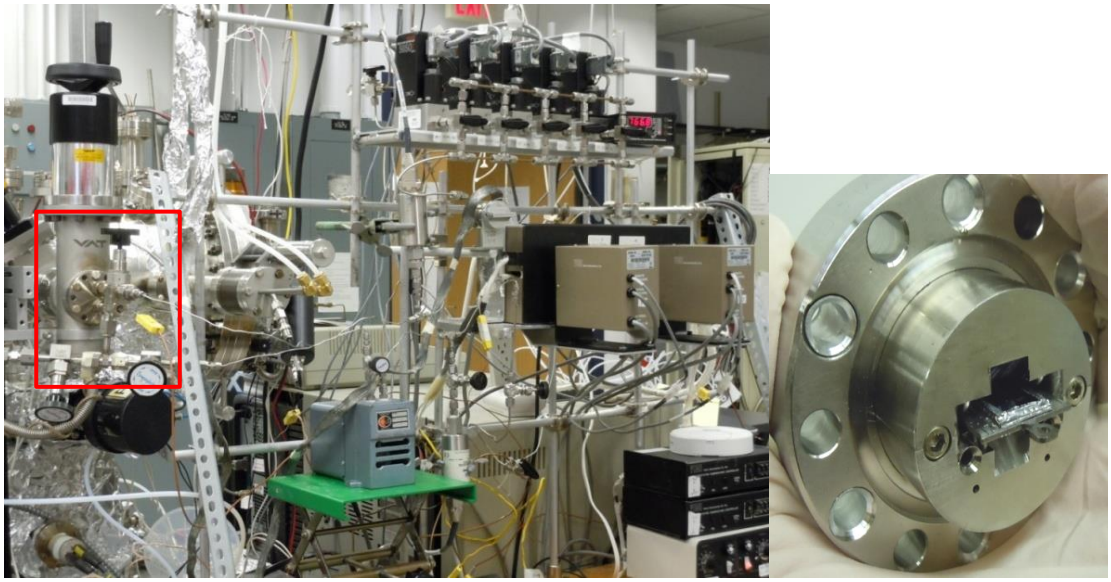

Figure 2.5:. Photographs of the recirculation loop reactor used in this work.[6]

reactor has a small dead volume and can operate in a recirculating fashion to build up product levels over time until they are at a quantity sufficient to detect. Reactant feed gases are configured using calibrated mass flow controllers, and products are analyzed via gas chromatography (GC) with either thermal conductivity detectors (TCD) or flame ionization detectors (FID). With this design, kinetics can be studied under near steady state conditions by replacing the gas lost to sampling injections with fresh feed gas so that the reactant concentrations are consistently maintained even over extended time periods.[6]

2.5 LOW ENERGY ELECTRON DIFFRACTION (LEED)

Most commonly used for determining surface structure, symmetry, and periodicity, or long range order, LEED is the observation of a diffraction pattern of electrons from a crystal surface. LEED operates on the principle that a beam of electrons

with an energy of about 150 eV has a wavelength on the order of 1 Å, which is shorter than most interatomic spacing and thus ideal for diffraction experiments.[1] Furthermore, that energy is low enough to fall near the minimum of the universal curve as shown in Figure 2.6, which makes those electrons very surface sensitive due to the short inelastic mean free path.[1] In LEED, an electron gun emits a focused, low-energy beam of electrons (generally in the range of 20-300 eV) perpendicular to the surface plane of the sample.[8] The inelastically-backscattered electrons are filtered out by a series of grids set at various potentials while the elastically-scattered electrons are allowed to pass and impinge on a phosphor screen, forming a pattern that can be viewed from the outside of the UHV chamber as depicted in Figure 2.7. The diffraction pattern can be used to determine whether a surface is symmetric or if it has undergone a reconstruction. It can be used to identify surface defects, steps, or islands on a clean surface, or it can be used to identify whether adsorbates are arranged in uniform or random overlayers. For the

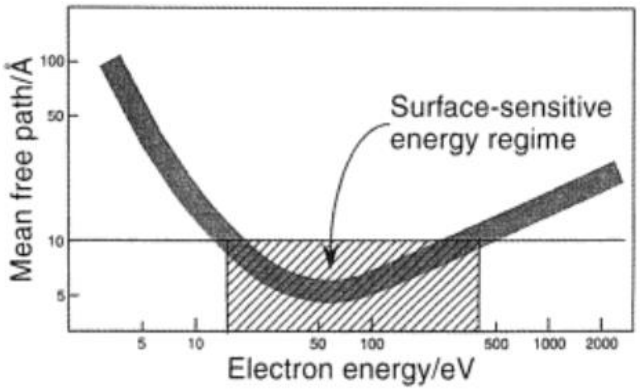

Figure 2.6: Universal curve for the electron inelastic mean free path (IMFP, Å) in elements as a function of electron energy (eV). Data source: Somorjai, G. A. *Science* **1985**, *227*, 902.[7]

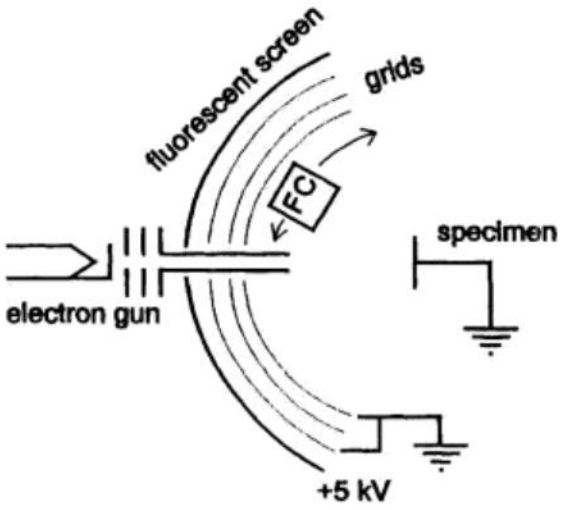

Figure 2.7: Schematic diagram of a typical LEED experimental setup. FC denotes a Faraday cup used to collect the diffracted electron current.[9]

purposes of this work, LEED was only used to positively identify the surface structure and crystallinity of the Pt(111) (Figure 2.8) and TiO_2(110)-(1x1) (Figure 2.9) surfaces, the latter of which is known to undergo reconstruction to a (1x2) surface over time with repeated or particularly harsh reduction cycles.

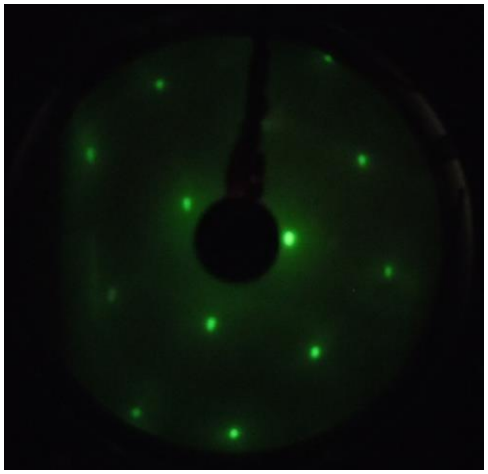

Figure 2.8: LEED of Pt(111).

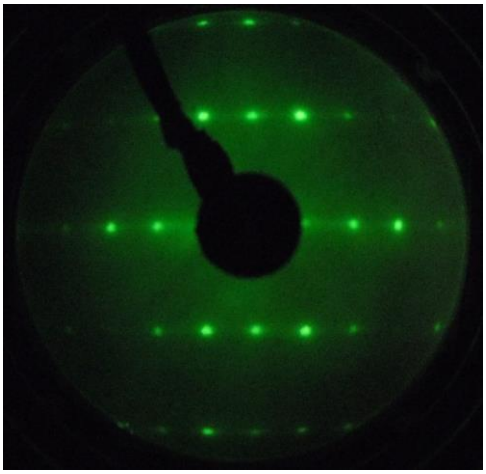

Figure 2.9: LEED of TiO_2(110)-(1x1).

2.6 SCANNING TUNNELING MICROSCOPY (STM)

Another technique which can also be used to determine surface structure is scanning tunneling microscopy. STM is a surface imaging technique developed by IBM scientists Gerd Binnig and Heinrich Rohrer, who won the Nobel Prize in Physics in 1986 for its use. As depicted in Figure 2.10, an atomically sharp, conductive tip is placed within a few angstroms away from the surface of a conductive or semiconductive sample, a tunneling voltage is applied to the system, and then a piezoelectric tube with feedback control scans the tip in raster fashion across the surface.[1] Operating on the principle of quantum tunneling, an image is generated by the electron density of the surface which can be correlated to a three-dimensional topographical map for surfaces with reasonably uniform electronic properties.[1] At its best, STM has a vertical resolution of 0.01 Å and a lateral resolution of 0.1 Å, which means it can be used to image surfaces on the atomic

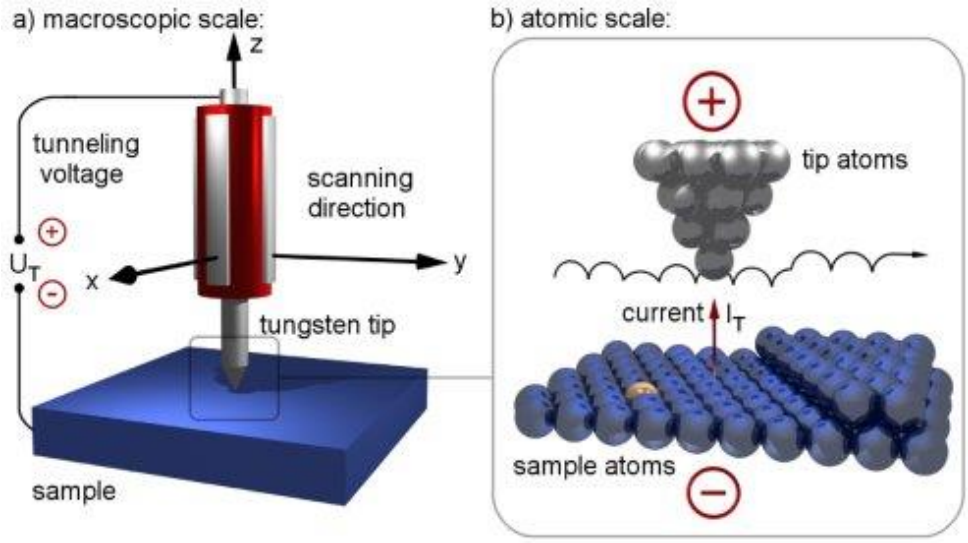

Figure 2.10: Schematic diagram of a typical STM experimental setup.[10]

level and is therefore extremely useful for identifying defect sites, determining surface roughness, and measuring the size of surface adsorbates.[1] In this work, STM was primarily used to establish surface cleanliness, characterize the growth of metal clusters on the support surfaces, monitor the changes in surface morphology as a function of sample temperature, and determine the conditions necessary for forming bimetallic clusters.

2.7 LOW ENERGY ION SCATTERING SPECTROSCOPY (LEIS)

Also commonly referred to generally as ion scattering spectroscopy (ISS), LEIS is a highly surface sensitive technique which is used to probe only the first atomic layer of a sample. In LEIS, the sample surface is bombarded with an ionized inert gas, commonly $^{4}He^{+}$, $^{3}He^{+}$, or $^{20}Ne^{+}$ (Figure 2.11), and an electrostatic analyzer measures the kinetic

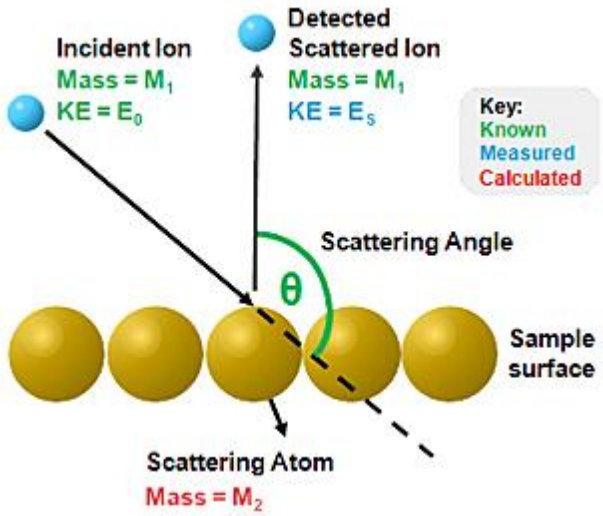

Figure 2.11: Schematic depicting the key event which takes place during an LEIS experiment: a probe ion impinging on a surface and elastically backscattering to a detector.[12]

energy of the ions that survive the backscattering process (Figure 2.11).[11] The ion energies used (typically 0.5-5 keV) are low compared to other ion scattering techniques such as Rutherford backscattering spectroscopy, but they are high enough to negate any contributions that might arise from thermal vibrations or phonons, which are generally on the order of an eV.[1] Thus the system of ion and target surface atom can be simplified to a two-body elastic collision, where according to the principle of conservation of momentum, the mass of the surface atom that scattered the He+ ion can be calculated, thus providing elemental identification of the surface atom.

The technique's sensitivity is limited to the topmost atomic layer because only the ions which have limited interaction with the surface are elastically backscattered still as ions that can be detected while the ions which penetrate deeper become neutralized by the grounded, conductive or semi-conductive sample and therefore have no chance of returning to the analyzer.

2.8 AUGER ELECTRON SPECTROSCOPY (AES)

Though briefly described in the previous section as occurring during XPS, the Auger process can occur outside of XPS as well. In AES, a core-level electron is initially ejected from the atom by an outside electron from a beam with sufficient energy (~1.5-5 keV) and intensity (1-100 μA), leaving a hole behind. A higher level electron lowers the energy of the system by falling into the core to fill the hole, and the excess energy is emitted as a third electron, known as the Auger electron, which are the ones analyzed. AES provides information about the elemental composition of the top 2-10 atomic layers of a sample and is therefore very surface sensitive.[1]

2.9 TEMPERATURE PROGRAMMED DESORPTION (TPD)

TPD is a technique relying on mass spectrometry that can be used to provide information about the composition of the topmost surface layer as well as its reactivity. In TPD, a saturating coverage of a probe molecule is adsorbed onto a surface at liquid nitrogen temperatures, and the surface is placed in front of a mass spectrometer and heated in a linear fashion. The mass spectrometer is used to detect the mass fragments of products desorbing from the surface, which are plotted in a TPD spectrum as a function of temperature. From the TPD spectrum, one can identify reaction products, quantify product yields, probe reaction kinetics, and determine heats of adsorption.

2.10 REFERENCES

(1) Vickerman, J. C. and Gilmore, I. S., Ed. *Surface Analysis: The Principal Techniques*. 2nd ed.; John Wiley & Sons: Chichester, UK, 2009.

(2) X-ray photoelectron spectroscopy. https://en.wikipedia.org/wiki/X-ray_photoelectron_spectroscopy (accessed February 6, 2016).

(3) X-ray Photoelectron Spectroscopy (XPS). https://wiki.utep.edu/pages/viewpage.action?pageId=39193783 (accessed February 6, 2016).

(4) Newberg, J. T.; Ahlund, J.; Arble, C.; Goodwin, C.; Khalifa, Y.; Broderick, A., A lab-based ambient pressure X-ray photoelectron spectrometer with exchangeable analysis chambers. *Rev. Sci. Instrum.* **2015,** *86* (8), 085113. 55.

(5) Salmeron, M.; Schlögl, R., Ambient pressure photoelectron spectroscopy: A new tool for surface science and nanotechnology. *Surf. Sci. Rep.* **2008,** *63* (4), 169-199.

(6) Tenney, S. A.; Xie, K.; Monnier, J. R.; Rodriguez, A.; Galhenage, R. P.; Duke, A. S.; Chen, D. A., Novel recirculating loop reactor for studies on model catalysts: CO oxidation on Pt/TiO_2(110). *Rev. Sci. Instrum.* **2013,** *84* (10), 104101. 56.

(7) Kolasinski, K. W., *Surface Science: Foundations of Catalysis and Nanoscience*. 1st ed.; John Wiley & Sons: Chichester, UK, 2002.

(8) D. P. Woodruff, T. A. D., *Modern Techniques of Surface Science*. 2nd ed.; Cambridge University Press: Cambridge, UK, 1994.

(9) Hudson, J. B., *Surface Science: An Introduction*. John Wiley & Sons: New York, 1998.

(10) Scanning tunneling microscope. http://www.physics.rutgers.edu/Bartgroup/STM.htm (accessed March 21, 2016).

(11) Hudson, J. B., *Surface Science: An Introduction*. John Wiley & Sons: New York, 1998.

(12) Low-energy ion scattering. http://xpssimplified.com/ion_scattering_spectroscopy.php (accessed March 21, 2016).

CHAPTER 3

IN SITU STUDIES OF CARBON MONOXIDE OXIDATION ON PLATINUM AND PLATINUM–RHENIUM ALLOY SURFACES[1]

[1] Reprinted (adapted) with permission from Duke, A. S.; Galhenage, R. P.; Tenney, S. A.; Sutter, P.; Chen, D. A. *In Situ* Studies of Carbon Monoxide Oxidation on Platinum and Platinum–Rhenium Alloy Surfaces. *J. Phys. Chem. C*, **2015**, *119* (1), 381-391. Copyright 2015 American Chemical Society.

3.1 INTRODUCTION

Bimetallic surfaces are known to exhibit superior catalytic properties compared to the pure metals due to electronic metal-metal interactions (ligand effects) or the creation of unique mixed-metal surface sites (ensemble effects).[1-5] The Pt-Re bimetallic system has been used as an industrial catalyst for naptha reforming since the 1960s;[6-8] the Pt-Re catalysts have greater long-term stability as well as greater resistance to poisoning by carbonaceous residues compared to Pt.[7,9-11] Pt and Re readily form bulk alloys over a wide compositional range,[12] and previous studies have reported significant electronic interactions between the two metals in Pt-Re alloys.[11,13-15] More recently, Pt-Re catalysts on carbon supports have attracted interest for aqueous phase reforming (APR) of biomass-derived carbohydrates to pure hydrogen, which can be used in hydrogen fuel cells and other catalytic applications.[16-25] The Dumesic group has found that Pt-Re/C catalysts are 5 times more active than pure Pt for APR of model polyols like glycerol, and this higher activity was primarily attributed to weaker binding of CO to Pt on the Pt-Re surfaces, resulting in decreased CO poisoning of Pt active sites.[16,17] Alternatively, Hensen and coworkers have proposed that the higher activity of Pt-Re in APR stems from greater activity for the water gas shift (WGS) reaction, which removes the undesired CO byproduct.[22-24] Specifically, the WGS reaction is facilitated by the presence of rhenium oxide, which provides active sites for activation of water, given that water is not easily dissociated at Pt sites. A number of other studies have also demonstrated that Pt-Re/TiO_2 has greater activity for the WGS reaction compared to Pt/TiO_2 due to dissociation of water on ReO_x.[26-30] Furthermore, density functional theory (DFT) calculations for the WGS reaction on $Pt_3Re(111)$ report that the active Pt-Re site is likely to contain partially

oxidized ensembles.[31] It has also been proposed that Re-OH formation promotes hydrogenolysis of glycerol through direct activation of C-OH bonds.[21] Thus, the exact role of Re as a promoter in Pt-Re catalysts for APR is still not completely understood.[19]

In this work, CO oxidation on Pt, Re films on Pt and Pt-Re surface alloys is investigated as a model system for understanding the interactions between CO and the Pt-Re surface under oxidizing reaction conditions. CO oxidation is selected as a probe reaction because CO oxidation has been well-studied on single-crystal Pt surfaces,[32-35] including near ambient pressure X-ray photoelectron spectroscopy (APXPS) experiments for CO oxidation on Pt(111).[36] Furthermore, CO oxidation on bimetallic Pt-Re surfaces in ultrahigh vacuum (UHV) show different behavior than on the pure metal surfaces since surface CO was completely removed by exposure to O_2 on Pt-Re but not on pure Pt or pure Re.[37] APXPS experiments are used here to investigate oxidation states of Re and surface species during reaction at pressures of 550 mTorr, and this represents the first study of Re oxidation states for Pt-Re surfaces under reaction conditions. Furthermore, these experiments allow the stability of ReO_x in an oxidizing reaction environment to be probed, and this is important because Re_2O_7 is known to sublime at relatively low temperatures ranging from 423 K for supported particles[38] to 500 K for bulk rhenium oxide.[39]

The results from these investigations demonstrate that CO binds less strongly to the Pt-Re alloy surface than to Pt(111), given that very little CO adsorbs during CO oxidation at 450 K on Pt-Re compared to Pt(111). The Pt-Re surface alloy consists of Re deposited on Pt(111) and annealed to 1000 K; STM and LEIS experiments indicate that under these conditions, the Re atoms diffuse into the Pt surface and the surface

composition is close to pure Pt. Oxygen is more easily dissociated on the Re film compared to Pt(111) at room temperature, and O_2 dissociation is also more facile on the Pt-Re alloy compared to Pt(111). CO oxidation activity is similar on all three surfaces although the Pt-Re alloy is the most active, followed by Pt(111). The Re film on Pt is unstable under CO oxidation conditions due to significant sublimation of Re around 450 K, and therefore the observed activity of the Re film is nearly identical to Pt(111).

3.2 EXPERIMENTAL

Experiments were carried out in two UHV chambers. The first chamber has been described in detail elsewhere[40-43] and is equipped with a variable-temperature STM (Omicron, VT-25), a hemispherical analyzer (Omicron, EA 125) for low energy ion scattering, and low energy electron diffraction optics (Omicron, Spec3). APXPS studies were conducted in the second chamber, which was on the X1A1 beamline at the National Synchrotron Light Source.[44,45] This chamber is equipped with a differentially pumped hemispherical analyzer (SPECS, Phoibos 150 NAP) with a CEM 9 channeltron detector; the analyzer is offset by 70° from the beam of incident radiation and 20° from the surface normal of the sample. Three stages of differential pumping allow the pressure in the chamber to be raised to ~5 Torr while maintaining high vacuum in the analyzer. The chamber could be quickly pumped down from elevated pressures via a 500 L/s turbomolecular pump (Pfeiffer TMU/H 521), and low pressures were monitored with an ion gauge (base pressure ~1.0×10^{-9} Torr). A stainless steel capillary tube (0.76 mm diameter) positioned ~1 mm from the surface of the crystal allowed analysis of the gaseous products formed on the surface while acquiring XPS data at elevated pressures.

This capillary tube is differentially pumped into an antechamber that houses a mass spectrometer (Pfeiffer Prisma Plus, QME220).

For the APXPS experiments involving CO oxidation, the chamber was backfilled with 500 mTorr O_2 (99.997%, Matheson) followed by 50 mTorr CO (99.998%, Matheson) through two separate variable leak valves. Chamber pressures in this range were monitored with a capacitance manometer. The surface of the crystal was positioned 500 μm away from a 500 μm aperture separating the first stage of the analyzer from the chamber. A 100 nm thick X-ray transparent Si_3N_4 window isolates the beamline from the chamber so that pressures of several Torr can be achieved while maintaining high vacuum in the beamline. The Re(4f), Pt(4f), and C(1s) regions were collected with an incident photon energy of 545 eV, while the O(1s) region was collected at 730 eV. Relative binding energies were set with respect to the valence band edge, and the absolute energies were determined by setting the Pt($4f_{7/2}$) binding energy at 71.0 eV, which is the binding energy of metallic Pt.[46] At 730 eV, the Pt($4f_{7/2}$) region was not acquired, and therefore the absolute binding energies were set according to the position of the Fermi edge in the valence band region. Peak fitting of the Re(4f) spectra was conducted with the shareware program fitXPS2 using a linear background and Gaussian-Lorentzian peak shapes with an asymmetry factor to generate a Doniach-Sunjic profile.

A Pt(111) single crystal (99.999%, Princeton Scientific Corp., 8 mm diameter, 2 mm thickness) was used for all experiments. The sample temperature was measured by a type K thermocouple spot welded directly to the edge of the crystal. In the first chamber (STM/LEIS), the crystal was mounted by press-fitting two Ta wires into 1.1 mm deep slots cut into the sides of the crystal. The Ta wires were spot welded onto a standard

Omicron sample plate with a 8.9x8.9 mm^2 window cut in it so that the back of the crystal could be directly heated by electron bombardment from a tungsten filament in the sample holder with the crystal biased at +600 V.[47] In the second chamber (APXPS), the crystal was pressed against a ceramic button heater (HeatWave Labs) covered by a Ta foil. The crystal was cleaned by cycles of Ar^+ ion sputtering at 1 kV for 10-20 minutes and subsequent annealing to 1000 K for 3 minutes. Surface cleanliness and crystallinity were established with a combination of scanning tunneling microscopy (STM), low energy electron diffraction (LEED), low energy ion scattering (LEIS) and XPS analysis.

Re was deposited at room temperature from a 2 mm diameter Re rod (ESPI, 99.99%) using a commercial Oxford Applied Research (EGC04) electron beam evaporator in the first chamber and a SPECS (EBE-1) evaporator in the second chamber. In the first chamber, the deposition rate was ~0.05 ML/min, and the Re coverage was measured using an independently calibrated quartz crystal microbalance.[48] One monolayer is defined as the packing density of the Re(0001) surface ($1.52x10^{15}$ atoms/cm^2). Re coverages for the APXPS experiments were estimated from the attenuation of the Pt($4f_{7/2}$) peak using a mean free path of 9.4 Å at 545 eV[49] for 20° off normal detection and assuming layer-by-layer growth of Re on Pt(111).[13] The deposition rate for the APXPS experiments was 0.1-0.2 ML/min.

In the STM experiments, the crystal was biased at +0.35 V with respect to the tip, and the images were collected at a constant tunneling current of ~4.0 nA. STM tips consisted of 0.38 mm tungsten wire that was electrochemically etched in NaOH and subjected to Ar^+ sputtering.[42] Average island heights for the 2.2 ML Re film before and after annealing to 800 K were determined from measuring 30 islands on the surface.

Low energy ion scattering (LEIS) experiments were conducted with 600 eV He^+ ions, and the acquisition parameters were adjusted to minimize damage from He^+ bombardment during successive scans. The peak intensity increased by only 13-15% after 3-5 scans, and therefore the amount of Re removed from the surface by He^+ bombardment during the LEIS experiment was relatively small.

3.3 RESULTS

Characterization of Re-Pt Surfaces

The Re films and Pt-Re alloy surfaces used in this study were prepared by depositing Re onto Pt(111) and annealing to various temperatures. Figure 3.1a shows an STM image of 2.2 ML of Re on Pt(111) deposited at room temperature in the absence of annealing. The surface consists of small Re islands with diameters ranging from 30-60 Å, and the average height of the islands is 2.4±0.5 Å, which corresponds to the height of a single layer of Re. These islands appear to reside on a Re film that has ~2.4 Å deep depressions in the regions where the film is not perfectly continuous. After heating the

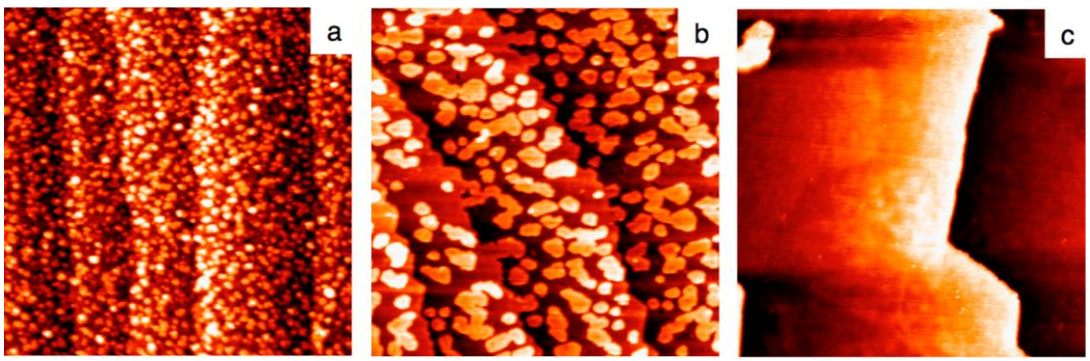

Figure 3.1: Scanning tunneling microscopy images for a 2.2 ML Re film deposited on Pt(111) at room temperature: a) before annealing; b) after annealing to 800 K for 1 min; and c) after annealing to 1000 K for 5 min. All images are 1000 Å x1000 Å.

surface to 800 K, (Figure 3.1b) the islands coalesce into larger, more regularly shaped structures that are still one atomic layer in height. After heating to 1000 K (Figure 3.1c), the Re islands diffuse into the surface, resulting in a Pt-Re alloy. This procedure for preparing the Pt-Re surface alloy was adapted from the work of Ramstad et al., in which Re films were also found to grow on Pt(111) in a layer-by-layer mode.[13]

The surface composition of the Pt-Re surface alloy was evaluated by LEIS experiments. Although the Pt and Re peaks cannot be clearly resolved due to the similar masses, it is still possible to extract qualitative information about surface composition. As shown in Figure 3.2, the spectrum for the 2.2 ML Re film (red trace) has a lower kinetic energy as well as a much lower intensity compared to the spectrum of clean Pt(111) (dotted trace). The relative sensitivity factors for Re and Pt were determined by

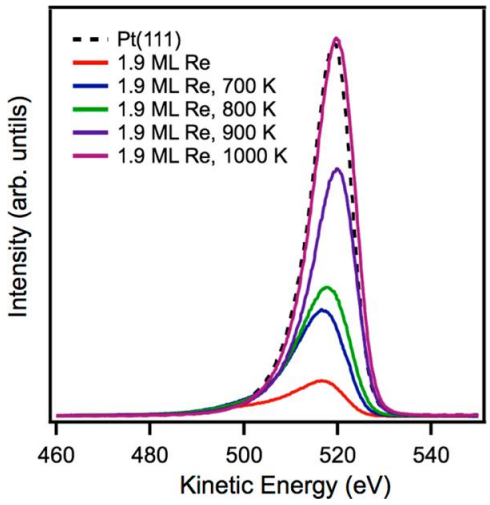

Figure 3.2: Low energy ion scattering spectra for a 2.2 ML Re film deposited on Pt(111) at room temperature and heated to 700 K, 800 K and 900 K for one minute each, and to 1000 K for 5 min. The dotted trace is the spectrum for the clean Pt(111) surface.

comparing intensities from polycrystalline Pt and Re foils with the same exposed surface areas. The LEIS experiment is 1.9 times more sensitive to Pt compared to Re, but the large disparity in intensities in Figure 3.2 is also partially attributed to the higher surface order for the Pt(111) surface compared to the unannealed Re film. After heating to 700 and 800 K, the overall increase in intensity is ascribed to exposure of Pt atoms at the surface, and this behavior is consistent with the STM image in Figure 3.1b that shows Re from the islands diffusing into the surface. At 900 K, the peak intensity continues to grow, and there is a clear shift to the higher kinetic energy associated with pure Pt. After heating to 1000 K for 5 min to prepare the Pt-Re alloy surface, the peak intensity and position are nearly identical to that of the Pt(111) surface, indicating that the top monolayer consists primarily of Pt atoms. Annealing at 1000 K for an additional 5 min did not change the LEIS spectrum.

XPS experiments established that the binding energy shifts for the Pt(4f) and Re(4f) peaks observed for Re on Pt(111) annealed to 1000 K are similar to those previously reported for other surface Pt-Re alloys.[13,37,50] For the clean Pt(111) surface, the Pt($4f_{7/2}$) peak is at 71.0 eV (Figure 3.3a). After the deposition of 2.9 ML of Re, the Pt intensity is attenuated by 47%, and the binding energy shifts to 71.55 eV. Annealing to 1000 K for 5 min does not change the binding energy, but the signal intensity increases to 70% of that on clean Pt(111) as surface Re atoms are driven into the bulk. The +0.55 eV shift in binding energy compared to clean Pt(111) is too high to be explained by a surface core level shift, given that the binding energies of the surface and bulk states are observed at 70.5 eV and 70.9 eV, respectively.[13,51] The Re($4f_{7/2}$) peak appears at 40.9 eV for the

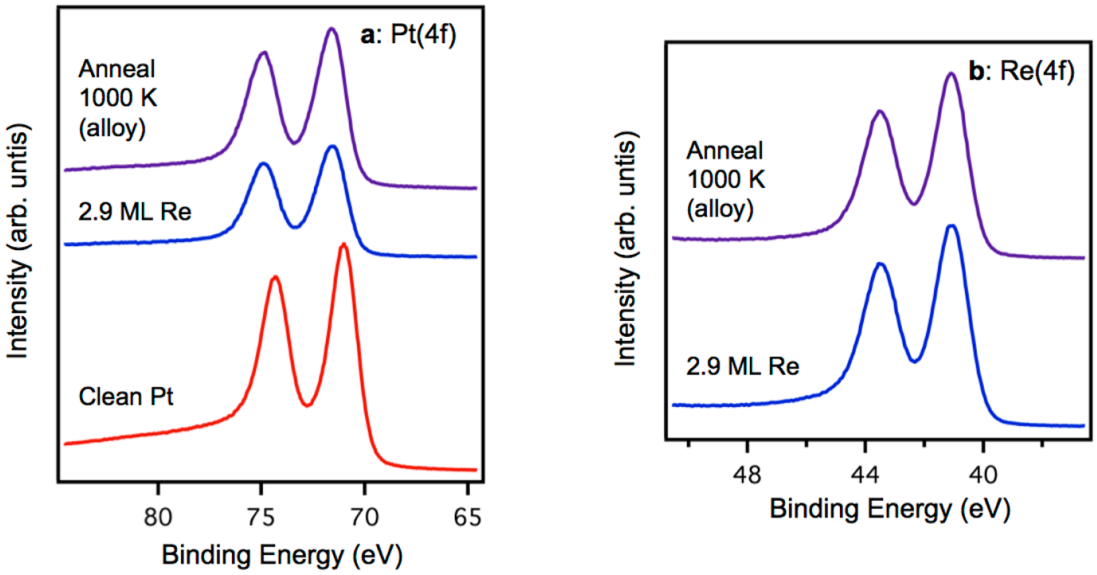

Figure 3.3: X-ray photoelectron spectroscopy data for a 2.9 ML Re film deposited at room temperature and heated to 1000 K for 5 min to prepare the Pt-Re surface alloy: a) Pt(4f); and b) Re(4f) regions. The incident photon energy was 545 eV.

2.9 ML Re film and does not shift upon annealing (Figure 3.3b). Furthermore, the 17% decrease in Re signal after heating to 1000 K is consistent with the calculated attenuation[49] of 20% for a model alloy surface, in which the top layer is pure Pt, and all of the Re atoms reside in the second, third, fourth and fifth layers, assuming a mean free path of 4.4 ML at an incident energy of 545 eV for the Re($4f_{7/2}$) photoelectrons. For comparison, the Re($4f_{7/2}$) peak is found at 40.3 eV for single-crystal Re surfaces with no appreciable surface core-level shift.[52,53] Thus, the higher Pt and Re binding energies for the Re/Pt surface are attributed to Re-Pt interactions in the alloy. Pt-Re alloys prepared by depositing 50-100 ML Pt films on polycrystalline Re and annealing to 1400 K resulted in Pt and Re($4f_{7/2}$) binding energies of 71.8-71.9 eV and 40.5-40.6 eV, respectively.[37,50] In addition, a study of a bulk Pt(68%)-Re(32%) alloy reported similar binding energies of 71.8 eV for Pt($4f_{7/2}$) and 40.8 eV for Re($4f_{7/2}$).[37] For Pt-Re surface alloys prepared by

depositing Re coverages up to 1 ML on Pt(111) and annealing to 1000 K, the Re($4f_{7/2}$) binding energy was 40.8-41.1 eV.[13]

The oxidation of a Re film and the Pt-Re alloy surface under 500 mTorr of O_2 was studied using APXPS in order to understand the various oxidation states of Re and the stability of Re oxide under reaction conditions. The Re(4f) region for a 1.6 ML Re film oxidized at room temperature and heated in oxygen up to 450 K is shown in Figure 3.4. For comparison, data for the Re film prepared in UHV before oxidation is also presented, and this spectrum is fit with one doublet with the Re($4f_{7/2}$) at 40.8 eV. For all of the Re(4f) fits, the splitting between the two peaks was fixed at 2.45±0.1 eV, and the $4f_{7/2}$:$4f_{5/2}$ peak area ratio was fixed at 4:3; the position of the Re($4f_{7/2}$) peak is used to designate the binding energies of both peaks in the doublet. The peak fits shown here are not unique, but in all cases the spectra were fit with the minimum number of peaks for the sake of simplicity, and the purpose of the peak fitting is to provide a general idea of the Re oxidation states present on these surfaces. After exposure to O_2 at room temperature, the main peak at 41.3 eV is assigned to Re^{+2}, given that ReO has a +1.0 eV shift from the bulk value of 40.3 eV.[54-56] Notably, atomic oxygen on metallic Re is also known to produce shifts of +0.2-0.7 eV from the binding energy of pure Re depending on the coordination number of the oxygen.[54,55,57] Higher oxidation states are observed with peaks at ~44 eV and 45.2 eV. After oxidation at 400 K, the 41.3 eV peak is still present, but the 44.0 eV peak becomes the most dominant feature. This peak is attributed to Re^{+5}, given that the binding energies for Re^{+6} (44.8-45.4 eV) are too high, and the binding energies of Re^{+4}(42.3-42.8 eV) are too low.[38,58-61] At 450 K, Re^{+5} is the primary oxidation state, but there is a smaller feature at 45.2 eV assigned to Re^{+6}, and this binding

energy species is also observed as a shoulder in the spectrum at 295 K. Although there is one report of Re^{+6} at 44.3 eV, the spectrum was not shown; the reported binding energy of Re^{+4} (43.2 eV) from the same work was also inconsistent with the other literature values, and the instrumental resolution based on data from other samples may preclude a definitive assignment.[62] There are only a few cases in which binding energies of 43.7-44.1 eV have been observed and tentatively assigned to Re^{+5}.[63-65] Pure Re_2O_5 is difficult to isolate and characterize because it is metastable in air, unstable in the presence of water and disproportionates into Re^{+4} and Re^{+7}.[66,67] It is therefore not surprising that the Re^{+5} oxidation state is not typically observed. However, under reaction conditions in a water-free environment, it is possible that the Re^{+5} could constitute the main oxidized Re species. A recent APXPS study of oxidation on Re foils have assigned the Re^{+7} and Re^{+6} oxidation states to 45.5 and 43.1 eV, respectively.[68] Since these assignments are in direct contradiction to all of the previous studies where Re^{+7} peaks are observed at 46.5-47 eV, and Re^{+6} at 44.8-45.4 eV we have followed the binding energy assignments supported by the existing literature.[38,58,61,62,69]

When the highly oxidized Re film is exposed to CO oxidation conditions of 500 mTorr O_2: 50 mTorr CO at 400 K, almost no Re signal is detected (Figure 3.4, top panel). The disappearance of the Re is attributed to sublimation of Re_2O_7, which is known to be highly volatile and reported to desorb at temperatures as low as 423 K-600 K.[38,39,58] Under CO oxidation conditions, it appears that Re(V) oxide is readily converted to Re_2O_7, which immediately sublimes, and consequently the highly oxidized Re film is not stable under CO oxidation conditions. However, the Pt-Re alloy surface is less easily oxidized than the Re film (Figure 3.5). At 500 K in O_2, there is still substantial

contribution from metallic Re observed at 40.8 eV for the Pt-Re alloy in UHV. The other main oxidation state is assigned again to Re^{+5} at 44.0 eV, and at 600 K, a large fraction of the Re is lost from the surface, presumably due to oxidation to Re_2O_7 and subsequent sublimation. Oxidation of the Pt-Re alloy at lower temperatures of 450 K does not result in significant formation of Re oxide, and most of the surface Re remains metallic (data not shown).

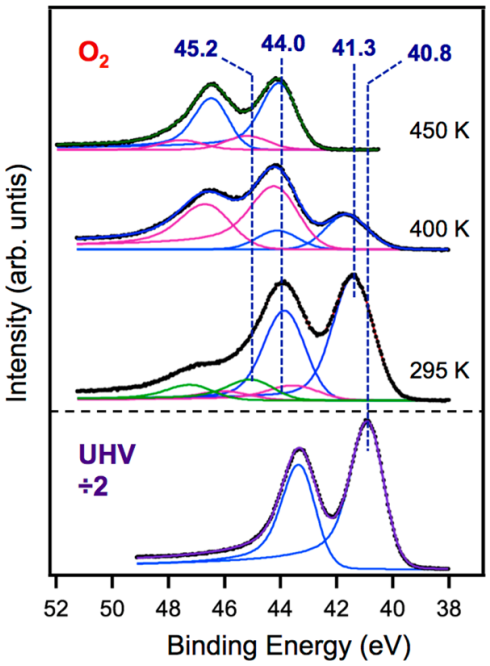

Figure 3.4: X-ray photoelectron spectroscopy data for the Re(4f) region for a 1.6 ML Re film on Pt(111): as prepared in UHV (bottom); after heating to various temperatures in 500 mTorr of O_2 (middle); and after heating the oxidized film to 400 K in 500 mTorr O_2 and 50 mTorr of CO (top). The incident photon energy was 545 eV. The vertical scale for the bottom panel is twice that for the top and middle panels.

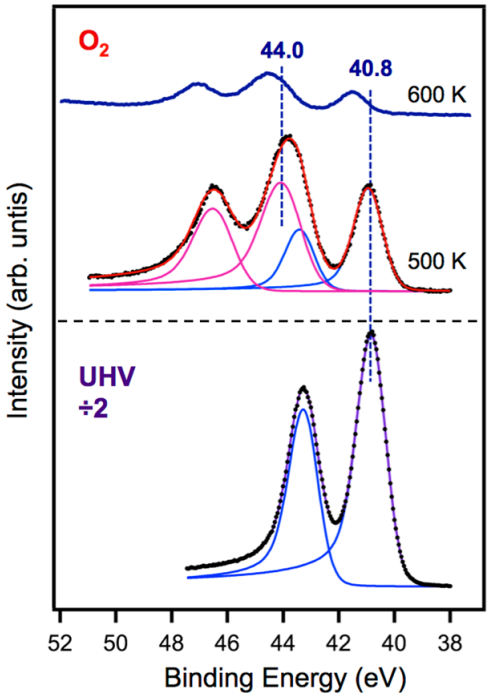

Figure 3.5: X-ray photoelectron spectroscopy data for the Re(4f) region for a 2.0 ML Re film on Pt(111) heated to 1000 K for 5 minutes to form the Pt-Re surface alloy: as prepared in UHV (bottom); and after heating to 500 and 600 K in 500 mTorr of O_2 (top). The incident photon energy was 545 eV. The vertical scale for the bottom panel is twice that for the top panel.

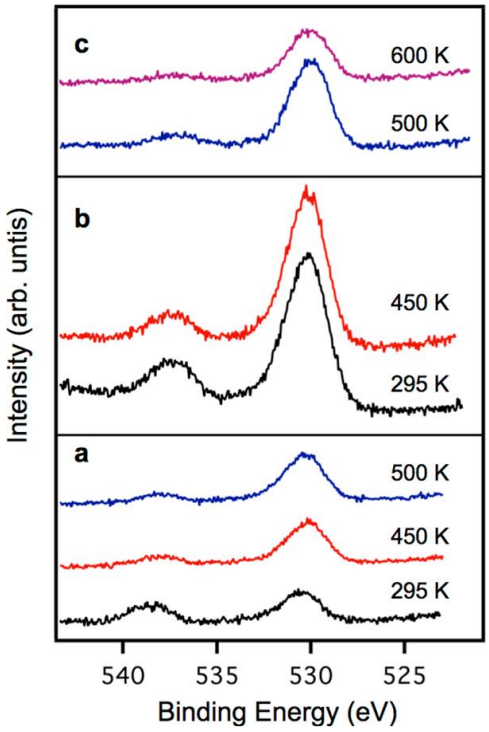

Figure 3.6: X-ray photoelectron spectroscopy data for the O(1s) region after heating the following surfaces to various temperatures in 500 mTorr O_2: a) Pt(111); b) a 1.6 ML Re film on Pt(111); and c) a 2.2 ML Re film on Pt(111) heated to 1000 K for 5 minutes to form the Pt-Re surface alloy. The incident photon energy was 730 eV.

The O(1s) region indicates that O_2 dissociation is more facile on the Re film and the Pt-Re surface compared to Pt(111) (Figure 3.6). The O(1s) peak appears at 530 eV on Pt(111) and is consistent with previous studies of atomic oxygen on Pt(111).[70,71] The O(1s) intensity is identical for oxidation at 295 K compared to 400 K (data not shown), and the high binding energy peak at ~538 eV is assigned to gas phase O_2.[72,73] Oxidation at 450 K results in a small increase in peak height, but there is no appreciable change

after oxidation at 500 K. There is no evidence for the shift in Pt($4f_{7/2}$) to higher binding energy associated with the formation of surface oxides.[70] Oxidation of the Re film at 295 K results in an O(1s) peak that is more than five times larger than on Pt(111) oxidized at the same temperature (Figure 3.6b). The peak intensity does not change after heating to 400 K and 450 K, and at higher temperatures the Re oxide decomposes and oxygen is lost from the surface. In the case of the Pt-Re alloy, oxidation at 500 K resulted in ~35% less surface oxygen than on the Re film at 450 K, but the integrated O(1s) intensity for the Pt-Re alloy was twice that of the Pt(111) surface oxidized at 500 K (Figure 3.6c). Oxidizing the Pt-Re alloy at 600 K caused the oxygen signal to diminish due to the decomposition of Re oxide at these higher temperatures. At 450 K, the O(1s) peak intensity on the PtRe alloy surface is similar to that on Pt(111) at the same temperature, and this behavior is consistent with the lack of Re oxide formation at 450 K.

Changes in the Re oxidation state during CO oxidation (500 mTorr O_2/50 mTorr CO) at various temperatures were also studied for the Re film and Pt-Re alloy. As shown in Figure 3.7a, the Re(4f) spectrum is almost unchanged for the Pt-Re alloy at 400 K. The metallic Re peak is the main spectral feature, and the only evidence for oxidation is a barely detectable shoulder around 47 eV and a distinct broadening of the Re($4f_{5/2}$) peak compared to the Pt-Re alloy spectrum collected in UHV. At 450 K, the peak at 47 eV increases, and the broadening of the Re($4f_{5/2}$) peak becomes more pronounced as the surface is further oxidized although the majority of Re is still in the metallic state. The high binding energy features can be fit with a peak at 44.6 eV, but it is not clear if this peak corresponds to the Re^{+5} or Re^{+6} oxidation states since this binding energy appears between the usual ranges for these two oxidation states. However, the binding energy is

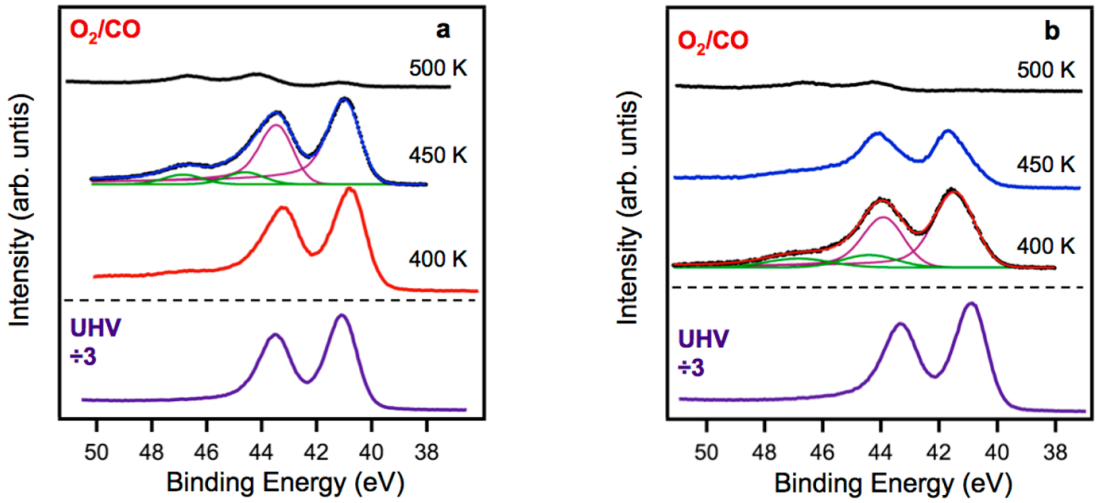

Figure 3.7: X-ray photoelectron spectroscopy data for the Re(4f) region for: a) the Pt-Re alloy surface prepared by depositing 2.9 ML Re on Pt(111) and heating to 1000 K for 5 min; and b) a 2.0 ML Re film on Pt(111). Spectra are shown for the surfaces immediately after preparation in UHV (bottom) and after heating in 500 mTorr O_2/50 mTorr CO to various temperatures (top). The incident photon energy was 545 eV. The vertical scale for the bottom panels is three times that for the top panels.

closer to 44.8 eV, which is the lowest of the Re^{+6} values reported in the literature.[38,58-61] At 500 K, the majority of the Re is lost via sublimation of Re_2O_7. For the Re film exposed to CO oxidation conditions without prior oxidation, substantial oxidation is observed even at 400 K (Figure 3.7b), indicating the reaction mixture of CO and O_2 is still highly oxidizing despite the presence of CO. The main peak is found at 44.5 eV and assigned to Re^{+5} or Re^{+6}, and the shoulder at 47 eV is more intense than for the Pt-Re alloy at the same temperature. At 450 K, the peaks continue to shift to higher binding energies as the Re becomes more oxidized, and the amount of Re remaining on the surface at 500 K is barely detectable.

During the APXPS experiments, the activity for CO oxidation was investigated by monitoring the 44 amu (CO_2), 28 amu (CO) and 32 amu signals (O_2) with the mass

spectrometer while the surfaces were under CO oxidation conditions. The surfaces were heated to 400 K, 450 K and 500 K and held at each temperature for 30-50 min until the mass spectrometer signals were constant while XPS data was collected. Data for CO_2 production (44 amu) are shown in Figure 3.8 for the Pt-Re alloy surface, Pt(111) and a Re film on Pt(111) as a function of reaction temperature. For all three surfaces, there is no activity for CO oxidation below 400 K, a sharp increase in CO_2 yield between 400 and 450 K, and only a small further increase in CO_2 production detected between 450 K and 500 K. Although the activities for all three surfaces are comparable, the Pt-Re alloy surface produces more CO_2 than Pt(111) over the entire temperature range. The Re film appears slightly less active than Pt(111) between 450 and 500 K, but this surface should

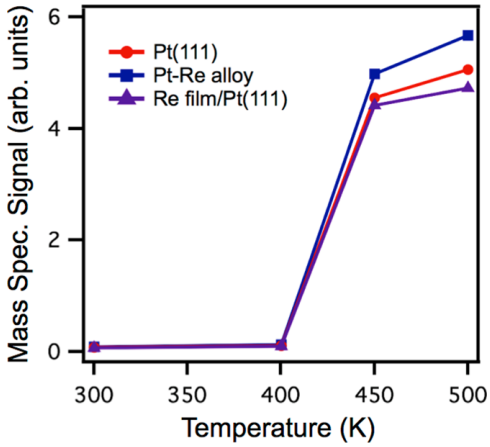

Figure 3.8: A plot of the CO_2 yield based on the mass spectrometer intensity at 44 amu as a function of temperature in 500 mTorr O_2/50 mTorr CO for reaction on: Pt(111) (circles); the Pt-Re alloy (2.9 ML Re on Pt(111), annealed at 1000 K for 5 min, squares); and a 2.0 ML Re film on Pt(111) (triangles).

be similar in composition to Pt(111) since the majority of Re(VII) has sublimed from the surface between 450 and 500 K.

The C(1s) and O(1s) regions during CO oxidation on Pt(111) indicate that CO remains on the surface until 450 K and desorbs after heating to 500 K (Figure 3.9). The C(1s) region at 295 K shows a major peak at 286.6 eV that is attributed to CO, given that the binding energy and peak shape are exactly the same as the peak observed when oxidized Pt(111) is exposed to 200 mTorr of CO at 295 K. In the higher binding energy region, the feature at 291 eV is assigned to gas phase CO;[72-74] when Pt(111) oxidized at 500 K is exposed to 200 mTorr of CO, a peak is observed at this same binding energy and disappears after the CO is pumped away. The feature at ~293 eV is attributed to gas

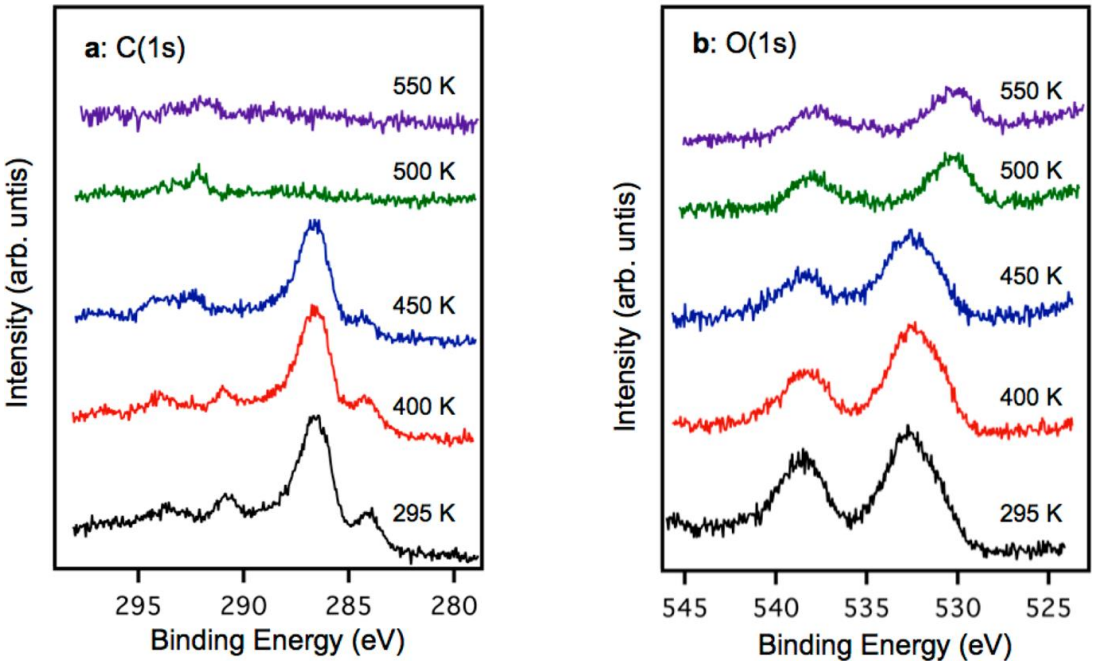

Figure 3.9: X-ray photoelectron spectroscopy data for the: a) C(1s); and b) O(1s) regions for Pt(111) while heating to various temperatures in 500 mTorr O_2/50 mTorr CO. The incident photon energies were 545 eV for the C(1s) region and 730 eV for the O(1s) region.

phase CO_2[72,73] and is also present in the spectra acquired at 400, 450, and 500 K. Furthermore, the peak at 284 eV is ascribed to atomic carbon,[75] which was still present on the surface after directly sputtering and annealing Pt(111) and is therefore not believed to be associated with CO adsorption or dissociation on the surface. After heating to 400 and 450 K, the intensity of the 286.6 eV peak is nearly unchanged, and the complete absence of this peak at 500 K indicates that all of the surface CO has desorbed. The O(1s) region at 295 K (Figure 3.9b) exhibits a feature at 532.6 eV assigned to surface CO, and the ~538 eV peak is attributed to gas phase CO[74,76] and O_2.[72,73] There is no decrease in intensity for the 532.6 eV peak at 400 K, but ~20% of the signal is lost at 450 K. At 500 K, the peak at 530.2 eV attributed to atomic oxygen on Pt is consistent with the binding energy of surface oxygen from O_2 dissociation. In addition, the 532.6 eV peak is absent at 500 K, in agreement with CO desorption at this temperature. Further heating to 550 K results in no additional changes in either the C(1s) or O(1s) spectra.

The C(1s) spectra collected during CO oxidation on the Pt-Re alloy demonstrate that the majority of the surface CO desorbs at 450 K, in contrast to what is observed on Pt(111). The surface CO peak at 286.6 eV initially diminishes after heating to 400 K, decreases to 33% of its intensity at 295 K after heating to 450 K, and is not detectable above the noise at 500 K (Figure 3.10a). No atomic carbon was detected on the surface after preparing the Pt-Re alloy in UHV, and therefore the 284 eV peak from atomic carbon is not observed. In the O(1s) region at 295 K (Figure 3.10b), both atomic oxygen and CO are detected on the surface at 530.3 and 532.5 eV, respectively. This confirms that the Pt-Re alloy surface dissociates O_2 more readily than Pt(111), given that a distinct peak from atomic oxygen is not observed on Pt(111) at this temperature. At 400 K, the

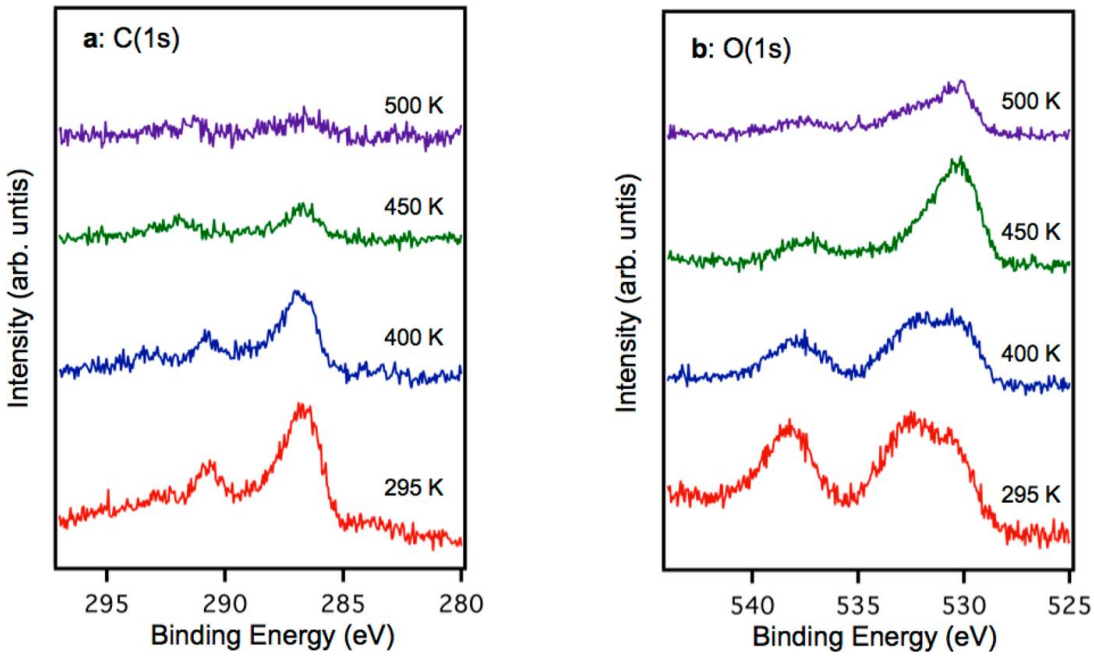

Figure 3.10: X-ray photoelectron spectroscopy data for the: a) C(1s); and b) O(1s) regions for the Pt-Re alloy (3.3 ML of Re on Pt(111), heated to 1000 K for 5 min) while heating to various temperatures in 500 mTorr O_2/50 mTorr CO. The incident photon energies were 545 eV for the C(1s) region and 730 eV for the O(1s) region.

intensity of the 532.5 eV peak decreases relative to the 530.3 eV peak due to the desorption of CO, and at 450 K atomic oxygen is the main surface species. The oxygen signal continues to diminish after heating to 500 K, presumably because Re_2O_7 sublimes from the surface at this temperature. The intensity of the O(1s) peak at 500 K is similar to that on the Pt(111) under the same conditions.

The Pt(4f) regions during CO oxidation for both Pt(111) and the Pt-Re alloy demonstrate that Pt is not oxidized under these reaction conditions (Figure A.1). For Pt(111), there is no change in peak shape due to the appearance of a higher binding energy shoulder from oxidized Pt, but the Pt($4f_{7/2}$) peak gradually shifts by +0.3 eV from the binding energy of clean Pt(111) as the reaction temperature increases to 500 K. Other

XPS studies also report a shift of around +0.3 eV in the Pt($4f_{7/2}$) binding energy for atomic oxygen on Pt(111).[71] Between 500 and 550 K, there is a -0.15 eV shift as most of the surface species desorb from the surface. For the Pt-Re alloy, the Pt($4f_{7/2}$) binding energy also shifts +0.3 eV between the value in UHV and the value at 450 K under reaction conditions. However, Re is removed from the surface at 500 K, and the peak position returns to the 71.0 eV observed for clean Pt(111).

3.4 DISCUSSION

Pt-Re surface alloys are prepared by annealing Re films on Pt(111) to 1000 K, as previously reported for lower coverage Re films on Pt(111).[13] STM experiments show that Re islands diffuse into Pt to form atomically flat surfaces, and LEIS studies demonstrate that the surface composition is ~ 100% Pt. The diffusion of Re into Pt(111) is in agreement with the lower surface free energy of Pt compared to Re (2.5 [77,78] vs. 3.6 J/m^2 [79-81]). Moreover, other studies in the literature have demonstrated that Pt should segregate to the surface of Pt-Re alloys. For example, a study of Pt films deposited on Re(0001) and annealed to 1000 K formed surface alloys that were Pt-rich.[82] An XPS study of a Re_3Pt polycrystalline alloy showed that the surface was enriched in Pt after annealing to 1200 K.[14] These results agree with Monte Carlo simulations for unsupported Pt-Re nanoparticles with sizes of 580-4000 atoms that also report surface segregation of Pt after annealing to 600 K.[83] The nanoparticles form core-shell structures in which the concentration of Pt at the surface is nearly 100% for $Pt_{75}Re_{25}$ and more than 85% for $Pt_{50}Re_{50}$ clusters; $Pt_{25}Re_{75}$ clusters smaller than 1000 atoms contain exclusively Re atoms in the core.

APXPS data illustrate that under CO oxidation conditions, CO desorbs from the Pt-Re alloy surface at lower temperature than on Pt(111). Specifically, there is no evidence for CO desorption on Pt(111) at 450 K, whereas the majority of CO has desorbed from the Pt-Re alloy surface. These results are in agreement with previous UHV investigations reporting that CO is more strongly bound to Pt(111) than to the Pt-Re alloy; temperature programmed desorption (TPD) studies of CO showed that onset temperature for CO desorption is lowered by more than 100 K on the Pt-Re alloy surface compared to Pt(111).[84] DFT calculations for CO on a Pt-Re alloy surface also support weaker CO adsorption on the Pt-Re alloy. For example, a 23% decrease in CO binding energy compared to Pt(111) was calculated for CO on a Pt-Re alloy surface modeled as a four-layer slab with the structure Pt-Re-Pt-Pt.[85] Similarly, a DFT study of CO adsorbed on 10-atom clusters showed that the adsorption energy for CO on Pt_6Re_4 was 36% lower than on Pt_{10}.[85] Based on these results and the lower adsorption energy of CO on Pt-Re/C compared to Pt/C catalysts measured by microcalorimetry,[16] it was proposed that the higher long-term activity of Pt-Re for oxidation reactions like APR is due to decreased CO poisoning since CO is more easily removed from Pt-Re compared to pure Pt.[16-18] In contrast, *in situ* infrared spectroscopy experiments carried out during the WGS reaction at 373 K on Pt/TiO_2 and $Pt\text{-}Re/TiO_2$ catalysts suggested that CO binds *more* strongly to Pt-Re than pure Pt, given the greater CO concentration observed on Pt-Re versus Pt.[86] It should also be noted that TPD of CO on Pt-Re/C and Pt/C catalysts showed higher desorption temperatures on Pt-Re/C.[16] However, the results reported here for *in situ* studies of CO oxidation on Pt-Re demonstrate that CO binds more strongly to Pt than Pt-

Re under oxidation conditions, and Pt is therefore more likely to be poisoned by CO during reactions in which CO is a byproduct.

Oxygen dissociates more readily on the Pt-Re alloy surface than on Pt(111) both under CO oxidation conditions and upon exposure to pure O_2. The amount of O_2 dissociated during CO oxidation at 295 K is significantly higher on Pt-Re compared to pure Pt, and this is true up to temperatures of 500 K when almost all of the Re(VII) has sublimed. For example, after exposure to pure O_2 at 500 mTorr, the amount of atomic oxygen formed on the Pt-Re alloy at 500 K is 1.5 times that on the Pt(111) surface, and a distinct peak from atomic oxygen is not observed in CO oxidation on Pt(111) but is observed on the Pt-Re alloy. However, UHV experiments for the adsorption of 20 L O_2 at room temperature reported that the resulting O(1s) signal was 30% lower on the Pt-Re alloy surface compared to Pt(111),[84] and there was no evidence for Re oxidation under these conditions. Our UHV experiments for the exposure of the Pt-Re alloy to O_2 at room temperature also show no oxidation of Re, and the concentration of surface oxygen is identical to that of Pt(111).[87] Higher oxygen exposure of 200 mTorr at room temperature for 2 hours induces oxidation of the Pt-Re alloy as well as an O(1s) signal that is 35% higher than on Pt(111).[87] These results imply that O_2 dissociation at higher pressures occurs more readily on the Pt-Re alloy than on Pt(111), whereas for lower O_2 exposures, the Pt-Re alloy and Pt(111) exhibit similar behaviors. It is assumed that the Re diffuses to the surface of the Pt-Re alloy to induce O_2 dissociation, given that Re oxidation and sublimation of Re_2O_7 are observed at temperatures of 450-500 K, and the higher O_2 pressures may promote diffusion of Re to the surface. Similarly, in Pt-Ni and Pt-Co alloys, surface segregation of Ni and Co occurred upon oxidation,[88-90] and oxygen-

induced segregation of other 3d metals was demonstrated by DFT studies for Pt-3d-Pt surface structures.[90,91] Another possibility is that the presence of Re under the Pt monolayer alters the chemical activity of Pt toward O_2 dissociation. However, DFT studies of Pt alloyed with the 3d metals in a 4-layer slab structure of Pt-3d-Pt-Pt show that the stability of the oxidized surface is greater for pure Pt than for the modified Pt surface;[92] likewise, DFT investigations of a Pt monolayer covering a Pt_3Co alloy surface indicate that the binding energy of oxygen is weaker on the Pt monolayer compared to the Pt(111).[93] Thus, there is no evidence that modification of Pt by an underlying transition metal like Re would enhance O_2 dissociation activity.

Under CO oxidation conditions at 400 K and above, the Re films on Pt(111) are unstable due to the formation and sublimation of the volatile Re_2O_7. However, the Pt-Re alloy is more resistant to Re oxidation and Re loss by sublimation. From this perspective, pure Re catalysts are not likely to be stable under highly oxidizing conditions although Re clusters supported on alumina are reported to be more resistant to sublimation than Re films on metal supports; for example, strong interactions between the support and partially oxidized Re are believed to inhibit oxidation to Re_2O_7 and subsequent sublimation for Re on alumina.[38] Furthermore, Re oxide particles on metal oxide supports are stable under methanol oxidation conditions up to 553 K.[60] Re-based catalysts are also better suited to oxidants such as water used in the WGS and APR reactions since water is less able to oxidize Re compared to O_2.[19,30,86]

3.5 CONCLUSIONS

CO binds less strongly to Pt-Re compared to Pt(111) during CO oxidation, implying that the Pt-Re alloy surface should be more resistant to poisoning by CO byproducts during oxidation reactions. Furthermore, Pt-Re dissociates O_2 more readily than pure Pt, and this suggests that the Pt-Re surfaces are less likely to be poisoned by carbonaceous residues during reaction since more atomic oxygen is available for oxidation of surface carbon. Re films on Pt are unstable in an oxidizing environment due to formation and sublimation of Re_2O_7 at temperatures below 500 K; however, the Pt-Re alloy surface, which consists of mainly Pt atoms in the top monolayer, is more resistant toward Re oxidation and sublimation.

3.6 REFERENCES

(1) Sinfelt, J. H. Bimetallic Catalysts. Discoveries, Concepts, and Applications; John Wiley and Sons: New York, 1983.

(2) Rodriguez, J. A. Physical and Chemical Properties of Bimetallic Surfaces. *Surf. Sci. Rep.*, **1996**, *24*, 223-287.

(3) Campbell, C. Bimetallic Surface-Chemistry. *Annu. Rev. Phys. Chem.*, **1990**, *41*, 775-837.

(4) Liu, P.; Norskov, J. K. Ligand and Ensemble Effects in Adsorption on Alloy Surfaces. *Phys. Chem. Chem. Phys.*, **2001**, *3*, 3814-3818.

(5) Chen, J. G.; Menning, C. A.; Zellner, M. B. Monolayer Bimetallic Surfaces: Experimental and Theoretical Studies of Trends in Electronic and Chemical Properties. *Surf. Sci. Rep.*, **2008**, *63*, 201-254.

(6) Somorjai, G. A. Introduction to Surface Chemistry and Catalysis; John Wiley and Sons, Inc.: New York, 1994.

(7) Carter, J. L.; McVicker, G. B.; Weissman, W.; Kmak, W. S.; Sinfelt, J. H. Bimetallic Catalysts - Application in Catalytic Reforming. *Appl. Catal.*, **1982**, *3*, 327-346.

(8) Kluksdahl, H. E. US Patent 3,415,737; UOP, 1968.

(9) Barbier, J. Deactivation of Reforming Catalysts by Coking - a Review. *Appl. Cat.*, **1986**, *23*, 225-243.

(10) Parera, J. M.; Beltramini, J. N. Stability of Bimetallic Reforming Catalysts. *J. Catal.*, **1988**, *112*, 357-365.

(11) Godbey, D. J.; Garin, F.; Somorjai, G. A. The Hydrogenolysis of Ethane over Re-Pt(111) and Pt-Re(0001) Bimetallic Crystal-Surfaces. *J. Catal.*, **1989**, *117*, 144-154.

(12) Binary Alloy Phase Diagrams; 2nd ed.; Massalski, T. B.; International, A.; Okamoto, H., Eds.; ASM International: Materials Park, OH, 1990.

(13) Ramstad, A.; Strisland, F.; Raaen, S.; Worren, T.; Borg, A.; Berg, C. Growth and Alloy Formation Studied by Photoelectron Spectroscopy and STM. *Surf. Sci.*, **1999**, *425*, 57-67.

(14) Mun, B. S.; Rossi, M.; Ross, P. N. The Study of Surface Segregation of Re_3Pt Polycrystalline Alloy with Photoelectron Spectroscopy. *J. Chem. Phys.*, **2008**, *129*, 174707.

(15) Godbey, D. J.; Somorjai, G. A. The Adsorption and Desorption of Hydrogen and Carbon-Monoxide on Bimetallic Re-Pt(111) Surfaces. *Surf. Sci.*, **1988**, *204*, 301-318.

(16) Kunkes, E. L.; Simonetti, D. A.; Dumesic, J. A.; Pyrz, W. D.; Murillo, L. E.; Chen, J. G. G.; Buttrey, D. J. The Role of Rhenium in the Conversion of Glycerol to Synthesis Gas over Carbon Supported Platinum-Rhenium Catalysts. *J. Catal.*, **2008**, *260*, 164-177.

(17) Simonetti, D. A.; Kunkes, E. L.; Dumesic, J. A. Gas-Phase Conversion of Glycerol to Synthesis Gas over Carbon-Supported Platinum and Platinum-Rhenium Catalysts. *J. Catal.*, **2007**, *247*, 298-306.

(18) Soares, R. R.; Simonetti, D. A.; Dumesic, J. A. Glycerol as a Source for Fuels and Chemicals by Low-Temperature Catalytic Processing. *Angew. Chem. Int. Edit.*, **2006**, *45*, 3982-3985.

(19) Zhang, L.; Karim, A. M.; Engelhard, M. H.; Wei, Z. H.; King, D. L.; Wang, Y. Correlation of Pt-Re Surface Properties with Reaction Pathways for the Aqueous-Phase Reforming of Glycerol. *J. Catal.*, **2012**, *287*, 37-43.

(20) King, D. L.; Zhang, L. A.; Xia, G.; Karim, A. M.; Heldebrant, D. J.; Wang, X. Q.; Peterson, T.; Wang, Y. Aqueous Phase Reforming of Glycerol for Hydrogen Production over Pt-Re Supported on Carbon. *Appl. Catal. B-Environ.*, **2010**, *99*, 206-213.

(21) Daniel, O. M.; DeLaRiva, A.; Kunkes, E. L.; Datye, A. K.; Dumesic, J. A.; Davis, R. J. X-Ray Absorption Spectroscopy of Bimetallic Pt-Re Catalysts for Hydrogenolysis of Glycerol to Propanediols. *ChemCatChem*, **2010**, *2*, 1107-1114.

(22) Ciftci, A.; Ligthart, D.; Hensen, E. J. M. Aqueous Phase Reforming of Glycerol over Re-Promoted Pt and Rh Catalysts. *Green Chem.*, **2014**, *16*, 853-863.

(23) Ciftci, A.; Ligthart, D.; Sen, A. O.; van Hoof, A. J. F.; Friedrich, H.; Hensen, E. J. M. Pt-Re Synergy in Aqueous-Phase Reforming of Glycerol and the Water-Gas Shift Reaction. *J. Catal.*, **2014**, *311*, 88-101.

(24) Ciftci, A.; Eren, S.; Ligthart, D.; Hensen, E. J. M. Platinum-Rhenium Synergy on Reducible Oxide Supports in Aqueous-Phase Glycerol Reforming. *ChemCatChem*, **2014**, *6*, 1260-1269.

(25) Kirilin, A. V.; Tokarev, A. V.; Manyar, H.; Hardacre, C.; Salmi, T.; Mikkola, J. P.; Murzin, D. Y. Aqueous Phase Reforming of Xylitol over Pt-Re Bimetallic Catalyst: Effect of the Re Addition. *Catal. Today*, **2014**, *223*, 97-107.

(26) Azzam, K. G.; Babich, I. V.; Seshan, K.; Mojet, B. L.; Lefferts, L. Stable and Efficient Pt-Re/TiO_2 Catalysts for Water-Gas-Shift: On the Effect of Rhenium. *ChemCatChem*, **2013**, *5*, 557-564.

(27) Azzam, K. G.; Babich, I. V.; Seshan, K.; Lefferts, L. Role of Re in Pt-Re/TiO_2 Catalyst for Water Gas Shift Reaction: A Mechanistic and Kinetic Study. *Appl. Catal. B Environ.*, **2008**, *80*, 129-140.

(28) Iida, H.; Igarashi, A. Difference in the Reaction Behavior between Pt-Re/TiO_2 (Rutile) and Pt-Re/ZrO_2 Catalysts for Low-Temperature Water Gas Shift Reactions. *Appl. Catal. A*, **2006**, *303*, 48-55.

(29) Iida, H.; Yonezawa, K.; Kosaka, M.; Igarashi, A. Low-Temperature Water Gas Shift Reaction over Pt-Re/TiO_2 Catalysts Prepared by a Sub-Critical Drying Method. *Catal. Commun.*, **2009**, *10*, 627-630.

(30) Azzam, K. G.; Babich, I. V.; Seshan, K.; Lefferts, L. A Bifunctional Catalyst for the Single-Stage Water-Gas Shift Reaction in Fuel Cell Applications. Part 2. Roles of the Support and Promoter on Catalyst Activity and Stability. *J. Catal.*, **2007**, *251*, 163-171.

(31) Carrasquillo-Flores, R.; Gallo, J. M. R.; Hahn, K.; Dumesic, J. A.; Mavrikakis, M. Density Functional Theory and Reaction Kinetics Studies of the Water-Gas Shift Reaction on Pt-Re Catalysts. *ChemCatChem*, **2013**, *5*, 3690-3699.

(32) Berlowitz, P. J.; Peden, C. H. F.; Goodman, D. W. Kinetics of CO Oxidation on Single-Crystal Pd, Pt, and Ir. *J. Phys. Chem.*, **1988**, *92*, 5213-5221.

(33) Campbell, C. T.; Ertl, G.; Kuipers, H.; Segner, J. A Molecular Beam Study of the Catalytic Oxidation of CO on a Pt(111) Surface. *J. Chem. Phys.*, **1980**, *73*, 5862-5873.

(34) Gland, J. L.; Kollin, E. B. Carbon Monoxide Oxidation on the Pt(111) Surface: Temperature Programmed Reaction of Coadsorbed Atomic Oxygen and Carbon Monoxide. *J. Chem. Phys.*, **1983**, *78*, 963-974.

(35) Ertl, G.; Norton, P. R.; Rustig, J. Kinetic Oscillations in the Platinum-Catalyzed Oxidation of CO. *Phys. Rev. Lett.*, **1982**, *49*, 177-180.

(36) Miller, D.; Casalongue, H. S.; Bluhm, H.; Ogasawara, H.; Nilsson, A.; Kaya, S. Different Reactivity of the Various Platinum Oxides and Chemisorbed Oxygen in CO Oxidation on Pt(111). *J. Am. Chem. Soc.*, **2014**, *136*, 6340-6347.

(37) Alnot, M.; Cassuto, A.; Ehrhardt, J. J.; Slavin, A.; Weber, B. Growth of Platinum on Rhenium and Evolution of the Interface under Thermal-Treatment. *Appl. Surf. Sci.*, **1982**, *10*, 85-99.

(38) Okal, J.; Tylus, W.; Kepinski, L. XPS Study of Oxidation of Rhenium Metal on Gamma-Al_2O_3 Support. *J. Catal.*, **2004**, *225*, 498-509.

(39) Shcheglov, P. A.; Drobot, D. V. Heterogeneous Equilibria in the Rhenium-Oxygen System. *Russ. J. Phys. Chem.*, **2006**, *80*, 1819-1825.

(40) Park, J. B.; Ratliff, J. S.; Ma, S.; Chen, D. A. Understanding the Reactivity of Oxide-Supported Bimetallic Clusters: Reaction of NO with CO on TiO_2(110)-Supported Pt-Rh Clusters. *J. Phys. Chem. C*, **2007**, *111*, 2165-2176.

(41) Zhou, J.; Ma, S.; Kang, Y. C.; Chen, D. A. Dimethyl Methylphosphonate Decomposition on Titania-Supported Ni Clusters and Films: A Comparison of Chemical Activity on Different Ni Surfaces. *J. Phys. Chem. B*, **2004**, *108*, 11633-11644.

(42) Park, J. B.; Conner, S. F.; Chen, D. A. Bimetallic Pt-Au Clusters on TiO_2(110): Growth, Surface Composition and Metal-Support Interactions. *J. Phys. Chem. C*, **2008**, *112*, 5490-5500.

(43) Tenney, S. A.; Ratliff, J. S.; He, W.; Roberts, C. C.; Ammal, S. C.; Heyden, A.; Chen, D. A. Adsorbate-Induced Changes in the Surface Composition of Bimetallic Clusters: Au-Pt on TiO_2(110). *J. Phys. Chem. C*, **2010**, *114*, 21652-21663.

(44) Tenney, S. A.; Lu, D. Y.; He, F.; Levy, N.; Perera, U. G. E.; Starr, D. E.; Muller, K.; Bluhm, H.; Sutter, P. Key Structure-Property Relationships in CO_2 Capture by Supported Alkanolamines. *J. Phys. Chem. C*, **2014**, *118*, 19252-19258.

(45) Robinson, A. M.; Montemore, M. M.; Tenney, S. A.; Sutter, P.; Medlin, J. W. Interactions of Hydrogen, CO, Oxygen, and Water with Molybdenum-Modified Pt(111). *J. Phys. Chem. C*, **2013**, *117*, 26716-26724.

(46) Wagner, C. D.; Riggs, W. M.; Davis, L. E.; Moulder, J. F. Handbook of X-Ray Photoelectron Spectroscopy; Perkin Elmer Corporation: Eden Prairie, MN, 1978.

(47) Illingworth, A.; Zhou, J.; Ozturk, O.; Chen, D. A. Design of a Heating-Cooling Stage for STM and TPD Experiments. *J. Vac. Sci. Technol. B*, **2004**, *22*, 2552-2554.

(48) Galhenage, R. P.; Ammal, S. C.; Yan, H.; Duke, A.; Tenney, S. A.; Heyden, A.; Chen, D. A. Nucleation, Growth and Adsorbate-Induced Changes in Composition for Co-Au Bimetallic Clusters on TiO_2. *J. Phys. Chem. C*, **2012**, *116*, 24616-24629.

(49) Surface Analysis: The Principal Techniques; Vickerman, J. C., Ed.; John Wiley and Sons: New York, 1997.

(50) Alnot, M.; Cassuto, A.; Ducros, R.; Ehrhardt, J. J.; Weber, B. XPS and UPS Study of the Reaction of Carbon-Monoxide with Oxygen and Nitrogen Monoxide on Platinum-Rhenium Alloy. *Surf. Sci.*, **1982**, *114*, L48-L56.

(51) Björneholm, O.; Nilsson, A.; Tillborg, H.; Bennich, P.; Sandell, A.; Hernnäs, B.; Puglia, C.; Martensson, N. Overlayer Structure from Adsorbate and Substrate Core Level Binding Energy Shifts: CO, CCH_3, and O on Pt(111). *Surf. Sci.*, **1994**, *315*, L983-L989.

(52) Martensson, N.; Saalfeld, H. B.; Kuhlenbeck, H.; Neumann, M. Structural Dependence of the 5d-Metal Surface Energies as Deduced from Surface Core-Level Shift Measurements. *Phys. Rev. B*, **1989**, *39*, 8181-8186.

(53) Chan, A. S. Y.; Wertheim, G. K.; Wang, H.; Ulrich, M. D.; Rowe, J. E.; Madey, T. E. Surface Atom Core-Level Shifts of Clean and Oxygen-Covered Re(1231). *Phys. Rev. B*, **2005**, *72*, 14643-14651.

(54) Chan, A. S. Y.; Chen, W.; Wang, H; Rowe, J. E.; Madey, T. E. Methanol Reactions over Oxygen-Modified Re Surfaces: Influence of Surface Structure and Oxidation. *J. Phys. Chem. B*, **2004**, *108*, 14643-14651.

(55) Ducros, R.; Fusy, J. Core Level Binding-Energy Shifts of Rhenium Surface Atoms for a Clean and Oxygenated Surface. *J. Electron Spectrosc. Relat. Phenom.*, **1987**, *42*, 305-312.

(56) Morant, C.; Galan, L.; Sanz, J. M. X-Ray Photoelectron Spectroscopic Study of the Oxidation of Polycrystalline Rhenium by Exposure to O_2 and Low-Energy O_2^+ Ions. *Anal. Chim. Acta*, **1994**, *297*, 179-186.

(57) Liu, P.; Shuh, D. K. Adsorption of O_2 on Polycrystalline Rhenium Metal at Room Temperature Studied by Synchrotron X-Ray Photoemission Spectroscopy. *J. Electron Spectrosc. Relat. Phenom.*, **2001**, *114*, 319-325.

(58) Tysoe, W. T.; Zaera, F.; Somorjai, G. A. An XPS Study of the Oxidation and Reduction of the Rhenium Platinum System under Atmospheric Conditions. *Surf. Sci.*, **1988**, *200*, 1-14.

(59) Yuan, Y. Z.; Shido, T.; Iwasawa, Y. The New Catalytic Property of Supported Rhenium Oxides for Selective Oxidation of Methanol to Methylal. *Chem. Commun.*, **2000**, 1421-1422.

(60) Yuan, Y. Z.; Iwasawa, Y. Performance and Characterization of Supported Rhenium Oxide Catalysts for Selective Oxidation of Methanol to Methylal. *J. Phys. Chem. B*, **2002**, *106*, 4441-4449.

(61) Okal, J.; Kepinski, L.; Krajczyk, L.; Tylus, W. Oxidation and Redispersion of a Low-Loaded Re/Gamma-Al_2O_3 Catalyst. *J. Catal.*, **2003**, *219*, 362-371.

(62) Shpiro, E. S.; Ryashentseva, M. A.; Minachev, K. M.; Antoshin, G. V.; Avaev, V. I. XPS Studies of Rhenium State in Supported Re Catalysts. *J. Catal.*, **1978**, 55, 402-406.

(63) Naor, A.; Eliaz, N.; Burstein, L.; Gileadi, E. Direct Experimental Support for the Catalytic Effect of Iron-Group Metals on Electrodeposition of Rhenium. *Electrochem. Solid State Lett.*, **2010**, *13*, D91-D93.

(64) Bazuev, G. V.; Chupakhina, T. I.; Korolyov, A. V.; Kuznetsov, M. V. Synthesis under Usual Conditions, X-Ray Photoelectron Spectroscopy and Magnetic Properties of $Re_{1-x}Mn_xO_2$ Oxides with Rutile Structure. *Mater. Chem. Phys.*, **2010**, *124*, 946-951.

(65) Nikonova, O. A.; Capron, M.; Fang, G.; Faye, J.; Mamede, A. S.; Jalowiecki-Duhamel, L.; Dumeignil, F.; Seisenbaeva, G. A. Novel Approach to Rhenium Oxide Catalysts for Selective Oxidation of Methanol to DMM. *J. Catal.*, **2011**, *279*, 310-318.

(66) Tribalat, S.; Delafosse.D; Piolet, C. Sur Un Nouvel Oxyde De Rhenium – L'oxyde De Rhenium V. *C. R. Hebd. Seances Acad. Sci.*, **1965**, *261*, 1008-1011.

(67) Cotton, F. A.; Wilkinson, G. Advanced Inorganic Chemistry: A Comprehensive Text, 4th ed.; John Wiley and Sons: New York, 1980.

(68) Greiner, M. T.; Rocha, T. C. R.; Johnson, B.; Klyushin, A.; Knop-Gericke, A.; Schlogl, R. The Oxidation of Rhenium and Identification of Rhenium Oxides During Catalytic Partial Oxidation of Ethylene: An in-Situ XPS Study. *Z. Phys. Chemie-Int.*, **2014**, *228*, 521-541.

(69) Okal, J. A Study of Effect of Particle Size on the Oxidation of Rhenium in the Re/Gamma-Al_2O_3 Catalysts. *Appl. Catal. A*, **2005**, *287*, 214-220.

(70) Miller, D. J.; Oberg, H.; Kaya, S.; Casalongue, H. S.; Friebel, D.; Anniyev, T.; Ogasawara, H.; Bluhm, H.; Pettersson, L. G. M.; Nilsson, A. Oxidation of Pt(111) under near-Ambient Conditions. *Phys. Rev. Lett.*, **2011**, *107*, 195502.

(71) Puglia, C.; Nilsson, A.; Hernnas, B.; Karis, O.; Bennich, P.; Martensson, N. Physisorbed, Chemisorbed and Dissociated O_2 on Pt(111) Studied by Different Core-Level Spectroscopy Methods. *Surf. Sci.*, **1995**, *342*, 119-133.

(72) Blomberg, S.; Hoffmann, M. J.; Gustafson, J.; Martin, N. M.; Fernandes, V. R.; Borg, A.; Liu, Z.; Chang, R.; Matera, S.; Reuter, K.; et. al. In Situ X-Ray Photoelectron Spectroscopy of Model Catalysts: At the Edge of the Gap. *Phys. Rev. Lett.*, **2013**, *110*, 117601.

(73) Gustafson, J.; Blomberg, S.; Martin, N. M.; Fernandes, V.; Borg, A.; Liu, Z.; Chang, R.; Lundgren, E. A High Pressure X-Ray Photoelectron Spectroscopy Study of CO Oxidation over Rh(100). *J. Phys.-Condens. Matter*, **2014**, *26*, 126102.

(74) Starr, D. E.; Bluhm, H. CO Adsorption and Dissociation on Ru(0001) at Elevated Pressures. *Surf. Sci.*, **2013**, *608*, 241-248.

(75) Freyer, N.; Pirug, G.; Bonzel, H. P. C(1s) Spectroscopy of Hydrocarbons Adsorbed on Pt(111). *Surf. Sci.*, **1983**, *126*, 487-494.

(76) Jugnet, Y.; Loffreda, D.; Dupont, C.; Delbecq, F.; Ehret, E.; Aires, F.; Mun, B. S.; Akgul, F. A.; Liu, Z. Promoter Effect of Early Stage Grown Surface Oxides: A near Ambient-Pressure XPS Study of CO Oxidation on PtSn Bimetallics. *J. Phys. Chem. Lett.*, **2012**, *3*, 3707-3714.

(77) Cohesion in Metals: Transition Metal Alloys; de Boer, F. R., Boom, R., Mattens, W. C. M., Miedema, A. R., Niessen, A. K., Eds.; North-Holland Physics Publishing: Amsterdam, 1998; Vol. 1.

(78) Jiang, Q.; Lu, H. M.; Zhao, M. Modelling of Surface Energies of Elemental Crystals. *J. Phys.: Condens. Matter*, **2004**, *16*, 521−530.

(79) Wagner, R.; Schlatterbeck, D.; Christmann, K. The Interaction of Copper with a Rhenium(0001) Surface: Structure, Energetics, and Growth Modes. *Surf. Sci.*, **1999**, *440*, 231-251.

(80) Vitos, L.; Ruban, A. V.; Skriver, H. L.; Kollár, J. The Surface Energy of Metals. *Surf. Sci.*, **1998**, *411*, 186-202.

(81) Tyson, W. R.; Miller, W. A. Surface Free-Energies of Solid Metals - Estimation from Liquid Surface-Tension Measurements. *Surf. Sci.*, **1977**, *62*, 267-276.

(82) Alnot, M.; Gorodetskii, V.; Cassuto, A.; Ehrhardt, J. J. Auger-Electron Spectroscopy, X-Ray Photoelectron-Spectroscopy, Work Function Measurements and Photoemission of Adsorbed Xenon on Thin-Films of Pt-Re(111) Alloys. *Thin Solid Films*, **1987**, *151*, 251-262.

(83) Wang, G. F.; Van Hove, M. A.; Ross, P. N.; Baskes, M. I. Monte Carlo Simulations of Segregation in Pt-Re Catalyst Nanoparticles. *J. Chem. Phys.*, **2004**, *121*, 5410-5422.

(84) Ramstad, A.; Strisland, F.; Raaen, S.; Borg, A.; Berg, C. CO and O_2 Adsorption on the Re/Pt(111) Surface Studied by Photoemission and Thermal Desorption. *Surf. Sci.*, **1999**, *440*, 290-300.

(85) Ishikawa, Y.; Liao, M. S.; Cabrera, C. R. Energetics of H_2O Dissociation and CO_{ads}+OH_{ads} Reaction on a Series of Pt-M Mixed Metal Clusters: A Relativistic Density-Functional Study. *Surf. Sci.*, **2002**, *513*, 98-110.

(86) Sato, Y.; Terada, K.; Hasegawa, S.; Miyao, T.; Naito, S. Mechanistic Study of Water-Gas-Shift Reaction over TiO_2 Supported Pt-Re and Pd-Re Catalysts. *Appl. Catal. A*, **2005**, *296*, 80-89.

(87) Seuser, G.; Galhenage, R. P.; Chen, D. A. Oxidation of Re-Pt Surfaces: Supported Clusters and Thin Films. manuscript in preparation.

(88) Weigand, P.; Novacek, P.; van Husen, G.; Neidhart, T.; Varga, P. Surface Analysis of Pt_xNi_{1-x} Single Crystals. *Surf. Sci., 1992, 269-270*, 1129-1134.

(89) Menning, C. A.; Hwu, H. H.; Chen, J. G. G. Experimental and Theoretical Investigation of the Stability of Pt-3d-Pt(111) Bimetallic Surfaces under Oxygen Environment. *J. Phys. Chem. B*, **2006**, *110*, 15471-15477.

(90) Thiel, P. A.; Behm, R. J.; Norton, P. R.; Ertl, G. The Interaction of CO and Pt(100). 2. Energetic and Kinetic-Parameters. *J. Chem. Phys.*, **1983**, *78*, 7448-7458.

(91) Menning, C. A.; Chen, J. G. Theoretical Prediction and Experimental Verification of Stability of Pt-3d-Pt Subsurface Bimetallic Structures: From Single Crystal Surfaces to Polycrystalline Films. *Top. Catal.*, **2010**, *53*, 338-347.

(92) Kitchin, J. R.; Norskov, J. K.; Barteau, M. A.; Chen, J. G. Role of Strain and Ligand Effects in the Modification of the Electronic and Chemical Properties of Bimetallic Surfaces. *Phys. Rev. Lett.*, **2004**, *93*, 156801.

(93) Xu, Y.; Ruban, A. V.; Mavrikakis, M. Adsorption and Dissociation of O_2 on Pt-Co and Pt-Fe Alloys. *J. Am. Chem. Soc.*, **2004**, *126*, 4717-4725.

CHAPTER 4

IN SITU AMBIENT PRESSURE X-RAY PHOTOELECTRON SPECTROSCOPY STUDIES OF METHANOL OXIDATION ON PT(111) AND PT-RE ALLOYS[2]

[2] Reprinted (adapted) with permission from Duke, A. S.; Galhenage, R. P.; Tenney, S. A.; Ammal, S. C.; Heyden, A.; Sutter, P.; Chen, D. A. *In Situ* Ambient Pressure X-ray Photoelectron Spectroscopy Studies of Methanol Oxidation on Pt(111) and Pt-Re Alloys. *J. Phys. Chem. C*, **2015**, *119* (40), 23082-23093. Copyright 2015 American Chemical Society.

4.1 INTRODUCTION

Pt−Re bimetallic systems constitute important industrial catalysts for hydrocarbon reforming and have been used commercially since the 1960s.[1−3] The addition of Re is known to promote activity as well as stability in Pt/Al_2O_3 reforming catalysts, and it is believed that Re prevents poisoning of Pt active sites by carbon residues.[1,3−6] More recently, Pt−Re catalysts have also been reported to exhibit superior activity compared to pure Pt in reactions involving oxidation processes. For example, Pt−Re/C catalysts have been used for aqueous phase reforming (APR) of glycerol to produce CO_2 and H_2;[7-12] this reaction is of particular interest because glycerol serves as a model compound for understanding the chemistry of the carbohydrates formed in biomass reforming. Furthermore, $Pt−Re/TiO_2$ catalysts show enhanced activity and longer lifetimes for the water-gas shift (WGS) reaction compared to Pt/TiO_2,[13−16] and the greater activity for WGS is attributed to more facile water dissociation at ReO_x sites.[13,14,17]

The exact role of Re in promoting APR is still a topic of debate. It has been proposed that Re changes the electronic properties of Pt so that CO adsorption to the metal is weakened, thereby preventing CO poisoning on Pt.[7] Alternatively, it has also been proposed that the increased activity for APR on the Pt−Re catalysts can be directly attributed to enhanced WGS activity that decreases CO coverage and increases overall activity.[9,10,18] Furthermore, there is still controversy as to whether CO binds more strongly or less strongly to Pt−Re compared to Pt. Temperature-programmed desorption studies in ultrahigh vacuum report that CO binding is weaker on a Pt−Re alloy surface compared to Pt(111),[19] and this result is supported by DFT calculations for CO on Pt−Re alloy surfaces.[20,21] In contrast, infrared spectroscopy studies show that CO adsorbs more

strongly to Pt−Re than Pt under WGS conditions,[15,22] but a recent study of steam reforming on Pt−Re/C suggests that spillover of CO from Pt to ReO_x[22] promotes CO desorption and CO_2 production.

We have studied methanol oxidation as a probe reaction to better understand oxidation chemistry on the Pt-Re bimetallic surfaces, given that this reaction has been well-studied on Pt surfaces.[23-27] Furthermore, Re particles on metal oxide supports are reported to be highly selective catalysts for the oxidation of methanol to methylal, and ReO_x rather than metallic Re is believed to serve as the active phase.[28−31] In the work presented here, we find that ReO_x does not play a major role in methanol oxidation activity because it is not stable under reaction conditions above 450 K. There is no evidence for increased CO poisoning on Pt compared to Pt−Re surfaces under reaction conditions, but the Pt−Re alloy surface is less susceptible to poisoning by carbonaceous residues than pure Pt. The presence of Re promotes the production of the fully oxidized products like CO_2 and H_2O over CO and H_2. Both of these results are attributed to increased O_2 dissociation on the Pt−Re alloy, providing a source of oxygen for carbon removal and oxidation of surface species. Although the Pt−Re alloy surface consists of a monolayer of pure Pt at the surface before exposure to adsorbates, Re atoms appear to diffuse to the surface at elevated temperature during methanol oxidation. The fact that the majority of Re atoms still reside subsurface in the Pt−Re alloy protects the Re from sublimation as Re_2O_7.

4.2 EXPERIMENTAL

All experiments were conducted in an ultrahigh vacuum chamber (base pressure $\sim 2 \times 10^{-9}$ Torr) at the X1A1 beamline at the National Synchrotron Light Source at

Brookhaven National Laboratory. This chamber is equipped with a differentially pumped hemispherical analyzer (SPECS Phoibos 150 NAP) with a CEM 9-channeltron detector for APXPS studies and a quadrupole mass spectrometer (Pfeiffer Prisma Plus, QME220) for monitoring gaseous reaction products; the details of this experimental setup have been described elsewhere.[32,33]

Experiments were carried out on a Pt(111) single crystal (99.999%, Princeton Scientific Corp., 8 mm diameter, 2 mm thickness). The crystal was heated by a ceramic button heater (HeatWave Labs), which was covered by a thin Ta foil and pressed against the back of the sample; the sample temperature was monitored by a chromel−alumel thermocouple spotwelded directly to the edge of the crystal. The Pt crystal was cleaned by cycles of Ar ion sputtering (10 min, 1 kV) in 1.0×10^{-5} Torr of Ar (99.9995%, Matheson), followed by annealing to 1000 K for 3 min. In order to remove residual carbon, the crystal was also heated to 550 K for 30 min in 500 mTorr of O_2 (99.997%, Matheson).

Re was deposited on the Pt(111) surface at room temperature using a commercial electron-beam evaporator (SPECS, EBE-1) from a 2mm diameter Re rod (ESPI, 99.99%). Re coverages were determined from XPS experiments, based on the attenuation of the Pt(4f) signal and assuming layer-by-layer growth for the Re films at room temperature;[32,34] the Re deposition rate was 0.2−0.3 monolayers (ML)/min. The Pt−Re surface alloys were prepared by heating Re films to 1000 K for 5 min,[32,34] and the attenuation of the Re(4f) XPS signal before and after annealing was consistent with Re in the second and third subsurface layers (Appendix B). Re films and alloy surfaces were oxidized at 450 or 490 K by heating in 500 mTorr of O_2 for 20−50 min.

For methanol oxidation experiments, the chamber was backfilled first with 200 mTorr of O_2, followed by the addition of 100 mTorr methanol (≥99.8%, Macron Fine Chemicals) through two separate variable leak valves, while maintaining the Pt(111) crystal temperature at 300 K. After multiple exposures of the chamber to the reactant gases, the base pressure rose to $\sim 2 \times 10^{-8}$ Torr. The methanol was purified by two freeze− pump−thaw cycles immediately before use. XPS spectra were collected over the range of 300−550 K in intervals of 25 or 50 K. Incident photon energies were 303 eV for Re(4f) and Pt(4f) spectra, 533 eV for the C(1s) spectra, and 725 or 716 eV for the O(1s) spectra. The relative binding energies were set according to the Fermi edge in the valence band region, and the absolute binding energies were determined by setting the Pt($4f_{7/2}$) peak for the clean Pt(111) surface at 71.0 eV.

In order to monitor chemical activity during the XPS experiments, a 0.76 mm diameter stainless steel capillary tube was positioned ~1 mm away from the surface of the crystal to allow sampling of the gaseous products evolving from the surface. The capillary tube was differentially pumped into an antechamber with a mass spectrometer, which monitored nine different masses (2, 16, 18, 28, 30, 31, 32, 44, and 46 amu) during the APXPS experiment.

Mass spectrometer signals were corrected for the mass fragmentation of other gaseous species, and the details of these corrections are given in Appendix B. Furthermore, daily variations in the mass spectrometer signals arising from instability of the electron multiplier were corrected by normalizing all of the signals to the 32 amu signal for pure O_2 leaked into the chamber at a known pressure.

Peak fitting was carried out with the shareware programs FitXPS2 for the Re(4f) region and XPSPeak for the C(1s) and O(1s) regions. A linear background and asymmetric peak shapes were used for the Re(4f) spectra, while a Shirley background and Gaussian−Lorentzian peak shapes were used for the C(1s) and O(1s) spectra.

4.3 COMPUTATIONAL DETAILS

Density functional theory (DFT) calculations for the Pt−Re alloy model were performed using the Vienna ab initio simulation package (VASP 5.3).[35,36] The projector augmented-wave (PAW)[37] potentials were used along with the exchange-correlation functionals parametrized by Perdew, Burke, and Ernzerhof (PBE)[38] for the generalized gradient approximation (GGA). The convergence criteria were chosen to be less than 10^{-6} eV for the electronic structure and 0.02 eV/ Å for the geometry optimization at an energy cutoff of 500 eV. An equilibrium lattice constant of Pt (3.976 Å) was calculated from the PBE functional and was used to build a [3 × 3] supercell for the Pt(111) surface slab, which had a thickness of five layers and a vacuum spacing of 15 Å. The Pt−Re alloy models were constructed by replacing a layer of Pt atoms with Re atoms. A (3 × 3 × 1) Monkhorst−Pack[39] k-mesh was used for structural relaxation while the bottom layer atoms of the slab model were fixed to their bulk coordinates. Energies were calculated with a (5 × 5 × 2) k-mesh. The electronic states were smeared using a first-order Methfessel−Paxton scheme[40] with a smearing of 0.2 eV, and the dipole corrections to the energy were taken into account using a modified version of the Markov and Payne method.[41] The adsorption energy (E_{ads}) of an oxygen atom on a metal slab was calculated using the formula, $E_{ads} = E_{slab-O} - E_{slab} - \frac{1}{2}E_{O_2}$ where E_{slab-O} is the total energy of

the metal slab with an adsorbed O atom, and E_{slab} and E_{O_2} represent the total energies of the clean metal slab and the oxygen molecule, respectively. The energy of an O_2 molecule is obtained from the experimental value of the H_2O splitting reaction to correct for the systematic O_2 overbinding error associated with DFT methods.[42,43]

4.4 RESULTS

APXPS Studies

Re(4f) and Pt(4f) Regions

Changes in Re oxidation state during methanol oxidation were studied as a function of increasing reaction temperature on an oxidized Re film as well as on oxidized and unoxidized Pt−Re alloy surfaces. For all Re(4f) spectra, the $4f_{7/2}$ and $4f_{5/2}$ peaks were separated by 2.42 ± 0.1 eV, and the peak area ratio was constrained to 4:3, respectively; peak positions of the Re(4f) doublet are designated by only the $4f_{7/2}$ binding energies for simplicity. Although the peak fits are not unique, they provide insight into the main Re oxidation states present, and in general, the spectra were fit with the minimum number of components.

The oxidized Re film was prepared by depositing 2.1 ML of Re on Pt(111) at room temperature and then exposing to 500 mTorr of O_2 at 450 K. The Re($4f_{7/2}$) peak for the unoxidized film appears at 40.8 eV, which is shifted by approximately +0.5 eV compared to the binding energy of single-crystal Re[44−46] surfaces; the 40.8 eV binding energy is in agreement with previous studies of Re films on Pt(111).[32] After oxidation, the Re($4f_{7/2}$) peaks appear at significantly higher binding energy compared to metallic Re (Figure 4.1a). The resulting spectrum is fit with peaks at 44.1 eV, which is attributed to

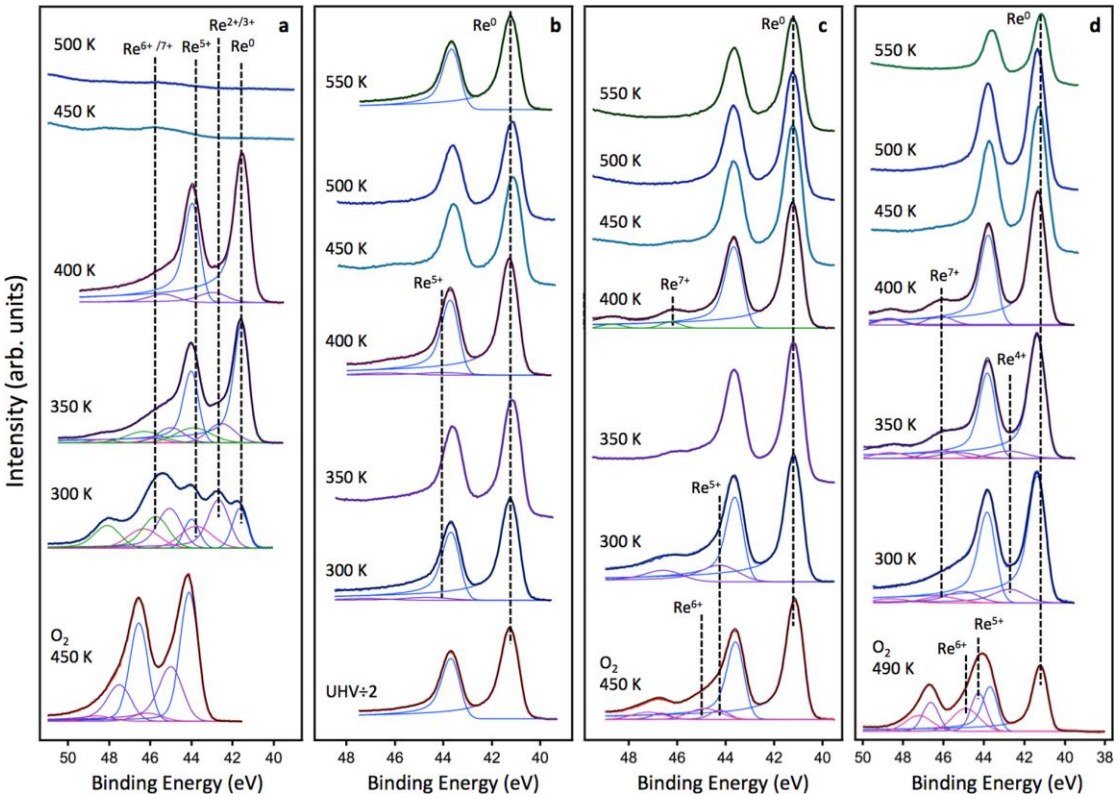

Figure 4.1: APXPS data for the Re(4f) region for the following surfaces heated to various temperatures under 200 mTorr of O_2 and 100 mTorr of methanol: a) Re film (2.1 ML) on Pt(111) after exposure to 500 mTorr of O_2 at 450 K; b) Pt-Re alloy (1.3 ML Re); c) Pt-Re alloy (1.8 ML Re) exposed to 500mTorr of O_2 at 450 K; and d) Pt-Re alloy (2.0 ML Re) after exposure to 500 mTorr of O_2 at 490 K. The bottom spectra in a, c and d were collected in 500 mTorr of O_2. The incident photon energy was 303 eV.

Re^{5+}, and 44.9 eV, which is assigned to Re^{6+} and accounts for 35% of the total integrated Re signal. There is also a minor (5%) contribution from a 46.0 eV peak assigned to Re^{7+}.[47–50] Although Re^{5+} is not commonly observed due to the instability of Re_2O_5 in the presence of air and water,[51,52] Re^{5+} has been previously reported by our group for oxidized Re surfaces studied with in situ XPS.[32] The binding energy of ~44 eV is also consistent with reports of Re^{5+} in other mixed metal systems,[53–55] and this value lies

between the accepted binding energies for Re^{6+} (44.8−45.4 eV) and Re^{4+} (42.3−42.8 eV).[28,29,47,48,56]

Exposure of the oxidized Re film to methanol oxidation conditions (200 mTorr of O_2/100 mTorr of methanol) at 300 K reduced the oxidized Re film. The resulting surface was composed of multiple Re oxidation states ranging from Re^{2+} or Re^{3+} at 41.7 eV, Re^{4+} at 42.6 eV, Re^{5+} at 43.7 eV, and Re^{6+} or Re^{7+} at 45.7 eV.[44,57,58] The 41.7 eV peak is higher in binding energy than the 41.3−41.4 eV reported in the literature for Re^{2+} and closer to the 42.0 eV value reported for Re^{3+},[44] but the Re($4f_{7/2}$) peak for metallic Re on Pt(111) is also ∼0.5 eV higher than the binding energy for pure metallic Re surfaces. The reactant mixture of O_2 and methanol is a highly reducing environment for the oxidized Re film at room temperature despite the presence of O_2 in the mixture. At 350 K, the surface is further reduced so that the dominant feature is at 41.5 eV although there are still minor contributions from Re^{4+} (17%), Re^{5+} (17%), and Re^{7+} (3%). At 400 K, the peak shape is mostly unchanged, but the contributions from the higher oxidation states disappear; the resulting spectrum can be fit with peaks corresponding to Re^{2+}/Re^{3+} and Re^{4+} only. At 450 and 500 K, the Re signals decrease to 6% and 2% of the values at 300 K, respectively, and this disappearance of Re is attributed to the formation and subsequent sublimation of volatile Re_2O_7 at the higher temperatures.[47,59] Our previous studies of the oxidation of Re films on Pt(111) reported similar loss of Re from the surface. Re disappeared from the surface when heated in O_2 or a mixture of CO and O_2 at O_2 pressures of ∼500 mTorr, whereas no Re loss was detected when heating in the absence of O_2.[32]

In contrast to the Re film, the exposure of the Pt−Re alloy surface to methanol oxidation conditions causes minimal Re oxidation (Figure 4.1b). Deposition of 1.3 ML of

Re on Pt(111) at room temperature results in a Re($4f_{7/2}$) peak at 40.9 eV, and after heating to 1000 K to form the alloy, the binding energy shifts to 41.2 eV. The spectrum for the Pt−Re alloy surface is fit with a single 4f doublet with a FWHM of 0.9 eV, and the peak shape is unchanged from that of the unannealed Re film. After this surface is exposed to methanol/O_2 at 300 K, a barely detectable shoulder appears at higher binding energy and is assigned to oxidation of Re. At 400 K under reaction conditions, the high binding energy shoulder is fit with a doublet at 43.8 eV and assigned to Re^{5+}. This small shoulder accounts for only 6.5−7% of the total Re(4f) area at both 300 and 400 K. At 500 K, the shoulder disappears, and the spectrum at 550 K is fit with a single doublet at 41.2 eV, indicating that only metallic Re is present. After the Pt−Re alloy surface is heated to 500 K under reaction conditions, the ratio of the Re/ Pt integrated intensities for the Pt($4f_{7/2}$) and Re($4f_{7/2}$) peaks increases by 12−15% compared to the values for this same surface immediately after preparation in UHV. This suggests that there is diffusion of Re to the surface upon heating under reaction conditions, but diffusion is not significant until 450 K, which is the temperature corresponding to the initial increase in Re/Pt ratio.

It is possible to induce substantial oxidation of the Pt−Re alloy by exposure to 500 mTorr of O_2 at 450 K (Figure 4.1c). The alloy surface was initially prepared by depositing 1.8 ML of Re on Pt(111) at room temperature and heating to 1000 K for 5 min prior to O_2 exposure. After oxidation, the main spectral feature is the metallic Re peak at 41.1 eV from alloyed Re, but the data are also fit with peaks at 44.2 and 44.8 eV assigned to Re^{5+} and Re^{6+}, respectively; oxidized Re accounts for 18% of the total Re signal. The Re alloy is not as readily oxidized as the Re film on Pt, given that metallic Re is still the main species after oxidation of the alloy surface. Upon exposure of this surface to the

methanol/O_2 reactant gases at 300 K, the Re^{6+} contribution disappears completely, and the spectrum is fit with peaks from metallic Re at 41.1 eV and Re^{5+} at 44.0 eV, with the latter accounting for 23% of the Re signal. At 350 K, the Re^{5+} contribution diminishes to 13% as the surface is further reduced. At 400 K, the appearance of a small feature at 46.3 eV assigned to Re^{7+} demonstrates that oxidation of Re can occur at this temperature, but the contribution of Re^{7+} is only 4% of the total signal. At higher temperatures of 450−550 K, only metallic Re is observed. The Re/Pt XPS ratio initially increases by 16% upon exposure of the alloy surface to O_2 at 450 K, indicating Re segregation to the surface during oxidation. However, the Re/Pt ratio during methanol oxidation at 500 K is 10% lower than that of the freshly prepared alloy surface; this suggests that additional Re does not diffuse to the surface during methanol oxidation at elevated temperatures, unlike for the unoxidized Pt−Re alloy, and the slight decrease in Re/Pt ratio at 500 K may be due to loss of Re from Re_2O_7 sublimation.

Changes in Re oxidation state under reaction conditions were also studied for a Pt−Re alloy (2.0 ML Re) surface oxidized in 500 mTorr of O_2 at a higher temperature of 490 K before exposure to methanol/O_2 (Figure 4.1d). Upon initial oxidation, metallic Re is observed at 41.2 eV, but higher oxidation states of +5 and +6 are also detected, and each accounts for ~25% of the Re signal intensity. After exposure to the reaction mixture at 300 K, the Re is reduced, and metallic Re accounts for 78% of the Re signal; in addition to Re^{4+} at 42.6 eV, a small amount (6%) of Re^{7+} is detected at 46.1 eV. At 350 K, metallic Re accounts for 83% of the total signal, whereas Re^{4+} and Re^{7+} each account for only 8−9% of the Re signal. At 400 K, only metallic Re and Re^{+7} at 46.1 eV are observed, with the latter comprising 8% of the Re signal. At higher reaction temperatures of

450−550 K, only metallic Re is observed on the surface. The Re/Pt XPS ratio for this alloy surface directly after exposure to O_2 at 490 K is significantly higher than that of the alloy exposed to O_2 at 450 K (0.15 vs 0.09) despite the similar Re coverages for both surfaces (2.0 vs 1.8 ML, respectively). This implies that the higher oxidation temperature for the alloy induced greater diffusion of Re to the surface. However, under methanol oxidation conditions at 450 and 500 K, the Re/Pt ratio for the 490 K oxidized surface is within ~5% of the value before exposure to the reactant gases, demonstrating that there is less change in Re composition under reaction conditions than for the unoxidized Pt−Re alloy.

Pt(4f) spectra were collected for all surfaces during methanol oxidation, and there was no broadening of the Pt($4f_{7/2}$) peak due to Pt oxidation (Figure B.1). However, there is a +0.2 eV shift to higher binding energy at all temperatures when the surface is exposed to reaction conditions compared to the ($4f_{7/2}$) binding energy of the clean Pt surface. This increase in binding energy is ascribed to a surface core level shift, which occurs when the intensity contributed by the lower coordination surface sites is lost due to binding to adsorbates, and therefore the Pt($4f_{7/2}$) peak appears to shift to higher binding energy.[34,60]

C(1s) Region

During the APXPS experiments, C(1s) spectra were acquired on various surfaces for methanol oxidation at different temperatures. On Pt(111), the C(1s) region at 300 K exhibits three distinct binding energy peaks at 283.9, 286.0, and 287.7 eV (Figure 4.2a). The peak at 283.9 eV is attributed to CH_x (x = 0−3) on Pt, based on binding energies reported in the literature for CH_x on Pt(111)[23] and atomic carbon on Pt(111),[23,33,61,62] as

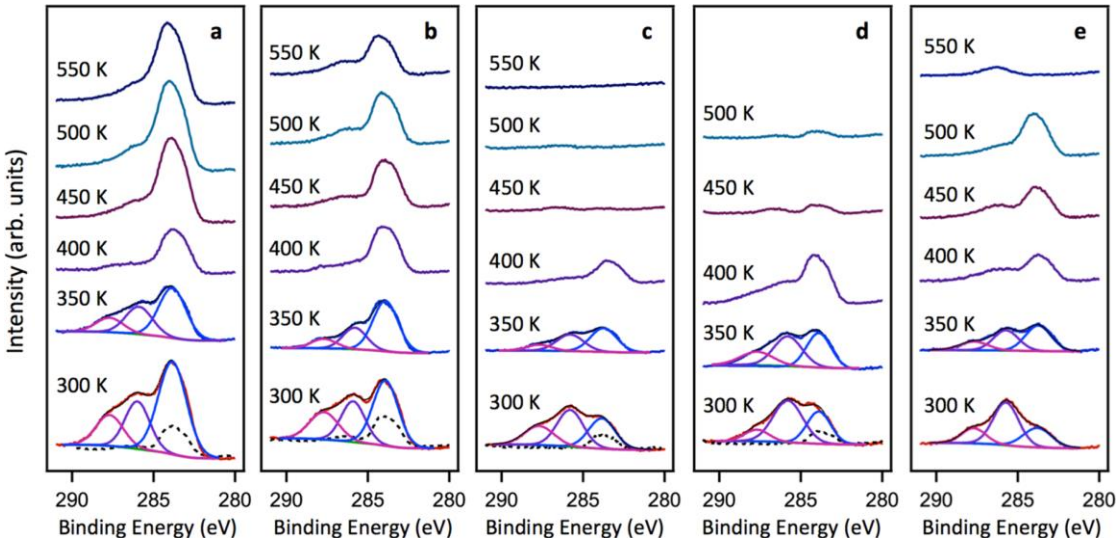

Figure 4.2: APXPS data for the C(1s) region for the following surfaces heated to various temperatures under 200 mTorr of O_2 and 100 mTorr of methanol: a) Pt(111); b) Pt-Re alloy (1.3 ML Re); c) Pt-Re alloy (1.8 ML Re) exposed to 500mTorr of O_2 at 450 K; and d) Re film (2.1 ML) on Pt(111) after exposure to 500 mTorr of O_2 at 450 K; and e) Pt-Re alloy (2.0 ML Re) after exposure to 500 mTorr of O_2 at 490 K. The incident photon energy was 533 eV, and the vertical scale is the same for all spectra so that intensities can be directly compared.

well as CH_3 on Pd(111).[63,64] Residual carbon was detected on the surface even after cleaning Pt(111) by sputtering and annealing, followed by heating in O_2. The carbon signal from the clean Pt surface in UHV before exposure to methanol is shown as a dotted black line after correcting for the attenuation expected in the reaction gas mixture. Not all of the atomic carbon originates from carbon on the surface before reaction, and the carbon signal before reaction accounts for <20% of the total carbon signal after exposure to methanol.

The peak at 286.0 eV occurs in the range associated with adsorbed CO on supported Pt clusters[65,66] and Pt(111);[23] this is also consistent with the detection of gaseous CO as a major product in methanol decomposition in UHV on oxidized and

unoxidized Pt single crystal surfaces.[24,67−70] Furthermore, CO is observed as a surface intermediate in methanol oxidation and decomposition on Pt(111) both in UHV[24,67] and under higher pressure conditions.[23,25] The binding energy associated with a methoxy intermediate also appears around 286 eV, but methoxy is not observed on Pt(111) at room temperature in UHV experiments because C−H bond scission occurs above 140 K.[24] Although methoxy has been detected on oxygen-covered Pt(111)[24,68,69] as well as on reconstructed (2 × 1)Pt(110),[67] methoxy decomposes above 200 K. Therefore, the main contribution to the 286.0 eV peak is believed to be from adsorbed CO rather than surface methoxy, which should not be stable at 300 K.

The 287.7 eV peak is assigned to either gaseous methanol or surface formate. Similar binding energies are reported for gaseous methanol in the literature.[23,64,71] However, a previous APXPS study of methanol oxidation on Pt(111) ascribed intensity at 287.7 eV to surface formate,[23] given that formate on Cu appears at 287.7 eV.[71,72] Formate is not observed as an intermediate for methanol decomposition in UHV, but it has been observed in infrared spectroscopy experiments for methanol oxidation on Pt(111) at high pressures (12 Torr of CH_3OH/10 Torr of O_2) and temperatures of 330−400 K.[25]

After heating to 350 K, the overall carbon signal on Pt(111) is diminished by ∼50% although the relative ratios of the three carbon species remain approximately the same. After heating to 400 K, 50% of the carbon signal is lost; CH_x becomes the main carbon-containing surface species, and contributions from the higher binding energy species account for ∼15% of the total signal. However, above 400 K, the carbon signal begins to increase, and at 450 K, it is twice as large as at 400 K. Most of the carbon intensity appears at ∼284 eV, and a shoulder around 286 eV is also visible, perhaps due

to transient intermediates such as CO on the surface. Additional heating to 500 and 550 K does not change the C(1s) peak shape and intensity. The ~284 eV binding energy peak at higher temperatures is most likely from atomic carbon rather than a CH_x species because C−H bond breaking occurs at low temperatures.[23] Specifically, C−H bond breaking in CH_3 during methanol decomposition on Pt(111) occurs at 220 K.[73]

Methanol oxidation was also carried out on the Pt−Re alloy surface under identical reaction conditions (Figure 4.2b). At 300 K, the total carbon signal is 25% lower than that on Pt(111), but the same three peaks at 283.9, 285.9, and 287.7 eV are observed and again assigned to CH_x (x = 0−3), CO, and gaseous methanol, respectively. The dashed black trace represents the carbon signal on the Pt−Re alloy before exposure to reactants, indicating that ~20% of the carbon is present on the Pt−Re alloy surface before any methanol decomposition. At 350 K, the 283.9 eV peak decreases to ~70% of the 300 K intensity, with the 285.9 and 287.7 eV peaks diminishing more rapidly than CH_x. At 400 K, the 283.9 eV signal intensity remains the same, while the higher binding energy peaks decrease almost to zero. There is little change in the carbon spectra between 400 and 550 K, in contrast to reaction on Pt(111), where the carbon peak increases significantly at 450 K. On the Pt−Re alloy, the total carbon signal decreases by 20% after heating from 500 to 550 K, and a shoulder around 286 eV is observed at 500 and 550 K. The amount of surface carbon at 550 K under reaction conditions is only half of that on Pt(111) at the same temperature. In addition, the amount of CO (286 eV) on the surface is the same on Pt versus the Pt−Re alloy and diminishes almost to zero at 400 K and above, indicating that CO poisoning is not an issue.

Experiments conducted on the Pt−Re alloy surface oxidized at 450 K before exposure to methanol show that very little carbon is deposited on the surface during methanol reaction, particularly at the higher temperatures (Figure 4.2c). The amount of carbon on the surface before methanol reaction (dotted trace) is reduced to <15% of the carbon initially on the unoxidized Pt−Re alloy. After exposure to reaction conditions at 300 K, the C(1s) spectrum exhibits peaks from the same three carbon-containing species, but the peak at ~286 eV is the dominant feature in the spectrum rather than CH_x at ~284 eV. Furthermore, the total carbon signal is <70% of that on the unoxidized alloy at the same temperature. After heating to 350 K, the decrease in the 284 eV peak is not as great as the attenuation of the two higher binding energy peaks. At 400 K, the 284 eV species accounts for 75% of the surface carbon, and at higher temperatures of 450−550 K, almost no surface carbon is detected.

Methanol oxidation was also studied on a Re film on Pt(111) that was oxidized at 450 K without annealing to form the alloy (Figure 4.2d). There is very little carbon present before exposure to reaction conditions, as indicated by the dotted trace, and the carbon signal before reaction is <12% of that after reaction at 300 K. The C(1s) spectrum at 300 K under reaction conditions is similar to that of the oxidized Pt−Re alloy. However, after heating to 350 K, the carbon signal is twice that on the oxidized Pt−Re alloy surface at the same temperature, and there is a greater contribution from the higher binding energy species, suggesting that there are more carbon-containing intermediates on the oxidized Re film. At 400 K, the major carbon species appears at 284 eV although the higher binding energy peaks account for 45% of the total signal; the total integrated

carbon intensity is 2.7 times greater than on the oxidized Pt−Re surface. At 450 and 500 K, almost all of the carbon is removed from the surface.

The Pt−Re alloy that was initially oxidized at higher temperature (490 K) to form Re oxide shows no surface carbon before methanol reaction (Figure 4.2e). At 300 K in methanol/O_2, the main carbon species appears at 285.7 eV although CH_x at 283.8 eV and gaseous methanol at 287.7 eV are also detected. At 350 K, the 285.7 eV peak is significantly attenuated such that the 283.8 eV peak has comparable intensity. At 400 and 450 K, the 285.7 eV peak continues to decrease while the 283.8 eV peak retains nearly the same intensity. After heating from 450 to 500 K, the carbon signal increases by 25%. Atomic carbon is the main carbon-containing surface species, and its intensity is similar to that on the unoxidized Pt−Re alloy under the same conditions. At 550 K, almost all of the surface carbon is removed, and only a small peak at 286.3 eV is detected.

O(1s) Region

The O(1s) spectra were collected as a function of temperature during methanol oxidation on different surfaces. The spectra for the Pt(111) and Pt−Re alloy surfaces have comparable peak shapes and intensities at room temperature (Figure 4.3a,b), where the spectra can be fit with three peaks at 530.6, 532.4, and 534.1 eV. The 530.6 eV peak is assigned to atomic oxygen since it is in general agreement with the binding energies observed after oxygen dissociation on Pt(111),[32,74,75] and the 532.4 eV peak has a binding energy that is consistent with CO on Pt(111)[32] and other metal surfaces.[76,77] The highest binding energy peak at 534.1 eV is attributed to gas-phase water or methanol, which appear around 534 and 535 eV, respectively.[71] At 350 K, the overall intensities decrease to 30−45% of their values at 300 K, and the 532.4 eV species (CO) becomes the

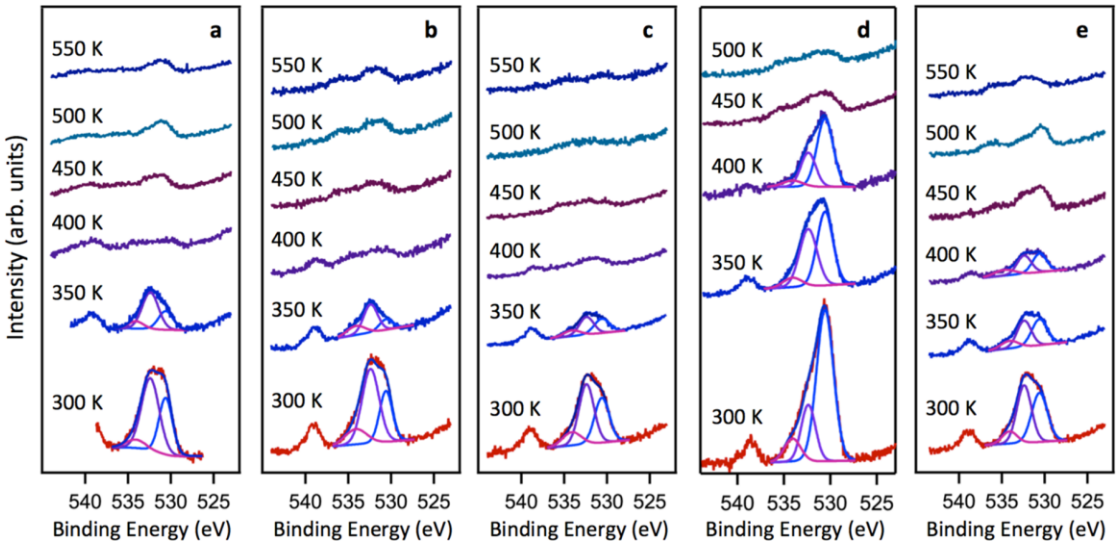

Figure 4.3: APXPS data for the O(1s) region for the following surfaces heated to various temperatures under 200 mTorr of O_2 and 100 mTorr of methanol: a) Pt(111); b) Pt-Re alloy (1.3 ML Re); c) Pt-Re alloy (1.8 ML Re) exposed to 500mTorr of O_2 at 450 K; and d) Re film (2.1 ML) on Pt(111) after exposure to 500 mTorr of O_2 at 450 K; and e) Pt-Re alloy (2.0 ML Re) after exposure to 500 mTorr of O_2 at 490 K. The incident photon energy was 725 eV for (b-d) and 716 eV for (a). The vertical scale is the same for all spectra so that intensities can be directly compared.

dominant feature. At 400 K, the O(1s) signal on both surfaces decreases nearly to zero, but a small amount of oxygen persists on the surface between 450 and 550 K. On Pt(111) and the Pt−Re alloy at 550 K, the main peak is centered around 531 eV and attributed to atomic oxygen. For reaction on the Pt−Re alloy oxidized at 450 K (Figure 4.3c), the spectrum at 300 K is similar in intensity and peak shape to that of Pt and unoxidized Pt−Re. At 350 K, the oxygen intensity decreases dramatically as intermediates desorb from the surface, and the overall intensity is 20−25% lower than that on unoxidized Pt−Re. At a reaction temperature of 400−550 K, the oxygen signal is barely detectable.

The O(1s) spectra during methanol reaction on the Re film oxidized at 450 K (Figure 4.3d) before exposure to the reactants is qualitatively different from the three

surfaces previously discussed because the oxidized Re film has a much higher concentration of surface oxygen. Specifically, the spectrum at 300 K is dominated by the peak at 530.6 eV from surface oxygen. The 532.4 eV and 534.1 eV features assigned to adsorbed CO and $H_2O_{(g)}$, respectively, have intensities that are similar to those on the other oxidized surfaces. At 350 K, the overall oxygen signal decreases mainly due to the loss of the 530.6 eV species. At 400 K, the oxygen peaks continue to diminish, but the total intensity is still ~75% of that at 350 K, in contrast to the other four surfaces, which have almost no detectable oxygen at 400 K. At 450 and 500 K, the concentration of oxygen remaining on the surface decreases substantially and is comparable to that observed on the Pt and Pt−Re alloy surfaces. Experiments were also carried out on the Pt−Re alloy surface oxidized at 490 K in order to form rhenium oxide (Figure 4.3e). The O(1s) spectrum at 300 K is almost identical to that of the alloy oxidized at 450 K under the same reaction conditions. However, the amount of surface oxygen at 350 K is 1.6 times greater than on the 450 K oxidized alloy. At 400 K, the intensity decreases slightly and does not change significantly between 400 and 500 K. At 550 K, the oxygen signal is barely detectable, but at all temperatures there is more surface oxygen than on the Pt−Re alloy oxidized at 450 K.

Mass Spectrometer Studies

Mass spectrometry experiments monitored the evolution of products while XPS data were collected under reaction conditions over the temperature range of 300 K to 500 or 550 K (Figure 4.4). The sample was maintained at the specified temperatures for 30−50 min during data collection, and the mass spectrometer signals reached constant values before heating to the next temperature. The mass spectrometer signals

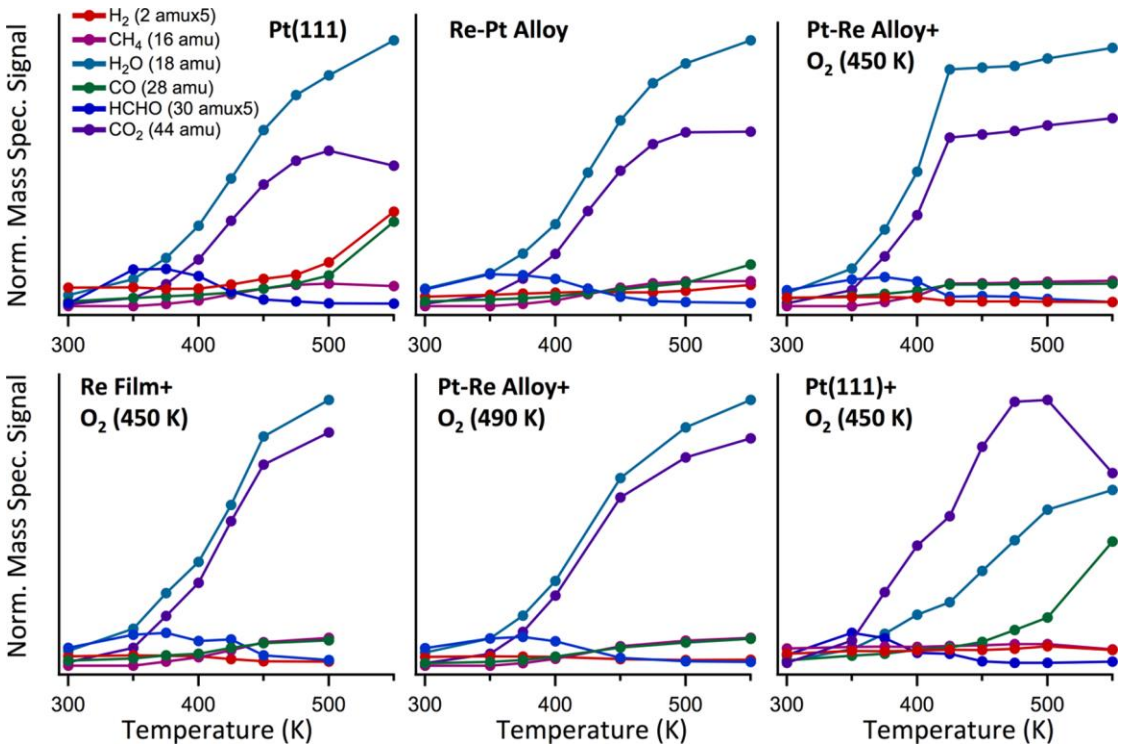

Figure 4.4: Mass spectrometer data collected during the APXPS experiments on various surfaces in 200 mTorr O_2 and 100 mTorr of methanol.

corresponding to each product have been corrected for the mass fragmentation of other gaseous species, as described in Appendix B. On the Pt(111) surface, the major products are H_2O (18 amu) and CO_2 (44 amu), and the yields of both of these products increase with temperature. Formaldehyde (30 amu) production is also observed at a lower temperatures with a maximum yield at around 375 K; no formaldehyde is detected at 300 K or at temperatures ≥450 K. CO (28 amu) evolution is observed at room temperature, and the CO yield remains relatively constant up to 500 K. Between 500 and 550 K, there is a sharp increase in CO production accompanied by an increase in H_2 (2 amu) as well as a decrease in CO_2, indicating that there is a change in selectivity favoring CO and H_2 production at the higher temperatures. Furthermore, after correcting the methane (16

amu) signal for the mass fragmentation of O_2 and CO, it appears that a small amount of methane is produced between 375 and 475 K.

Methanol reaction on the Pt−Re alloy surface is similar to that on Pt(111), given that water and CO_2 are the major products, and these signals increase monotonically over the 300−500 K range. Formaldehyde is again produced at low temperatures with a maximum around 350−375 K, and the methane yield also follows the same trend as on Pt(111). A major difference between activity on the Pt−Re alloy versus Pt is that the change in selectivity above 500 K is not as apparent on the alloy. Specifically, the increase in CO and decrease in CO_2 are less pronounced, and there is no clear increase in H_2 yield at 550 K.

The Pt−Re alloy oxidized at 450 K before methanol reaction achieves maximum activity for CO_2 and H_2O production at lower temperature than the unoxidized Pt−Re alloy and Pt(111) surfaces. On the oxidized alloy, CO_2 and H_2O yields reach nearly their maximum values at 425 K rather than continually rising between 425 and 500 K, as on the unoxidized surface. There is also no change in selectivity favoring CO and H_2 production above 500 K. Production of formaldehyde and methane follows the same trend on all three surfaces.

In order to understand the potential role of surface ReO_x in methanol oxidation, activity was studied on two surfaces containing ReO_x: the oxidized Re film and the Pt−Re alloy oxidized at 490 K. Based on the Re(4f) XPS data, ReO_x remains on the surface under reaction conditions at or below 450 K for the Re film and oxidized alloy. On both of these surfaces, CO_2 and H_2O are still the main products, which increase monotonically with temperature, while formaldehyde is produced with a maximum

around 375 K. Almost no H_2 is produced, and the CO and methane yields exhibit relatively small increases between 350 and 450 K. The product distributions for these two surfaces in the lower temperature regime are the same as on Pt(111) and the Pt−Re alloy, indicating the ReO_x does not substantially change selectivity in the methanol oxidation reaction. In the higher temperature regime of 450 K and above, the CO_2 and H_2O signals for both oxidized surfaces follow the same profiles with temperature, and there is no shift in selectivity to CO that would result in a decrease in CO_2 signal.

Methanol oxidation on the Pt(111) preoxidized at 450 K exhibits the same change in selectivity at higher temperatures that is observed on the unoxidized Pt(111) surface. Specifically, the CO_2 production decreases while the CO production increases between 500 and 550 K. Thus, the lack of change in selectivity from CO_2 to CO on the oxidized Re and Pt−Re alloy surfaces cannot be attributed to the preoxidation treatment because the shift in selectivity still occurs on oxidized Pt(111). Instead, the continued production of the fully oxidized product CO_2 is believed to be related to the presence of Re on the surface rather than oxygen only. At lower temperatures, the product distribution on oxidized Pt(111) is similar to the other surfaces studied.

It is difficult to compare absolute product yields for the different surfaces due to instability of the mass spectrometer signals from experiment to experiment. When signals were corrected with a scaling factor based on the absolute signals for O_2 (32 amu) normalized by the O_2 pressure, which was measured by the pressure gauge on the main chamber, the relative activities of the surfaces were roughly compared by their relative water (18 amu) and CO_2 (44 amu) yields at 500 K. All of the surfaces have water yields within 20% of that on Pt(111), and the CO_2 yields were within 25% except for the

oxidized Pt(111) surface. For the other five surfaces, it is believed that the overall activities are approximately the same within the error of the experimental measurements. The methanol oxidation experiment on the oxidized Pt(111) surfaces was carried out during a different time period than the other experiments, and the absolute mass spectrometer signals are lower by an order of magnitude. Although the corrected 18 amu signal for water is within 5% of that for reaction on clean Pt(111), the corrected CO (28 amu) is unusually high compared to the water signal. Thus, it is difficult to compare the absolute corrected signals for the oxidized Pt(111) surface with the other experiments, but the selectivity trends for the different products in the reaction on oxidized Pt(111) should still be correct.

Density Functional Theory Calculations

DFT calculations were carried out to understand the binding of oxygen to the Pt−Re alloy surfaces. Three different alloy surface structures were created by replacing a layer of Pt by Re atoms in the first, second, and third layers of the five-layer Pt(111) slab (Figure 4.5a−c). The relative energies of these surface structures with respect to the Re-terminated surface structure (Re−Pt−Pt−Pt−Pt) shown in Table 4.1 suggest that it is energetically favorable for Re to reside in subsurface layers in the absence of any surface adsorbates. The structures with Re atoms in the second and third layers are more stable than the Re-terminated surface by 7.56 and 10.89 eV, respectively, implying that Re prefers to diffuse deeper into the bulk than just the first subsurface layer. An exchange of one Re atom from the third layer with a Pt atom in the top layer ($Pt(Re_1)$−Pt−$Re(Pt_1)$−Pt−Pt) results in a less stable structure than the one with only Pt atoms at the surface (Pt−Pt−Re−Pt−Pt). The relatively high energy for the structure with Re in the top

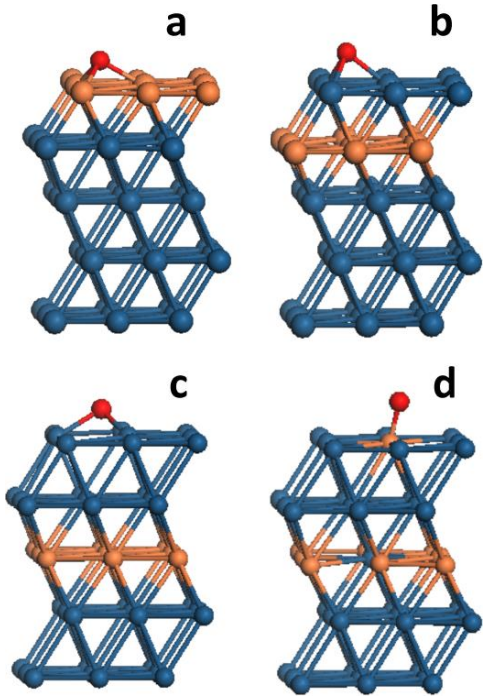

Figure 4.5: Structures for the density functional theory calculations shown in Table 3.1 with a single oxygen atom at the surface: a) Re-Pt-Pt-Pt-Pt; b) Pt-Re-Pt-Pt-Pt; c) Pt-Pt-Re-Pt-Pt; and d) Pt(Re_1)-Pt-Re(Pt_1)-Pt-Pt. Pt atoms are shown in blue, Re atoms in orange, and oxygen atoms in red.

layer is consistent with experimental results presented here as well as the higher surface free energy for Re compared to Pt (3.6 J/m^2 for Re versus 2.5 J/m^2 for Pt).[78] The stability of these alloy surface structures were then examined in the presence of oxygen. The calculated adsorption energies (E_{ads}) presented in Table 4.1 indicate that the oxygen atom adsorbs more strongly on a surface Re atom compared to a surface Pt atom. However, the relative energies of these surface structures with an adsorbed oxygen atom reveal that the most stable structure is the one with a single Re atom from the third layer exchanged with

Table 4.1: Computed Relative Energies (E_{rel}) for Pt-Re Bimetallic Structures in the Presence and Absence of an Oxygen Atom and the Calculated Adsorption Energies (E_{ads}) for an Oxygen Atom on These Structures

Structure	E_{rel} (eV), clean	E_{rel} (eV), with O	E_{ads} (eV)
Re-Pt-Pt-Pt-Pt	0.00	0.00	-3.90
Pt-Re-Pt-Pt-Pt	-7.56	-4.76	-1.10
Pt-Pt-Re-Pt-Pt	-10.89	-8.03	-1.04
$Pt(Re_1)$-Pt-$Re(Pt_1)$-Pt-Pt	-9.41	-8.89	-3.37

a Pt atom from the first layer (O−$Pt(Re_1)$−Pt−$Re(Pt_1)$− Pt−Pt, Figure 4.5d). For this structure, the energy is minimized by forming a strong Re−O bond at the surface as well as strong Pt−Re bonds in the subsurface layers. The structure without Re exchange (Figure 4.5c) becomes less stable by 0.86 eV than the structure with Re exchange (Figure 4.5d) as a consequence of the weaker Pt−O bonds. The Re-terminated surface remains the highest energy structure even in the presence of an adsorbed oxygen atom due to the greater surface free energy of Re. These results demonstrate that the Re atoms in the Pt−Re alloy remain in the bulk in the absence of surface adsorbates; however, in the presence of oxygen, it is thermodynamically favorable for a Re atom to diffuse to the surface to form a strong Re−O bond rather than forming a weaker Pt−O bond.

4.5 DISCUSSION

On all surfaces investigated, methanol oxidation reactions form similar products, particularly at low temperature, and the same general trends in reaction selectivities are followed as a function of temperature. Specifically, CO_2 and H_2O are primary reaction products, and the yields of these products increase with increasing temperature. Formaldehyde is also formed at lower temperatures with a maximum yield around

350−375 K, whereas the yields of other minor products such as CO, H_2, and CH_4 increase with temperature. At 300 and 350 K, all of the surfaces exhibit similar C(1s) spectra, given that three peaks are observed and assigned to gaseous methanol, surface CO, and CH_x. The O(1s) signals are also similar for all surfaces except for the oxidized Re film, which contains a much higher concentration of surface oxygen at 300 K. The product distributions observed here are consistent with other studies of methanol oxidation and decomposition on Pt and oxidized Pt surfaces. Under UHV conditions, CO, H_2, and H_2O are typically observed, with CO_2 and formaldehyde production on some surfaces. For example, on unoxidized Pt(111)[24] and reconstructed (2 × 1)-Pt(110), CO and H_2 are detected as the[67] reaction products. On oxidized Pt(111), methanol decomposes in UHV to CO, H_2O, and H_2,[24,68,69] and on oxidized (2 × 1)-Pt(110), CO_2 and formaldehyde are observed in addition to CO, H_2, and H_2O.[70]

A major difference between methanol oxidation activity on Pt(111) and the Re-containing surfaces is that carbon fouling is more prevalent on Pt(111) in the temperature range of 450− 550 K. In this temperature regime, there is also a change in selectivity on Pt(111) from CO_2 to CO, with an accompanying increase in H_2 production, whereas the selectivity change from CO_2 to CO is less pronounced on the Pt−Re alloy. Both of these differences in activity for Pt(111) vs the Pt−Re alloy are attributed to a lack of available surface oxygen on Pt(111) for oxidation of CO to CO_2 and for oxidation of carbonaceous residues. XPS data for both surfaces show that almost no oxygen is present on the surface at 400−450 K, indicating that surface oxygen is consumed by reaction as soon as it is formed. At higher temperatures of 500−550 K, a small oxygen feature appears again in the XPS spectrum, and this is ascribed to the greater dissociation of O_2 on Pt(111) at

higher temperatures, as reported in our previous study.[32] Given that O_2 dissociates on the Pt−Re alloy surface more readily than on Pt(111),[32] more surface oxygen should be available on Pt−Re for formation of the fully oxidized products and removal of carbonaceous residues on the surface. There is no evidence for decreased CO poisoning on the Pt−Re alloy compared to Pt(111), as has been proposed in APR reactions. Under methanol oxidation conditions studied here, CO is removed from both surfaces at temperatures <400 K, and therefore CO poisoning does not play a role in these reactions.

Previous studies of the Pt−Re alloy surface indicate that the top monolayer is composed of pure Pt, and Re exists in the subsurface layers.[32,34] This result is consistent with the lack of Re oxidation for the Pt−Re alloy under methanol oxidation conditions since the subsurface Re is not readily accessible by gaseous O_2. It is therefore not surprising that the Pt−Re alloy surface has nearly identical activity to that of Pt(111) at temperatures ≤400 K. However, at higher temperatures, the increased Re/Pt XPS ratio indicates that Re diffuses to the surface under methanol oxidation conditions, and consequently differences in activity are more apparent at these higher temperatures. DFT studies for model Pt−Re surfaces show that there is a thermodynamic driving force for Re to diffuse to the surface in the presence of oxygen. Furthermore, DFT calculations demonstrate that oxygen bound to Re at the surface is more stable than oxygen bound to Pt with an underlying Re layer. The enhanced activity of the Pt−Re alloy for O_2 dissociation is attributed to Re diffusion to the surface rather than dissociation of O_2 on a Pt monolayer electronically modified by underlying Re. Notably, only a small fraction of the total number of Re atoms diffuse to the surface for the Pt−Re alloy under reaction conditions, and consequently, the loss of Re due to Re_2O_7 sublimation is minimized.

The Pt−Re alloy oxidized at 450 K is the surface that achieves the maximum CO_2 and H_2O production in the intermediate temperature range of 400−450 K without any change in the selectivity for CO at higher temperatures. This preoxidized Pt−Re alloy has a greater concentration of surface Re at 400−450 K than the Pt−Re alloy because the O_2 treatment before exposure to the reactants induces diffusion of Re to the surface, based on the increase in the Re/Pt XPS ratio. For the Pt−Re alloy oxidized at 450 K, the majority of Re is in the metallic state with only a small (<15%) contribution from ReO_x under methanol oxidation conditions at 350 K. The other unique feature of the 450 K-oxidized Pt−Re alloy is that this surface is free of carbonaceous residues at temperatures of 450 K and higher. The lack of surface carbon at higher temperature and the high selectivity for the fully oxidized products like CO_2 are both explained by the greater fraction of Re at the surface for facilitating O_2 dissociation. In addition, this surface also has almost no surface oxygen species at reaction temperatures of 400 K and above. Thus, methanol oxidation occurs rapidly enough that neither carbon nor oxygen species accumulate on the surface at higher temperatures, and the lack of carbon and oxygen species on the surface also ensures that active sites are not blocked. Similarly, APXPS studies of methanol oxidation on Pd(111) surfaces have reported that the reaction rate is higher on the surfaces with lower concentrations of adsorbed surface species.[64]

The presence of ReO_x on the surface before methanol reaction for the oxidized Re film and Pt−Re alloy oxidized at 490 K did not significantly change the selectivity and activity for methanol oxidation. Specifically, the activities of both surfaces at 300−350 K, when ReO_x still exists on the surface, are similar to that of Pt(111) and the Pt−Re alloy in terms of product yields and distributions. However, it should be noted that none of the

surfaces have high activity in this low temperature regime. Furthermore, Re in its higher oxidation states of +4−6 was not stable under methanol oxidation conditions at any temperature. Initially, the oxidized Re film contained only ReO_x, whereas the Pt−Re alloy oxidized at 490 K was a mix of both metallic Re and ReO_x; subsurface Re remained metallic, while Re that diffused to the surface was oxidized. Re^{+n} (n = 4− 6) in the oxidized Re film is immediately reduced during methanol oxidation at 300 K even in the presence of O_2 in the reaction mixture, and a decrease in surface oxygen is observed with ReO_x reduction. Although almost no Re is detected on the surface above 450 K due to formation and subsequent sublimation of Re_2O_7, the oxidized Re film is not expected to have identical activity to Pt(111) because the latter has a significantly higher concentration of surface carbon. In contrast to the unoxidized Pt and Pt−Re alloy, both ReO_x-containing surfaces do not show the change in selectivity from CO_2 to CO at high temperatures observed on Pt(111), exhibit minimal carbon contamination at 500 K, and have a higher concentration of surface oxygen species at 300−450 K. Given that oxidized Re surfaces consisting of a film of ReO and Re_2O_3 are reported to be inactive for methanol decomposition in UHV,[44] the activity observed here for ambient pressure studies on the highly oxidized Re film demonstrates that activities can be substantially different in UHV compared to higher pressures of reactant gases.

Comparison with a previous APXPS investigation of methanol decomposition and oxidation on Pt(111) conducted at a lower total gas pressure of ~8 mTorr[23] shows that at the higher pressures in this study (300 mTorr) the Pt(111) surface is more active at lower temperature and more susceptible to carbon contamination. Specifically, no activity was observed below 450 K at 8 mTorr, whereas significant formaldehyde, H_2O, and CO_2

production occurs even at 350−400 K at 300 mTorr. In the lower pressure study, the lack of activity below 450 K was attributed to blocking of active sites by CO and carbon species; oxidation of carbonaceous residues as well as CO desorption above 450 K resulted in much higher activities at the elevated temperatures. At 300 mTorr, gaseous products are formed even when there is a relatively high concentration of surface carbon and oxygen species at the lower temperatures. The concentration of surface carbon increases with increasing reaction temperature above 400 K; thus, the rate of carbon deposition at 300 mTorr is higher than the rate of removal by oxidation, in contrast to the results reported for methanol oxidation with the same gas compositions at 8 mTorr. However, the high and low pressure studies are the same in terms of reaction pathways and product distributions. For example, the major reaction pathways in the 8 mTorr studies were fast dehydrogenation to CO and slower methanol decomposition via C−O bond scission. The main gaseous products were CO, H_2, CO_2, and H_2O, with the selectivity for the fully oxidized products increasing with higher O_2:methanol ratios in the reaction mixture. It was proposed that methanol dehydrogenation occurred via a methoxy intermediate, which underwent stepwise C−H bond breaking to form formaldehyde, formyl, and then CO, and this reaction mechanism is also consistent with the results of our experiments at 300 mTorr.

Methanol decomposition on Pt can occur via C−O bond scission to produce carbonaceous residues even though C−H bonds are easier to cleave in methoxy than C−O bonds. In some cases, no C−O bond scission was observed in UHV studies of methanol decomposition on Pt(111), where CO and H_2 were formed as the main gaseous products.[24] However, other UHV studies of methanol on Pt(111) showed that C−O bond

breaking occurred above 175 K to produce CH_3, which then dehydrogenated to form atomic carbon around 220 K.[73] Furthermore, on Pt(110), C−O bond scission occurred at 140 K to produce CH_x, which decomposed to surface carbon at higher temperatures.[26] Similarly, the APXPS study of methanol at 8 mTorr on Pt(111) reported that CH_x species were formed on the surface at temperatures of 300 K and above, and CH_3 was believed to dehydrogenate to atomic carbon even at room temperature.[23] Thus, it is expected that carbonaceous deposits can form during methanol decomposition, and this can lead to deactivation of the surface, particularly at higher pressure.

4.6 CONCLUSIONS

Pt−Re alloy surfaces are less susceptible to carbon fouling than pure Pt surfaces during methanol oxidation reactions, and the selectivity for CO_2 production is also higher on Pt−Re at temperatures above 500 K. These differences are attributed to the increased ability to dissociate O_2 on the Pt−Re surfaces compared to Pt, allowing carbonaceous residues as well as CO to be more easily oxidized. Although the Pt−Re alloys initially consist of pure Pt at the surface, there is evidence that under reaction conditions Re can diffuse to the surface and participate in the reaction; DFT studies confirm that it is thermodynamically favorable for Re to diffuse to the surface in the presence of oxygen. Furthermore, Pt−Re alloy surfaces that are preoxidized at 450 K show the greatest activity for CO_2 and H_2O production at low temperatures because Re is already extracted to the surface during the oxidation treatment. An oxidized Re film containing significant ReO_x had similar activity to Pt and the Pt−Re alloy at lower temperatures, but ReO_x is reduced under methanol oxidation conditions and sublimes as the volatile Re_2O_7 above 450 K. Thus, the desirable selectivity and stability of the Pt−Re alloy surface for

methanol oxidation are achieved by the gradual diffusion of Re to the surface under reaction conditions; the presence of a low concentration of Re at the surface enhances O_2 dissociation, and the fact that the majority of the Re resides subsurface in the alloy prevents rapid Re sublimation as Re_2O_7.

4.7 REFERENCES

(1) Kluksdahl, H. E. (Chevron). Reforming a Sulfur-Free Naphtha with a Platinum-Rhenium Catalyst. US Patent 3,415,737, 1968.

(2) Somorjai, G. A. Introduction to Surface Chemistry and Catalysis; John Wiley and Sons, Inc.: New York, 1994.

(3) Carter, J. L.; McVicker, G. B.; Weissman, W.; Kmak, W. S.; Sinfelt, J. H. Bimetallic Catalysts - Application in Catalytic Reforming. *Appl. Catal.*, **1982**, *3*, 327-346.

(4) Barbier, J. Deactivation of Reforming Catalysts by Coking - A Review. *Appl. Cat.*, **1986**, *23*, 225-243.

(5) Parera, J. M.; Beltramini, J. N. Stability of Bimetallic Reforming Catalysts. *J. Catal.*, **1988**, *112*, 357-365.

(6) Godbey, D. J.; Garin, F.; Somorjai, G. A. The Hydrogenolysis of Ethane over Re-Pt(111) and Pt-Re(0001) Bimetallic Crystal-Surfaces. *J. Catal.*, **1989**, *117*, 144-154.

(7) Kunkes, E. L.; Simonetti, D. A.; Dumesic, J. A.; Pyrz, W. D.; Murillo, L. E.; Chen, J. G. G.; Buttrey, D. J. The Role of Rhenium in the Conversion of Glycerol to Synthesis Gas over Carbon Supported Platinum-Rhenium Catalysts. *J. Catal.*, **2008**, *260*, 164-177.

(8) Simonetti, D. A.; Kunkes, E. L.; Dumesic, J. A. Gas-Phase Conversion of Glycerol to Synthesis Gas over Carbon-Supported Platinum and Platinum-Rhenium Catalysts. *J. Catal.*, **2007**, *247*, 298-306.

(9) Ciftci, A.; Ligthart, D.; Hensen, E. J. M. Influence of Pt Particle Size and Re Addition by Catalytic Reduction on Aqueous Phase Reforming of Glycerol for Carbon-Supported Pt(Re) Catalysts. *Appl. Catal. B*, **2015**, *174*, 126-135.

(10) Ciftci, A.; Ligthart, D.; Hensen, E. J. M. Aqueous Phase Reforming of Glycerol over Re-Promoted Pt and Rh Catalysts. *Green Chem.*, **2014**, *16*, 853-863.

(11) Zhang, L.; Karim, A. M.; Engelhard, M. H.; Wei, Z. H.; King, D. L.; Wang, Y. Correlation of Pt-Re Surface Properties with Reaction Pathways for the Aqueous-Phase Reforming of Glycerol. *J. Catal.*, **2012**, *287*, 37-43.

(12) King, D. L.; Zhang, L. A.; Xia, G.; Karim, A. M.; Heldebrant, D. J.; Wang, X. Q.; Peterson, T.; Wang, Y. Aqueous Phase Reforming of Glycerol for Hydrogen Production over Pt-Re Supported on Carbon. *Appl. Catal. B*, **2010**, *99*, 206-213.

(13) Azzam, K. G.; Babich, I. V.; Seshan, K.; Mojet, B. L.; Lefferts, L. Stable and Efficient Pt-Re/TiO_2 Catalysts for Water-Gas-Shift: On the Effect of Rhenium. *ChemCatChem*, **2013**, *5*, 557-564.

(14) Azzam, K. G.; Babich, I. V.; Seshan, K.; Lefferts, L. A Bifunctional Catalyst for the Single-Stage Water-Gas Shift Reaction in Fuel Cell Applications. Part 2. Roles of the Support and Promoter on Catalyst Activity and Stability. *J. Catal.*, **2007**, *251*, 163-171.

(15) Sato, Y.; Terada, K.; Hasegawa, S.; Miyao, T.; Naito, S. Mechanistic Study of Water-Gas-Shift Reaction over TiO_2 Supported Pt-Re and Pd-Re Catalysts. *Appl. Catal. A*, **2005**, *296*, 80-89.

(16) Iida, H.; Igarashi, A. Difference in the Reaction Behavior between Pt-Re/TiO_2 (Rutile) and Pt-Re/ZrO_2 Catalysts for Low-Temperature Water Gas Shift Reactions. *Appl. Catal. A*, **2006**, *303*, 48-55.

(17) Azzam, K. G.; Babich, I. V.; Seshan, K.; Lefferts, L. Role of Re in Pt-Re/TiO_2 Catalyst for Water Gas Shift Reaction: A Mechanistic and Kinetic Study. *Appl. Catal. B*, **2008**, *80*, 129-140.

(18) Ciftci, A.; Eren, S.; Ligthart, D.; Hensen, E. J. M. Platinum-Rhenium Synergy on Reducible Oxide Supports in Aqueous-Phase Glycerol Reforming. *ChemCatChem*, **2014**, *6*, 1260-1269.

(19) Ramstad, A.; Strisland, F.; Raaen, S.; Borg, A.; Berg, C. CO and O_2 Adsorption on the Re/Pt(111) Surface Studied by Photoemission and Thermal Desorption. *Surf. Sci.*, **1999**, *440*, 290-300.

(20) Greeley, J.; Mavrikakis, M. Near-Surface Alloys for Hydrogen Fuel Cell Applications. *Catal. Today*, **2006**, *111*, 52-58.

(21) Ishikawa, Y.; Liao, M. S.; Cabrera, C. R. Energetics of H_2O Dissociation and CO_{ads}+OH_{ads} Reaction on a Series of Pt-M Mixed Metal Clusters: A Relativistic Density-Functional Study. *Surf. Sci.*, **2002**, *513*, 98-110.

(22) Wei, Z. H.; Karim, A. M.; Li, Y.; King, D. L.; Wang, Y. Elucidation of the Roles of Re in Steam Reforming of Glycerol over Pt-Re/C Catalysts. *J. Catal.*, **2015**, *322*, 49-59.

(23) Miller, A. V.; Kaichev, V. V.; Prosvirin, I. P.; Bukhtiyarov, V. I. Mechanistic Study of Methanol Decomposition and Oxidation on Pt(111). *J. Phys. Chem. C*, **2013**, *117*, 8189−8197.

(24) Sexton, B. A. Methanol Decomposition on Pt(111). *Surf. Sci.*, **1981**, *102*, 271−281.

(25) Endo, M.; Matsumoto, T.; Kubota, J.; Domen, K.; Hirose, C. Oxidation of Methanol by Molecularly Adsorbed Oxygen on Pt(111) under Vacuum and Ambient Pressure Conditions Studied by Infrared Reflection Absorption Spectroscopy: Identification of Formate Intermediate. *Surf. Sci.*, **1999**, *441*, L931−L937.

(26) Wang, J. H.; Masel, R. I. C-O Bond Scission During Methanol Decomposition on (1 × 1)Pt(110). *J. Am. Chem. Soc.*, **1991**, *113*, 5850−5856.

(27) McCabe, R. W.; McCready, D. F. Kinetics and Reaction Pathways of Methanol Oxidation on Platinum. *J. Phys. Chem.*, **1986**, *90*, 1428−1435.

(28) Yuan, Y. Z.; Shido, T.; Iwasawa, Y. The New Catalytic Property of Supported Rhenium Oxides for Selective Oxidation of Methanol to Methylal. *Chem. Commun.*, **2000**, 1421-1422.

(29) Yuan, Y. Z.; Iwasawa, Y. Performance and Characterization of Supported Rhenium Oxide Catalysts for Selective Oxidation of Methanol to Methylal. *J. Phys. Chem. B*, **2002**, *106*, 4441-4449.

(30) Yoboue, A.; Susset, A.; Tougerti, A.; Gallego, D.; Ramani, S. V.; Kalyanikar, M.; Dolzhnikov, D. S.; Wubshet, S. G.; Wang, Y. L.; Cristol, S.; et al. An Easily Accessible Re-Based Catalyst for the Selective Conversion of Methanol: Evidence for an Unprecedented Active Site Structure through Combined Operando Techniques. *Chem. Commun.*, **2011**, *47*, 4285-4287.

(31) Secordel, X.; Berrier, E.; Capron, M.; Cristol, S.; Paul, J. F.; Fournier, M.; Payen, E. TiO_2-Supported Rhenium Oxide Catalysts for Methanol Oxidation: Effect of Support Texture on the Structure and Reactivity Evidenced by an Operando Raman Study. *Catal. Today*, **2010**, *155*, 177-183.

(32) Duke, A. S.; Galhenage, R. P.; Tenney, S. A.; Sutter, P.; Chen, D. A. In Situ Studies of Carbon Monoxide Oxidation on Platinum and Platinum-Rhenium Alloy Surfaces. *J. Phys. Chem. C*, **2015**, *119*, 381-391.

(33) Tenney, S. A.; Lu, D. Y.; He, F.; Levy, N.; Perera, U. G. E.; Starr, D. E.; Muller, K.; Bluhm, H.; Sutter, P. Key Structure-Property Relationships in CO_2 Capture by Supported Alkanolamines. *J. Phys. Chem. C*, **2014**, *118*, 19252-19258.

(34) Ramstad, A.; Strisland, F.; Raaen, S.; Worren, T.; Borg, A.; Berg, C. Growth and Alloy Formation Studied by Photoelectron Spectroscopy and STM. *Surf. Sci.*, **1999**, *425*, 57-67.

(35) Kresse, G.; Furthmuller, J. Efficient Iterative Schemes for Ab Initio Total-Energy Calculations Using a Plane-Wave Basis Set. *Phys. Rev. B*, **1996**, *54*, 11169-11186.

(36) Kresse, G.; Joubert, D. From Ultrasoft Pseudopotentials to the Projector Augmented-Wave Method. *Phys. Rev. B*, **1999**, *59*, 1758-1775.

(37) Blochl, P. E. Projector Augmented-Wave Method. *Phys. Rev. B*, **1994**, *50*, 17953-17979.

(38) Perdew, J. P.; Burke, K.; Ernzerhof, M. Generalized Gradient Approximation Made Simple. *Phys. Rev. Lett.*, **1996**, *77*, 3865-3868.

(39) Monkhorst, H. J.; Pack, J. D. Special Points for Brillouin-Zone Integrations. *Phys. Rev. B*, **1976**, *13*, 5188-5192.

(40) Methfessel, M.; Paxton, A. T. High-Precision Sampling for Brillouin-Zone Integration in Metals. *Phys. Rev. B*, **1989**, *40*, 3616-3621.

(41) Makov, G.; Payne, M. C. Periodic Boundary-Conditions in Ab-Initio Calculations. *Phys. Rev. B*, **1995**, *51*, 4014-4022.

(42) Norskov, J. K.; Rossmeisl, J.; Logadottir, A.; Lindqvist, L.; Kitchin, J. R.; Bligaard, T.; Jonsson, H. Origin of the Overpotential for Oxygen Reduction at a Fuel-Cell Cathode. *J. Phy. Chem. B*, **2004**, *108*, 17886-17892.

(43) Suthirakun, S.; Arnmal, S. C.; Munoz-Garcia, A. B.; Xiao, G.; Chen, F.; zur Loye, H.-C.; Carter, E. A.; Heyden, A. Theoretical Investigation of H_2 Oxidation on the $Sr_2Fe_{1.5}Mo_{0.5}O_6$(001) Perovskite Surface under Anodic Solid Oxide Fuel Cell Conditions. *J. Am. Chem. Soc.*, **2014**, *136*, 8374-8386.

(44) Chan, A. S. Y.; Chen, W. H.; Wang, H.; Rowe, J. E.; Madey, T. E. Methanol Reactions over Oxygen-Modified Re Surfaces: Influence of Surface Structure and Oxidation. *J. Phys. Chem. B*, **2004**, *108*, 14643-14651.

(45) Ducros, R.; Alnot, M.; Ehrhardt, J. J.; Housley, M.; Piquard, G.; Cassuto, A. A Study of the Adsorption of Several Oxygen-Containing Molecules (O_2, CO, NO, H_2O) on Re(0001) by XPS, UPS and Temperature Programmed Desorption. *Surf. Sci.*, **1980**, *94*, 154-168.

(46) Martensson, N.; Saalfeld, H. B.; Kuhlenbeck, H.; Neumann, M. Structural Dependence of the 5d-Metal Surface Energies as Deduced from Surface Core-Level Shift Measurements. *Phys. Rev. B*, **1989**, *39*, 8181-8186.

(47) Okal, J.; Tylus, W.; Kepinski, L. XPS Study of Oxidation of Rhenium Metal on Gamma-Al_2O_3 Support. *J. Catal.*, **2004**, *225*, 498-509.

(48) Okal, J.; Kepinski, L.; Krajczyk, L.; Tylus, W. Oxidation and Redispersion of a Low-Loaded Re/Gamma-Al_2O_3 Catalyst. *J. Catal.*, **2003**, *219*, 362-371.

(49) Okal, J. A Study of Effect of Particle Size on the Oxidation of Rhenium in the Re/Gamma-Al_2O_3 Catalysts. *Appl. Catal. A*, **2005**, *287*, 214-220.

(50) Shpiro, E. S.; Ryashentseva, M. A.; Minachev, K. M.; Antoshin, G. V.; Avaev, V. I. XPS Studies of Rhenium State in Supported Re Catalysts. *J. Catal.*, **1978**, *55*, 402-406.

(51) Tribalat, S.; Delafosse, D.; Piolet, C. Sur Un Nouvel Oxyde De Rhenium – L'oxyde De Rhenium V. *C. R. Hebd. Seances Acad. Sci.*, **1965**, *261*, 1008-1011.

(52) Cotton, F. A.; Wilkinson, G. Advanced Inorganic Chemistry: A Comprehensive Text, 4th ed.; John Wiley and Sons: New York, 1980.

(53) Naor, A.; Eliaz, N.; Burstein, L.; Gileadi, E. Direct Experimental Support for the Catalytic Effect of Iron-Group Metals on Electrodeposition of Rhenium. *Electrochem. Solid State Lett.*, **2010**, *13*, D91-D93.

(54) Bazuev, G. V.; Chupakhina, T. I.; Korolyov, A. V.; Kuznetsov, M. V. Synthesis under Usual Conditions, X-Ray Photoelectron Spectroscopy and Magnetic Properties of $Re_{1-x}Mn_xO_2$ Oxides with Rutile Structure. *Mater. Chem. Phys.*, **2010**, *124*, 946-951.

(55) Nikonova, O. A.; Capron, M.; Fang, G.; Faye, J.; Mamede, A. S.; Jalowiecki-Duhamel, L.; Dumeignil, F.; Seisenbaeva, G. A. Novel Approach to Rhenium Oxide Catalysts for Selective Oxidation of Methanol to DMM. *J. Catal.*, **2011**, *279*, 310-318.

(56) Tysoe, W. T.; Zaera, F.; Somorjai, G. A. An XPS Study of the Oxidation and Reduction of the Rhenium Platinum System under Atmospheric Conditions. *Surf. Sci.*, **1988**, *200*, 1-14.

(57) Ducros, R.; Fusy, J. Core Level Binding-Energy Shifts of Rhenium Surface Atoms for A Clean and Oxygenated Surface. *J. Electron Spectrosc. Relat. Phenom.*, **1987**, *42*, 305-312.

(58) Morant, C.; Galan, L.; Sanz, J. M. X-Ray Photoelectron Spectroscopic Study of the Oxidation of Polycrystalline Rhenium by Exposure to O_2 and Low-Energy O_2^+ Ions. *Anal. Chim. Acta*, **1994**, *297*, 179-186.

(59) Shcheglov, P. A.; Drobot, D. V. Heterogeneous Equilibria in the Rhenium-Oxygen System. *Russ. J. Phys. Chem.*, **2006**, *80*, 1819-1825.

(60) Björneholm, O.; Nilsson, A.; Tillborg, H.; Bennich, P.; Sandell, A.; Hernnäs, B.; Puglia, C.; Martensson, N. Overlayer Structure from Adsorbate and Substrate Core Level Binding Energy Shifts: CO, CCH_3, and O on Pt(111). *Surf. Sci.*, **1994**, *315*, L983-L989.

(61) Imamura, G.; Saiki, K. Synthesis of Nitrogen-Doped Graphene on Pt(111) by Chemical Vapor Deposition. *J. Phys. Chem. C*, **2011**, *115*, 10000−10005.

(62) Starr, D. E.; Pazhetnov, E. M.; Stadnichenko, A. I.; Boronin, A. I.; Shaikhutdinov, S. K. Carbon Films Grown on Pt(111) as Supports for Model Gold Catalysts. *Surf. Sci.*, **2006**, *600*, 2688−2695.

(63) Chen, J. J.; Jiang, Z. C.; Zhou, Y.; Chakraborty, B. R.; Winograd, N. Spectroscopic Studies of Methanol Decomposition on Pd(111). *Surf. Sci.*, **1995**, *328*, 248-262.

(64) Kaichev, V. V.; Miller, A. V.; Prosvirin, I. P.; Bukhtiyarov, V. I. In Situ XPS and MS Study of Methanol Decomposition and Oxidation on Pd(111) under Millibar Pressure Range. *Surf. Sci.*, **2012**, *606*, 420-425.

(65) Pozdnyakova, O.; Teschner, D.; Wootsch, A.; Krohnert, J.; Steinhauer, B.; Sauer, H.; Toth, L.; Jentoft, F. C.; Knop-Gericke, A.; Paal, Z.; et al. Preferential CO Oxidation in Hydrogen (PROX) on Ceria-Supported Catalysts, Part I: Oxidation State and Surface Species on Pt/CeO_2 under Reaction Conditions. *J. Catal.*, **2006**, *237*, 1-16.

(66) Croy, J. R.; Mostafa, S.; Heinrich, H.; Cuenya, B. R. Size-Selected Pt Nanoparticles Synthesized Via Micelle Encapsulation: Effect of Pretreatment and Oxidation State on the Activity for Methanol Decomposition and Oxidation. *Catal. Lett.*, **2009**, *131*, 21-32.

(67) Wang, J. H.; Masel, R. I. Methanol Adsorption and Decomposition on (2x1) Pt(110)- Enhanced Stability of the Methoxy Intermediate on a Stepped Surface. *Surf. Sci.*, **1991**, *243*, 199-209.

(68) Akhter, S.; White, J. M. A Static Sims TPD Study of the Kinetics of Methoxy Formation and Decomposition on O/Pt(111). *Surf. Sci.*, **1986**, *167*, 101-126.

(69) Liu, Z. X.; Sawada, T.; Takagi, N.; Watanabe, K.; Matsumoto, Y. Reaction Intermediates in the Oxidation of Methanol on a Pt(111)-(2x2)O Surface. *J. Chem. Phys.*, **2003**, *119*, 4879-4886.

(70) Wang, J.; Deangelis, M. A.; Zaikos, D.; Setiadi, M.; Masel, R. I. Methanol Oxidation on (2x1)Pt(110) - Formaldehyde on A Stepped Surface. *Surf. Sci.*, **1994**, *318*, 307-320.

(71) Bluhm, H.; Havecker, M.; Knop-Gericke, A.; Kleimenov, E.; Schlogl, R.; Teschner, D.; Bukhtiyarov, V. I.; Ogletree, D. F.; Salmeron, M. Methanol Oxidation on a Copper Catalyst Investigated Using in Situ X-Ray Photoelectron Spectroscopy. *J. Phys. Chem. B*, **2004**, *108*, 14340-14347.

(72) Carley, A. F.; Owens, A. W.; Rajumon, M. K.; Roberts, M. W.; Jackson, S. D. Oxidation of Methanol at Copper Surfaces. *Catal. Lett.*, **1996**, *37*, 79-87.

(73) Levis, R. J.; Jiang, Z.; Winograd, N.; Akhter, S.; White, J. M. Methyl Formation from Methanol Decomposition on Pd{111} and Pt{111}. *Catal. Lett.*, **1988**, *1*, 385-389.

(74) Miller, D. J.; Oberg, H.; Kaya, S.; Casalongue, H. S.; Friebel, D.; Anniyev, T.; Ogasawara, H.; Bluhm, H.; Pettersson, L. G. M.; Nilsson, A. Oxidation of Pt(111) under Near-Ambient Conditions. *Phys. Rev. Lett.*, **2011**, *107*, 195502.

(75) Puglia, C.; Nilsson, A.; Hernnas, B.; Karis, O.; Bennich, P.; Martensson, N. Physisorbed, Chemisorbed and Dissociated O_2 on Pt(111) Studied by Different Core-Level Spectroscopy Methods. *Surf. Sci.*, **1995**, *342*, 119-133.

(76) Jugnet, Y.; Loffreda, D.; Dupont, C.; Delbecq, F.; Ehret, E.; Aires, F.; Mun, B. S.; Akgul, F. A.; Liu, Z. Promoter Effect of Early Stage Grown Surface Oxides: A Near Ambient-Pressure XPS Study of CO Oxidation on PtSn Bimetallics. *J. Phys. Chem. Lett.*, **2012**, *3*, 3707-3714.

(77) Starr, D. E.; Bluhm, H. CO Adsorption and Dissociation on Ru(0001) at Elevated Pressures. *Surf. Sci.*, **2013**, *608*, 241-248.

(78) Cohesion in Metals: Transition Metal Alloys; de Boer, F. R.; Boom, R.; Mattens, W. C. M.; Miedema, A. R.; Niessen, A. K., Eds.; North-Holland Physics Publishing: Amsterdam, 1998; Vol. 1.

(79) Daniel, O. M.; DeLaRiva, A.; Kunkes, E. L.; Datye, A. K.; Dumesic, J. A.; Davis, R. J. X-Ray Absorption Spectroscopy of Bimetallic Pt-Re Catalysts for Hydrogenolysis of Glycerol to Propanediols. *ChemCatChem*, **2010**, *2*, 1107-1114.

CHAPTER 5

X-RAY PHOTOELECTRON SPECTROSCOPY AND REACTOR STUDIES FOR METHANOL OXIDATION ON PT AND PT-RE ALLOY SURFACES[3]

[3] Duke, A. S.; Xie, K.; Monnier, J. R.; Chen, D. A. "X-ray Photoelectron Spectroscopy and Reactor Studies for Methanol Oxidation on Pt and Pt-Re Alloy Surfaces," in preparation.

5.1 INTRODUCTION

Bimetallic surfaces often make highly desirable catalysts due to the well-known fact that their properties differ from those of their monometallic counterparts, stemming from the generation of new and unique metal-metal interactions and metal-support interactions.[1-5] Historically used in hydrocarbon reforming since the 1960s, bimetallic Pt-Re systems are reported to have increased activity, better selectivity, and longer catalyst lifetime than their monometallic Pt catalyst counterparts, reportedly due to an increased resistance to the accumulation of carbonaceous species which block active sites.[6-11] Some studies have suggested that the improved activity can be attributed to the alloying of Pt and Re in the bulk and the coinciding strong metal-metal electronic interactions; yet, the role that Re plays is not well understood.[11-15]

Pt-Re systems have more recently garnered attention as catalysts for oxidation reactions due to the role they might play in the reforming of biomass-derived products such as alcohols to hydrogen for renewable fuel sources.[16-25] In the aqueous reforming of model polyols such as glycerol, Dumesic and coworkers observed the addition of Re to Pt/C catalysts made the system 5 times more active than the original monometallic catalyst and increased the turnover frequencies for H_2, CO, CO_2 production.[16,17] They attributed the improvement to weaker binding of CO to Pt in the presence of Re as well as to decreased sintering of Pt nanoparticles under reaction conditions. Dumesic's team also proposed that the improved activity might be due to the formation of Re-OH sites, which facilitate the hydrogenolysis of glycerol, and they suggested the addition of Re to the catalyst led to an increased rate of the water-gas shift reaction.[16,23] Others such as Ciftci et al. and Azzam et al. agree that the improved activity is due to increased activity

for the water-gas shift reaction, but more specifically, they claim that it is caused by the formation of ReO_x by dissociation of water, thereby removing CO from the surface so it cannot poison Pt active sites.[18,19,24,26-31] At present, it is still unclear whether CO binds more or less strongly to Pt-Re surfaces than to pure Pt. Infrared spectroscopy of Pt and Pt-Re surfaces in WGS environments report that CO binds more strongly to the Pt-Re surfaces than to pure Pt,[31,32] but density functional theory (DFT) studies and temperature programmed desorption (TPD) experiments in ultra-high vacuum agree on the opposite result that CO binds more strongly to a pure Pt(111) surface than it does to a Pt-Re alloy surface.[33-35]

Here, model Pt and Pt-Re bimetallic systems were studied with XPS and an ambient pressure reactor for the oxidation of methanol as a model alcohol in order to investigate the effect of Re on Pt catalysts in oxidizing environments. Methanol is an ideal model system since it is the simplest of alcohols and has relevance for the fuel industry as it can be used both in classical internal combustion engines as well as in the development of modern direct methanol fuel cells.[36-38] The oxidation of alcohols such as methanol is industrially relevant given that it forms the basis for the production of many fine commodity chemicals.[39] The selective oxidation of methanol to formaldehyde, formic acid, methyl formate, and dimethoxymethane is highly useful as these products are used as diesel fuel additives, starting reagents for other organic syntheses, and low-toxicity solvents.[40] Methanol decomposition and oxidation have been previously studied for these and other purposes on model and real Pt catalysts as well as supported Re and Re oxide catalysts, but less is known about methanol oxidation on the bimetallic Pt-Re system.[36,41-49] In this work, samples were prepared in vacuum using a polycrystalline Pt

foil for a model Pt surface and physical vapor deposition to create Re films on a polycrystalline Pt foil, which were annealed to create model Pt-Re alloy surfaces. Methanol oxidation experiments were carried out from 60 to 170 °C under oxygen-rich conditions (2% methanol/4% O_2/balance He) on a clean Pt foil and Pt-Re alloy surface in a small flow reactor coupled to an ultra-high vacuum chamber for sample preparation and XPS analysis. Nearly identical distributions of products typical of methanol oxidation, such as CO_2, H_2O, formic acid, and formaldehyde, are seen on both surfaces in this work, while methyl formate, generated by some oxide supported Pt catalysts, and dimethoxymethane, generated by some oxide-supported Re catalysts, are not.[44-46] Pt-Re alloy surfaces maintain oxygen on the surface for longer periods of time and at higher temperatures than the pure Pt surfaces, and at the same time, they show less accumulation of carbon species and consequently have improved activity and catalyst lifetime over extended periods of time as compared to Pt surfaces. However, the oxidizing environments cause the loss of Re as Re_2O_7 from the surface over time.

5.2 EXPERIMENTAL

Experiments were performed in an ultra-high vacuum chamber ($P < 3 \times 10^{-10}$ Torr) coupled to a homemade microreactor, which has been described in detail elsewhere.[50] Some of the advantages of the microreactor are its high sensitivity and automated sampling design, which provides full kinetic analysis over long time intervals; however, one disadvantage of the reactor system is its limitation to temperatures below 200 °C. The UHV chamber is pumped by a 400 L/s ion pump (Varian, 912-7022) as well as a 360 L/s turbomolecular pump (Leybold Heraeus, TMP 360) and is coupled to a loadlock assembly pumped by a 150 L/s turbomolecular pump (Leybold Heraeus, TMP

150) for rapid introduction and transfer of samples without compromising the vacuum of the chamber. The chamber is equipped with a mass spectrometer (Stanford Research Systems, RGA 300), a dual Al/Mg anode X-ray source (Leybold Heraeus, RQ 20/63), a hemispherical analyzer (SPECS, EA10) for X-ray photoelectron spectroscopy (XPS), a set of retractable optics with a retarding field analyzer (SPECS, ErLEED-4) for low energy electron diffraction (LEED) and Auger electron spectroscopy (AES), and differentially-pumped BaF_2 windows for infrared reflection absorption spectroscopy (IRAS) in a cell that can be valved off to the rest of the UHV chamber for experiments in UHV or at pressures up to ~1 Torr using an FTIR spectrometer (Bruker, Tensor 27).

A polycrystalline Pt foil (ESPI Metals, 99.95%, 10 mm x 10 mm x 0.5 mm) was mounted to a Ta sample plate (Omicron) and cleaned by cycles of Ar^+ sputtering (20 minutes, 1 kV, 10 mA, 5 μA) and annealing (3 minutes, 1000 K) in vacuum until XPS showed the foil was clean. The foil was heated via electron bombardment of the Ta backplate, and the temperature of the foil was measured by an infrared pyrometer (Heitronics, CT18.04). 2.4 ML Re was deposited on the Pt foil at room temperature from a 2 mm diameter Re rod (ESPI, 99.99%) in a four-pocket electron-beam evaporator (Oxford Applied Research, EGC04), and a Pt-Re surface alloy was formed by annealing the Re film deposited on the Pt foil to 1000 K for 5 minutes. Re coverages were determined by a UHV bakeable quartz crystal microbalance (Inficon). One monolayer of Re is defined according to the packing density of Re (0001) (1.52×10^{15} atoms/cm^2).

XPS spectra were collected before and after reactor experiments at 30° off normal with respect to the analyzer using Al-Kα X-rays produced with an anode voltage of 10 kV and an emission current of 30 mA. Peak fitting for the C(1s) and O(1s) spectra was

carried out with the shareware program XPSPeak using a Shirley background and Gaussian-Lorentzian peak shapes.

After XPS was collected on the freshly prepared surface, the reactor was evacuated by the 150 L/s turbo pump so that the two manual gate valves isolating the reactor from the UHV chamber could be opened. A homemade gripping device was used to grab the Ta sample plate from the homemade sample holder and transfer it to the reactor while the pressure in the chamber with the loadlock and reactor open remained below 1 x 10^{-7} Torr the entire time so that the sample was never exposed to air. The sample was removed from the reactor in the same way for post-reaction XPS without exposure to air.

In the reactor, the sample was heated and cooled in 50 sccm continuous flow of He (Airgas, 99.999%) to temperatures between 60 °C to 170 °C at a rate of ~1.5-2 °C /min by heating tapes (Briskheat, BWHD) wrapped around the exterior of the reactor housing which were regulated by a feedback loop on a temperature controller (Auber, SYL-4342P) to ensure uniform heating and cooling. The temperature of the sample was estimated by a type K thermocouple (Omega, KMQSS-040G-6) welded into the feed gas inlet, close to the surface of the sample. The gas lines were maintained at 60 °C using two Valco Instruments temperature controllers. Once the sample reached the desired temperature, the feed gas of 2% methanol (Fisher Chemical, 99.9%)/ 4% O_2 (Airgas, 99.5%)/ 94% He was mixed and introduced. Both O_2 and He were introduced via independently calibrated mass flow controllers (Brooks, 5850e and 5850i) with the total flow rate of all feed gas maintained at 58 sccm as determined by a digital flow meter (Agilent Technologies, ADM2000). Methanol vapor was induced into the feed gas line

by a homemade vapor-liquid equilibrator (VLE) filled with liquid methanol, where helium served as the sweep gas and was introduced via a mass flow controller. The temperature of the VLE was controlled by a refrigerating/heating circulating bath (VWR), and the concentration of methanol in the vapor outlet was calculated using the Antoine equation for pure methanol. Pressure was monitored by two capacitance manometers (MKS Instruments, Baratron 722A) located upstream of the reactor in the feed gas line (790 Torr ~ 800 Torr) and downstream of the reactor (770 Torr ~ 780 Torr).

All activity tests were performed under single-pass mode.[50] For the activity tests performed over extended periods of time at a single temperature, the automated system was switched to sampling mode every 20 min, and a sample of the gas (~1.096 cm^3) was injected to a gas chromatograph (HP 5890A) which is equipped with a PoraPLOT Q capillary GC column leading to a thermal conductivity detector (TCD). Methanol oxidation was observed for 10h and 24h periods over a temperature range of 60-150 °C. To determine the activation energy of the reaction, a freshly prepared sample was first stabilized in the reaction mixture at 60 °C for 10 h, then stabilized at 80 °C, 100 °C, 130 °C, and 150 °C for 80 min each while four sampling injections were taken for each temperature. The reaction rate and % selectivity calculations are based on the formation rate of all detected carbon products (CO_2, formaldehyde, and formic acid). The background activity of the empty reactor and sample support was verified to be zero before and after all experiments. For some experiments, the surface was pre-oxidized in a 4% O_2/ 96% He flow for 2 h or the feed gas composition was changed to 8% methanol/ 4% O_2/ 94% He.

5.3 RESULTS

The Pt-Re alloy surfaces used in this study were prepared by depositing a 2.4 ML film of Re onto a polycrystalline Pt foil and annealing to 1000 K for 5 min after the method devised by Ramstad et al. for creating a Pt-Re surface alloy on a Pt(111) crystal.[14] Under these conditions, the Re film on the Pt surface is driven underneath the Pt so that the top monolayer of the surface is ~100% Pt.[14,51] XPS experiments corroborate this as shown in Figure 5.1. The binding energy for the Pt($4f_{7/2}$) peak of the

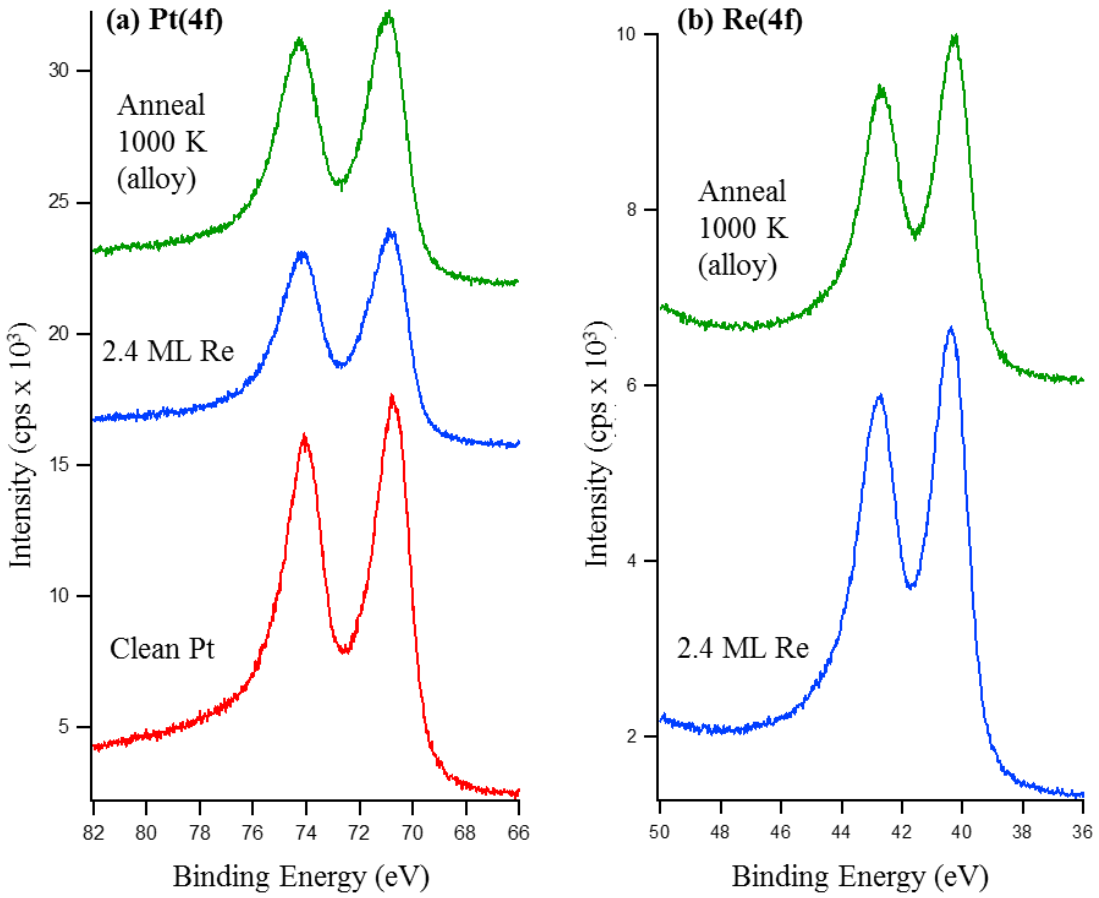

Figure 5.1: X-ray photoelectron spectroscopy data for a 2.4 ML Re film deposited on a Pt foil at room temperature and heated to 1000 K for 5 min to create a Pt−Re surface alloy: (a) Pt(4f) and (b) Re(4f) regions.

clean Pt foil is located at 70.8 eV, close to that of the standard value of 71.0 eV for Pt metal (Figure 5.1a).[14,52,53] After depositing 2.4 ML film of Re, the intensity of the Pt($4f_{7/2}$) peak is attenuated to 59% of its initial value, and after annealing to 1000 K for 5 min, the Pt($4f_{7/2}$) peak intensity increases back to 73% of its initial value, indicating that the Re atoms are being driven into the bulk of the Pt foil. The binding energy for the Re($4f_{7/2}$) peak of the 2.4 ML Re film appears at 40.4 eV, which is very near to the standard value of 40.3 eV for Re metal (Figure 5.1b).[54,55] After annealing, the Re($4f_{7/2}$) peak intensity is attenuated to 78% of its initial value, which is consistent with models and previous studies for surfaces where the top monolayer is 100% Pt and the Re atoms are distributed throughout the topmost subsurface layers as is expected for the Pt-Re surface alloy.[51,56]

Methanol oxidation (2% methanol, 4% O_2, balance He) was investigated in the UHV-coupled microreactor on the clean Pt foil and 2.4 ML Re alloy surfaces at temperatures of 60, 80, 100, 130, 150, 170 °C. Experiments were conducted over 80 min, 10 h, and 24 h periods at each temperature in single-pass mode, and the reaction gas mixture was sampled every 20 min by the automated system, using the GC-TCD to analyze the concentration of all products. The number of moles of each product was determined from the integrated area for each product peak along with a response factor of the GC-TCD system for each product which was calculated from a calibration performed independently for each product.

Figure 5.2 shows the activity of the Pt foil under methanol oxidation as a function of temperature. The detected products on the Pt foil included CO_2, H_2O, formaldehyde, and formic acid. The distribution of carbon products formed in μmol/h (Figure 5.2a)

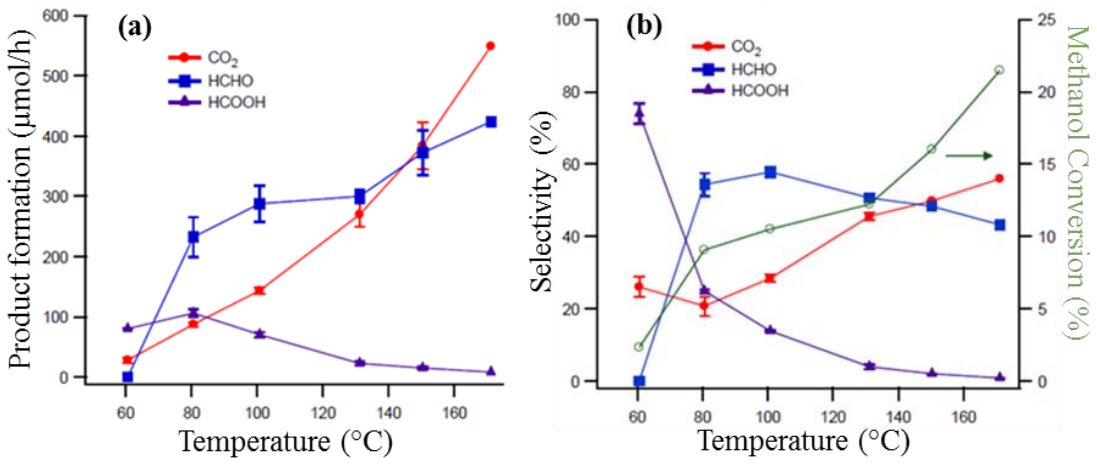

Figure 5.2: Activity of the Pt foil under methanol oxidation conditions as a function of temperature: (a) product distribution; (b) % selectivity and % methanol conversion.

shows that at 60 °C, the major product is formic acid, followed by CO_2, but no formaldehyde is formed. At 80 °C, formaldehyde production increases sharply so that it becomes the main product, while CO_2 production increases to a similar level as the formic acid, which stays approximately the same as it was at 60 °C. This indicates a possible change in reaction mechanism around this temperature. At 100 °C, formaldehyde and CO_2 production have increased at approximately the same rate as each other, but formic acid production decreases. At 130 °C, formaldehyde production has leveled off while the CO_2 production has risen to become very similar to it, and the formic acid production declines sharply. By 150 °C, formaldehyde and CO_2 production are identical, and virtually no formic acid is detected. At 170 °C, CO_2 production surpasses formaldehyde production so that CO_2 becomes the main product detected while the formic acid is still essentially zero.

The trends in selectivity to the various products are more clearly illustrated in Figure 5.2b which tracks the changes in selectivity and total methanol conversion as a function of temperature. At the lowest temperature where the conversion of methanol to products is only 3%, the reaction is ~25% selective for CO_2 production and ~75% selective to formic acid, but that selectivity to formic acid decays exponentially as the temperature of the system is increased. As the temperature is increased to 80 °C and the selectivity to formic acid decreases, the selectivity to CO_2 stays fairly constant, but the conversion of methanol increases to 9% while the selectivity to formaldehyde sharply increases from 0% to ~55%. The selectivity to formaldehyde and CO_2 as well as the conversion of methanol stay more or less the same, increasing only very slightly between 80 °C and 100 °C. By 130 °C, the methanol conversion has increased to 12%, and the selectivities to formaldehyde and CO_2 have become almost equivalent, with selectivity to formaldehyde at about 50%, selectivity to CO_2 at about 45%, and selectivity to formic acid only about 5%. At 150 °C, the selectivities to formaldehyde and CO_2 are identical at almost 50% each, and the methanol conversion has increased just above 15%. By 170 °C, the reaction achieves 22% total methanol conversion, and CO_2 becomes the dominant product at a selectivity of ~55% as the selectivity to formaldehyde drops to ~45% and formic acid drops completely to 0%.

Figure 5.3 shows the activity of the 2.4 ML Pt-Re alloy under methanol oxidation as a function of temperature. The detected products from the alloy surface included CO_2, H_2O, formaldehyde, and formic acid, which are the same products as detected on the Pt foil. The total carbon product formation in µmol/h on the Pt-Re alloy surface is identical to that of the Pt foil at 60 °C as shown in Figure 5.3a. At all of the higher temperatures

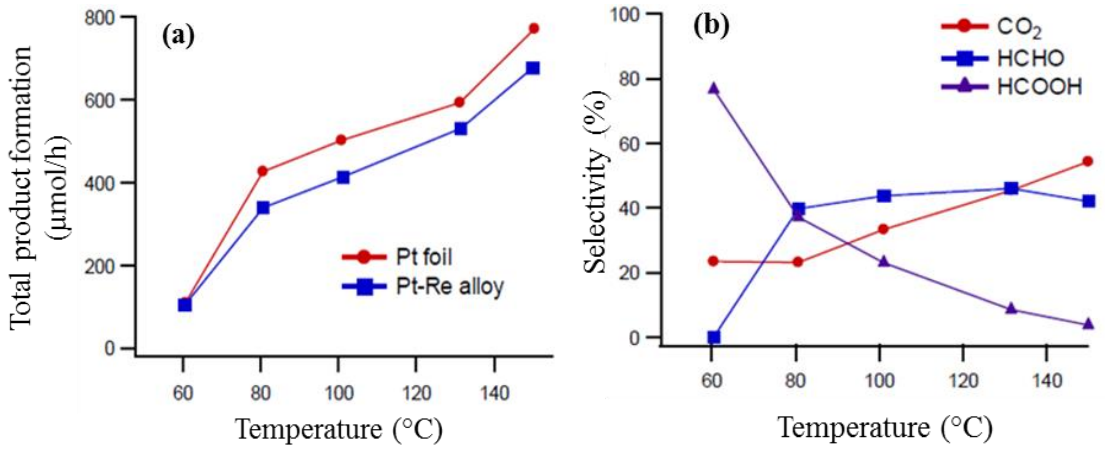

Figure 5.3: Activity of the 2.4 ML Pt-Re alloy under methanol oxidation conditions as a function of temperature: (a) product distribution; (b) % selectivity.

between 80 °C and 150 °C, the total product formation on the Pt-Re alloy is 10-20% lower than that on the Pt foil. Not shown are results from data collected at temperatures above 150 °C given that at those higher temperatures in an oxidizing environment, Re is known to oxidize to the Re(+7) state where it quickly becomes unstable and volatilizes off of the surface.[57-59]

A plot is displayed in Figure 5.3b of selectivity to the various carbon products as a function of temperature for methanol oxidation on the Pt-Re alloy surface. The trends in selectivity are very similar to those for the Pt foil. At 60 °C, the reaction is ~25% selective for CO_2 production and ~75% selective for formic acid with no formaldehyde production. The selectivity to formic acid on the alloy surface decays exponentially and the selectivity to formaldehyde increases as the temperature of the system is increased, just as on the Pt foil. At 80 °C the selectivity to formic acid and formaldehyde are equivalent at ~40% each while the selectivity to CO_2 stays constant. The selectivity to CO_2 increases to ~35% by 100 °C while the selectivity to formaldehyde stays more or

less the same and the selectivity to formic acid continues to decrease. By 130 °C, the selectivities to formaldehyde and CO_2 are equivalent at ~45% each with selectivity to formic acid making up the other 10%. At 150 °C, the selectivity to CO_2 increases to ~55%, making it the primary product, while the selectivity to formaldehyde stays close to its previous value, dropping slightly to ~40% and formic acid drops to ~5%.

Arrhenius plots can be constructed for methanol oxidation at these temperatures of 60 °C to 150 °C on the Pt foil and Pt-Re alloy as shown in Figures 5.4 and 5.5, respectively. In the plot constructed from the formation of all products on the Pt foil (Figure 5.4a), the points from 100°C to 150 °C appear to have a linear relationship, but there is a clear discontinuity between the points measured at 80 °C and 100 °C. Constructing an Arrhenius plot for only CO_2 formation on the Pt foil (Figure 5.4b) also shows a discontinuity at the lowest temperature points, in this case between 60 °C and 80 °C, but the points from 80 °C to 150 °C fall in a straight line, yielding an activation energy of 27.9 ± 0.2 kJ/mol for CO_2 formation on the Pt foil. Likewise, in constructing an Arrhenius plot for only CO_2 formation on the Pt-Re alloy (Figure 5.5), there is the same discontinuity between 60 °C and 80 °C, but the rest of the points from 80 °C to 150 °C are linear, giving an activation energy of 27.0 ± 1.0 kJ/mol for CO_2 formation on the Pt-Re alloy.

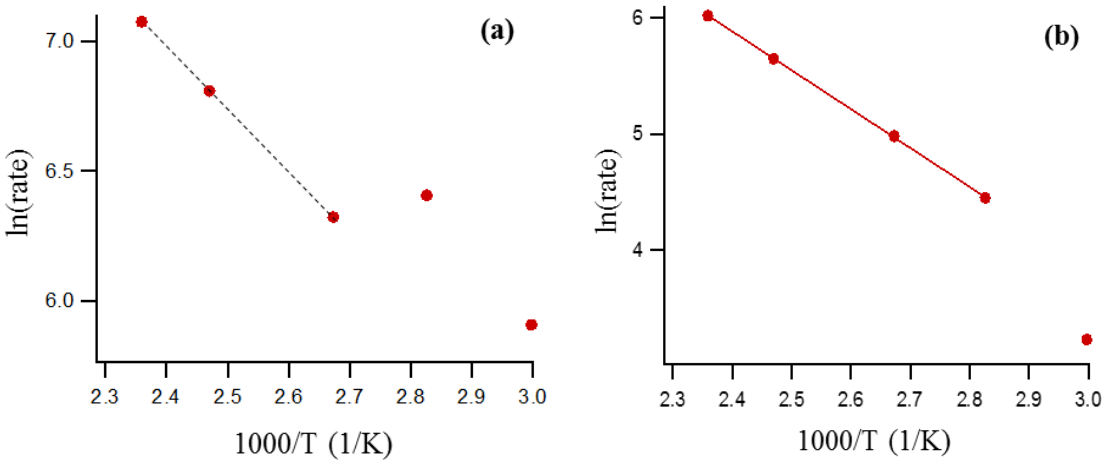

Figure 5.4: Arrhenius plots for methanol oxidation on the Pt foil: (a) for formation of all products; (b) for CO_2 formation only. The dashed black line indicates linearity. The red line indicates linear range of points used to calculate activation energy.

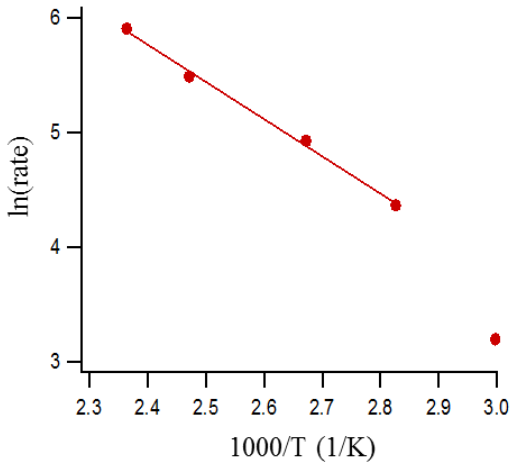

Figure 5.5: Arrhenius plot for CO_2 formation during methanol oxidation on a 2.4ML Pt-Re alloy surface.

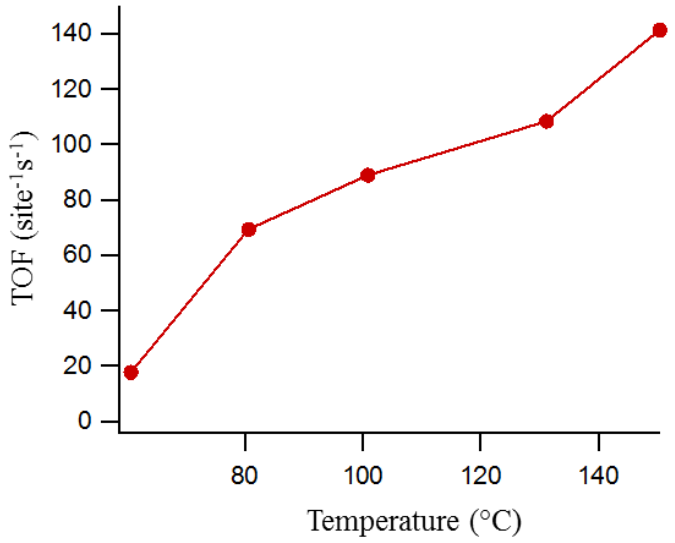

Figure 5.6: Turnover frequency (TOF) for methanol oxidation on Pt foil as a function of temperature.

A turnover frequency (TOF) can be estimated for the methanol oxidation reaction on the Pt foil. Though it is difficult to determine the exact number of active sites on the foil surface, the number can be approximated based on the open surface area of the foil inside the reactor and the assumption that the surface should behave primarily as the lowest energy surface available for Pt, which is the (111) surface. An approximate value calculated in this way is 1.0×10^{15} active sites for the Pt foil surface. Figure 5.6 shows the estimated TOF for the Pt foil as a function of temperature from 60 °C. to 150 °C. At the lowest temperature point when total methanol conversion is only about 3%, the TOF is close to 20 $site^{-1}s^{-1}$. The TOF increases to about 70 $site^{-1}s^{-1}$ at 80 °C, then to 90 $site^{-1}s^{-1}$ at 100 °C, 110 $site^{-1}s^{-1}$ at 130 °C, and 140 $site^{-1}s^{-1}$ at 150 °C.

The Pt foil and Pt-Re alloy were monitored for extended periods of time at single temperatures to study catalyst stability. Figure 5.7 shows the total product formation in

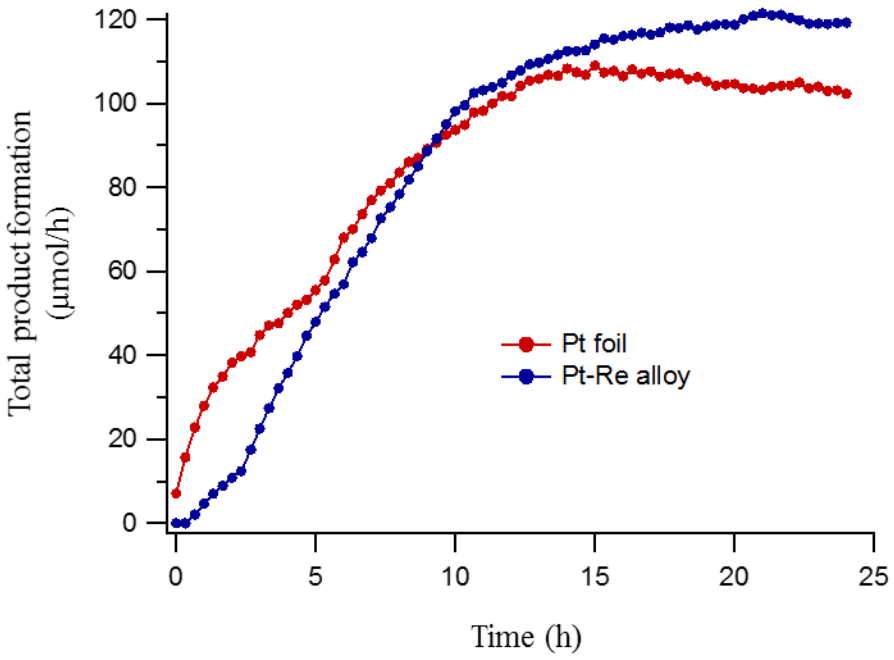

Figure 5.7: Total product formation for methanol oxidation on the Pt foil (red) and Pt-Re alloy (blue) as a function of time over 24 h at 60 °C.

µmol/h for the Pt foil and the Pt-Re alloy over a 24 h period at 60 °C. Initially, the Pt foil starts out with low activity at 10 µmol/h while the Pt-Re alloy has zero activity. After the initial data point, the two surfaces both increase in activity at approximately the same rate for the first 5 hours so that the Pt foil maintains the higher activity of the two. Between 5 and 9 hours, the Pt-Re alloy surface increases its rate of product formation faster than the Pt foil until at 9 hours, the two traces converge at ~90 µmol/h. Between 9 and 14 hours, the total product formation for both surfaces continues to increase at a similar though slower rate than before. At 14 hours, the total product formation on the Pt foil peaks at 110 µmol/h before beginning a steady downward decline while the total product formation on the Pt-Re surface has mostly stabilized at 120 µmol/h with a slight upward trend.

Post-reaction XPS data of these surfaces is shown in Figure 5.8. Figure 5.8a shows that after 24 h of methanol oxidation at 60 °C, the C(1s) region of the Pt foil (red) exhibits a substantial peak at 283.9 eV, attributed to atomic carbon, and a much smaller peak centered at 286.0 eV, corresponding to adsorbed CO.[36,41,42,49,51,60-64] Similarly, the C(1s) region of the Pt-Re alloy surface (blue) exhibits a very small peak at 283.6 eV and a small peak centered at 286.0 eV, though the Pt-Re alloy surface shows a much lesser accumulation of atomic carbon compared to the Pt foil Figure 5.8b shows that after 24 h of methanol oxidation at 60 °C, the O(1s) regions of the Pt foil (red) contain a large peak at 531.0 eV, corresponding to atomic oxygen, and a less intense peak at 532.4 eV, corresponding to strongly adsorbed hydroxyls as well as some CO which is removed from the surface when flashed to high temperature.[36,49,51,65] The O(1s) region of the Pt-Re alloy surface (blue) shows similar features, only both peaks are shifted by 0.5-0.6 eV

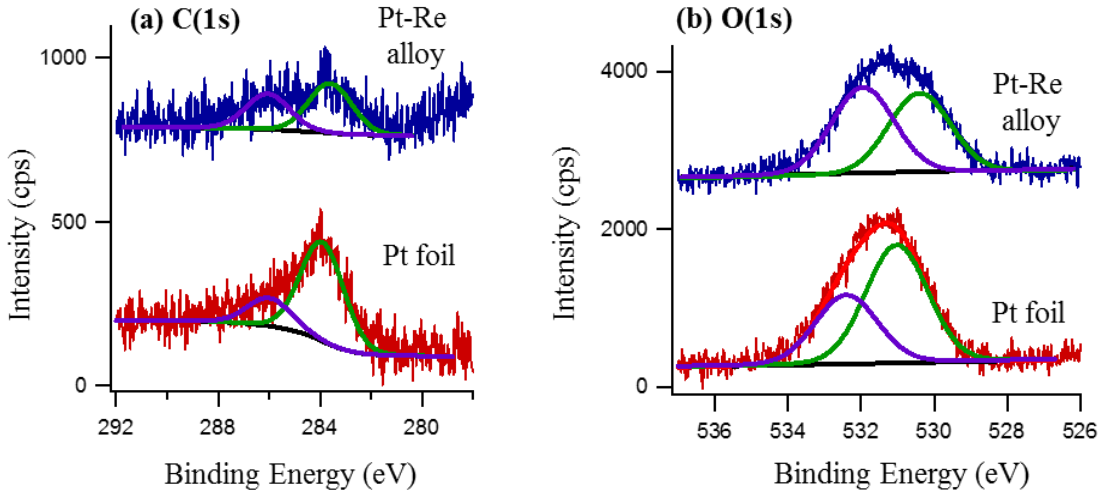

Figure 5.8: Post-reaction XPS data for the Pt foil (red) and Pt-Re alloy (blue) after methanol oxidation for 24 h at 60 °C. (a) C(1s) region; (b) O(1s) region.

to lower binding energies: the atomic oxygen peak appears at 530.4 eV, while the OH peak appears at 531.9 eV.

Atomic carbon also builds up on the Pt foil over shorter times at higher temperatures. Figure 5.9a shows post-reaction XPS data for the C(1s) region of the Pt foil after methanol oxidation for 10 h at 60 °C, 100 °C, and 150 °C with a fresh surface having been prepared for each temperature. At 60 °C, there is some accumulation of atomic carbon at 283.9 eV as compared to the spectrum from the clean Pt surface taken immediately before reaction. After 10 h at 100 °C, the C(1s) signal is not significantly different from that at 60 °C except that the tiny adsorbed CO feature at 286.0 eV becomes more defined, but after 10 h at 150 °C, the atomic carbon level at 283.9 eV has

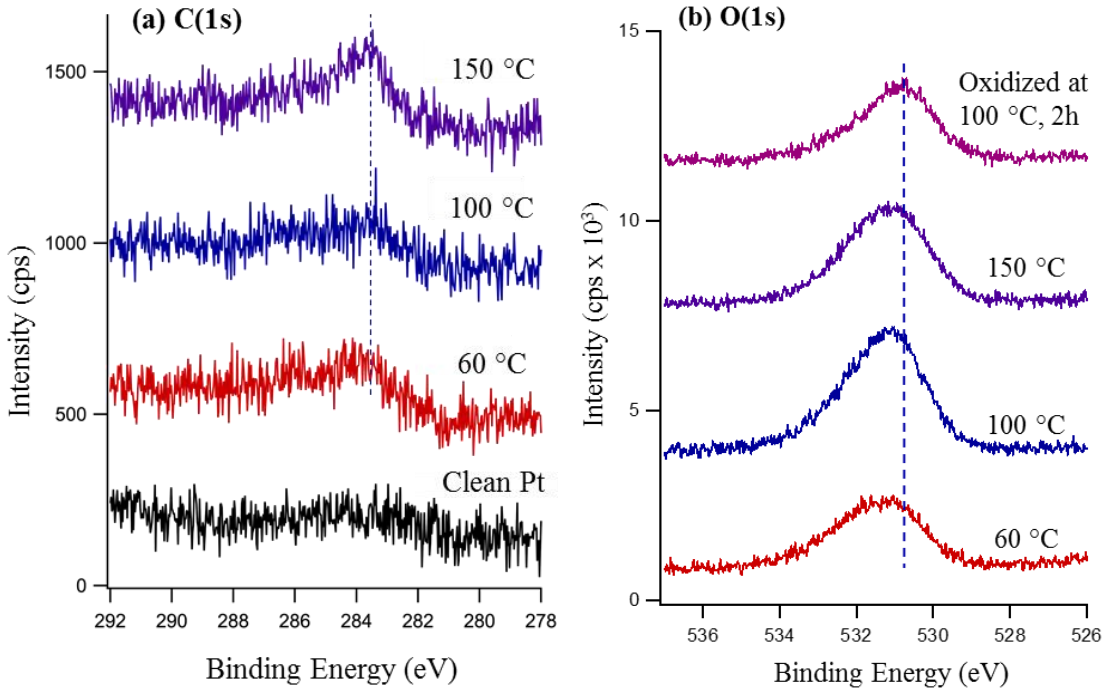

Figure 5.9: Post-reaction XPS for the Pt foil after methanol oxidation for 10 h for each temperature and for one Pt foil surface that was oxidized in pure O_2 without exposure to methanol: (a) C(1s) region; (b) O(1s) region. Dashed lines indicate the position of atomic C and atomic O, respectively.

dramatically increased. Figure 5.9b shows post-reaction XPS data for the O(1s) region of the Pt foil after methanol oxidation for 10 h at 60 °C, 100 °C, and 150 °C, with a fresh surface having been prepared for each temperature, as well as for a Pt foil that was oxidized in pure O_2 at 100 °C for 2 h and did not undergo reaction with methanol. After 10 h at 60 °C, there is accumulation of atomic O on the surface at 531.0 eV, which is similar though slightly lower in intensity than that on the surface oxidized in pure O_2, as well as hydroxyls and CO at 532.4 eV, which are not seen on the surface oxidized in pure O_2. After 10 h at 100 °C, both atomic O, OH, and CO signals have increased in intensity, though the atomic O signal at 531.0 eV has increased to a greater extent than the adsorbed OH/CO signal. After 10 h at 150 °C, the intensities of both peaks have diminished slightly as compared to the surface at 100 °C, but they are still greater than the signals seen at 60 °C.

In contrast to the Pt foil, which accumulates atomic carbon over just 10 h of reaction, the Pt-Re alloy surface does not accumulate substantial amounts of carbon even after 24 h on-line. Figure 5.10a shows post-reaction XPS data for the C(1s) region of the Pt-Re alloy after methanol oxidation for 24 h at 60 °C, 80 °C, 100 °C, 130 °C, and 150 °C with a fresh surface having been prepared for each temperature. After 24 h at 60 °C, the spectrum shows small peaks corresponding to atomic carbon at 283.6 eV and adsorbed CO at 286.0 eV. These features do not change after 24 h at 80 °C or 24 h at 100 °C. However, after 24 h at 130 °C, the atomic carbon peak at 283.6 eV has disappeared from the spectrum while the small adsorbed CO feature remains at 286.0 eV. After 24 h at 150 °C the atomic carbon is still gone, and the CO feature has not changed in intensity. Figure 5.10b shows post-reaction XPS data for the O(1s) region of the Pt-Re alloy after

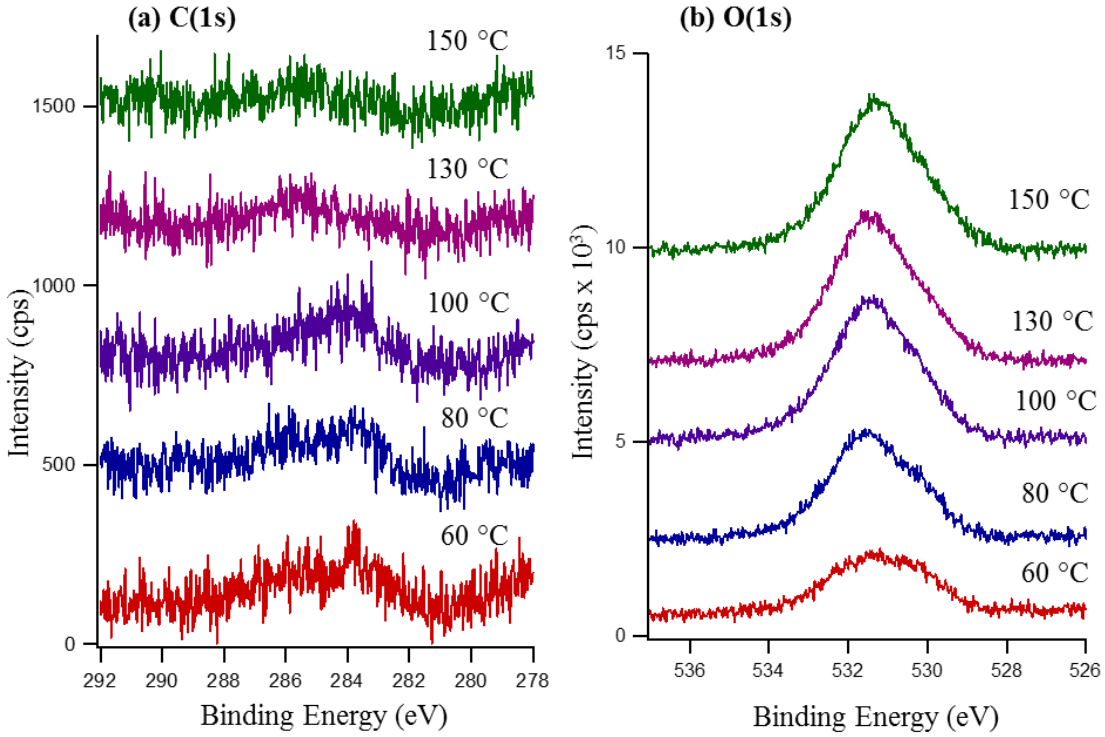

Figure 5.10: Post-reaction XPS for the Pt-Re alloy after methanol oxidation for 24 h at each temperature: (a) C(1s) region; (b) O(1s) region.

methanol oxidation for 24 h at 60 °C, 80 °C, 100 °C, 130 °C, and 150 °C with a fresh surface having been prepared for each temperature. After 24 h at 60 °C, a broad feature appears in the spectrum, corresponding to almost identical intensities for atomic O at 530.4 eV and adsorbed OH and CO at 531.9 eV. After 24 h at 80 °C as well as after 24 h at 100 °C, oxygen species continue to build up on the surface, with the adsorbed OH and CO feature increasing in intensity more than the atomic O feature. Between 100 °C and 150 °C, there is no further buildup or change in the ratio of the atomic O and adsorbed OH/CO signals.

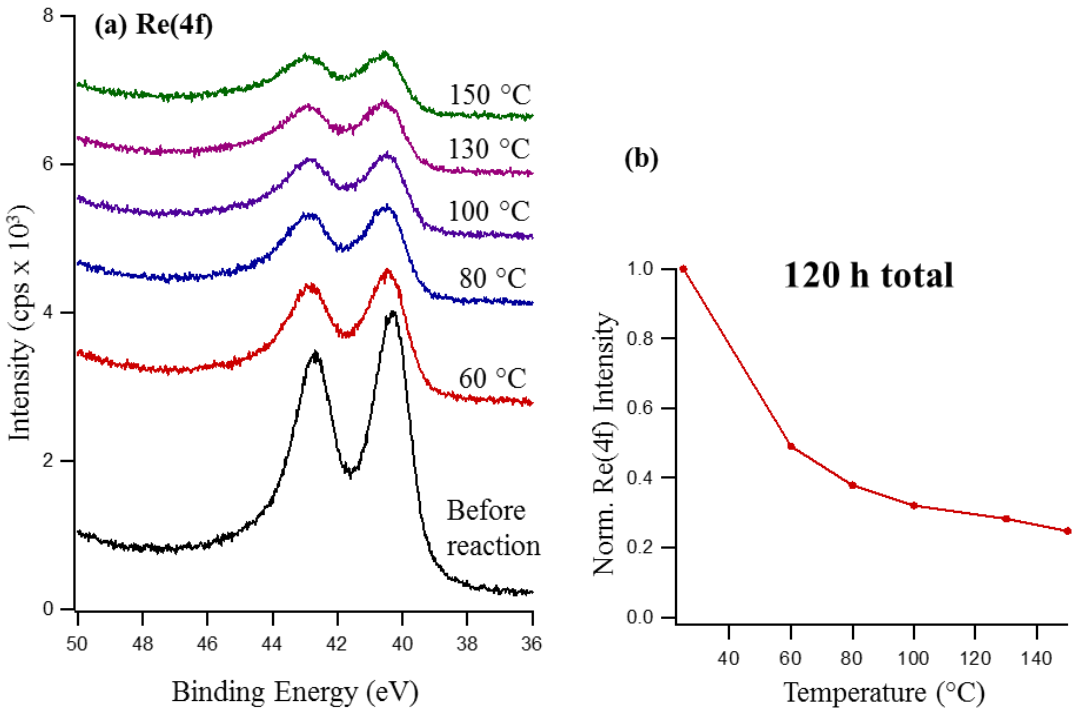

Figure 5.11: (a) Post-reaction XPS of the Re(4f) region for the Pt-Re alloy after methanol oxidation for 24 h at each temperature. (b) Integrated normalized Re(4f) signal as a function of temperature.

Figure 5.11 tracks the disappearance of Re from the Pt-Re alloy under the same conditions just described of methanol oxidation for 24 h at 60 °C, 80 °C, 100 °C, 130 °C, and 150 °C with a fresh surface having been prepared for each temperature. After 24 h at 60 °C, the integrated area of the Re(4f) signal for the Pt-Re alloy has decreased to about 50% of its value before reaction. After 24 h at 80 °C, the decline in signal is less sharp, and a little less than 40% of the original intensity remains. The normalized signal intensity continues to drop slowly after 100 °C and 130 °C as well until it is only ~25% of the original signal after 24 h at 150 °C. This decrease in Re(4f) signal intensity on the Pt-Re alloy does not occur when the sample is heated to each of these temperatures for 24

h in an inert atmosphere of pure He but only when the sample is in an oxidizing environment.

The Pt foil and Pt-Re alloy were also monitored for extended periods of time at a single temperature under different feed gas compositions to establish the different effects of oxygen-rich and methanol-rich conditions. Figure 5.12 shows the total product formation in µmol/h for the Pt foil and the Pt-Re alloy over a 24 h period at 60 °C for a feed gas composition of 8% methanol/ 4% O_2/ 94% He compared to that of the Pt foil under the usual feed gas composition of 2% methanol/ 4% O_2/ 94% He. Under methanol-rich conditions both the Pt and Pt-Re alloy surfaces follow the same upward trend, increasing less rapidly and to a lower overall total product formation than the Pt foil

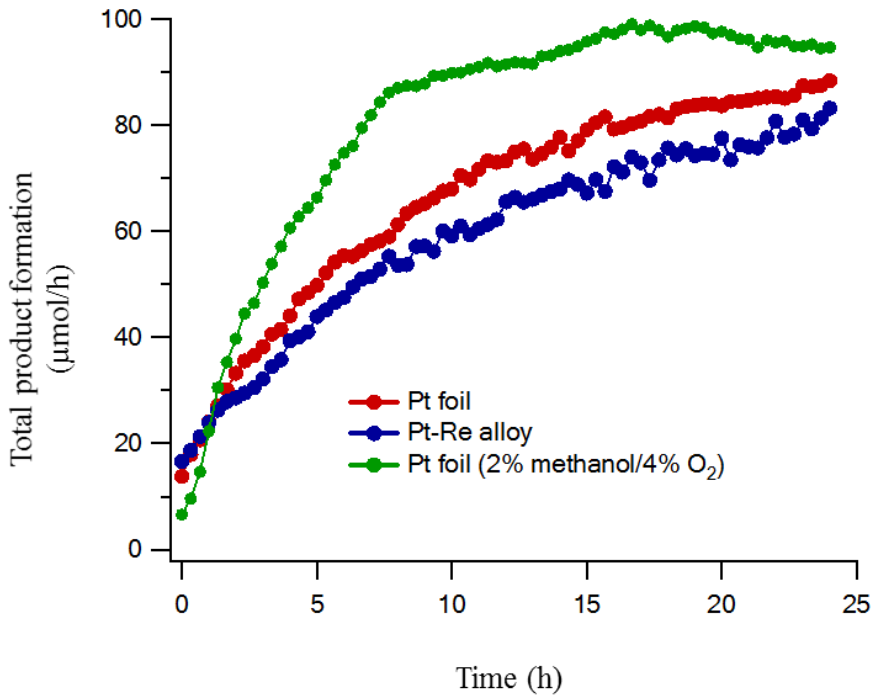

Figure 5.12: Total product formation for methanol oxidation with a feed gas composition of 8% methanol/ 4% O_2/ 94% He on the Pt foil (red) and Pt-Re alloy (blue) as a function of time over 24 h at 60 °C compared to the usual feed gas composition of 2% methanol/ 4% O_2/ 94% He on the Pt foil (green).

under oxygen-rich conditions with the Pt-Re alloy showing consistently lower activity than either Pt surface.

Figure 5.13 shows post-reaction XPS data of the Pt foil and Pt-Re alloy after methanol oxidation with a feed gas composition of 8% methanol/ 4% O_2/ 94% He for 24 h at 60 °C and after briefly heating the post-reaction surfaces to 700 K. Like the surfaces under oxygen-rich conditions, the C(1s) region of the post-reaction Pt foil (Figure 5.13a) contains an atomic carbon peak at 283.9 eV, and the post-reaction Pt-Re alloy surface (blue) contains an atomic carbon peak at 283.6 eV. Unlike the surfaces under oxygen-rich conditions, the post-reaction Pt and Pt-Re alloy surface exhibit substantial, broad features stretching from 285 eV to 288 eV corresponding to larger quantities of CO at 286 eV than seen for the oxygen-rich environment and possibly formate at 287 eV.[36,42,49] The O(1s) region of the post-reaction Pt foil (Figure 5.13b) contains a large atomic oxygen feature at 531.0 eV, and the post-reaction Pt-Re alloy contains an atomic oxygen

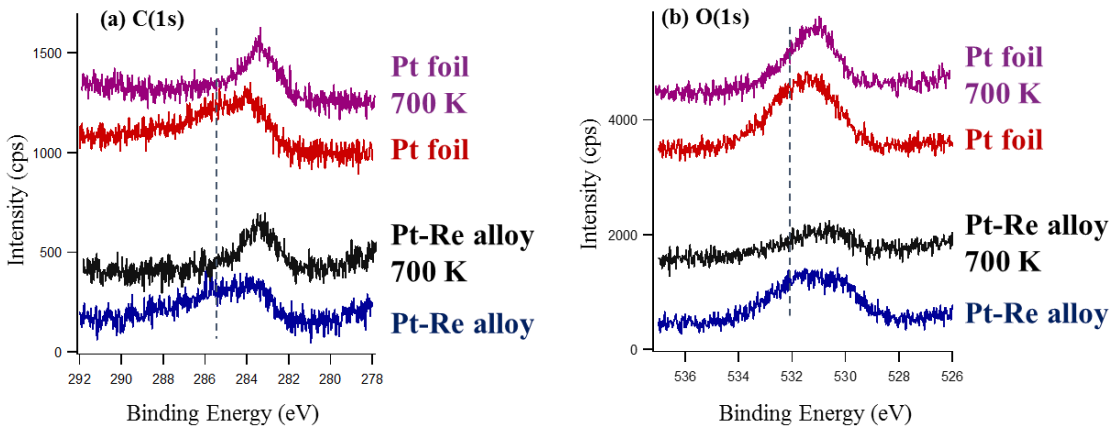

Figure 5.13: Post-reaction XPS data for the Pt foil (red) and Pt-Re alloy (blue) after methanol oxidation with a feed gas composition of 8% methanol/ 4% O_2/ 94% He for 24 h at 60 °C and after flashing the Pt foil (purple) and Pt-Re alloy (black) to 700 K. (a) C(1s) region; (b) O(1s) region.

peak at 530.4 eV as in the oxygen-rich conditions. However, both of these features are broadened, indicating larger surface hydroxyl and CO peaks on both surfaces at 532 eV than were seen in oxygen-rich environments. After briefly flashing both surfaces to 700 K, the higher binding energy peaks in the C(1s) regions on both surfaces disappear, indicating removal of CO species, leaving only atomic carbon behind. The higher binding energy species in both O(1s) regions decrease somewhat in intensity, corresponding to the removal of CO species, but the remaining intensity indicates surface hydroxyls and atomic oxygen left behind.

Pre-oxidized surfaces were also studied to determine the impact of larger quantities of surface oxygen on activity. As shown in Figure 5.14, an as-prepared Pt foil

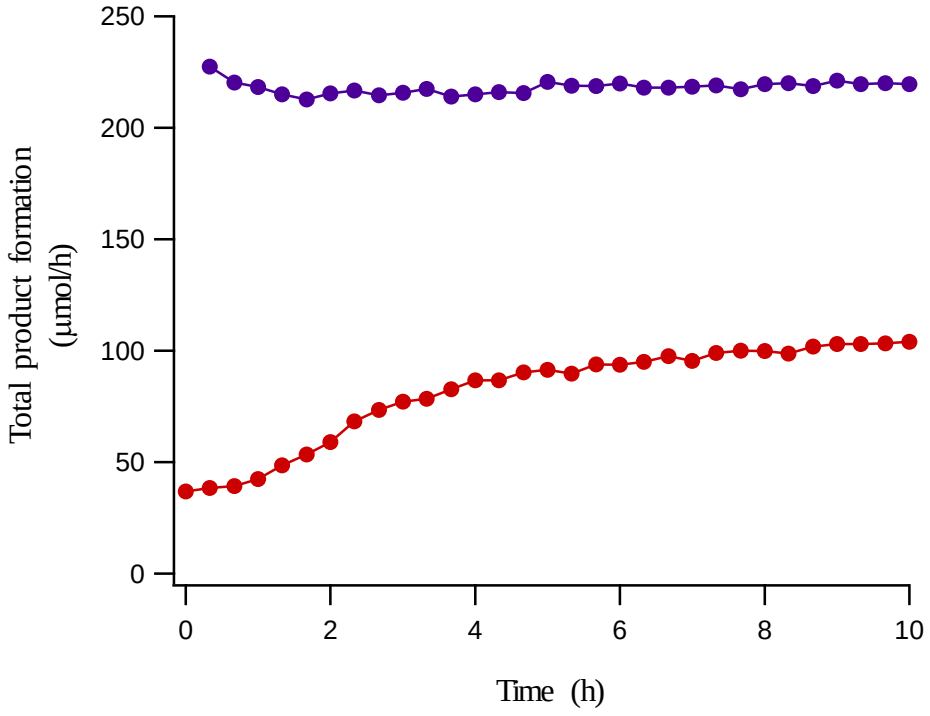

Figure 5.14: Total product formation for methanol oxidation over an as-prepared Pt foil (red) and a Pt foil that was pre-oxidized at 130 °C (blue) as a function of time over 10 h at 100 °C.

shows initially low activity, which gradually increases during the course of the reaction before plateauing. In contrast, a Pt foil which was first oxidized for 2 hours at 130 °C in a 4% O_2/ 96% He flow initially shows more than double the activity of the unoxidized Pt foil without any onset time. Furthermore, the selectivity to formaldehyde production increases from 0% to 40% for the pre-oxidized surface.

5.4 DISCUSSION

The Pt foil and Pt-Re alloy generate the same products and exhibit similar trends in product formation for methanol oxidation over all temperatures studied. On both surfaces, formic acid is the main product at low temperatures of 60 °C, formaldehyde is the main product between 80 and 130 °C, and CO_2 becomes the main product at temperatures above 130 °C. Similar products have been observed in the literature on Pt(111) and oxidized Pt wires, with H_2, CO, and H_2O being the primary products detected under UHV conditions on Pt(111) and Pt(110)-(2x1).[41,42,44,62,64,66,67] In the studies reported here, water is formed at all temperatures, and although the GC-TCD setup used in these studies is not sensitive to the formation of H_2 or CO, the products detected are very similar to what has already been reported in the literature. Endo et al. observed only surface formate species and surface CO species with IRAS and CO_2 formation from mass spectrometry studies in UHV and at much higher pressures (1.3 kPa O_2/0.16 kPa methanol).[42,68] As McCabe notes, the formation of formaldehyde is extremely sensitive to reaction conditions in that it has a strong dependence on the level of oxygen in the system as well as the temperature.[44] In oxygen-rich feeds on heavily oxidized Pt wires at 127 °C and above, McCabe and coworkers reported formation of CO_2, H_2O, and formaldehyde but did not report seeing the formation of formic acid, perhaps because the

temperature range was too high.[44] However, Gentry et al. also reported formation of CO_2, H_2O, and formaldehyde but no formic acid even within the low temperature range of 37-77 °C.[66] Additionally, they observed traces of methyl formate, which is a commonly detected product on highly-dispersed alumina supported Pt catalysts; however, it was not detected in these studies.[44,66] Dimethoxymethane was also not observed in these experiments although it is typically observed on titania supported Re catalysts.[45,46]

As the formation of formic acid peaks around 60 to 80 °C and drops off exponentially to zero at higher temperatures, the formaldehyde production increases from zero on both surfaces. This indicates a possible change in reaction mechanism within this temperature range. The Arrhenius plots for formation of all products on both surfaces show a distinct disjunction between the formation rates at low temperatures and those above 80 °C, further indicating a change in reaction mechanism. The activation energies (E_a) for only CO_2 formation are similar for the Pt foil and Pt-Re alloy at 27.9 ± 0.2 kJ/mol for the Pt foil and 27.0 ± 1.0 kJ/mol for the Pt-Re alloy surface over a temperature range of 80-150 °C, and are similar to those reported in the literature. Endo et al. reported an E_a for CO_2 formation of 22 kJ/mol on a Pt(111) surface over a temperature range of 127-277 °C.[68] Gentry et al. reported an E_a for CO_2 formation of 33 kJ/mol over a temperature range of 53-72 °C.[66] McCabe et al. reported an E_a for CO_2 formation of 42 kJ/mol on heavily oxidized Pt wires over a temperature range of 127-277 °C.[44] Gentry and coworkers also report a TOF of ~50 s^{-1} at 100 °C compared to the somewhat higher estimation obtained in this work for the Pt foil of 90 s^{-1} at 100 °C.[66]

The most apparent differences between the Pt foil and Pt-Re alloy are the total activity of the two surfaces over time and the correlated accumulation of either atomic

carbon or atomic oxygen on the surfaces with the Pt-Re alloy showing slightly higher long-term activity and less carbon deposition than the Pt foil. When studied over a range of temperatures, the Pt foil and Pt-Re alloy follow similar trends in total product formation, but the Pt-Re surface consistently shows 10-20% less activity than the Pt foil except at 60 °C where the total product formation is identical for both surfaces. The fact that the surfaces behave identically at first can be attributed to the fact that the Re present in the alloy is initially entirely subsurface so that both surfaces behave essentially as pure Pt. After exposure to the high levels of O_2 in the feed gas, the subsurface Re diffuses to the surface of the substrate, as predicted by DFT studies of model Pt-Re surfaces which indicate a strong thermodynamic driving force for the diffusion of Re to the surface in oxygen environments. When the two surfaces are studied at 60 °C for 24 h, both surfaces show an initial activation period where the activity slowly increases over the first several hours before reaching maximum activity. This activation corresponds to a period of time where oxygen accumulates on both surfaces, according to post-reaction XPS results and activity results from pre-oxidized surfaces. It appears that the initial activation of the Pt-Re alloy surface is delayed by 1-2 h compared to the Pt foil, possibly due to the diffusion of Re to the surface, which could initially block Pt active sites or inhibit active Pt ensembles, thereby lowering the activity compared to pure Pt. For the first 5 h at 60 °C, the Pt-Re alloy surface follows almost the same trend as the Pt foil until the rate of product formation on the Pt begins to slow compared to the alloy. Between 5 and 9 h, the alloy still has consistently less activity than the Pt, but its rate of product formation is still increasing while the rate of product formation on the Pt is slowing. By 9 h, the activities of the two surfaces are exactly the same. After those first 10 h, the activity of the Pt-Re

alloy is consistently higher than that on the Pt foil so that after 24 h, the Pt-Re alloy surface has 15% higher activity than the Pt foil. This is correlated with an accumulation of atomic carbon on the Pt foil, which is 40% greater than on the Pt-Re alloy. Atomic carbon accumulates on the Pt foil over shorter periods of time at higher temperatures as well. After just 10 h of methanol oxidation over the Pt foil, there is substantial accumulation of atomic carbon the Pt foil, whereas there is virtually no carbon detected on the Pt-Re alloy surface at the same temperature for 24 h. While both surfaces gradually build up increasing levels of surface oxygen from 60 to 100 °C, the Pt-Re alloy maintains a larger quantity of oxygen on the surface at higher temperatures like 150 °C than the Pt foil. The alloy's ability to maintain the high levels of oxygen at high temperatures is due to the ability of Re to dissociate O_2 more readily than Pt. At higher temperatures there is a constant supply of subsurface Re diffusing to the surface of the substrate in the presence of oxygen. This is because oxygen bound to surface Re atoms is thermodynamically more stable than oxygen bound to Pt on top of subsurface Re, according to DFT calculations. However, the Pt-Re alloy surface must eventually be unstable under such quantities of oxygen since post-reaction XPS shows that the amount of Re in the surface decreases exponentially as a function of temperature under reaction conditions. This is due to the fact that oxophilic Re at the surface can form volatile Re_2O_7, which then sublimes. Increasing the methanol to oxygen ratio decreases the overall activity for both the Pt foil and Pt-Re alloy surfaces because there is insufficient accumulation of oxygen on the surface in the reducing environment. Studies of as-prepared and pre-oxidized surfaces show that as-prepared surfaces require an initial onset period for accumulation of dissociated oxygen on the surface with initially low to no

activity while pre-oxidation leads to initially higher activity. Under reducing conditions, the Pt-Re alloy surface consistently maintains lower activity than the Pt surface due to the fact that the reaction conditions are too reducing to extract Re to the surface, which precludes any effects of its enhanced ability to dissociate oxygen.

5.5 CONCLUSIONS

Pt and Pt-Re alloy surfaces show similar selectivity for the methanol oxidation reaction. On both surfaces, formic acid is the primary product formed at low temperatures, followed by formaldehyde at intermediate temperatures, and then CO_2 at high temperatures across the range of 60-170 °C. Pt surfaces deactivate much faster than Pt-Re alloy surfaces under identical conditions due to buildup of atomic carbon on the Pt surface. Pt-Re alloy surfaces show a delay in their activation due to the diffusion of Re to the surface of the alloy in the presence of O_2. The diffusion of Re to the surface of the alloy leads to a buildup of oxygen species on the alloy surface due to the oxophilicity of Re and its ability to dissociate O_2 more readily than Pt, which in turn allows for the oxidation of surface carbon species, thus increasing the overall activity and catalyst lifetime compared to the pure Pt surface. Pt-Re alloy surfaces suffer a loss of Re over time on stream due to the formation of volatile Re(+7) species, which sublime under steady flows of oxygen-rich gas and more quickly at temperatures above 150 °C.

5.6 REFERENCES

(1) Sinfelt, J. H., Bimetallic Catalysts. Discoveries, Concepts, and Applications. John Wiley and Sons: New York, 1983.

(2) Campbell, C. Bimetallic Surface-Chemistry. *Annu. Rev. Phys. Chem.*, **1990**, *41*, 775-837.

(3) Rodriguez, J. A. Physical and Chemical Properties of Bimetallic Surfaces. *Surf. Sci. Rep.*, **1996**, *24*, 223-287.

(4) Liu, P.; Norskov, J. K. Ligand and Ensemble Effects in Adsorption on Alloy Surfaces. *Phys. Chem. Chem. Phys.*, **2001**, *3*, 3814-3818.

(5) Chen, J. G.; Menning, C. A.; Zellner, M. B. Monolayer Bimetallic Surfaces: Experimental and Theoretical Studies of Trends in Electronic and Chemical Properties. *Surf. Sci. Rep.*, **2008**, *63*, 201-254.

(6) Kluksdahl, H. E. (Chevron). Reforming a Sulfur-Free Naphtha with a Platinum-Rhenium Catalyst. US Patent 3,415,737, 1968.

(7) Carter, J. L.; McVicker, G. B.; Weissman, W.; Kmak, W. S.; Sinfelt, J. H. Bimetallic Catalysts - Application in Catalytic Reforming. *Appl. Catal.*, **1982**, *3*, 327-346.

(8) Somorjai, G. A. Introduction to Surface Chemistry and Catalysis; John Wiley and Sons, Inc.: New York, 1994.

(9) Barbier, J. Deactivation of Reforming Catalysts by Coking - a Review. *Appl. Cat.*, **1986**, *23*, 225-243.

(10) Parera, J. M.; Beltramini, J. N. Stability of Bimetallic Reforming Catalysts. *J. Catal.*, **1988**, *112*, 357-365.

(11) Godbey, D. J.; Garin, F.; Somorjai, G. A. The Hydrogenolysis of Ethane over Re-Pt(111) and Pt-Re(0001) Bimetallic Crystal-Surfaces. *J. Catal.*, **1989**, *117*, 144-154.

(12) Godbey, D. J.; Somorjai, G. A. The Adsorption and Desorption of Hydrogen and Carbon-Monoxide on Bimetallic Re-Pt(111) Surfaces. *Surf. Sci.*, **1988**, *204*, 301-318.

(13) Binary Alloy Phase Diagrams; 2nd ed.; Massalski, T. B.; International, A.; Okamoto, H., Eds.; ASM International: Materials Park, OH, 1990.

(14) Ramstad, A.; Strisland, F.; Raaen, S.; Worren, T.; Borg, A.; Berg, C. Growth and Alloy Formation Studied by Photoelectron Spectroscopy and STM. *Surf. Sci.*, **1999**, *425*, 57-67.

(15) Mun, B. S.; Rossi, M.; Ross, P. N. The Study of Surface Segregation of Re_3Pt Polycrystalline Alloy with Photoelectron Spectroscopy. *J. Chem. Phys.*, **2008**, *129*, 174707.

(16) Kunkes, E. L.; Simonetti, D. A.; Dumesic, J. A.; Pyrz, W. D.; Murillo, L. E.; Chen, J. G. G.; Buttrey, D. J. The Role of Rhenium in the Conversion of Glycerol to Synthesis Gas over Carbon Supported Platinum-Rhenium Catalysts. *J. Catal.*, **2008**, *260*, 164-177.

(17) Simonetti, D. A.; Kunkes, E. L.; Dumesic, J. A. Gas-Phase Conversion of Glycerol to Synthesis Gas over Carbon-Supported Platinum and Platinum-Rhenium Catalysts. *J. Catal.*, **2007**, *247*, 298-306.

(18) Ciftci, A.; Ligthart, D.; Hensen, E. J. M. Aqueous Phase Reforming of Glycerol over Re-Promoted Pt and Rh Catalysts. *Green Chem.*, **2014**, *16*, 853-863.

(19) Ciftci, A.; Ligthart, D.; Hensen, E. J. M. Influence of Pt Particle Size and Re Addition by Catalytic Reduction on Aqueous Phase Reforming of Glycerol for Carbon-Supported Pt(Re) Catalysts. *Appl. Catal. B*, **2015**, *174*, 126-135.

(20) Zhang, L.; Karim, A. M.; Engelhard, M. H.; Wei, Z. H.; King, D. L.; Wang, Y. Correlation of Pt-Re Surface Properties with Reaction Pathways for the Aqueous-Phase Reforming of Glycerol. *J. Catal.*, **2012**, *287*, 37-43.

(21) King, D. L.; Zhang, L. A.; Xia, G.; Karim, A. M.; Heldebrant, D. J.; Wang, X. Q.; Peterson, T.; Wang, Y. Aqueous Phase Reforming of Glycerol for Hydrogen Production over Pt-Re Supported on Carbon. *Appl. Catal. B-Environ.*, **2010**, *99*, 206-213.

(22) Soares, R. R.; Simonetti, D. A.; Dumesic, J. A. Glycerol as a Source for Fuels and Chemicals by Low-Temperature Catalytic Processing. *Angew. Chem. Int. Edit.*, **2006**, *45*, 3982-3985.

(23) Daniel, O. M.; DeLaRiva, A.; Kunkes, E. L.; Datye, A. K.; Dumesic, J. A.; Davis, R. J. X-Ray Absorption Spectroscopy of Bimetallic Pt-Re Catalysts for Hydrogenolysis of Glycerol to Propanediols. *ChemCatChem*, **2010**, *2*, 1107-1114.

(24) Ciftci, A.; Eren, S.; Ligthart, D.; Hensen, E. J. M. Platinum-Rhenium Synergy on Reducible Oxide Supports in Aqueous-Phase Glycerol Reforming. *ChemCatChem*, **2014**, *6*, 1260-1269.

(25) Kirilin, A. V.; Tokarev, A. V.; Manyar, H.; Hardacre, C.; Salmi, T.; Mikkola, J. P.; Murzin, D. Y. Aqueous Phase Reforming of Xylitol over Pt-Re Bimetallic Catalyst: Effect of the Re Addition. *Catal. Today*, **2014**, *223*, 97-107.

(26) Azzam, K. G.; Babich, I. V.; Seshan, K.; Lefferts, L. A Bifunctional Catalyst for the Single-Stage Water-Gas Shift Reaction in Fuel Cell Applications. Part 2. Roles of the Support and Promoter on Catalyst Activity and Stability. *J. Catal.*, **2007**, *251*, 163-171.

(27) Azzam, K. G.; Babich, I. V.; Seshan, K.; Lefferts, L. Role of Re in Pt-Re/TiO_2 Catalyst for Water Gas Shift Reaction: A Mechanistic and Kinetic Study. *Appl. Catal. B Environ.*, **2008**, *80*, 129-140.

(28) Azzam, K. G.; Babich, I. V.; Seshan, K.; Mojet, B. L.; Lefferts, L. Stable and Efficient Pt-Re/TiO_2 Catalysts for Water-Gas-Shift: On the Effect of Rhenium. *ChemCatChem*, **2013**, *5*, 557-564.

(29) Iida, H.; Igarashi, A. Difference in the Reaction Behavior between Pt-Re/TiO_2 (Rutile) and Pt-Re/ZrO_2 Catalysts for Low-Temperature Water Gas Shift Reactions. *Appl. Catal. A*, **2006**, *303*, 48-55.

(30) Iida, H.; Yonezawa, K.; Kosaka, M.; Igarashi, A. Low-Temperature Water Gas Shift Reaction over Pt-Re/TiO_2 Catalysts Prepared by a Sub-Critical Drying Method. *Catal. Commun.*, **2009**, *10*, 627-630.

(31) Sato, Y.; Terada, K.; Hasegawa, S.; Miyao, T.; Naito, S. Mechanistic Study of Water-Gas-Shift Reaction over TiO_2 Supported Pt-Re and Pd-Re Catalysts. *Appl. Catal. A*, **2005**, *296*, 80-89.

(32) Wei, Z. H.; Karim, A. M.; Li, Y.; King, D. L.; Wang, Y. Elucidation of the Roles of Re in Steam Reforming of Glycerol over Pt-Re/C Catalysts. *J. Catal.*, **2015**, *322*, 49-59.

(33) Ramstad, A.; Strisland, F.; Raaen, S.; Borg, A.; Berg, C. CO and O_2 Adsorption on the Re/Pt(111) Surface Studied by Photoemission and Thermal Desorption. *Surf. Sci.*, **1999**, *440*, 290-300.

(34) Ishikawa, Y.; Liao, M. S.; Cabrera, C. R. Energetics of H_2O Dissociation and CO_{ads}+OH_{ads} Reaction on a Series of Pt-M Mixed Metal Clusters: A Relativistic Density-Functional Study. *Surf. Sci.*, **2002**, *513*, 98-110.

(35) Greeley, J.; Mavrikakis, M. Near-Surface Alloys for Hydrogen Fuel Cell Applications. *Catal. Today*, **2006**, *111*, 52-58.

(36) Miller, A. V.; Kaichev, V. V.; Prosvirin, I. P.; Bukhtiyarov, V. I. Mechanistic Study of Methanol Decomposition and Oxidation on Pt(111). *J. Phys. Chem. C*, **2013**, *117*, 8189-8197.

(37) Spendelow, J. S.; Wieckowski, A. Electrocatalysis of Oxygen Reduction and Small Alcohol Oxidation in Alkaline Media. *Phys. Chem. Chem. Phys.*, **2007**, *9*, 2654-75.

(38) Shabaker, J. W.; Davda, R. R.; Huber, G. W.; Cortright, R. D.; Dumesic, J. A., Aqueous-phase reforming of methanol and ethylene glycol over alumina-supported platinum catalysts. *J. Catal.* **2003,** *215* (2), 344-352.

(39) Tenney, S. A.; Cagg, B. A.; Levine, M. S.; He, W.; Manandhar, K.; Chen, D. A. Enhanced Activity For Supported Au Clusters: Methanol Oxidation on Au/TiO_2(110). *Surf. Sci.*, **2012**, *606*, 1233-1243.

(40) Chen, S.; Wang, S.; Ma, X.; Gong, J. Selective Oxidation of Methanol to Dimethoxymethane Over Bifunctional VO(x)/TS-1 Catalysts. *Chem Commun.*, **2011**, *47*, 9345-9347.

(41) Sexton, B. A. Methanol Decomposition on Pt(111). *Surf. Sci.*, **1981**, *102*, 271−281.

(42) Endo, M.; Matsumoto, T.; Kubota, J.; Domen, K.; Hirose, C. Oxidation of Methanol by Molecularly Adsorbed Oxygen on Pt(111) under Vacuum and Ambient Pressure Conditions Studied by Infrared Reflection Absorption Spectroscopy: Identification of Formate Intermediate. *Surf. Sci.*, **1999**, *441*, L931−L937.

(43) Wang, J. H.; Masel, R. I. C-O Bond Scission During Methanol Decomposition on (1 × 1)Pt(110). *J. Am. Chem. Soc.*, **1991**, *113*, 5850−5856.

(44) McCabe, R. W.; McCready, D. F. Kinetics and Reaction Pathways of Methanol Oxidation on Platinum. *J. Phys. Chem.*, **1986**, *90*, 1428−1435.

(45) Yuan, Y. Z.; Shido, T.; Iwasawa, Y. The New Catalytic Property of Supported Rhenium Oxides for Selective Oxidation of Methanol to Methylal. *Chem. Commun.*, **2000**, 1421-1422.

(46) Yuan, Y. Z.; Iwasawa, Y. Performance and Characterization of Supported Rhenium Oxide Catalysts for Selective Oxidation of Methanol to Methylal. *J. Phys. Chem. B*, **2002**, *106*, 4441-4449.

(47) Yoboue, A.; Susset, A.; Tougerti, A.; Gallego, D.; Ramani, S. V.; Kalyanikar, M.; Dolzhnikov, D. S.; Wubshet, S. G.; Wang, Y. L.; Cristol, S.; et al. An Easily Accessible Re-Based Catalyst for the Selective Conversion of Methanol: Evidence for an Unprecedented Active Site Structure through Combined Operando Techniques. *Chem. Commun.*, **2011**, *47*, 4285-4287.

(48) Secordel, X.; Berrier, E.; Capron, M.; Cristol, S.; Paul, J. F.; Fournier, M.; Payen, E. TiO_2-Supported Rhenium Oxide Catalysts for Methanol Oxidation: Effect of Support Texture on the Structure and Reactivity Evidenced by an Operando Raman Study. *Catal. Today*, **2010**, *155*, 177-183.

(49) Duke, A. S.; Galhenage, R. P.; Tenney, S. A.; Ammal, S. C.; Heyden, A.; Sutter, P.; Chen, D. A. *In Situ* Ambient Pressure X-ray Photoelectron Spectroscopy Studies of Methanol Oxidation on Pt(111) and Pt-Re Alloys. *J. Phys. Chem. C*, **2015**, *119*, 23082-23093.

(50) Tenney, S. A.; Xie, K.; Monnier, J. R.; Rodriguez, A.; Galhenage, R. P.; Duke, A. S.; Chen, D. A. Novel Recirculating Loop Reactor For Studies on Model Catalysts: CO Oxidation on $Pt/TiO_2(110)$. *Rev. Sci. Instrum.*, **2013**, *84*, 104101.

(51) Duke, A. S.; Galhenage, R. P.; Tenney, S. A.; Sutter, P.; Chen, D. A. *In Situ* Studies of Carbon Monoxide Oxidation on Platinum and Platinum–Rhenium Alloy Surfaces. *J. Phys. Chem. C*, **2015**, *119*, 381-391.

(52) Alnot, M.; Cassuto, A.; Ehrhardt, J. J.; Slavin, A.; Weber, B. Growth of Platinum on Rhenium and Evolution of the Interface under Thermal-Treatment. *Appl. Surf. Sci.*, **1982**, *10*, 85-99.

(53) Björneholm, O.; Nilsson, A.; Tillborg, H.; Bennich, P.; Sandell, A.; Hernnäs, B.; Puglia, C.; Martensson, N. Overlayer Structure from Adsorbate and Substrate Core Level Binding Energy Shifts: CO, CCH_3, and O on Pt(111). *Surf. Sci.*, **1994**, *315*, L983-L989.

(54) Martensson, N.; Saalfeld, H. B.; Kuhlenbeck, H.; Neumann, M. Structural Dependence of the 5d-Metal Surface Energies as Deduced from Surface Core-Level Shift Measurements. *Phys. Rev. B*, **1989**, *39*, 8181-8186.

(55) Chan, A. S. Y.; Wertheim, G. K.; Wang, H.; Ulrich, M. D.; Rowe, J. E.; Madey, T. E. Surface Atom Core-Level Shifts of Clean and Oxygen-Covered Re(1231). *Phys. Rev. B*, **2005**, *72*, 14643-14651.

(56) Surface Analysis: The Principal Techniques. 2nd ed.; John Wiley & Sons: Chichester, UK, 2009.

(57) Okal, J.; Tylus, W.; Kepinski, L. XPS Study of Oxidation of Rhenium Metal on Gamma-Al_2O_3 Support. *J. Catal.*, **2004**, *225*, 498-509.

(58) Tysoe, W. T.; Zaera, F.; Somorjai, G. A. An XPS Study of the Oxidation and Reduction of the Rhenium Platinum System under Atmospheric Conditions. *Surf. Sci.*, **1988**, *200*, 1-14.

(59) Shcheglov, P. A.; Drobot, D. V. Heterogeneous Equilibria in the Rhenium-Oxygen System. *Russ. J. Phys. Chem.*, **2006**, *80*, 1819-1825.

(60) Chen, J. J.; Jiang, Z. C.; Zhou, Y.; Chakraborty, B. R.; Winograd, N. Spectroscopic Studies of Methanol Decomposition on Pd(111). *Surf. Sci.*, **1995**, *328*, 248-262.

(61) Wang, J. H.; Masel, R. I. Methanol Adsorption and Decomposition on (2x1) Pt(110)- Enhanced Stability of the Methoxy Intermediate on a Stepped Surface. *Surf. Sci.*, **1991**, *243*, 199-209.

(62) Akhter, S.; White, J. M. A Static Sims TPD Study of the Kinetics of Methoxy Formation and Decomposition on O/Pt(111). *Surf. Sci.*, **1986**, *167*, 101-126.

(63) Liu, Z. X.; Sawada, T.; Takagi, N.; Watanabe, K.; Matsumoto, Y. Reaction Intermediates in the Oxidation of Methanol on a Pt(111)-(2x2)O Surface. *J. Chem. Phys.*, **2003**, *119*, 4879-4886.

(64) Wang, J.; Deangelis, M. A.; Zaikos, D.; Setiadi, M.; Masel, R. I. Methanol Oxidation on (2x1)Pt(110) - Formaldehyde on A Stepped Surface. *Surf. Sci.*, **1994**, *318*, 307-320.

(65) Puglia, C.; Nilsson, A.; Hernnas, B.; Karis, O.; Bennich, P.; Martensson, N. Physisorbed, Chemisorbed and Dissociated O_2 on Pt(111) Studied by Different Core-Level Spectroscopy Methods. *Surf. Sci.*, **1995**, *342*, 119-133.

(66) Gentry, S. J.; Jones, A.; Walsh, P. T. Kinetics of Methanol Oxidation Over Platinum Wire Catalysts. *J. C. S. Faraday I*, **1980**, *76*, 2084-2095.

(67) Sexton, B. A.; Rendulic, K. D.; Hughes, A. E. Decomposition Pathways of C1-C4 Alcohols Adsorbed on Platinum (111). *Surf. Sci.*, **1982**, *121*, 181-198.

(68) Endo, M.; Matsumoto, T.; Kubota, J.; Domen, K.; Hirose, C. In Situ IRAS Observation of Catalytic Deep Oxidation of Methanol on Pt(111) under Ambient Pressure Conditions. *J. Phys. Chem. B*, **2001**, *105*, 1573-1577.

CHAPTER 6

X-RAY PHOTOELECTRON SPECTROSCOPY AND REACTOR STUDIES FOR WATER-GAS SHIFT ON PT-RE BIMETALLIC CLUSTERS ON $TiO_2(110)$[4]

[4] Duke, A. S.; Xie, K.; Brandt, A. J.; Monnier, J. R.; Chen, D. A. " X-ray Photoelectron Spectroscopy and Reactor Studies for Water-Gas Shift on Pt-Re Bimetallic Clusters on $TiO_2(110)$," in preparation.

6.1 INTRODUCTION

Supported bimetallic catalysts play an instrumental role in the generation of energy, fuels, and commodity chemicals because they exhibit enhanced activity, stability, and selectivity compared to bulk and supported pure metals due to metal-metal and metal-support interactions.[1-6] In particular, the positive effects generated by addition of Re to Pt have been known for half a century, having been seen on single crystal surfaces as well as on Pt-Re clusters distributed on a variety of supports like alumina, silica, ceria, zirconia, titania, and carbon. Pt-Re catalysts have shown enhanced activity, selectivity, and stability compared to either Pt or Re for various types of hydrocarbon and biomass reforming in the production of clean H_2.[7-24] A variety of explanations have been proposed for the role of Re in improving Pt catalysts including electronic modification,[25-27] decreased deactivation by coking and/or CO-poisoning of Pt active sites,[8-14, 16-20, 28] increased Pt dispersion and reduced sintering, especially on oxide supports,[18, 24, 29-31] and improved dissociation of O_2 on the surface with improved selectivity for the water-gas shift (WGS) reaction by ReO_x.[29, 32-39]

Currently, the main process for generating H_2 is the steam reforming of hydrocarbons; however, this process also generates CO.[40-44] This is problematic since CO is a well-known poison for Pt catalysts, and its formation alongside hydrogen also creates a pathway for the methanation reaction, which therefore decreases hydrogen production. Removal of CO via the WGS reaction is a critical step. Current industrial processes require the use of two catalysts in a two-stage process at low and high temperatures, but a single catalyst capable of facilitating the WGS reaction at lower temperatures during reforming would be ideal. In the aqueous phase reforming of

glycerol, the addition of Re to Pt/C was found to increase the total formation of H_2 and CO_2 by weakening the binding of CO to Re-modified Pt active sites, indicating that the presence of Re facilitates the WGS reaction.[22,38, 45-53] Additionally, Re has been shown to improve the WGS reaction in Pt-Re/TiO_2 catalysts for potentially one or more reasons: Re oxidizes to form ReO_x, which facilitates the activation of water for efficient CO removal, and/or Re interacts strongly with the oxide support, which increases the initial dispersion of Pt on the surface and inhibits sintering under reaction conditions.[29, 32-36, 46, 49, 54-58] Furthermore, it is known that reducible oxide supports like TiO_2 definitely play a role in the water-gas shift activity of the supported Pt catalyst, especially since the active sites are believed to be at a three-phase boundary of the reducible oxide support, the metal cluster, and the gas phase.[33, 50, 59-60] TiO_2 has also proved to be a better support for the Pt-Re clusters compared to others such as CeO_2 and Al_2O_3 in the aqueous phase reforming of polyols.[46, 50-51, 61]

Though there have been numerous studies of Pt-Re catalysts, the exact role of Re in enhancing the WGS on Pt/TiO_2 catalysts is still somewhat unclear. Part of the confusion stems from the fact that current knowledge of these systems is based on materials which are prepared and handled in air and subjected to a variety of pretreatments, such as reduction in H_2.[17, 22, 24, 29, 34, 62-69] For materials containing Re, this poses a problem since Re readily oxidizes in air, and once oxidized, it is very difficult to re-reduce it. A detailed study of these systems under a controlled environment where the surfaces can be well-characterized before and after reaction without exposure to air has thus far been lacking, hence the motivation for this work.

Here, TiO_2(110)-supported Pt, Re, and Pt-Re bimetallic clusters have been studied using X-ray photoelectron spectroscopy (XPS) and an ambient pressure reactor to determine the role of Re in improving Pt/TiO_2 catalysts for the water-gas shift. In this work, model catalysts were prepared under ultrahigh vacuum using rutile TiO_2(110) single crystals and physical vapor deposition to create Pt, Re, and Pt-Re bimetallic clusters with a wide spectrum of metal ratios. The water-gas shift reaction was conducted from 130 to 190 °C under 3% CO/7% H_2O/balance He in a recirculating reactor coupled to an ultra-high vacuum chamber for sample preparation and XPS analysis.

6.2 EXPERIMENTAL

Experiments were conducted in an ultrahigh vacuum chamber ($P < 3x10^{-10}$ Torr) which is coupled to homemade microreactor, both of which have been described in detail elsewhere.[70,71] The chamber is equipped with a residual gas analyzer (Stanford Research Systems, RGA 300), a hemispherical analyzer for XPS (SPECS, EA10), optics for performing LEED and AES (SPECS, ErLEED-4), and a high-pressure cell coupled to an external FTIR spectrometer for infrared reflection absorption spectroscopy (IRAS) (Bruker, Tensor 27).[71]

Platinum and rhenium clusters were deposited onto a rutile TiO_2(110) crystal (Princeton Scientific Corporation, 10 mm x 10 mm x 1 mm) which was mounted on a thick Ta foil plate using thin Ta foil straps. The sample was heated radiatively by a tungsten filament from behind and by electron bombardment from the filament with a positive bias applied to the sample. The sample temperature was monitored via an infrared pyrometer (Heitronics). The crystal was cleaned by cycles of Ar^+ sputtering (20

minutes, 1 kV, 10 mA, 3.0-3.2 μA) and annealing (3 minutes, 950-1000 K) in vacuum. In this way, the titania support is made into an n-type semiconductor by the removal of lattice oxygen, which makes it sufficiently conductive for electron based characterization techniques. A combination of XPS, LEED, and AES were used to confirm the cleanliness and crystallinity of the TiO_2(110)-(1x1) surface.

Pt and Re were deposited sequentially onto the titania surface from a Pt rod (ESPI, 2 mm diameter, 99.95%) and a Re rod (ESPI, 2 mm diameter, 99.99%), respectively, using a four-pocket electron-beam evaporator (Oxford Applied Research, EGC04). The metal flux was calibrated with a UHV bakeable quartz crystal microbalance (QCM, Inficon, XTM-2) before each deposition. Metal deposition rates were approximately 0.05-0.1 ML/min. One monolayer of Pt is defined according to the packing density of Pt(111) (1.50×10^{15} atoms/cm^2), and one monolayer of Re is defined according to the packing density of Re(0001) (1.52×10^{15} atoms/cm^2).

XPS data were collected before and after reactor experiments using Al-Kα X-rays (10 kV/30 mA), a 0.2 s dwell time, and a 0.025 eV step size. The surface was positioned normal to the analyzer. Samples were prepared in the chamber and then transferred in and out of the microreactor without exposing the sample to air. In the reactor, the sample was heated and cooled in a continuous flow of fresh feed gas, which was a mixture of 3% CO (Praxair)/ 7% H_2O/ 90% He (Airgas, 99.999%) with a flow rate of 60 sccm as determined by a digital flow meter (Agilent Technologies, ADM2000). The CO was passed through an alumina trap heated to 150 °C for removing metal carbonyl contaminants from the gas before it entered the feed gas manifold. Water vapor was induced into the feed gas line by a homemade vapor-liquid equilibrator (VLE) filled with

ultrapure liquid water (18.2 MΩ resistivity, Barnstead EasyPure II 7138), where helium served as the sweep gas. The temperature of the VLE was controlled by a refrigerating/ heating circulating bath (VWR), and the concentration of water in the vapor outlet was calculated using the Antoine equation for pure water. Both CO and He were introduced via independently calibrated mass flow controllers (Brooks, 5850e and 5850i). The sample was heated to temperatures between 130 °C and 190 °C at a rate of ~1.5-2 °C /min by heating tapes (Briskheat, BWHD) wrapped around the exterior of the reactor housing which were regulated by a feedback loop on a temperature controller (Auber, SYL-4342P) to ensure uniform heating and cooling. The temperature of the sample was estimated by a type K thermocouple (Omega, KMQSS-040G-6) welded into the feed gas inlet, close to the surface of the sample. The gas lines were maintained at ~65 °C using two Valco Instruments temperature controllers. Pressure was monitored by two capacitance manometers (MKS Instruments, Baratron 722A) located upstream of the reactor in the feed gas line (790 Torr ~ 800 Torr) and downstream of the reactor (770 Torr ~ 780 Torr).

All activity tests were performed under recirculation mode where the reactant gases are forced to recirculate over the catalyst surface once every 2 min.[70] The automated system was switched to sampling mode every 20 min, and a sample of the gas (~1.096 cm^3) was injected on a gas chromatograph (HP 5890A) which is equipped with a PoraPLOT Q capillary GC column leading to a thermal conductivity detector (TCD). The total number of moles of CO_2 produced was determined to be the sum of the number of moles of CO_2 detected by the GC-TCD plus the number of moles present in the recirculation loop, which was calculated using the ratio of the volume of the sampling

loop to the recirculation loop and the ideal gas law. Water-gas shift was observed for 2h periods at 130 °C, 145 °C, 160 °C, 175 °C, and 190 °C so that the activation energy of the reaction could be determined. The background activity of the empty reactor and sample support were evaluated and found to contribute minor amounts of CO_2 to the overall activity. For some experiments, the surface was pre-oxidized in a 4% O_2/ 96% He flow for 1 h at 25 °C.

6.3 RESULTS AND DISCUSSION

In this study, surfaces consisting of 2 ML Pt + *x* ML Re (*x* = 0, 0.125, 0.25, 0.5, 1, and 2) and 2 ML Re + *y* ML Pt (*y* = 0, 1, 2, 3) clusters supported on TiO_2(110) were studied for the water-gas shift reaction. Surfaces consisting of 2 ML Pt, 1.7 ML Re, 2 ML Pt + 1.7 ML Re, and 1.7 ML Re + 2 ML Pt each supported on TiO_2(110) single crystals have already been characterized by scanning tunneling microscopy (STM), low-energy ion scattering (LEIS), X-ray photoelectron spectroscopy (XPS), and temperature programmed desorption (TPD) in a previous work by Galhenage et al.[72] STM studies from that work show that bimetallic clusters are formed in either order of deposition for 1.7 ML Re deposited on 2 ML Pt (Pt + Re) or 2 ML Pt deposited on 1.7 ML Re (Re + Pt). Though the previous studies indicate that bimetallic clusters are formed from an initial coverage of 1.7-2.0 ML of metal seed clusters for both orders of metal deposition, the morphology of each surface was shown to be different with the Pt + Re surfaces having fewer clusters which were larger than clusters on the Re + Pt surfaces.

Figure 6.1 compares the average rate of CO_2 formation as a function of temperature for the pure 2 ML Pt and 2 ML Re surfaces with the bimetallic surfaces generated from depositing Pt first. Though there is some CO_2 formation from the empty

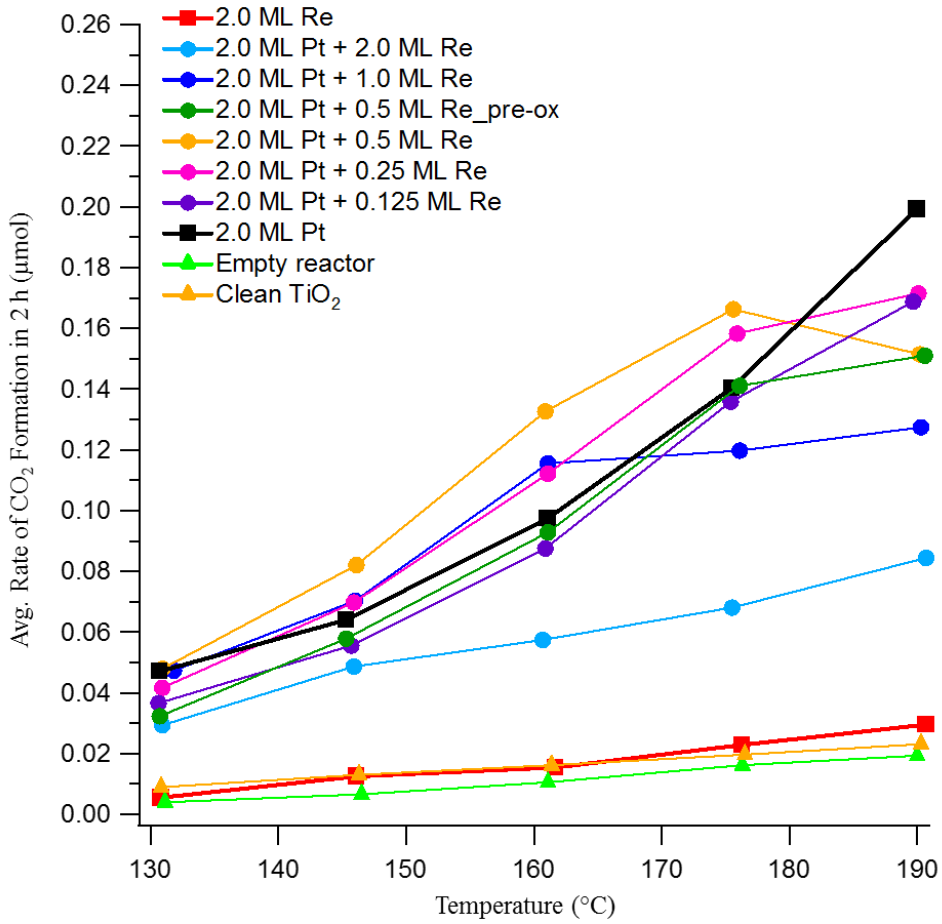

Figure 6.1: Average rate of CO_2 formation in 2 h at each temperature for: (▲) the empty reactor and clean TiO_2; (■) 2 ML Pt/TiO_2 and 2 ML Re/TiO_2; (●) bimetallic clusters on TiO_2 with 2 ML Pt deposited first.

reactor, no CO_2 formation above the background is detected on 2 ML Re or the clean TiO_2 support. The pure 2 ML Pt clusters show much higher activity than the 2 ML Re clusters at 130 °C and continue to increase in activity at every temperature as the sample is heated to 190 °C. This concurs with the studies performed by Azzam and coworkers who found that Re/TiO_2 showed no activity for the WGS reaction.[33] It is also consistent with CO TPD studies performed in previous work on these surfaces, which indicated that in spite of their greater dispersion on the surface, pure Re clusters have much lower

activity than pure Pt.[72] The addition of 0.125 ML Re to the 2 ML Pt surface does not significantly change the activity of the Pt, maintaining the same overall trend of increasing activity with increasing temperature. Similarly, the addition of 0.25 ML Re to the 2 ML Pt surface does not change the activity of the Pt at 130 °C or 145 °C, but at 160 °C and 175 °C, the 2 ML Pt + 0.25 ML Re surface exhibits higher activity than the pure Pt surface. The 2 ML Pt + 0.5 ML Re surface exhibits the same activity as the pure Pt surface at 130 °C, but at 145 °C, 160 °C, and 175 °C, its activity is higher than pure Pt or any of the other Pt + Re surfaces. This is consistent with previous CO TPD studies on these surfaces, which showed that depositing 0.43 ML Re on top of 2 ML Pt clusters adds just enough Re to diminish substantially the 500 K molecular CO desorption peak from Pt step sites as compared to pure Pt clusters, but not quite enough Re for CO dissociation to occur.[72] Galhenage et al. attributed this behavior to the diffusion of a great fraction of the Re into the Pt, which is due to the lower surface free energy of Pt as compared to Re (2.5 J/m^2 vs. 3.6 J/m^2). It could be that the diffusion of Re underneath the Pt modifies the clusters so that the number of Pt step sites are greatly reduced or the binding of CO to those sites is weakened, or else it could be that having a very small quantity of Re at the surface of the clusters beneficially blocks Pt step sites. Adding 1 ML Re to the 2 ML Pt surface results in less activity than the 2 ML Pt + 0.5 ML Re surface. In fact, the activity of the 2 ML Pt + 1 ML Re surface looks identical to that 2 ML Pt + 0.25 ML Re surface at 130 °C, 145 °C, and 160 °C, but then instead of continuing to increase, it plateaus. This drop in activity could be due to the larger coverage of Re at the surface. After reaction, the ratio of integrated Re(4f)/Pt(4f) areas for the 2 ML Pt + 1 ML Re surface is 98% of what it was before reaction. This is notably higher than the Re/Pt ratio for the 2

ML Pt + 0.5 ML Re surface after reaction, which is 82% of what it was before reaction. Based on the previous CO-TPD studies, it could be that a smaller fraction of the 1 ML Re coverage is able to diffuse into the Pt clusters as compared to the 2 ML Pt + 0.5 ML Re surface, and the greater amount of Re at the surface blocks Pt active sites.[72] Thus it appears that having only a small quantity of Re at the surface can be beneficial, but more than that lowers the overall activity of the surface. Indeed, the 2 ML Pt + 2 ML Re surface is completely different from the other bimetallic surfaces in that it follows the trend of the 2 ML Re surface instead of the 2 ML Pt, showing much lower activity at all temperatures than any of the other surfaces though still more activity than the pure Re. This seems to counter the results published by Azzam et al. who found that a nearly 50/50 composition of Pt-Re/TiO_2 showed better activity than Pt/TiO_2, which is not the case for this order of deposition.[33] However, the results shown here are consistent with the LEIS studies performed by Galhenage and coworkers, which showed that depositing 1.7 ML Re on top of 2 ML Pt attenuates the Pt signal as the Re covers some but not all of the Pt clusters due to the lower surface free energy of Pt and diffusion of some but not all Re into the Pt clusters. The previous CO TPD studies support this as well, suggesting that for 2 ML Pt + x ML Re coverages with x > 0.5 ML, a greater fraction of the Re remains at the surface, blocking active sites.[72]

At 190 °C the activities of all of the bimetallic 2 ML Pt + *x* ML Re surfaces are lower than that of the pure Pt clusters. Previous studies of Pt-Re surfaces have shown that in an oxidizing environment at temperatures of 175 °C and above, subsurface Re is induced to diffuse to Pt surfaces where it becomes oxidized.[39,71,73] Thus it is possible that the decrease in activity for bimetallic clusters above 175 °C is due to increased diffusion

of Re to the surface of the clusters which blocks Pt active sites. This is more pronounced for the higher Re coverage surfaces like the +1 ML Re and +2 ML Re surfaces, which show diminished activity at 175 °C because there is already a large fraction of Re at the surface of those clusters unlike the lower Re coverage surfaces in which a greater proportion of Re had first diffused underneath the Pt. To test this, a 2 ML Pt + 0.5 ML Re surface was pre-oxidized by exposing the cluster surface to 4% O_2 in He for 1 h at 25 °C so that the Re stayed at the surface of the clusters. The WGS reaction was then performed on the pre-oxidized surface in the same way as all of the other surfaces. The activity of the pre-oxidized surface is consistently lower than that of its freshly prepared counterpart up until 190 °C at which point the activities of the freshly prepared and pre-oxidized surfaces are identical. This indicates that ReO_x is not the active species in the WGS reaction, and in fact, it appears to diminish the activity of what should otherwise have been the most active surface.

Figure 6.2 shows a comparison of the average rate of CO_2 formation as a function of temperature for the pure 2 ML Pt and 2 ML Re surfaces with the bimetallic surfaces generated from depositing Re first. The activity of the 2 ML Re + 1 ML Pt is slightly lower than that of the pure Pt but still much higher than that of the pure Re, behaving very similarly to the 2 ML Pt + 0.125 ML Re surface. The 2 ML Re + 2 ML Pt shows the most activity out of any surface, regardless of the order of metal deposition. This 50/50 mixture of Pt-Re now supports the results published by Azzam et al, suggesting that their 50/50 catalysts must have consisted of Re covered by Pt at the surface, not the other way around.[33] Adding another monolayer of Pt to make a 2 ML Re + 3 ML Pt surface does not further increase the activity. It could be that the effects of Pt-Re

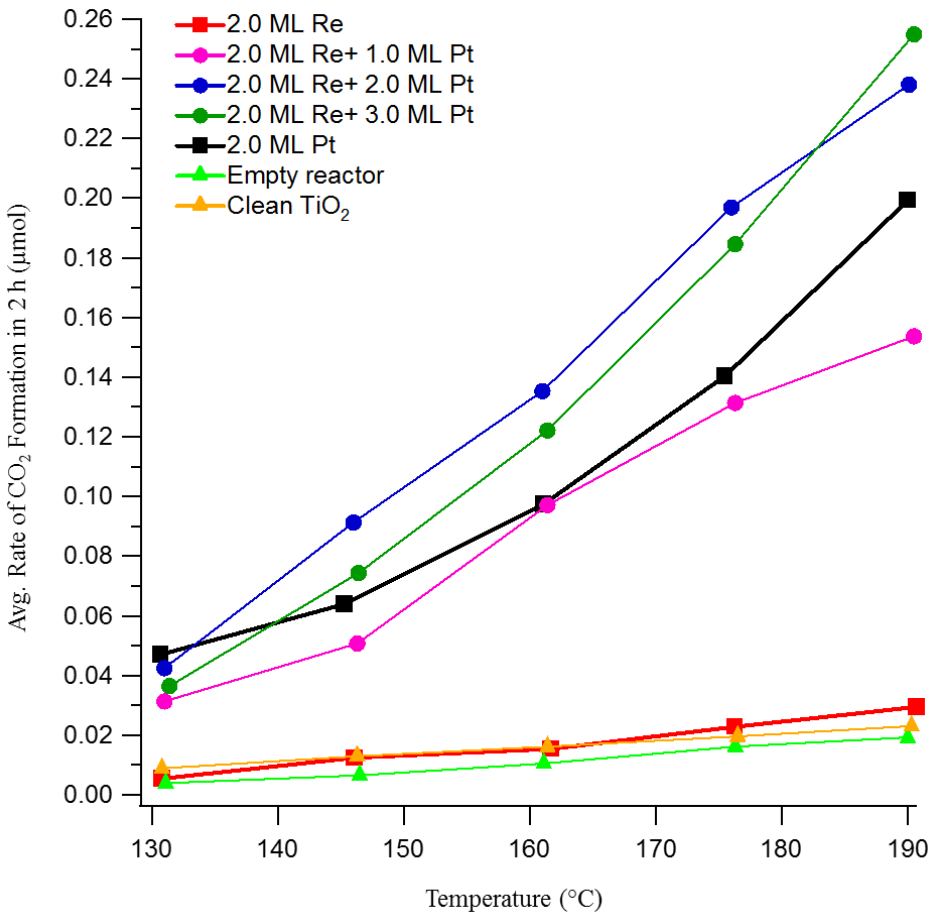

Figure 6.2: Average rate of CO_2 formation in 2 h at each temperature for: (▲) the empty reactor and clean TiO_2; (■) 2 ML Pt/TiO_2 and 2 ML Re/TiO_2; (●) bimetallic clusters on TiO_2 with 2 ML Re deposited first.

interactions are diminished at the higher coverage of Pt, or perhaps the surface is saturated at a coverage of 2 ML Re + 2 ML Pt such that the addition of still more Pt does not create new active surface Pt sites but only adds to the bulk of the clusters, so that the number of active Pt sites at the surface remains relatively unchanged. LEIS studies of Re + Pt surfaces performed by Galhenage et al. showed that the top monolayer of the surfaces is ~100% Pt, which is consistent with the fact that Pt is energetically favored to

remain at the surface. Thus these results indicate that the best activity for the WGS reaction on Pt-Re/TiO_2 comes from having Re clusters covered by Pt at the surface.

It has been proposed that the improved activity on Re + Pt surfaces is due to a decrease in sintering of Pt clusters due to the presence of Re underneath. Iida and Igrashi reported that one of the roles of Re in water-gas shift catalysts generated by impregnating Pt on top of Re on TiO_2 was to anchor the Pt due to strong interactions between Pt and Re and Re and TiO_2. Their claim was based on TEM results which showed the more active Pt-Re catalyst had 2.1 nm Pt particles after reaction while the less active pure Pt catalyst had 3.2 nm Pt particles after reaction.[29] However, this is unlikely to explain the improved activity of the Re + Pt surfaces here since the temperatures in these studies are far below those at which significant Pt sintering should occur.

Post-reaction XPS data confirm that the activity of the bimetallic catalyst is not enhanced by the presence of oxidized Re at the surface but rather by Re in its metallic form underneath the Pt. XPS of the Re(4f) region of the 2 ML Pt + 0.5 ML Re/TiO_2 surface before and after oxidation as well as after reaction are shown in Figure 6.3. The peak at 37 eV corresponds to the Ti(3p) signal from the titania substrate, and the feature above 50 eV is from the Pt(5p) region of the 2 ML Pt clusters deposited first. The Re($4f_{7/2}$) peak for the freshly deposited metallic Re on Pt clusters is located at 40.55 eV, compared to 40.3 eV established for Re(0001) single crystals.[73-75] After reaction, the Re($4f_{7/2}$) peak remains in the same position with no significant change to the shape of the spectrum to indicate oxidation of Re. In contrast, the Re($4f_{7/2}$) peak for pre-oxidized 2 ML Pt + 0.5 ML Re clusters shows the formation of several high oxidation states. With the Re($4f_{7/2}$) and Re($4f_{5/2}$) doublet peaks separated by 2.42 eV and a peak area ratio of

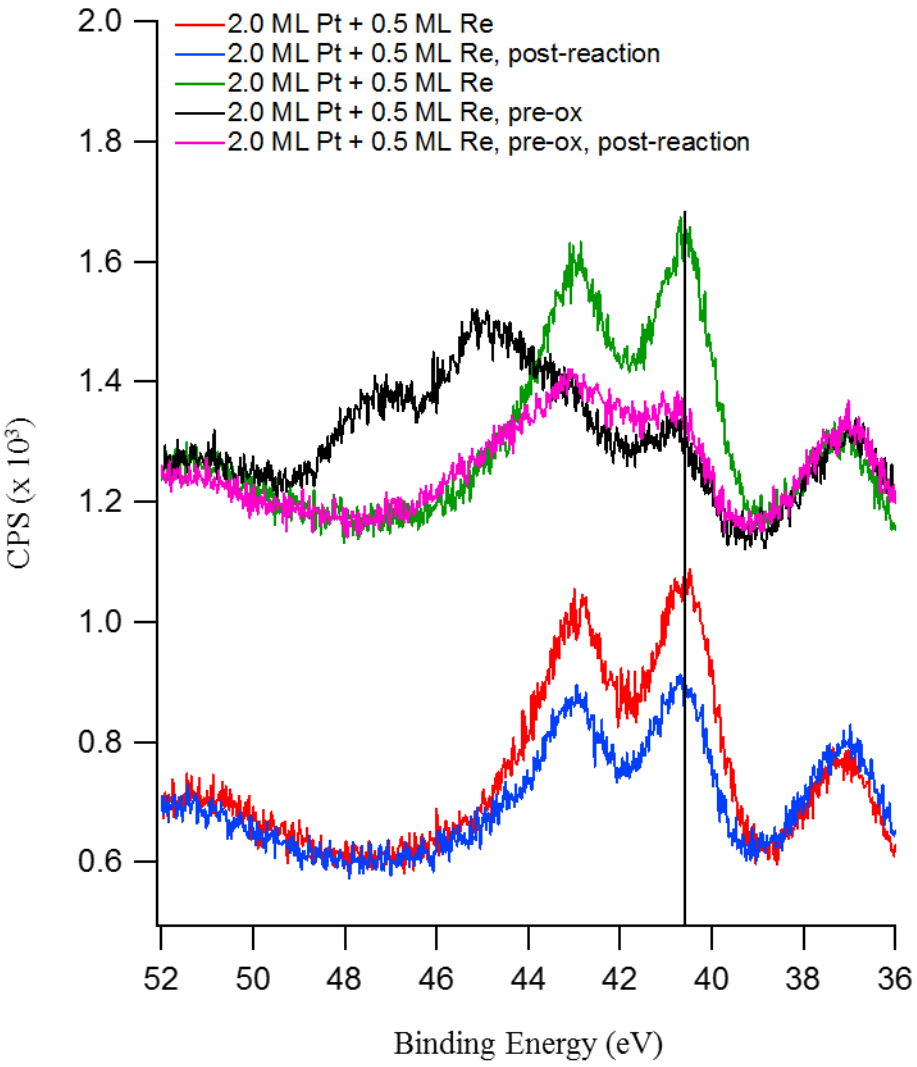

Figure 6.3: X-ray photoelectron spectroscopy data of the Re(4f) region for the freshly prepared and pre-oxidized 2 ML Pt + 0.5 ML Re/TiO_2 surfaces pre- and post-reaction.

4:3, the pre-oxidized Re spectrum can be fit with peaks at 40.9 eV, 42.5 eV, 44.1 eV, and 45.2 eV, corresponding to Re^0, Re^{+4}, Re^{+5}, and Re^{+6}, respectively. After the pre-oxidized surface is exposed to reaction conditions, the higher oxidation states of Re^{+5} and Re^{+6} disappear, leaving the post-reaction surface to look only slightly more oxidized than the post-reaction surface of the freshly prepared sample which showed identical activity at

the highest temperature before removal from the reactor for XPS. This indicates that the higher oxidation states on the pre-oxidized surface, which initially lowered the activity, might have sublimed from the surface as they became more heavily oxidized at and above 175 °C. The decreased amount of ReO_x on the pre-oxidized surface at 190 °C explains why the freshly prepared and pre-oxidized surfaces showed identical activity at the highest temperature.

Figure 6.4 shows the Re(4f) region for 2 ML of pure Re clusters and bimetallic surfaces containing 2 ML Re before and after reaction. In conjunction with the previous studies performed by Galhenage and coworkers, XPS indicates that the as-deposited clusters are metallic in the pure Pt and pure Re surfaces as well as the bimetallic surfaces. For all surfaces, the as-deposited 2 ML Re signals show a Re($4f_{7/2}$) binding energy of 40.3 eV, characteristic of Re metal. After undergoing the water-gas shift reaction, the 2 ML Re + 2 ML Pt surface (light blue), which showed the best activity of all the surfaces, shows no oxidation of Re due to the fact that the Pt completely covers the Re clusters underneath, so the exposure of the Re clusters to the reaction environment is minimized. For the post-reaction 2 ML Re + 1 ML Pt surface (light red), which showed comparable activity to the pure 2 ML Pt surface, the Re($4f_{7/2}$) binding energy appears at 40.4 eV, which is not significantly different than the 2 ML Re + 2 ML Pt surface, again indicating there is enough Pt to cover the metallic Re clusters underneath. However, the post-reaction 2 ML Pt + 2 ML Re surface (light green), which showed the lowest activity of all the bimetallic surfaces, shows some Re oxidation with the Re($4f_{7/2}$) binding energy shifting to 40.6 eV. This is due to the fact that not all of the 2 ML Re is able to diffuse into the Pt clusters, and so some Re remains behind at the surface and is therefore

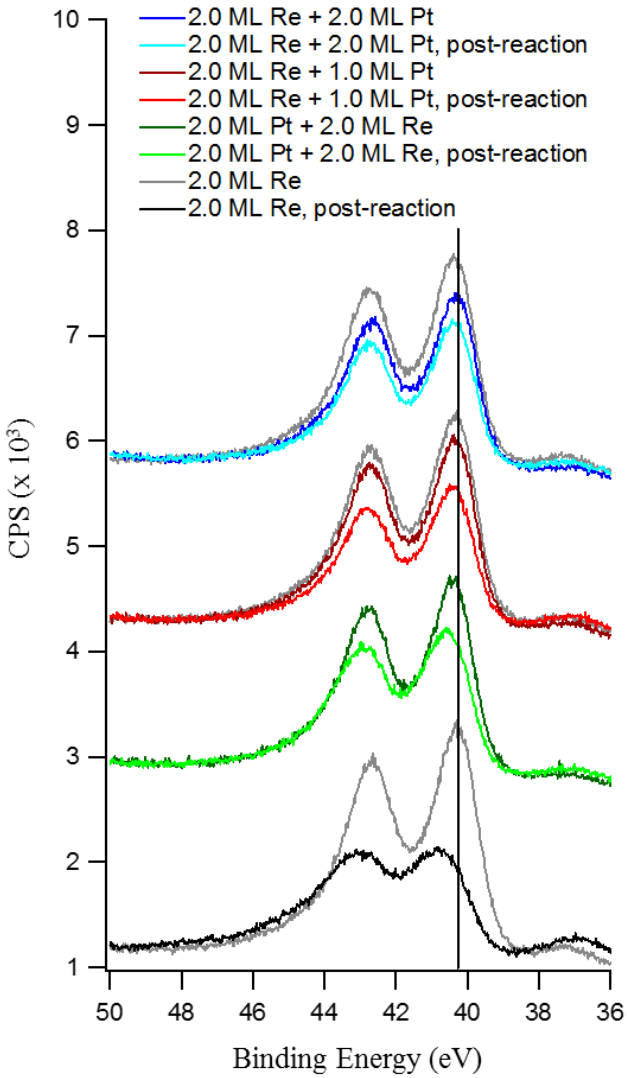

Figure 6.4: X-ray photoelectron spectroscopy data of the Re(4f) region for pre- and post-reaction surfaces containing 2 ML Re on TiO_2. Gray traces indicate only 2 ML Re deposited on the TiO_2 surface. The vertical black line drawn through all spectra indicates the binding energy of metallic Re at 40.3 eV.

exposed to the reaction mixture. This mixture of metallic and oxidized Re at the surface of the clusters is then responsible for blocking Pt active sites and causing diminished activity compared to all of the other bimetallic and pure Pt clusters. For the post-

reaction pure Re surface (black), which had no activity above the background, there is significant oxidation. The Re($4f_{7/2}$) binding energy shifts by 0.5 eV to 40.8 eV, which is consistent with a 0.4 eV shift to higher binding energy reported by Sato et al. for the oxidation of the Re surface by water.[37] Since the surfaces with the best activity do not show any oxidation of Re, it appears that ReO_x at the surface is not an active species in the water-gas shift reaction. This seems to refute the suggestions made by Azzam and Ciftci that the main influence of Re in the bimetallic catalyst was the fact that Re binds oxygen species very strongly, which facilitates the activation of water, thereby producing hydroxyl species which are involved in the water-gas shift reaction.[34, 48] In fact, it may be that the oxophilic nature of Re does play a role in that as-deposited Re is initially surrounded with oxygen from the support lattice before Pt deposition, but XPS indicates that the dominant Re oxidation state in the highly-active surfaces is Re^0.

From these data, the clearest result is that the WGS reaction is improved when Re resides beneath the Pt. This can be achieved in two ways: either a small amount of Re is deposited on top of the Pt and diffuses underneath, or else the Re is deposited first and remains below the Pt, both due to thermodynamics. In the first case, there is no evidence to suggest that the Re deposited on top of Pt interacts with the support at all, yet the activity can be improved. In the second case, the Re does interact with the support first, which may be a factor in explaining why the Re + Pt surfaces yield the best activity. The LEIS studies conducted by Galhenage and co-workers indicate that some amount of oxygen and Ti^{3+} from the reduced titania support diffuses onto the pure Re clusters at room temperature due to a strong metal-support interaction.[72] XPS from this work as well as from the previous work confirms that unlike the deposition of Pt, deposition of Re

reduces the titania support; though, the reducing effect on the support is somewhat minimized for bimetallic clusters. Thus they proposed that the partially encapsulated Re facilitates CO_2 production by funneling oxygen from the support to the CO that binds to Pt on top of Re. Additionally, as mentioned earlier, previous studies have shown that in an oxidizing environment it is energetically favorable for Re to diffuse to a Pt surface where it dissociates molecular O_2,[39,71,73] and so perhaps it is also possible that the presence of Re underneath the Pt could facilitate the dissociation of water on the surface. Thus the presence of Re and the increased amount of reduced TiO_x available at the cluster-support interface may both facilitate water dissociation and further increase CO_2 production in the water-gas shift. This could have a large effect on the activity of the catalyst since the reaction steps of oxygen vacancy formation and H_2O dissociation on the titania support are both believed to contribute the most to the overall rate of reaction; the reaction step of CO adsorption on the Pt is also believed to contribute significantly to the rate, though to a lesser extent than H_2O dissociation.[59]

6.4 CONCLUSIONS

In order to investigate the role of Re in improving Pt/TiO_2 catalysts, Pt, Re, and Pt-Re bimetallic clusters have been grown on $TiO_2(110)$ and studied for the water-gas shift reaction using an ambient pressure reactor and X-ray photoelectron spectroscopy (XPS). XPS analysis before reaction shows that the pure metal and bimetallic clusters are all initially metallic, but after reaction, the Re clusters at the surface become oxidized by the reaction mixture unless they are sufficiently covered with Pt. Reactor studies indicate that Re oxide formed at the surface of the bimetallic clusters does not improve the activity of the Pt/TiO_2 catalyst, and in fact, neither does metallic Re at the surface of

the bimetallic clusters. Rather, improved activity was seen only when a significant coverage of Re was present beneath the Pt surface, either by diffusion of Re into Pt seed clusters or else by depositing Re first, with the latter yielding the best results.

6.5 REFERENCES

(1) Sinfelt, J. H., *Bimetallic Catalysts. Discoveries, Concepts, and Applications*; John Wiley and Sons: New York, 1983.

(2) Campbell, C., Bimetallic Surface-Chemistry. *Annu. Rev. Phys. Chem.* **1990**, *41*, 775-837.

(3) Rodriguez, J. A., Physical and Chemical Properties of Bimetallic Surfaces. *Surf. Sci. Rep.* **1996**, *24*, 223.

(4) Liu, P.; Norskov, J. K., Ligand and Ensemble Effects in Adsorption on Alloy Surfaces. *Phys. Chem. Chem. Phys.* **2001**, *3*, 3814-3818.

(5) Chen, J. G.; Menning, C. A.; Zellner, M. B., Monolayer Bimetallic Surfaces: Experimental and Theoretical Studies of Trends in Electronic and Chemical Properties. *Surf. Sci. Rep.* **2008**, *63*, 201-254.

(6) Cheng, D.; Wang, W.; Huang, S., Core–Shell-Structured Bimetallic Clusters and Nanowires. *Journal of Physics: Condensed Matter* **2007**, *19*, 356217.

(7) Kluksdahl, H. E. Reforming a Sulfur-Free Naphtha with a Platinum-Rhenium Catalyst. 1968.

(8) Johnson, M. F. L.; Leroy, V. M., State of Rhenium in Pt-Re-Alumina Catalysts. *J. Catal.* **1974**, *35*, 434-440.

(9) Carter, J. L.; McVicker, G. B.; Weissman, W.; Kmak, W. S.; Sinfelt, J. H., Bimetallic Catalysts - Application in Catalytic Reforming. *Applied Catalysis* **1982**, *3*, 327-346.

(10) Barbier, J., Deactivation of Reforming Catalysts by Coking - a Review. *Appl. Cat.* **1986**, *23*, 225-243.

(11) Biswas, J.; Bickle, G. M.; Gray, P. G.; Do, D. D.; Barbier, J., The Role of Deposited Poisons and Crystallite Surface Structure in the Activity and Selectivity of Reforming Catalysts. *Catal.Rev.-Sci.Eng* **1988**, *30*, 161-247.

(12) Parera, J. M.; Beltramini, J. N., Stability of Bimetallic Reforming Catalysts. *J. Catal.* **1988**, *112*, 357-365.

(13) Godbey, D. J.; Garin, F.; Somorjai, G. A., The Hydrogenolysis of Ethane over Re-Pt(111) and Pt-Re(0001) Bimetallic Crystal-Surfaces. *J. Catal.* **1989**, *117*, 144-154.

(14) Ribeiro, F. H. B., A. L.; Kim, C.; Somorjai, G. A. , Transformation of Platinum into a Stable, High-Temperature, Dehydration-Hydrogenation Catalyst by Ensemble Size Reduction with Rhenium and Sulfur. *J. Catal.* **1994**, *150*, 186-198.

(15) Ribeiro, F. H.; Bonivardi, A. L.; Somorjai, G. A., Ensemble Size-Reduction by Rhenium Sulfur as a Method to Lower the Rate of Deactivation of Hydrocarbon Reactions over Pt Catalysts. *Catal. Lett.* **1994**, *27*, 1-10.

(16) Querini, C. A.; Fung, S. C., Coke and Product Profiles Formed Along the Catalyst Bed During N-Heptane Reforming .1. Nonsulfided Pt/Al_2O_3 and $Pt-Re/Al_2O_3$. *J. Catal.* **1993**, *141*, 389-406.

(17) Huang, Z.; Fryer, J. R.; Park, C.; Stirling, D.; Webb, G., Transmission Electron-Microscopy and Energy-Dispersive X-Ray Spectroscopy Studies of $Pt-Re/Alpha/Al_2O_3$ Catalysts. *J. Catal.* **1994**, *148*, 478-492.

(18) Fung, A. S.; Kelley, M. J.; Koningsberger, D. C.; Gates, B. C., $Gamma-Al_2O_3$-Supported Re-Pt Cluster Catalyst Prepared from $Re_2Pt(CO)_{12}$: Characterization by Extended X-Ray Absorption Fine Structure Spectroscopy and Catalysis of Methylcyclohexane Dehydrogenation. *J. Am. Chem. Soc.* **1997**, *119*, 5877-5887.

(19) Bliznyuk, V. N.; Rinderspacher, F.; Tsukruk, V. V., On the Structure of Polyamidoamine Dendrimer Monolayers. *Polymer* **1998**, *39*, 5249-5252.

(20) Macleod, N.; Fryer, J. R.; Stirling, D.; Webb, G., Deactivation of Bi- and Multimetallic Reforming Catalysts: Influence of Alloy Formation on Catalyst Activity. *Catal. Today* **1998**, *46*, 37-54.

(21) Manyar, H. G.; Paun, C.; Pilus, R.; Rooney, D. W.; Thompson, J. M.; Hardacre, C., Highly Selective and Efficient Hydrogenation of Carboxylic Acids to Alcohols Using Titania Supported Pt Catalysts. *Chem. Commun.* **2010**, *46*, 6281-6281.

(22) Daniel, O. M.; DeLaRiva, A.; Kunkes, E. L.; Datye, A. K.; Dumesic, J. A.; Davis, R. J., X-Ray Absorption Spectroscopy of Bimetallic Pt-Re Catalysts for Hydrogenolysis of Glycerol to Propanediols. *ChemCatChem* **2010**, *2*, 1107-1114.

(23) Chen, B.; Li, F.; Huang, Z.; Yuan, G., Tuning Catalytic Selectivity of Liquid-Phase Hydrogenation of Furfural Via Synergistic Effects of Supported Bimetallic Catalysts. *Appl. Catal. A-Gen.* **2015**, *500*, 23-29.

(24) Falcone, D. D.; Hack, J. H.; Klyushin, A. Y.; Knop-Gericke, A.; Schlögl, R.; Davis, R. J., Evidence for the Bifunctional Nature of Pt-Re Catalysts for Selective Glycerol Hydrogenolysis. *ACS Catal.* **2015**, *5*, 5679-5695.

(25) Ramstad, A.; Strisland, F.; Raaen, S.; Worren, T.; Borg, A.; Berg, C., Growth and Alloy Formation Studied by Photoelectron Spectroscopy and STM. *Surf. Sci.* **1999**, *425*, 57-67.

(26) Ramstad, A.; Strisland, F.; Raaen, S.; Borg, A.; Berg, C., CO and O_2 Adsorption on the Re/Pt(111) Surface Studied by Photoemission and Thermal Desorption. *Surf. Sci.* **1999**, *440*, 290-300.

(27) Godbey, D. J., Somorjai, G. A., The Adsorption and Desorption of Hydrogen and Carbon Monoxide on Bimetallic Re-Pt(111) Surfaces. *Surf. Sci.* **1988**, *204*, 301-318.

(28) Sanchez, S. I.; Moser, M. D.; Bradley, S. A., Mechanistic Study of Pt–Re/Γ-Al_2O_3 Catalyst Deactivation by Chemical Imaging of Carbonaceous Deposits Using Advanced X-Ray Detection in Scanning Transmission Electron Microscopy. *ACS Catal.* **2014**, *4*, 220-228.

(29) Iida, H.; Igarashi, A., Structure Characterization of Pt-Re/TiO_2 (Rutile) and Pt-Re/ZrO_2 Catalysts for Water Gas Shift Reaction at Low-Temperature. *Appl. Catal. A-Gen.* **2006**, *303*, 192-198.

(30) Dexpert, H.; Lagarde, P.; Bournonville, J. P., EXAFS Studies of Bimetallic Pt-Re/Al_2O_3 Catalysts. *J. Mol. Catal.* **1984**, *25*, 347-355.

(31) Rezgui, S.; Jentoft, R.; Gates, B. C., Supported Pt and Re-Pt on Alumina Prepared by Sol-Gel Synthesis with in Situ Water Formation: Role of Rhenium. *J. Catal.* **1996**, *163*, 496-500.

(32) Azzam, K. G.; Babich, I. V.; Seshan, K.; Lefferts, L., A Bifunctional Catalyst for the Single-Stage Water-Gas Shift Reaction in Fuel Cell Applications. Part 2. Roles of the Support and Promoter on Catalyst Activity and Stability. *J. Catal.* **2007**, *251*, 163-171.

(33) Azzam, K. G.; Babich, I. V.; Seshan, K.; Lefferts, L., Role of Re in Pt-Re/TiO_2 Catalyst for Water Gas Shift Reaction: A Mechanistic and Kinetic Study. *Appl. Catal. B-Environ.* **2008**, *80*, 129-140.

(34) Azzam, K. G.; Babich, I. V.; Seshan, K.; Mojet, B. L.; Lefferts, L., Stable and Efficient Pt-Re/TiO_2 Catalysts for Water-Gas-Shift: On the Effect of Rhenium. *ChemCatChem* **2013**, *5*, 557-564.

(35) Iida, H.; Igarashi, A., Difference in the Reaction Behavior Between Pt-Re/TiO_2 (Rutile) and Pt-Re/ZrO_2 Catalysts for Low-Temperature Water Gas Shift Reactions. *Appl. Catal. A-Gen.* **2006**, *303*, 48-55.

(36) Iida, H.; Yonezawa, K.; Kosaka, M.; Igarashi, A., Low-Temperature Water Gas Shift Reaction over Pt-Re/TiO_2 Catalysts Prepared by a Sub-Critical Drying Method. *Catal. Commun.* **2009**, *10*, 627-630.

(37) Sato, Y.; Terada, K.; Hasegawa, S.; Miyao, T.; Naito, S., Mechanistic Study of Water-Gas-Shift Reaction over TiO_2 Supported Pt-Re and Pd-Re Catalysts. *Appl. Catal. A-Gen.* **2005**, *296*, 80-89.

(38) Kunkes, E. L.; Simonetti, D. A.; Dumesic, J. A.; Pyrz, W. D.; Murillo, L. E.; Chen, J. G. G.; Buttrey, D. J., The Role of Rhenium in the Conversion of Glycerol to Synthesis Gas over Carbon Supported Platinum-Rhenium Catalysts. *J. Catal.* **2008**, *260*, 164-177.

(39) Duke, A. S.; Galhenage, R. P.; Tenney, S. A.; Ammal, S. C.; Heyden, A.; Sutter, P.; Chen, D. A., In Situ Ambient Pressure X-Ray Photoelectron Spectroscopy Studies of Methanol Oxidation on Pt(111) and Pt-Re Alloys. *J. Phys. Chem. C* **2015**, *119*, 23082-23093.

(40) Suh, D. J.; Kwak, C.; Kim, J.-H.; Kwon, S. M.; Park, T.-J., Removal of Carbon Monoxide from Hydrogen-Rich Fuels by Selective Low-Temperature Oxidation over Base Metal Added Platinum Catalysts. *J. Power Sources* **2005**, *142*, 70-74.

(41) R. D. Cortright, R. R. D. J. A. D., Hydrogen from Catalytic Reforming of Biomass-Derived Hydrocarbons in Liquid Water. *Nature* **2002**, *418*, 964.

(42) A. Haryanto, S. F., N. Murali, S. Adhikari, Current Status of Hydrogen Production Techniques by Steam Reforming of Ethanol: A Review. *Energy & Fuels* **2005**, *19*, 2098.

(43) Holladay, J. D.; Hu, J.; King, D. L.; Wang, Y., An Overview of Hydrogen Production Technologies. *Catal. Today* **2009**, *139*, 244-260.

(44) Igarashi, H.; Uchida, H.; Suzuki, M.; Sasaki, Y.; Watanabe, M., Removal of Carbon Monoxide from Hydrogen-Rich Fuels by Selective Oxidation Over Platinum Catalyst Supported on Zeolite. *Appl. Catal. A-Gen.* **1997**, *159*, 159-169.

(45) Wei, Z. H.; Karim, A. M.; Li, Y.; King, D. L.; Wang, Y., Elucidation of the Roles of Re in Steam Reforming of Glycerol over Pt-Re/C Catalysts. *J. Catal.* **2015**, *322*, 49-59.

(46) Ciftci, A.; Eren, S.; Ligthart, D.; Hensen, E. J. M., Platinum-Rhenium Synergy on Reducible Oxide Supports in Aqueous-Phase Glycerol Reforming. *ChemCatChem* **2014**, *6*, 1260-1269.

(47) Ciftci, A.; Ligthart, D.; Hensen, E. J. M., Aqueous Phase Reforming of Glycerol over Re-Promoted Pt and Rh Catalysts. *Green Chemistry* **2014**, *16*, 853-863.

(48) Ciftci, A.; Ligthart, D.; Sen, A. O.; van Hoof, A. J. F.; Friedrich, H.; Hensen, E. J. M., Pt-Re Synergy in Aqueous-Phase Reforming of Glycerol and the Water-Gas Shift Reaction. *J. Catal.* **2014**, *311*, 88-101.

(49) Ciftci, A.; Ligthart, D.; Hensen, E. J. M., Influence of Pt Particle Size and Re Addition by Catalytic Reduction on Aqueous Phase Reforming of Glycerol for Carbon-Supported Pt(Re) Catalysts. *Appl. Catal. B-Environ.* **2015**, *174*, 126-135.

(50) Zhang, L.; Karim, A. M.; Engelhard, M. H.; Wei, Z. H.; King, D. L.; Wang, Y., Correlation of Pt-Re Surface Properties with Reaction Pathways for the Aqueous-Phase Reforming of Glycerol. *J. Catal.* **2012**, *287*, 37-43.

(51) Kirilin, A. V.; Tokarev, A. V.; Manyar, H.; Hardacre, C.; Salmi, T.; Mikkola, J. P.; Murzin, D. Y., Aqueous Phase Reforming of Xylitol over Pt-Re Bimetallic Catalyst: Effect of the Re Addition. *Catal. Today* **2014**, *223*, 97-107.

(52) Huber, G. W.; Chheda, J. N.; Barrett, C. J.; Dumesic, J. A., Production of Liquid Alkanes by Aqueous-Phase Processing of Biomass-Derived Carbohydrates. *Science* **2005**, *308*, 1446-1450.

(53) Simonetti, D. A.; Kunkes, E. L.; Dumesic, J. A., Gas-Phase Conversion of Glycerol to Synthesis Gas over Carbon-Supported Platinum and Platinum-Rhenium Catalysts. *J. Catal.* **2007**, *247*, 298-306.

(54) Choung, S. Y.; Ferrandon, M.; Krause, T., Pt-Re Bimetallic Supported on CeO_2-ZrO_2 Mixed Oxides as Water-Gas Shift Catalysts. *Catal. Today* **2005**, *99*, 257-262.

(55) Purnell, S. K.; Chang, J. R.; Gates, B. C., NaY Zeolite-Supported Re-Pt Catalysts Prepared from Organometallic Precursors - Evidence of the Re-Pt Interaction from Infrared and X-Ray-Absorption Spectroscopies. *J. Phys. Chem.* **1993**, *97*, 4196-4205.

(56) Sato, Y.; Terada, K.; Hasegawa, S.; Miyao, T.; Naito, S., Mechanistic Study of Water-Gas-Shift Reaction over TiO_2 Supported Pt-Re and Pd-Re Catalysts. *Appl. Catal. A-Gen.* **2005**, *296*, 80-89.

(57) Wei, Z.; Karim, A. M.; Li, Y.; King, D. L.; Wang, Y., Elucidation of the Roles of Re in Steam Reforming of Glycerol over Pt–Re/C Catalysts. *J. Catal.* **2015**, *322*, 49-59.

(58) Ciftci, A.; Ligthart, D. A. J. M.; Hensen, E. J. M., Aqueous Phase Reforming of Glycerol over Re-Promoted Pt and Rh Catalysts. *Green Chemistry* **2014**, *16*, 853-863.

(59) Ammal, S. C.; Heyden, A., Origin of the Unique Activity of Pt/TiO_2 Catalysts for the Water-Gas Shift Reaction. *J. Catal.* **2013**, *306*, 78-90.

(60) Ammal, S. C.; Heyden, A., Water-Gas Shift Catalysis at Corner Atoms of Pt Clusters in Contact with a TiO_2 (110) Support Surface. *ACS Catal.* **2014**, *4*, 3654-3662.

(61) King, D. L.; Zhang, L. A.; Xia, G.; Karim, A. M.; Heldebrant, D. J.; Wang, X. Q.; Peterson, T.; Wang, Y., Aqueous Phase Reforming of Glycerol for Hydrogen Production over Pt-Re Supported on Carbon. *Appl. Catal. B-Environ.* **2010**, *99*, 206-213.

(62) Prestvik, R.; Moljord, K.; Grande, K.; Holmen, A., The Influence of Pretreatment on the Metal Function of a Commercial $Pt-Re/Al_2O_3$ Catalyst. *J. Catal.* **1998**, *174*, 119-129.

(63) Prestvik, R.; Totdal, B.; Lyman, C. E.; Holmen, A., Bimetallic Particle Formation in Pt-Re/Al_2O_3 Reforming Catalysts Revealed by Energy-Dispersive X-Ray Spectrometry in the Analytical Electron Microscope. *J. Catal.* **1998**, *176*, 246-252.

(64) Ronning, M.; Gjervan, T.; Prestvik, R.; Nicholson, D. G.; Holmen, A., Influence of Pretreatment Temperature on the Bimetallic Interactions in Pt-Re/Al_2O_3 Reforming Catalysts Studied by X-Ray Absorption Spectroscopy. *J. Catal.* **2001**, *204*, 292-304.

(65) Pieck, C. L.; Marecot, P.; Querini, C. A.; Parera, J. M.; Barbier, J., Influence of Pt-Re Interaction on Activity and Selectivity of Reforming Catalysts. *Appl. Catal. A-Gen.* **1995**, *133*, 281-292.

(66) Fung, A. S.; McDevitt, M. R.; Tooley, P. A.; Kelley, M. J.; Koningsberger, D. C.; Gates, B. C., A Model Gamma-Al_2O_3-Supported Re-Pt Catalyst Prepared from $Re_2Pt(CO)_{12}$ .1. Synthesis and Spectroscopic Characterization. *J. Catal.* **1993**, *140*, 190-208.

(67) Bastein, A.; Toolenaar, F.; Ponec, V., Adsorption of Carbon-Monoxide on Platinum Alloys - an Infrared Investigation. *J. Catal.* **1984**, *90*, 88-95.

(68) Bolivar, C.; Charcosset, H.; Frety, R.; Primet, M.; Tournayan, L.; Betizeau, C.; Leclercq, G.; Maurel, R., Platinum-Rhenium-Alumina Catalysts .2. Study of Metallic Phase after Reduction. *J. Catal.* **1976**, *45*, 163-178.

(69) Charcosset, H.; Frety, R.; Leclercq, G.; Mendes, E.; Primet, M.; Tournayan, L., State of Re in Pt-Re-Gamma-Al_2O_3 Catalysts. *J. Catal.* **1979**, *56*, 468-471.

(70) Tenney, S. A.; Xie, K.; Monnier, J. R.; Rodriguez, A.; Galhenage, R. P.; Duke, A. S.; Chen, D. A., Novel Recirculating Loop Reactor for Studies on Model Catalysts: CO Oxidation on Pt/TiO_2(110). *Rev. Sci. Instrum.* **2013**, *84*, 104101.

(71) Duke, A. S. X., K.; Monnier, J. R.; Chen, D. A., X-Ray Photoelectron Spectroscopy and Reactor Studies for Methanol Oxidation on Pt and Pt-Re Alloy Surfaces, in preparation.

(72) Galhenage, R. P.; Xie, K.; Yan, H.; Seuser, G. S.; Chen, D. A., Understanding the Growth, Activity and Cluster-Support Interactions for Pt-Re Bimetallic Clusters on TiO_2(110), Submitted to *J. Phys. Chem C* **2016**.

(73) Ducros, R.; Alnot, M.; Ehrhardt, J. J.; Housley, M.; Piquard, G.; Cassuto, A., A Study of the Adsorption of Several Oxygen-Containing Molecules (O_2, CO, NO, H_2O) on Re(0001) by XPS, UPS, and Temperature Programmed Desorption. *Surf. Sci.* **1980**, *94*, 154-168.

(74) Chan, A. S. Y.; Chen, W.; Wang, H.; Rowe, J. E.; Madey, T. E., Methanol Reactions over Oxygen-Modified Re Surfaces: Influence of Surface Structure and Oxidation. *J Phys Chem B* **2004**, *108*, 14643-14651.

(75) Martensson, N.; Saalfeld, H. B.; Kuhlenbeck, H.; Neumann, M., Structural Dependence of the 5d-Metal Surface Energies as Deduced from Surface Core-Level Shift Measurements. *Phys. Rev. B* **1989**, *39*, 8181-8186.

CHAPTER 7

ACTIVE SITES IN COPPER-BASED METAL–ORGANIC FRAMEWORKS: UNDERSTANDING SUBSTRATE DYNAMICS, REDOX PROCESSES, AND VALENCE-BAND STRUCTURE [5]

[5] Reprinted (adapted) with permission from Duke, A. S.; Dolgopolova, E. A.; Galhenage, R. P.; Ammal, S. C.; Heyden, A.; Smith, M. D.; Chen, D. A.; Shustova, N. B. Active Sites in Copper-Based Metal–Organic Frameworks: Understanding Substrate Dynamics, Redox Processes, and Valence-Band Structure. *J. Phys. Chem. C*, **2015**, *119* (49), 27457-27466. Copyright 2015 American Chemical Society.

7.1 INTRODUCTION

The use of metal−organic frameworks (MOFs) provides a unique and powerful opportunity for precise control over the architecture of reactive metal sites. The reactive metal centers in MOFs consist of unsaturated metal sites (UMS), which are typically formed by removing metal-coordinated solvents by heating under reduced pressure. The exploration of chemical activity at these UMS is critical for understanding MOF chemistry and also impacts a wide variety of related practical applications.[1−16] For example, MOFs have proven to be effective materials for use in gas purification and storage,[1,17−19] sensing,[20] and enhanced catalytic activity.[21−23] MOFs have also recently demonstrated great potential for efficient gas separation (e.g., for CO_2/N_2 or CO_2/H_2 gas mixtures)[1,18] and temperature-dependent, highly selective sensing.[20] Moreover, MOFs can help address the current challenges in heterogeneous catalysis. The majority of commercial heterogeneous catalysts are based on metal particles deposited on high surface area supports, such as metal oxides. However, control of active site geometry cannot be achieved through traditional catalyst preparation techniques such as wet impregnation; furthermore, changes in structure and composition of supported metal particles also occur upon heating and exposure to reactant gases[24−28] due to sintering,[29−31] surface reconstruction,[32,33] and redistribution of metal atoms between the surface and the bulk. In contrast, the geometry and composition of UMS in MOFs can be synthetically tuned by the ligand and/or metal node design, fully characterized by single-crystal X-ray crystallography, and should remain unchanged under reaction conditions.

The development of MOFs that can provide a high density of chemically active sites is a complex problem and should be tackled from many directions. In this work, we

report a systematic and integrated approach that combines optimization of MOF ligand/node design and synthetic methodology, X-ray photoelectron spectroscopy (XPS) studies for characterization of MOF UMS, and theoretical calculations that provide insight into the chemical processes occurring at the active UMS. Specifically, we have achieved the following: (1) extensive reduction of Cu^{+2} to Cu^{+1} at the MOF metal nodes while retaining the original MOF structure, (2) a change in the valence band structure and electronic properties of the MOF after significant reduction of Cu^{+2} to Cu^{+1}, and (3) selective binding of adsorbates as a function of the UMS oxidation state. The described approach focusing on gas−solid state dynamics has great potential for industrial impact, given that the majority of industrial catalytic reactions occur in the gas phase. In contrast to liquid-phase studies, there have been only a few investigations of gas-phase reactions in a MOF matrix.[34–37] Thus, we envision that the studies presented here will significantly impact the use of MOFs for heterogeneous catalysis and gas purification; in addition, this work will also guide the development of new avenues for controlling the conductivity of typically insulating MOF materials.

7.2 EXPERIMENTAL

Materials

$Cu(NO_3)_2 \cdot 2.5H_2O$ (98.3%, Mallinckrodt AR), $Cu(CH_3COO)_2 \cdot H_2O$ (95%, TCI America), 1,3,5-benzenetricarboxylic acid (98%, Alfa Aesar), 2-methylimidazole (97%, Alfa Aesar), 5-nitroisophtalic acid (98%, Alfa Aesar), *N*,*N*-dimethylformamide (ACS grade, BDH), ethanol (Decon Laboratories, Inc). The compounds $Cu_3(BTC)_2(H_2O)_3$ (**1**)[1] and $[Cu_5(NIP)_4(OH)_2(H_2O)_6] \cdot (H_2O)_5$ (**2**)[2] were prepared according to the reported procedures.[a]

X-ray Crystal Structure Determination

$[Cu_5(NIP)_4(OH)_2(H_2O)_6]\cdot(H_2O)_5$ ($C_{32}H_{36}Cu_5N_4O_{37}$, **2**, the crystallographic data are shown in Table C.1 and Figures C.1 and C.2). X-ray intensity data from a light blue plate crystal were collected at 100(2) K using a Bruker SMART APEX diffractometer (Mo K_α radiation, λ = 0.71073 Å).[3] The raw area detector data frames were reduced and corrected for absorption effects using the SAINT+ and SADABS programs.[3] Final unit cell parameters were determined by least-squares refinement of 9131 reflections from the data set. The structure was solved by direct methods with SHELXS.[4] Subsequent difference Fourier calculations and full-matrix least-squares refinement against F^2 were performed with SHELXL-2014[4] using OLEX2.[5]

Other Physical Measurements

Powder X-ray diffraction patterns were recorded on a Rigaku Miniflex II diffractometer with accelerating voltage and current of 30 kV and 15 mA, respectively. Thermogravimetric analysis (TGA) was performed on a SDT Q600 thermogravimetric analyzer using an alumina boat as a sample holder at a heating rate of 5 °C/min (Figure C.3). FT-IR spectra were obtained on a PerkinElmer Spectrum 100 (Figure C.4).

X-ray Photoelectron Spectroscopy (XPS) Studies

The XPS studies on MOF samples were carried out using a Kratos AXIS Ultra DLD system equipped with a monochromatic Al Kα source, a hemispherical analyzer, charge neutralizer, catalysis cell, and a load lock chamber for rapid introduction of samples without breaking vacuum. The base pressure in the XPS analysis chamber was 2

$\times 10^{-9}$ Torr before sample introduction and $\leq 2 \times 10^{-8}$ Torr during experiments. The samples could be directly transferred from the XPS analysis chamber to the catalysis cell without exposure to air. In the catalysis cell, samples were exposed to a flow of pure gases (Ar, O_2, H_2, and CO) at temperatures ranging from room temperature to 225 °C. Pure gases were obtained from the following vendors: Ar (Airgas, UHP 99.999%), O_2 (Airgas, UHP 99.994%), CO (Praxair, 99.99%), and H_2 (Airgas, UHP 99.999%).

XPS data were collected with a step size of 0.06 eV and dwell times of 600 s for O(1s), 800 s for C(1s) and N(1s), and 1600 s for Cu(2p), the Cu($L_3M_5M_5$) region, and the valence band region unless otherwise specified. Because of the insulating nature of the MOF samples, a charge neutralizer was used to compensate for sample charging by bombarding the sample with low-energy electrons; electrons are generated by a hot filament, and the trajectories of the electrons toward the sample are by controlled electric and magnetic fields. Binding energies were set according to the Cu($L_3M_5M_5$) Auger peak for metallic Cu, which was fixed at 567.9 eV[6,7] for the MOF that was heated in H_2 at 225 °C for 1 h in order to reduce all of the Cu to the metallic species (Figure C.5). The C(1s) peaks for this reduced sample appeared at 284.8 and 288.7 eV, corresponding to the aromatic and carboxylate carbons, respectively; since the ratio of the low to high binding energy peaks was greater than 2:1, as expected based on stoichiometry, adventitious carbon is believed to have a significant contribution to the 284.8 eV peak. The binding energies for all of the other MOF samples were calibrated according to the position of the 284.8 eV peak. Notably, the binding energy for adventitious carbon/aromatic carbon was unchanged after the sample was reduced in H_2. The Cu($2p_{3/2}$) peak position was not used as the calibration standard because there is more variation in the literature regarding the

exact binding energy for metallic Cu (932.2−932.5 eV)[6,8,9] compared to the Cu($L_3M_5M_5$) position (918.6−918.7 eV kinetic energy).[6,7]

MOF XPS samples were either in powder form or consisted of the powder pressed into a ~0.5 mm thick pellet using a hydraulic press at 60 tons for 20 s. The powdered samples and pellets were heated under vacuum on a Schlenk line in order to remove residual solvent before introduction into the vacuum chamber for XPS analysis. Immediately after heating on the Schlenk line, the MOF samples were transferred to a closed glass vial and placed in an aluminum holder that had been heated to the same temperature as the sample to minimize water uptake from air. The samples remained in the aluminum holder while being transported to the XPS facility and were still hot when introduced into the load lock chamber. The standard preparation for **1** involved heating at 160 °C for 48 h. The color of **1** was dark blue after heating on the Schlenk line and remained this color until turning lighter blue during loading into the sample holder; after evacuation in the load lock chamber overnight, the sample returned to the dark blue color. Framework **2** changed from blue to green after heating on the Schlenk line and then turned dark green after heating in Ar for 14 h at 200 °C. To confirm MOF crystallinity, each sample was characterized by PXRD analysis prior to thermal treatment and after XPS experiments (Figures C.6−C.11).

Survey scans were acquired to establish that there were no contaminants introduced during sample preparation, and the following regions were collected for each sample unless otherwise specified: C(1s), O(1s), Cu(2p), Cu($L_3M_5M_5$), valence band, and N(1s). A small N(1s) peak was observed for the as-received MOF sample and is attributed to the presence of dimethylformamide from the solvent during synthesis. This

N(1s) peak decreased almost to zero after heating the MOF in Ar at 225 °C in the catalysis cell for 14 h. Experiments involving heating in the vacuum chamber and exposure to O_2 gas were carried out on both the powder and pellet samples with the same results. The samples were heated by means of a shielded boron nitride button heater in the XPS analysis chamber and catalysis cell. The sample temperature was measured by a type K thermocouple affixed to the sample stage in the analysis chamber and by a type K thermocouple pin on which the sample holder rested in the catalysis cell.

Theoretical Calculations

A finite size cluster model cut out from the crystallographically-determined structure of $Cu_3(BTC)_2$ was used to study the adsorption behavior of Cu^{+2} and Cu^{+1} sites using density functional theory (DFT). The initial cluster model (Figure C.12a), which contains 82 atoms was formed from a Cu^{+2} dimer and four BTC units after saturating the carboxylates with H atoms. The calculations were performed using the TURBOMOLE 6.6 program package.[12] Geometry optimization and energy calculations were carried out employing the hybrid B3LYP method[13-15] (Becke's three-parameter exchange functional and the correlation functional from Lee, Yang, and Parr) and the def2-TZVPP basis set[16,17] (Ahlrichs' split-valence triple-zeta basis set with polarization functions on all atoms with additional polarization functions). The dispersion corrections for the non-bonding van der Waals interactions were included using Grimme's DFT-D3 method.[18] The adsorption energies (E_{ads}) between the gas molecules and the MOF cluster were calculated using the formula, $E_{ads} = E_{MOF-gas} - E_{MOF} - E_{gas}$ where $E_{MOF-gas}$ is the total energy of the MOF cluster with adsorbed gas molecule, E_{MOF} and E_{gas} represent the

total energies of the MOF cluster and the gas molecule, respectively. The calculated adsorption energies were then corrected for the basis set superposition error (BSSE) using the full counterpoise correction method.[19] The atomic charges on the Cu metal atoms were calculated using natural population analysis (NPA)[20] and the density of states (DOS) for the clusters were obtained using Gaussian smearing of Kohn–Sham orbital energies.

7.3 RESULTS AND DISCUSSION

Cu^{+2}/Cu^{+1} Reduction at MOF Metal Nodes

The initial criteria for the selection of MOFs to be studied by XPS were high thermal stability, ability to retain the structure after MOF activation, and the presence of secondary building units consisting of coordinatively unsaturated metal ions at the MOF nodes. Additional restrictions, such as a difference in UMS ensemble sizes, were applied to the chosen MOFs to ensure an ability to explore the effect of UMS geometry. We also imposed the requirement that at least one of the chosen MOFs should possess a known behavior (e.g., activation procedure, synthesis, and thermal stability) and be very well characterized by a variety of solid-state techniques. In this manner, we can establish clear structure−property relationships based on our experimental data and theoretical calculations in combination with previously reported studies. As a result, $Cu_3(BTC)_2(H_2O)_3$ (**1**, BTC = benzene-1,3,5-tricarboxylate) and $[Cu_5(NIP)_4(OH)_2(H_2O)_6]\cdot(H_2O)_5$ (**2**, NIP = 5-nitroisophthalate) were chosen for synthesis (Figure 7.1). For preparation of **1**, copper nitrate was heated in the presence of the H_3BTC ligand at 75 °C for 24 h.[38] Framework **2** was prepared by a solvothermal procedure, which includes heating of copper acetate and H_2NIP at 100 °C for 48 h using

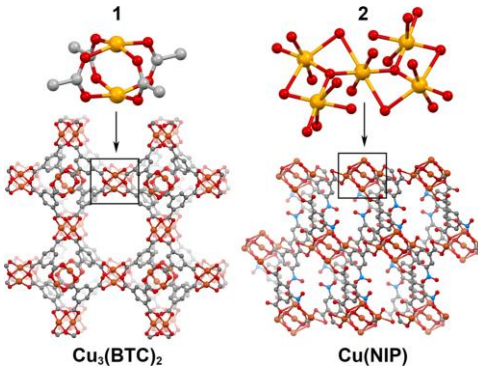

Figure 7.1: Single-crystal X-ray structures of **1** and **2** highlighting dimetal and pentameric secondary building units. Orange, gray, blue, and red spheres represent copper, carbon, nitrogen, and oxygen atoms, respectively. Hydrogen atoms and coordinated and noncoordinated solvent molecules are omitted for clarity.

water as a reaction medium.[39] Prepared **1** and **2** were characterized by single-crystal and powder X-ray diffraction (PXRD), thermogravimetric analysis (TGA), and Fourier transform infrared (FTIR) spectroscopy (Figure 7.2; Table C.1, Figures C.1− C.4).

As shown in Figure 7.1, **1** contains dinuclear paddle wheel secondary building units bridged by four carboxylate groups, $M_2(O_2C^-)_4$. The activation procedure developed for **1** facilitated removal of the solvent molecules, which occupy the axial sites on each Cu^{+2} ion, by heating under vacuum to generate UMS. In contrast to the dinuclear nodes in **1**, **2** has an unusual pentameric copper-based building unit, Cu_5 (Figure 7.1). The asymmetric unit consists of three copper ions, one of which is located on a crystallographic inversion center, two NIP^{2-} ligands, one OH^- group, three coordinated water molecules, and three noncoordinated water molecules (Figure 7.1, Figures C.1 and

C.2). The connection of these Cu_5 clusters with fully deprotonated NIP^{2-} ligands resulted in the formation of the three-dimensional framework **2** (Figure 7.1 and Figure C.1). Thus, prepared **1** and **2** frameworks satisfy all criteria mentioned above: they are thermally stable,[22,39] able to preserve crystallinity after the activation procedure (Figure 7.2), contain UMS, and possess two distinctively different UMS geometries.

For **1**, XPS data for the Cu($2p_{3/2}$) region show two distinct peaks at 935.0 and 933.3 eV, which are assigned to Cu^{+2} and Cu^{+1}, respectively (Figure 7.3a). Although these binding energies are ~0.5−1.5 eV higher than those typically observed for Cu^{+1} and Cu^{+2} oxidation states in Cu_2O and CuO,[40–42] our binding energies are consistent with the values that have been observed in Cu^{+1} and Cu^{+2} complexes.[43,44] The Cu($2p_{3/2}$) region cannot be used to distinguish between metallic Cu and Cu^{+1} given the similar binding

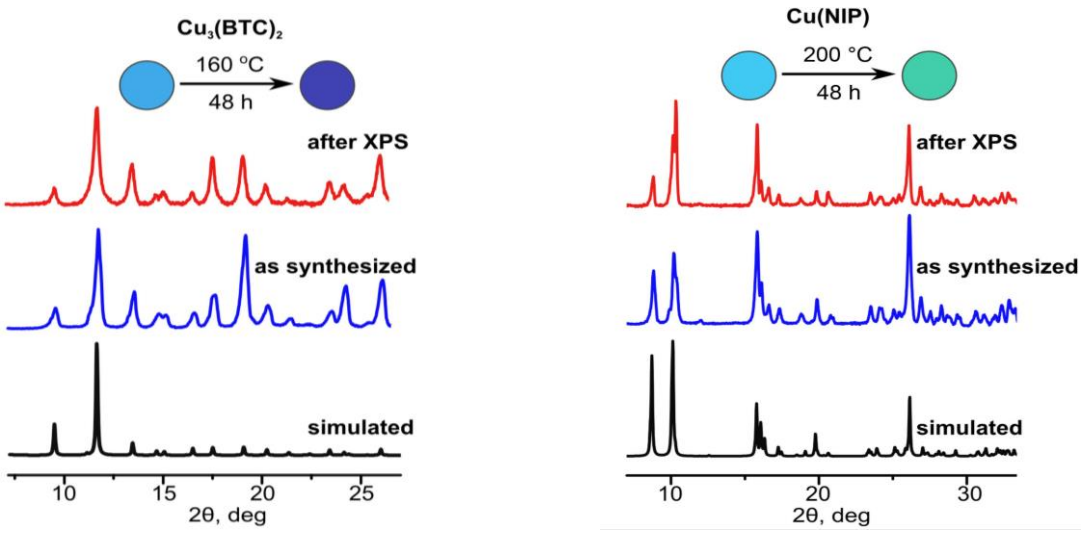

Figure 7.2: (top) PXRD patterns of **1**: simulated (black), as synthesized (blue), and after XPS measurements (red). The inset shows the color change observed for **1** during heating on the Schlenk line at 160 °C for 48 h. (bottom) PXRD patterns of **2**: simulated (black), as synthesized (blue), and after XPS measurements (red). The inset shows the color change observed for **2** during heating on the Schlenk line at 200 °C for 48 h.

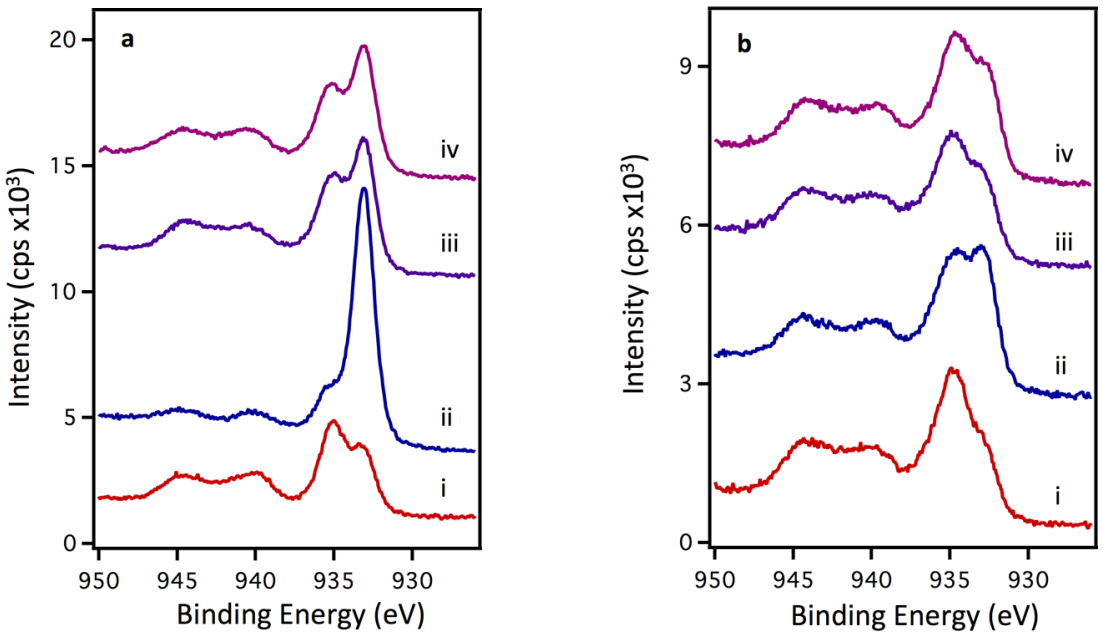

Figure 7.3: XPS data for the Cu($2p_{3/2}$) region for (a) **1** powder and (b) **2** powder after the following successive treatments on the same samples: (a, i) as-received; (a, ii) heated in Ar at 225 °C for 14 h; (a, iii) exposed to pure oxygen at room temperature for 2 h; (a, iv) heated in vacuum at 275 °C for 5 h; (b, i) as-received; (b, ii) heated in Ar at 200 °C for 14 h; (b, iii) exposed to pure oxygen at room temperature for 2 h; and (b, iv) heated in vacuum at 200 °C for 2 h.

energies,[40,42] but the Cu(LMM) Auger peak shapes can distinguish between metallic Cu and oxidized Cu.[45] The Auger spectra in Figure 7.4 correspond to **1** as received and after the thermal and gas treatments described in Figure 7.3. The spectrum of metallic Cu, which was produced by decomposing **1** in H_2 at 225 °C for 1 h, is also shown for comparison. The peak shapes for the Cu^{+1} and Cu^{+2} species are similar to each other and are consistent with Cu(LMM) data in the literature for CuO and Cu_2O,[45] whereas the peak shape for metallic Cu is distinctly different. The other spectral regions corresponding to this H_2 treatment for **1** are shown in Figure C.5. For all of the XPS experiments, PXRD of the sample after data collection showed that the MOF samples were still crystalline; the only exception was when **1** was heated in H_2 to intentionally reduce all of the Cu ions to

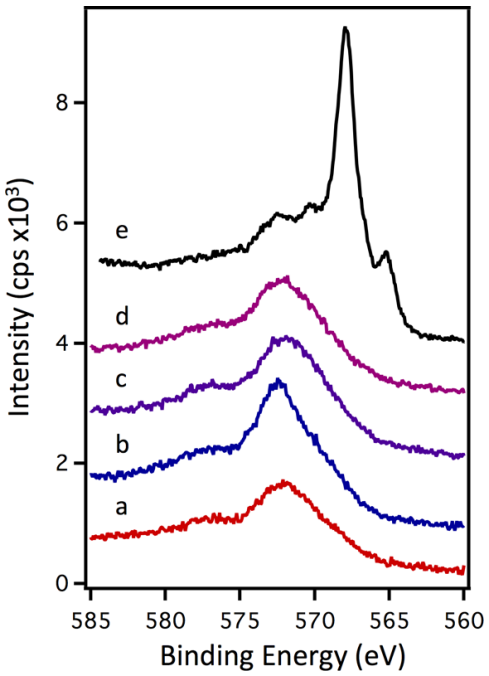

Figure 7.4: XPS data for the Cu(LMM) Auger region for **1** powder after the following successive treatments on the same sample: (a) as-received; (b) heated in Ar at 225 °C for 14 h; (c) exposed to pure oxygen at room temperature for 2 h; (d) heated in vacuum at 275 °C for 5 h; and (e) a pellet of **1** heated in flowing H_2 at 225 °C for 1 h in order to decompose the MOF and reduce all of the Cu ions to metallic Cu. The intensity of (e) is reduced by a factor of 2 since the pellet samples provided more intensity than the powders.

metallic Cu. This retention of crystal structure for the samples is further chemical evidence that copper is in its ionic rather than metallic form.

After heating the sample in the catalysis cell in flowing Ar for 14 h at 225 °C, there is a dramatic increase in the Cu^{+1}/Cu^{+2} ratio from 0.76 to 5.6 (Figure 7.3a,ii). This thermal treatment is believed to convert Cu^{+2} to Cu^{+1}, given that more extensive heating

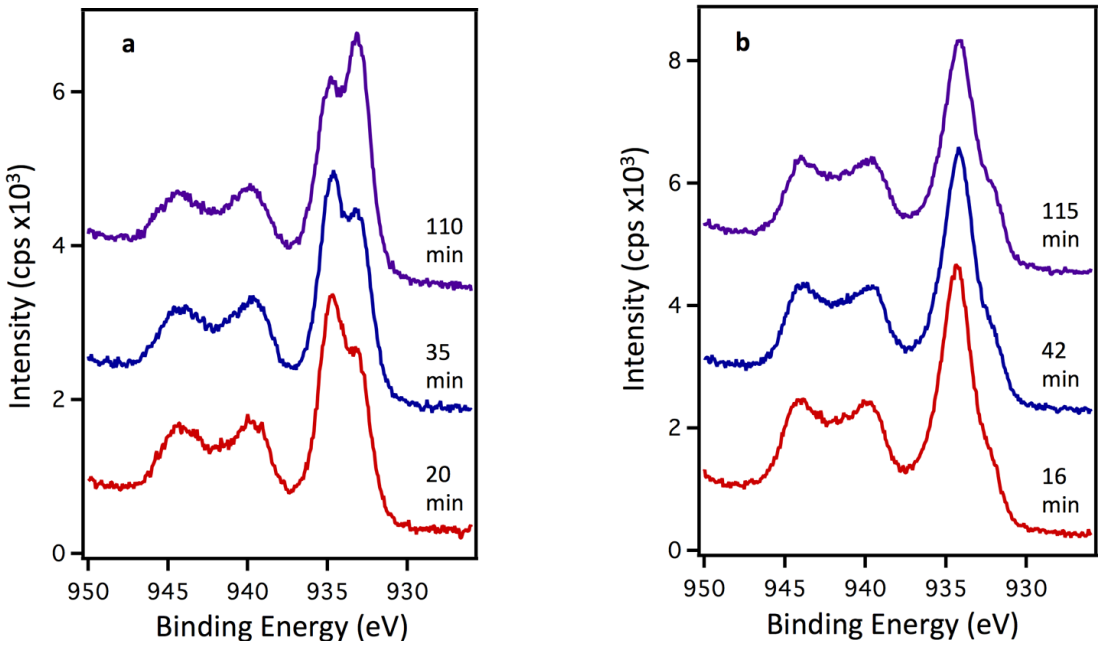

Figure 7.5: XPS data for the Cu($2p_{3/2}$) region after exposure to X-rays and the charge neutralizer for various times for (a) **1** powder and (b) anhydrous Cu(II) acetate powder.

in Ar (35 h) achieved ~100% complete conversion (Figure C.13); the near absence of the satellite peaks at 940.5 and 944.8 eV establishes that the sample is almost exclusively Cu^{+1} since distinct satellite peaks are observed only for Cu^{+2}.[42] Exposure of reduced **1** to O_2 for 2 h at room temperature diminishes the Cu^{+1}/Cu^{+2} ratio to a value of 1.5, suggesting that oxygen preferentially binds to Cu^{+1} sites and converts Cu^{+1} to Cu^{+2} (Figure 7.3a,iii). Heating the O_2-exposed sample to 275 °C in a vacuum for 5 h does not change the peak shape, and this implies that desorption of oxygen does not occur (Figure 7.3a,iv). The C(1s) and O(1s) regions before thermal treatment are in agreement with the spectra reported for films and powders of **1** in the literature,[46,47] and these spectra do not change after heating at 225 °C in Ar for 14 h or after exposure to gases (Figure C.14).

Two earlier reports of XPS for **1** in the literature do not show a clear Cu^{+1} peak. However, one of the studies has much lower energy resolution in the XPS data based on the lack of distinct structure for the satellite peaks at 940.5 and 944.8 eV,[10] and it is likely that the resolution is not sufficient to distinguish Cu^{+1} and Cu^{+2}. In the second study, the exact preparation and data acquisition procedures for the XPS samples were not described, including how the binding energies were calibrated.[11] Our own investigations show that the ratio of Cu^{+1}/Cu^{+2} in the as-received sample is highly sensitive to the prior thermal treatment, exposure time to air between thermal treatment and introduction into the vacuum chamber, and exposure time to the X-ray source and charge neutralizer. For example, a spectrum corresponding to almost exclusively Cu^{+2} was observed for a MOF sample initially heated at 160 °C for 48 h on the Schlenk line and then stored in a closed vial for 48 h before loading into the XPS analysis chamber. Previous studies of powders and films of **1** have reported that Cu^{+2} can be partially reduced by heating in a vacuum,[46,48,49] but almost complete conversion of Cu^{+2} to Cu^{+1} while retaining MOF crystallinity has never been previously observed in a MOF matrix. The presence of Cu^{+1} cannot be attributed to Cu_2O impurities[50,51] or unbound carboxylate ligands[48] because the resulting MOF contains almost exclusively Cu^{+1} sites. Our XPS experiments support an infrared spectroscopy study of **1** that also concluded that the presence of Cu^{+1} cannot be attributed to impurities or defects alone.[49] Thus, for the first time we were able to prepare a MOF with ~100% reduction of Cu^{+2} to Cu^{+1} at the UMS while preserving the framework integrity.

The observation of mixed copper oxidation states is also observed for **2** although the Cu^{+1}/Cu^{+2} ratio is significantly higher for **1** (Figure 7.3b). After heating **2** to 200 °C

for 14 h in Ar, the Cu^{+1}/Cu^{+2} ratio increases from 0.53 to 1.1 (Figure 7.3b,ii). Upon exposure to O_2 at room temperature for 2 h, the Cu^{+1}/Cu^{+2} ratio decreases to 0.76, suggesting oxidation of Cu^{+1} to Cu^{+2} and preferential binding of oxygen at Cu^{+1} sites (Figure 7.3b,iii). Heating **2** in vacuum for 2 h at 200 °C increases the absolute intensity of both peaks as adsorbates desorb, but the ratio of Cu^{+1}/Cu^{+2} remains the same (Figure 7.3b,iv). Therefore, **1** and **2** exhibit similar behavior in the sense that mixed valences are observed and thermal treatment enhances Cu^{+1} formation while exposure to O_2 oxidizes Cu^{+1} to Cu^{+2}. However, the Cu^{+2} in **1** is more easily reduced than in **2** based on the significantly higher Cu^{+1}/Cu^{+2} ratio for **1**; this could be attributed to the differences in geometries and/or sizes of the UMS.

Conversion of Cu^{+2} to Cu^{+1} in **1** is also induced by exposure of the MOF to the X-ray source and charge neutralizer during XPS data collection. Figure 7.5a shows that the ratio of Cu^{+1}/ Cu^{+2} increases from 0.75 to 1.3 with exposure times of 20 to 110 min. In contrast, an identical experiment carried out on a copper(II) acetate sample exhibits much less pronounced reduction during acquisition of XPS data over the same time interval (Figure 7.5b). Furthermore, **1** turned a dark purplish-blue color during the reduction process whereas the copper(II) acetate did not undergo any color change. These results demonstrate that the propensity for copper center reduction is intrinsically higher in the MOF matrix compared to other Cu-containing salts.

The following three experiments were conducted in order to gain mechanistic insight into the reduction process occurring at the Cu^{+2} sites. In the first experiment, **1** was heated on the Schlenk line at lower temperature (12 h, 120 °C) to minimize possible thermal reduction while still removing the solvent from the MOF pores, and the sample

remained light blue after heating. Notably, this ex situ heating procedure is always required for introduction of the MOF sample into the XPS vacuum chamber. Only the Cu($2p_{3/2}$) region was collected during a fast (21 s) scan after no more than 2 min of exposure to the X-ray source and charge neutralizer (Figure C.15). A series of five scans collected at 1 min intervals show that the Cu^{+1} peak is initially present, and this peak increases in intensity over 4 min of exposure; the spectrum acquired after 20 min using higher dwell times is nearly identical to the spectrum after 6 min. Thus, it appears that Cu^{+1} is present after initial heating to 120 °C and is not due solely to the conversion of Cu^{+2} to Cu^{+1} under XPS data collection conditions. In a second experiment, **1** was again heated to the lower temperature of 120 °C and was then exposed to the charge neutralizer only in vacuum (Figure C.16). A 1 h exposure showed significant growth in the Cu^{+1} peak, which continued to increase after an additional 1 h exposure. This experiment demonstrates that bombardment from the low-energy electrons of the charge neutralizer is sufficient to induce partial reduction of Cu^{+2} to Cu^{+1} even in the absence of X-ray irradiation. A third experiment showed that heating at 225 °C in Ar for 14 h could not promote extensive reduction Cu^{+2} to Cu^{+1} without prior extensive (75 min) exposure to X-rays/charge neutralizer. Therefore, full reduction of Cu^{+2} to Cu^{+1} can only be achieved by exposure to the X-rays/charge neutralizer followed by heating to 225 °C, even though thermal treatment or exposure to X-rays/charge neutralizer alone can induce partial reduction. Our results are in agreement with previous studies reporting X-ray induced reduction of Cu^{+2} in **1**[46] as well as in Cu(II) acetate and other organic Cu(II) compounds.[52] The earlier work did not explore the effects of low-energy electron bombardment on MOF reduction.

Gas-Phase Substrate Dynamics

To further probe adsorption behavior on **1**, samples were exposed to other gaseous analytes such as CO, air, and H_2. Figure 7.6a shows that exposure to CO decreases the intensity of the Cu^{+1} peak, which suggests coordination of CO to Cu^{+1}. This observation is in a good agreement with catalytic activity of Cu^{+1} sites previously reported in copper-containing proteins and supported by the existence of a variety of molecular copper(I) carbonyl complexes.[53–55] Based on the lack of change in the Cu($2p_{3/2}$) spectrum, CO is not removed from the metal sites after heating to 225 °C in a vacuum, implying that CO is strongly bound to the UMS. When a pellet of **1** is exposed to air for 10−15 min, water is believed to adsorb at the metal sites rather than N_2 or O_2.[56]

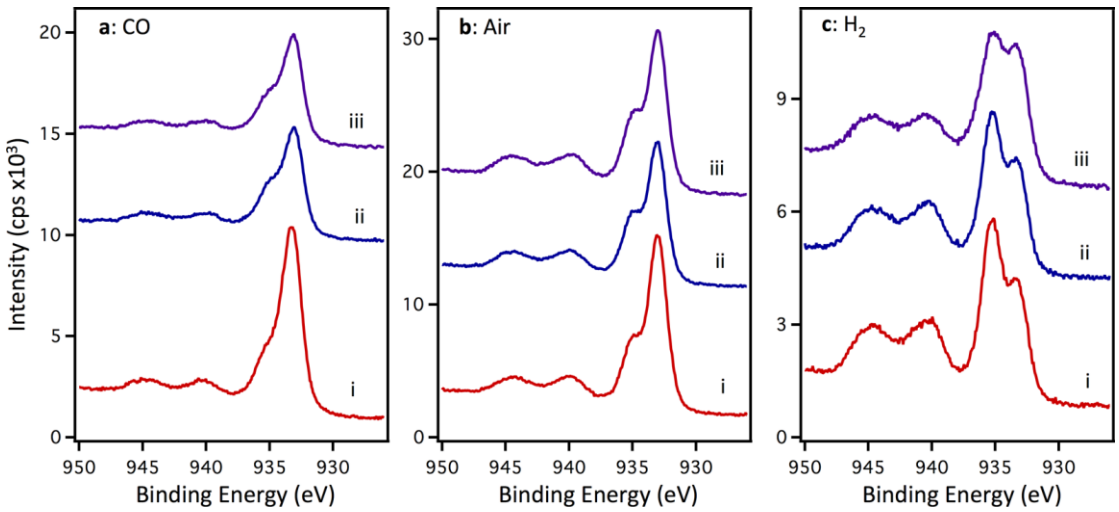

Figure 7.6: XPS data for the Cu($2p_{3/2}$) region after exposure of **1** to CO (a), air (b), and H_2 (c). Sample treatments are as follows: (a, i) **1** powder heated in Ar at 225 °C for 14 h; (a, ii) exposed to pure CO at room temperature for 2 h; (a, iii) heated in vacuum at 225 °C for 1 h; (b, i) **1** pellet heated in vacuum at 225 °C for 1 h; (b, ii) exposed to air at room temperature for 10-15 min; and (b, iii) heated in vacuum at 225 °C for 1 h; (c, i) **1** powder heated in Ar at 225 °C for 10 h; (c, ii) after exposure to pure hydrogen at 50 °C for 1 h; and (c, iii) after exposure to pure hydrogen at 100 °C for 2 h.

The attenuation of the Cu^{+1} peak only (Figure 7.6b) implies that water preferentially adsorbs at the Cu^{+1} sites, and heating to 225 °C in vacuum increases the intensity of both the Cu^{+1} and Cu^{+2} peaks. For H_2 exposure at 50 °C, the Cu($2p_{3/2}$) spectrum does not change significantly (Figure 7.6c). However, exposure to H_2 at 100 °C increases the Cu^{+1}/Cu^{+2} ratio from 0.67 to 0.98, indicating either reduction of Cu^{+2} to Cu^{+1} or preferential adsorption of hydrogen at Cu^{+2} sites. Although slight broadening of the O(1s) peak is observed after heating in H_2 at 100 °C, PXRD analysis of the MOF sample confirmed its crystallinity (Figure C.9).

To understand the observed gaseous analyte−MOF dynamics, we probed analyte binding energies to Cu^{+2} and Cu^{+1} sites through DFT calculations. Optimization of the neutral cluster model (Figure C.12a) created from the crystallographically determined structure of **1** yields two Cu^{+2} ions separated by 2.54 Å. In agreement with earlier computational studies,[48,57,58] the ground state of this paddle wheel unit is found to be an open-shell singlet, antiferromagnetic state (Cu↑···Cu↓). The ferromagnetic state and the closed shell δ-bond state are less stable than the antiferromagnetic state by 3 and 125.2 kJ/mol, respectively. Adsorption of gas molecules (H_2O, O_2, CO, and H_2) are initially considered on one of these Cu^{+2} sites of the neutral cluster model. Table 7.1 summarizes the adsorption energies calculated at B3LYP-D3/def2-TZVPP level of theory, and the optimized structures are provided in the Supporting Information (Figure C.12b−e). We note that the contribution of basis set superposition error (BSSE) to the calculated adsorption energies at this level of theory is about 1−6 kJ/mol depending on the adsorption strength. On the two Cu^{+2} ions in the neutral cluster model of $Cu_2(BTC)_4$ the natural charges are determined to be +1.35e per copper cation. Our calculated adsorption

Table 7.1: Calculated Adsorption Energies (E_{ads}) and Natural Charges (q) for the Adsorption of Different Gas Molecules on the Cu^{+2}/Cu^{+2} Dimer of the Neutral $Cu_2(BTC)_4$ Unit and Cu^{+1}/Cu^{+2} Dimer of the Negatively Charged $Cu_2(BTC)_4$ Unit

	$Cu_2(BTC)_4$			$Cu_2(BTC)_4^{-1}$		
	E_{ads} (kJ/mol)[a]	q_{Cu1} (e)	q_{Cu2} (e)	E_{ads} (kJ/mol)[a]	q_{Cu1} (e)	q_{Cu2} (e)
$Cu_2(BTC)_4$	--	+1.35	+1.35	--	+0.80	+1.38
$Cu_2(BTC)_4\ldots OH_2$	-53.63	+1.37	+1.35	-75.85	+0.81	+1.38
$Cu_2(BTC)_4\ldots O_2$	-8.84	+1.34	+1.35	-21.84	+1.08	+1.37
$Cu_2(BTC)_4\ldots CO$	-29.23	+1.32	+1.36	-63.84	+0.94	+1.37
$Cu_2(BTC)_4\ldots H_2$	-12.56	+1.35	+1.35	-6.81	+0.81	+1.38
$Cu_2(BTC)_4\ldots H$	-57.76	+0.84	+1.36	--	--	--

energy of a H_2O molecule on this neutral cluster (−53.63 kJ/mol) is in close agreement with the adsorption energies calculated with a smaller $Cu_2(HCOO)_4$ cluster at the CCSD(T)/CBS level of theory (−51.2 kJ/mol)[59] as well as with a periodic model calculated at PW91-GGA level of theory (−47.3 kJ/mol).[57] The interaction of CO, O_2, and H_2 with this Cu^{+2} site is calculated to be much weaker than H_2O, as suggested by much lower adsorption energies as well as very minimal changes in the Cu···Cu distance and natural charges on the Cu atoms compared to the clean cluster model (Table 7.1 and Figure C.12).

Since our experimental XPS data strongly suggests the presence of Cu^{+1} ions in the $Cu_3(BTC)_2$ system, we next examined the adsorption of these gas molecules on a Cu^{+1} site. In our model, the Cu^{+1} site is created by adding an electron to the neutral $Cu_2(BTC)_4$ model. This is justified by the fact that the conversion of Cu^{+2} to Cu^{+1} in the MOF is induced by its exposure to the X-ray source and charge neutralizer which could provide

the extra electrons. Optimization of the cluster model with an additional electron converges to a structure with mixed Cu^{+1}/Cu^{+2} sites with small changes in the overall geometry (Figure C.17a). The Cu···Cu distance in the negatively charged cluster model is increased to 2.69 Å, and the Cu^{+1} ion is bound to only two oxygen atoms of the BTC units. The calculated charges listed in Table 7.1 clearly indicate that one of the copper ions is reduced to Cu^{+1} (q_{Cu} = +0.80e). The minimum-energy structures calculated for the adsorption of gas molecules at the Cu^{+1} site are illustrated in Appendix C (Figure C.17b−e). The Cu···Cu and Cu−X (X =H_2O, O_2, CO, and H_2) distances shown in Figure C.17 and the adsorption energies listed in Table 7.1 provide clear evidence of strong adsorption of these gas molecules at the Cu^{+1} site compared to the Cu^{+2} site of the neutral cluster model. Zhou et al.[60] also reported such enhanced binding of CO and O_2 on the negatively charged $Cu_2(BTC)_4$ model compared to the neutral system using DFT-GGA and LDA levels of theory. In contrast, the H_2 molecule prefers to interact with the Cu^{+2} site rather than Cu^{+1} site although the interaction is very weak in both cases. These results are in good agreement with the trend observed from our experimental data. XPS data reveal that the exposure of **1** to O_2 and CO decreases the intensity of the Cu^{+1} peak. In accordance with this observation, computations predict an increase in the positive charge on Cu^{+1} ion from +0.80e to +1.08e and +0.94e in the case of O_2 and CO adsorption, respectively. This again confirms the chemisorptive nature of the interaction of these gas molecules with the Cu^{+1} ion, which transfers electrons from Cu to the gas molecules. While the H_2O molecule also binds strongly at the Cu^{+1} site with a Cu− OH_2 bond distance of 1.96 Å, the calculations do not predict any change in the charge of the Cu ions.

XPS data further indicate that the exposure of **1** to H_2 at 100 °C increases the Cu^{+1}/Cu^{+2} ratio from 0.67 to 0.98. Our calculations suggest that the H_2 molecule is weakly physisorbed on both the Cu^{+2} and Cu^{+1} sites, which do not affect the structural or electronic properties of the $Cu_2(BTC)_4$ cluster. In order to elucidate the experimental observations in the presence of H_2, we computed the adsorption of an H atom on the neutral cluster model. Our calculations predict that the H atom prefers to bind to the carboxylate oxygen by breaking the Cu−O bond and reducing the neighboring copper cation from Cu^{+2} to Cu^{+1} (Figure C.12f). The adsorption energy calculated with reference to the energy of a half H_2 molecule is found to be −57.76 kJ/mol, and the optimized structure is similar to the negatively charged $Cu_2(BTC)_4$ cluster. This explains the increased reduction of Cu^{+2} observed experimentally upon exposure to H_2. In addition, the slight broadening of O(1s) peak observed on exposure to H_2 could be due to the bonding of H to the carboxylate oxygen rather than the copper cation.

Valence Band Structure Studies

XPS experiments also addressed changes in the electronic properties of the MOFs upon heating. Valence band spectra (Figure 7.7a) demonstrate that **1** becomes more conductive after heating to 225 °C for 14 h since there is a pronounced increase in intensity near the Fermi edge for the heated MOF, which consists primarily of Cu^{+1}. Subsequent exposure to oxygen decreases the intensity at the Fermi edge, and this behavior is consistent with the oxidation of Cu^{+1} back to the less conductive Cu^{+2} and readsorption of O_2 on Cu^{+1} sites. In contrast to **1**, the valence band spectra for **2** (Figure 7.7b) does not change significantly after heating to 225 °C, but it should be noted that **1** contains mostly Cu^{+1} whereas **2** has a significant fraction of Cu^{+2}. After exposure to O_2,

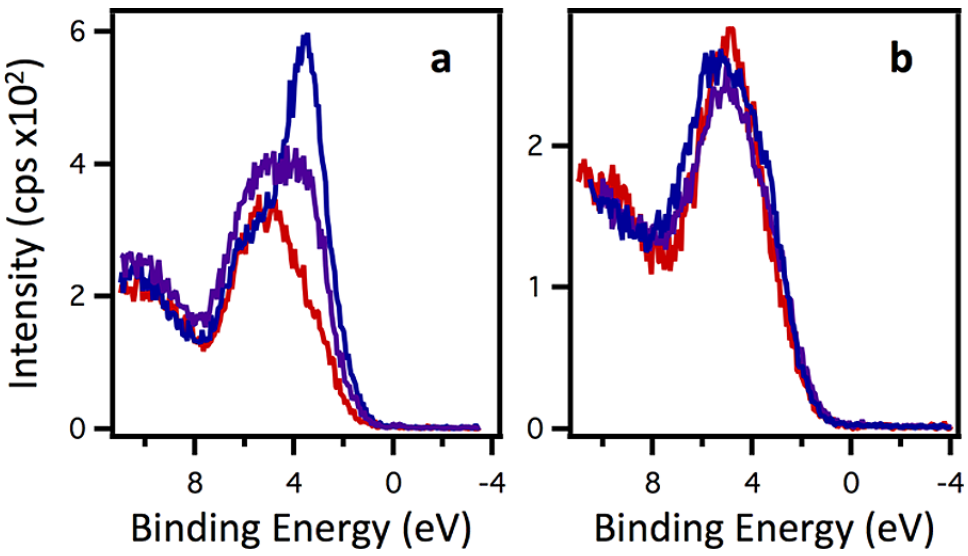

Figure 7.7: XPS data for the valence band region for (a) **1** powder: as-received (red), heated in Ar at 225 °C for 14 h (blue), and exposed to pure oxygen at room temperature for 2 h (purple); and (b) **2** powder: as-received (red), heated in Ar at 200 °C for 14 h (blue), and exposed to pure oxygen at room temperature for 2 h (purple).

the valence band spectrum of **2** closely resembles the spectrum before heating, and this is consistent with the similar Cu^{+1}/Cu^{+2} ratios observed in the $Cu(2p_{3/2})$ region. To rationalize the observed changes in the valence band region, the density of states (DOS) of a $Cu_2(BTC)_4$ cluster was investigated by DFT calculations. The neutral cluster is used to examine the DOS of exclusively Cu^{+2} sites, and the structures of a H atom adsorbed on the neutral cluster and the negatively charged $Cu_2(BTC)_4$ cluster are used to probe the DOS of mixed-valence Cu^{+1}/Cu^{+2} metal sites. As shown in Figure 7.8a, the DOS of the neutral $Cu_2(BTC)_4$ with Cu^{+2} ions is characteristic of a wide band gap insulator with a band gap of 3.8 eV, and the Fermi level is mostly dominated by the electronic contribution from oxygen atoms. This agrees well with the recently reported DOS calculated with a periodic model of $Cu_3(BTC)_2$ employing the HSE06 hybrid functional.[58]

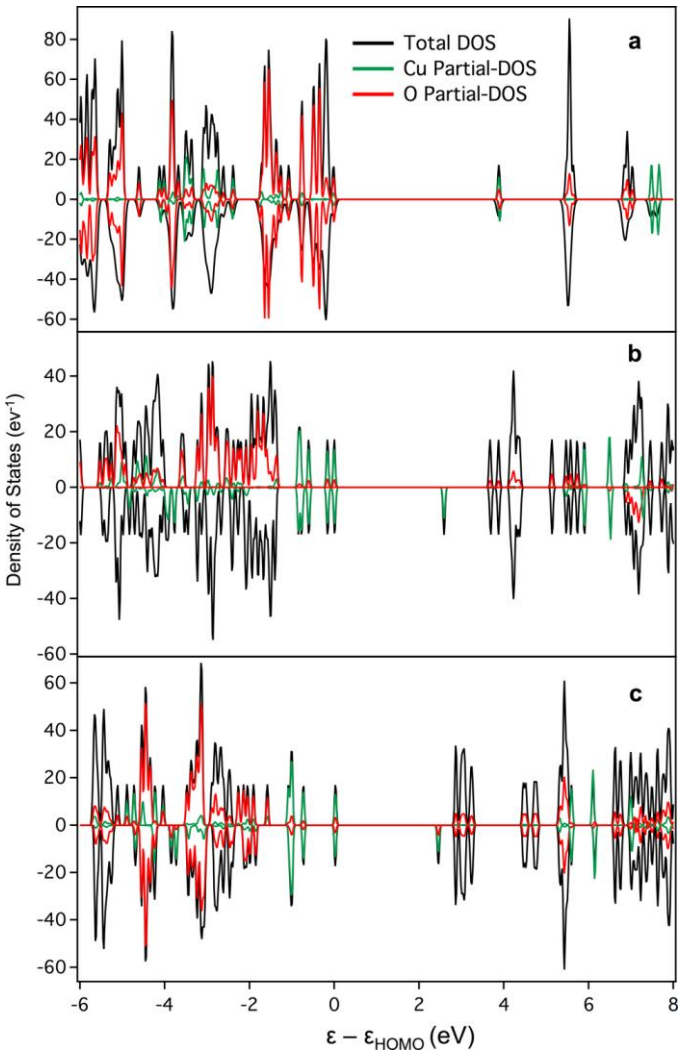

Figure 7.8: Total and partial density of states (DOS) of (a) neutral $Cu_2(BTC)_4$, (b) H atom adsorbed on the neutral $Cu_2(BTC)_4$, and (c) negatively charged $Cu_2(BTC)_4$ cluster models computed using the B3LYP-D3//def2-TZVPP level of theory.

When we have the mixed Cu^{+1}/ Cu^{+2} sites, as shown in Figures 7.8b and 7.8c, the band gap is reduced, and a midgap state appears at around 2.5 eV in both cases. This gap state and the Fermi level are dominated by electronic contribution from the copper cations rather than oxygen atoms. Thus, the MOFs with mixed Cu^{+1}/Cu^{+2} sites could become

more conductive through an electron hopping mechanism. This result is in full agreement with the experimental changes observed in the valence band region by XPS. In addition, these findings are in line with the very recent conductivity measurements of the Cu(I)-containing MOFs performed by Cheetham and co-workers.[61] Interestingly, there are only a few MOFs known to date exhibiting conductivity comparable with semiconducting polymers despite the fact that the highly ordered MOF structures should be beneficial for charge transport. The insulating nature of MOF-based materials could be explained by several factors, including high localization of organic states and weak hybridization with the metal nodes. The integrated XPS studies and DFT calculations presented here could potentially open new directions for modeling and tuning conductivity in typically insulating MOF materials.

7.4 CONCLUSIONS

The results from these investigations demonstrate the ability to achieve extensive reduction of Cu^{+2} to Cu^{1+} at MOF metal nodes, accompanied by a change in the valence band structure of the material. XPS measurements coupled with DFT calculations establish that selective adsorption of gas molecules occurs as a function of the oxidation state of the UMS. The combined XPS and DFT studies also reveal that introduction of mixed valence copper sites changes the electronic properties of the MOF; specifically, the increased density of states near the Fermi edge observed for the reduced MOF should lead to higher conductivity. Thus, these studies open a new avenue for potentially enhancing electron transport by accessing mixed valence states in the typically insulating crystalline frameworks.

7.5 REFERENCES

(1) Kapelewski, M. T.; Geier, S. J.; Hudson, M. R.; Stu, D.; Mason, J. A.; Nelson, J. N.; Xiao, D. J.; Hulvey, Z.; Gilmour, E.; Fitzgerald, S. A.; Head-Gordon, M.; Brown, C. M.; Long, R. *J. Am. Chem. Soc.*, **2014**, *136*, 12119.

(2) Getman, R. B. *Nat. Chem.*, **2012**, *4*, 777.

(3) Dietzel, P. D. C.; Besikiotis V.; Blom, R. *J. Mater. Chem.*, **2009**, *19*, 7362.

(4) Rowsell, J. L. C.; Yaghi, O. M. *J. Am. Chem. Soc.*, **2006**, *128*, 1304.

(5) Wang, C.; Liu, D.; Lin, W. *J. Am. Chem. Soc.*, **2013**, *135*, 13222.

(6) Fei, H.; Cohen, S. M. *J. Am. Chem. Soc.*, **2015**, *137*, 2191.

(7) Bae, Y.-S.; Farha, O. K.; Spokoyny, A. M.; Mirkin, C. A.; Hupp, J. T.; Snurr, R. Q. *Chem. Commun.*, *2008*, 4135.

(8) Sculley, J.; Yuan. D.; Zhou, H.-C. *Energy Environ. Sci.*, **2011**, *4*, 2721.

(9) Mishra, P.; Edubilli, S.; Mandal, B.; Gumma, S. *J. Phys. Chem. C*, **2014**, *118*, 6847.

(10) Li, B.; Zhang, Y.; Ma, D.; Li, L.; Li, G.; Li, G.; Shi, Z.; Feng, S. *Chem. Commun.*, **2012**, *48*, 6151.

(11) Ma, J.-P.; Zhao, C.-W.; Wang, S.-Q.; Zhang, J.-P.; Niu, X.; Dong, Y.-B. *Chem. Commun.*, **2015**, DOI 10.1039/c5cc04268b.

(12) Elsaidi, S. K.; Mohamed, M. H.; Wojtas, L.; Chanthapally, A.; Pham, T.; Space, B.; Vittal, J. J.; Zaworotko, M. J. *J. Am. Chem. Soc.*, **2014**, *136*, 5072.

(13) Eddaoudi, M.; Sava, D. F.; Eubank, J. F.; Adil, K.; Guillerm, V. *Chem. Soc. Rev.*, **2015**, *44*, 228.

(14) Wang, Y.; Yang, J.; Li, Z.; Zhang, Z.; Li, J.; Yang, Q.; Zhong, C. *RSC Adv.*, **2015**, *5*, 33432.

(15) Peng, X.; Lin, L.-C.; Sun, W.; Smit, B. *AIChE J.*, **2015**, *61*, 677.

(16) Koh, H. S.; Rana, M. K.; Wong-Foy, A. G.; Siegel, D. J. *J. Phys. Chem. C*, **2015**, *119*, 13451.

(17) Chen, L.; Morrison, C. A.; Düren, T. *J. Phys. Chem. C*, **2012**, *116*, 18899.

(18) Bloch, E. D.; Hudson, M. R.; Mason, J. A.; Chavan, S.; Crocella, V.; Howe, J. D.; Lee, K.; Dzubak, A. L.; Queen, W. L.; Zadrozny, J. M.; Geier, S. J.; Lin, L.;

Gagliardi, L.; Smit, B.; Neaton, B.; Bordiga, S.; Brown, C. M.; Long, R. *J. Am. Chem. Soc.*, **2014**, *136*, 10752.

(19) Dincă, M.; Long, J. R. *Angew. Chemie Int. Ed.*, **2008**, *47*, 6766.

(20) Shustova, N. B.; Cozzolino, A. F.; Reineke, S.; Baldo, M.; Dincă, M. *J. Am. Chem. Soc.*, **2013**, *135*, 13326.

(21) Ren, H.-Y.; Yao, R.-X.; Zhang, X.-M. *Inorg. Chem.*, **2015**, *54*, 6312.

(22) Yepez, R.; García, S.; Schachat, P.; Sánchez-Sánchez, M.; González-Estefan, J. H.; González-Zamora, E.; Ibarra, I. A.; Aguilar-Pliego, J. *New J. Chem.*, **2015**, *39*, 5112.

(23) Horike, S.; Dinca, M.; Tamaki, K.; Long, J. R. *J. Am. Chem. Soc.*, **2008**, *130*, 5854.

(24) Tenney, S. A.; Ratliff, J. S.; Roberts, C. C. ; He, W.; Ammal, S. C.; Heyden, A.; Chen, D. A. *J. Phys. Chem. C*, **2010**, *114*, 21652.

(25) Galhenage, R. P.; Ammal, S. C.; Yan, H.; Duke, A. S.; Tenney, S. A.; Heyden, A.; Chen, D. A. *J. Phys. Chem. C*, **2012**, *116*, 24616.

(26) Tenney, S. A.; He, W.; Roberts, C. C.; Ratliff, J. S.; Shah, S. I.; Shafai, G. S.; Turkowski, V.; Rahman, T. S.; Chen, D. A. *J. Phys. Chem. C*, **2011**, *115*, 11112.

(27) Tao, F.; Grass, M. E.; Zhang, Y.; Butcher, D. R.; Aksoy, F.; Aloni, S.; Altoe, V.; Alayoglu, S.; Renzas, J. R.; Tsung, C.-K.; Zhu, Z.; Liu, Z.; Salmeron, M.; Somorjai, G. A. *J. Am. Chem. Soc.*, **2010**, *132*, 8697.

(28) Tao, F.; Grass, M. E.; Zhang, Y.; Butcher, D. R.; Renzas, J. R.; Liu, Z.; Chung, J. Y.; Mun, B. S.; Salmeron, M.; Somorjai, G. A. *Science*, **2008**, *322*, 932.

(29) Campbell, C. T. *Surf. Sci. Rep.*, **1997**, *27*, 1.

(30) Henry, C. R. *Surf. Sci. Rep.*, **1998**, *31*, 231.

(31) Besenbacher, F.; Nørskov, J. K. *Prog. Surf. Sci.*, **1993**, *44*, 5.

(32) Tao, F.; Dag, S.; Wang, L.-W.; Liu, Z.; Butcher, D. R.; Bluhm, H.; Salmeron, M.; Somorjai, G. A. *Science*, **2010**, *327*, 850.

(33) Hansen, P. L.; Wagner, J. B.; Helveg, S.; Rostrup-Nielsen, J. R.; Clausen, B. S.; Topsøe, *Science*, **2002**, *295*, 2053.

(34) Noei, H.; Amirjalayer, S.; Müller, M.; Zhang, X.; Schmid, R.; Muhler, M.; Fischer, R. A.; Wang, Y. *ChemCatChem*, **2012**, *4*, 755.

(35) Noei, H.; Kozachuk, O.; Amirjalayer, S.; Bureekaew, S.; Kauer, M.; Schmid, R.; Marler, B.; Muhler, M.; Fischer, R. A.; Wang, Y. *J. Phys. Chem. C*, **2013**, *117*, 5658.

(36) Denysenko, D.; Werner, T.; Grzywa, M.; Puls, A.; Hagen, V.; Eickerling, G.; Jelic, J.; Reuter, K.; Volkmer, D. *Chem. Commun.*, **2012**, *48*, 1236.

(37) Fu, Y.; Sun, D.; Qin, M.; Huang, R., Li, Z. *RSC Adv.*, **2012**, *2*, 3309.

(38) Liu, J.; Wang, Y.; Benin, A. I.; Jakubczak, P.; Willis, R. R.; LeVan, M. D. *Langmuir*, **2010**, *26*, 14301.

(39) Zhao, Y.; Padmanabhan, M.; Gong, Q.; Tsumori, N.; Xu, Q.; Li, J. *Chem. Commun.*, **2011**, *47*, 6377.

(40) Wagner, C. D.; Riggs, W. M.; Davis, L. E.; Moulder, J. F.; Muilenberg, G. E. Handbook of X-Ray Photoelectron Spectroscopy, Perkin Elmer Corporation: Eden Prairie, MN, 1978.

(41) Tahir, D.; Tougaard, S. *J. Phys. Condens. Matter*, **2012**, *24*, 175002.

(42) Ghijsen, J.; Tjeng, L. H.; van Elp, J; Eskes, H.; Westerink, J.; Sawatzky, G.; Czyzyk, M. *Phys. Rev. B. Condens. Matter*, **1988**, *38*, 11322.

(43) Sun, Y.-H.; Yu, J.-H.; Jin, X.-J.; Song, J.-F.; Xu, J.-Q.; Ye, L. *Inorg. Chem. Commun.*, **2006**, *9*, 1087.

(44) Gagne, R. R.; Allison, J. L.; Koval, C. A.; Mialki, W. S.; Smith, T. J.; Walton, R. A. *J. Am. Chem. Soc.*, **1980**, *102*, 1905.

(45) Deroubaix, G.; Marcus, P. *Surf. Interface Anal.*, **1992**, *18*, 39.

(46) Nijem, N.; Bluhm, H.; Ng, M. L.; Kunz, M.; Leone, S. R.; Gilles, M. K. *Chem. Commun.*, **2014**, *50*, 10144.

(47) Senthil Kumar, R.; Senthil Kumar S.; Anbu Kulandainathan, M. *Microporous Mesoporous Mater.*, **2013**, *168*, 57.

(48) St Petkov, P.; Vayssilov, G. N.; Liu, J.; Shekhah, O.; Wang, Y.; Wöll, C.; Heine, T. *ChemPhysChem*, **2012**, *13*, 2025.

(49) Szanyi, J.; Daturi, M.; Clet, G.; Baer, D. R.; Peden, C. H. F. *Phys. Chem. Chem. Phys.*, **2012**, *14*, 4383.

(50) Prestipino, C.; Regli, L.; Vitillo, J. G.; Bonino, F.; Damin, A.; Lamberti, C.; Zecchina, A.; Solari, P. L.; Kongshaug, K. O.; Bordiga, S. *Chem. Mater.*, **2006**, *18*, 1337.

(51) Alaerts, L.; Séguin, E.; Poelman, H.; Thibault-Starzyk, F.; Jacobs, P. A.; De Vos, D. E. *Chemistry*, **2006**, *12*, 7353.

(52) Yang, J.; Regier, T.; Dynes, J. J.; Wang, J.; Shi, J.; Peak, D.; Zhao, Y.; Hu, T.; Chen, Y.; Tse, J. S. *Anal. Chem.*, **2011**, *83*, 7856.

(53) Klaeui, W.; Lenders, B.; Hessner, B.; Evertz, K. *Organometallics*, **1988**, *7*, 1357.

(54) Pike, R. D. *Organometallics*, **2012**, *31*, 7647.

(55) Ugozzoli, F.; Manotti Lanfredi, A. M.; Marsich, N.; Camus, A. *Inorganica Chim. Acta*, **1997**, *256*, 1.

(56) Castillo, J. M.; Vlugt, T. J. H.; Calero, S. *J. Phys. Chem. C*, **2008**, *112*, 15934.

(57) Watanabe, T.; Sholl, D. S. *J. Chem. Phys.*, **2010**, *133*, 094509.

(58) Hendon, C.; Walsh, A. *Chem. Sci.*, **2015**, *6*, 3674.

(59) Grajciar, L.; Bludský, O.; Nachtigall, P. *J. Phys. Chem. Lett.*, **2010**, *1*, 3354.

(60) Zhou, C.; Cao, L.; Wei, S.; Zhang, Q.; Chen, L. *Comput. Theor. Chem.*, **2011**, *976*, 153.

(61) Tominaka, S.; Hamoudi, H.; Suga, T.; Bennett, T. D.; Cairns, A. B.; Cheetham, A. K. *Chem. Sci.*, **2015**, *6*, 1465.

APPENDIX A

SUPPLEMENTAL FOR CHAPTER 3

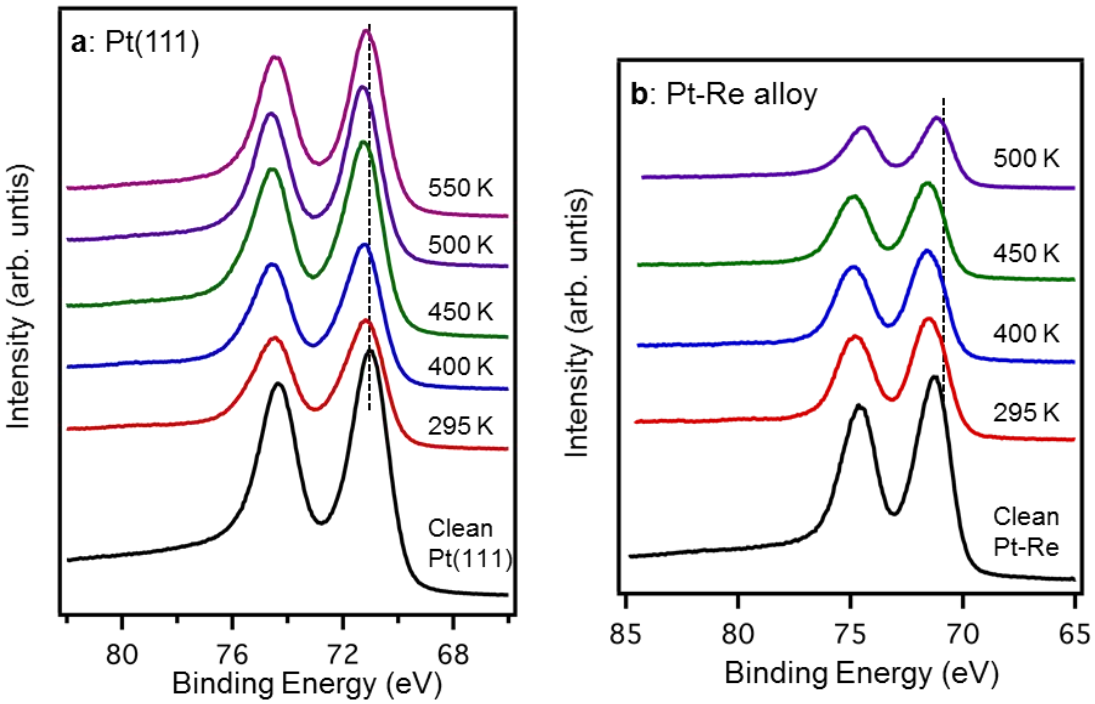

Figure A.1: X-ray photoelectron spectroscopy data for the Pt(4f) region for: a) Pt(111) and b) the Pt-Re alloy surface prepared by depositing 3.3 ML Re on Pt(111) and heating to 1000 K for 5 min. Spectra are shown for the surfaces immediately after preparation in UHV (bottom); and after heating in 500 mTorr O_2/50 mTorr CO to various temperatures (top). The incident photon energy was 545 eV.

APPENDIX B

SUPPLEMENTAL FOR CHAPTER 4

Supplemental 1

Calculation of fraction of Re in subsurface layers was based on the attenuation of the Re($4f_{7/2}$) peak after annealing the Re films to 1000 K to form the Pt-Re alloy surface. Using an incident beam energy of 303 eV and a Pt layer thickness of 2.263 Å, the mean free path was calculated to be 3.164 monolayers.[1] At a 20 degree off normal detection angle, the experimental attenuation of the Re($4f_{7/2}$) peak was consistent with 40±10% of Re in the 2nd subsurface layer and 60±10% in the 3rd subsurface layer for the 1.3 and 1.8 ML Re films annealed to 1000 K.

Supplemental 2

Mass spectrometer signals were corrected for contribution from the fragmentation of other products as follows:

1. The 16 amu signal assigned to methane was corrected for mass fragmentation at 16 amu from CO using a 16:28 ratio of 0.03, and from O_2 using a 16:32 ratio of 0.15.
2. The 28 amu signal assigned to CO was corrected for mass fragmentation from methanol using a 28:31 ratio of 0.1.
3. The 32 amu signal assigned to O_2 was corrected for mass fragmentation from methanol using a 31:32 ratio of 0.7.

These ratios were determined from the NIST Database[2] and fragmentation patterns for pure CO using a quadrupole mass spectrometer (Hiden) in our laboratory.[3] In the case of 31:32 for methanol and 16:28 for CO, the NIST and measured values were identical. For 28:31 in methanol, an average of the NIST and measured ratios was used. For 16:32 in O_2, limited data was available from the mass spectrometer on the X1A1 endstation itself,

and an average of the X1A1 value, the NIST value, and the values carefully measured by the mass spectrometer in our laboratory was used.

(1) Surface Analysis: The Principal Techniques; Vickerman, J. C., Ed.; John Wiley and Sons: New York, 1997.

(2) Stein, S. E. NIST Standard Reference Database Number 69: NIST Chemistry WebBook; National Institute of Standards and Technology (NIST), 2011.

(3) Varazo, K.; Parsons, F. W.; Ma, S.; Chen, D. A. Methanol Chemistry on Cu and Oxygen-Covered Cu Nanoclusters Supported on TiO_2(110). *J. Phys. Chem. B* **2004** *108*, 18274-18283.

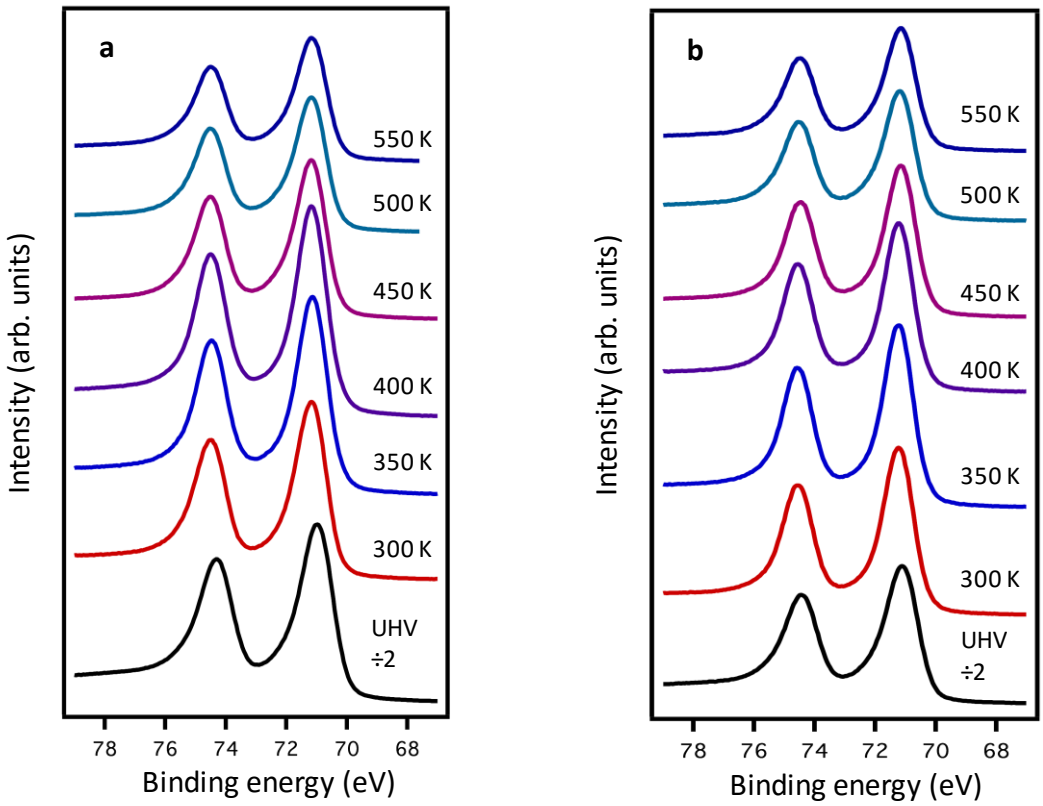

Figure B.1: APXPS data for the Pt(4f) region for the following surfaces heated to various temperatures under 200 mTorr of O_2 and 100 mTorr of methanol: a) Pt(111); and b) the Pt-Re alloy (1.3 ML Re). The incident photon energy was 303 eV.

APPENDIX C

SUPPLEMENTAL FOR CHAPTER 7

Table C.1: X-ray Structure Refinement Data for **2**[a].

compound	$Cu_5(NIP)_4(OH)_2(H_2O)_6]\cdot(H_2O)_5$
formula	$C_{32}H_{36}Cu_5N_4O_{37}$
FW	1386.35
T, K	100(2)
crystal system	Triclinic
space group	P-1
Z	1
a, Å	10.8179(10)
b, Å	11.4517(11)
c, Å	11.5461(11)
α, °	75.633(2)
β, °	62.674(2)
γ, °	62.097(2)
V, $Å^3$	1122.01(19)
$d_{calc,}$ g/cm^3	2.052
μ, mm^{-1}	2.457
F(000)	697.0
crystal size/mm^3	0.12 × 0.10 × 0.04
theta range	3.974 to 52.13
index ranges	$-13 \le h \le 13$ $-14 \le k \le 14$ $-13 \le l \le 14$
refl. collected	18149
data/restraints/parameters	4419/11/399
GOF on F^2	1.042
Largest peak/hole, e/$Å^3$	0.55/-0.38
R_1 (wR_2), %, [$I \ge 2sigma(I)$][c]	0.0331/0.0738

[a] Mo-K_α (λ = 0.71073 Å) radiation;
[b] Formula is given based on single-crystal X-ray data and does not include disordered solvent molecules (complete formula was determined based on elemental analysis);
[c] $R_1 = \Sigma||F_o| - |F_c||/ \Sigma |F_o|$, $wR_2 = \{ \Sigma [w(F_o^2-F_c^2)^2]/ \Sigma [w(F_o^2)^2]\}^{1/2}$

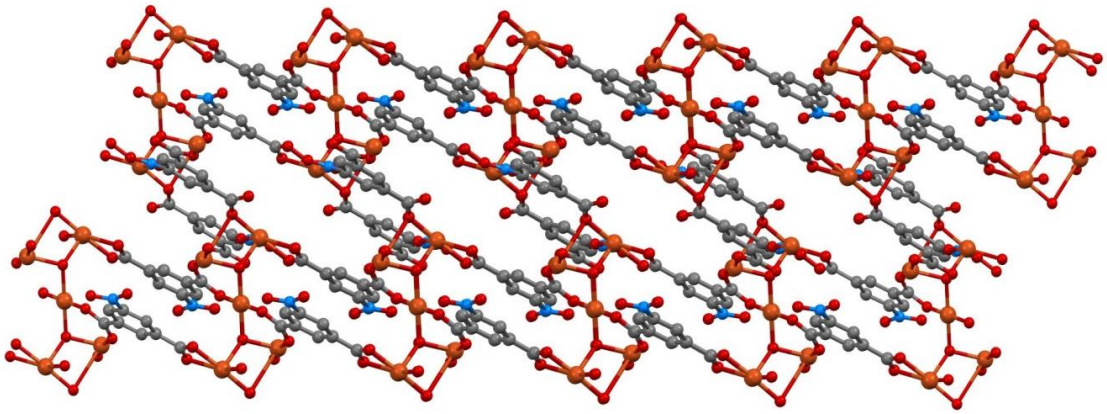

Figure C.1: The single-crystal X-ray structure of **2**. Orange, blue, grey, and red spheres represent copper, nitrogen, carbon, and oxygen atoms, respectively. The hydrogen atoms and solvent molecules are omitted for clarity.

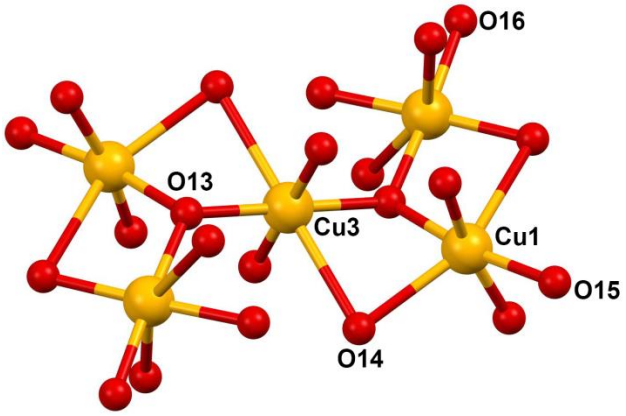

Figure C.2: The secondary building unit in **2**. The asymmetric unit consists of three copper atoms, one of which (Cu3) is located on a crystallographic inversion center, two $C_8H_3NO_6^{2-}$ ligands, one OH– group (O13), three coordinated water molecules (O14–O16), and three noncoordinated water molecules (O17–O19, Figure C.2). The interstitial water O19 is located on a crystallographic inversion center. Orange and red spheres represent copper and oxygen atoms, respectively.

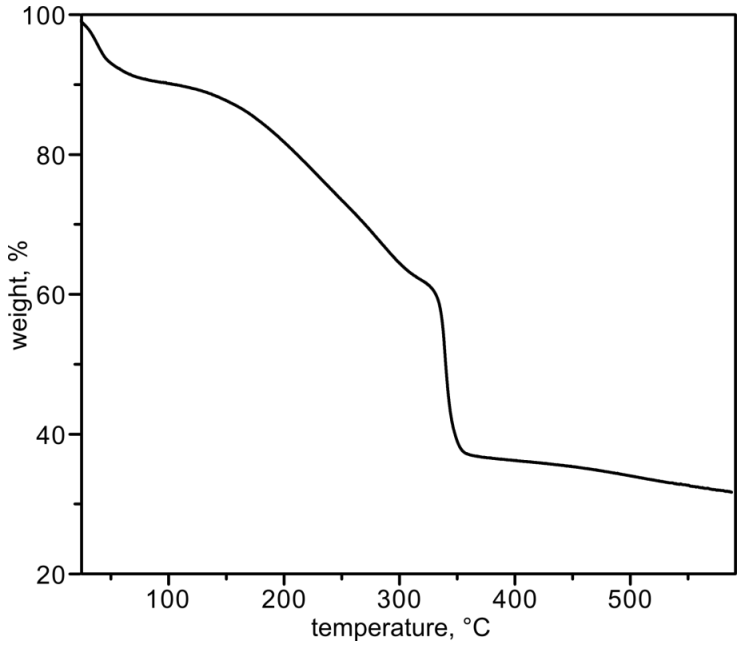

Figure C.3: Thermogravimetric analysis plot of **1**.

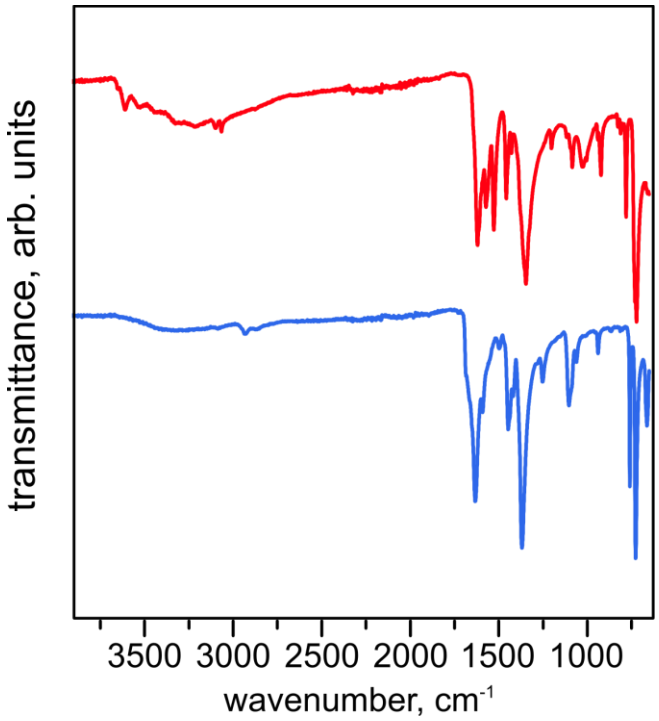

Figure C.4: FTIR spectra of **1** (——) and **2** (——).

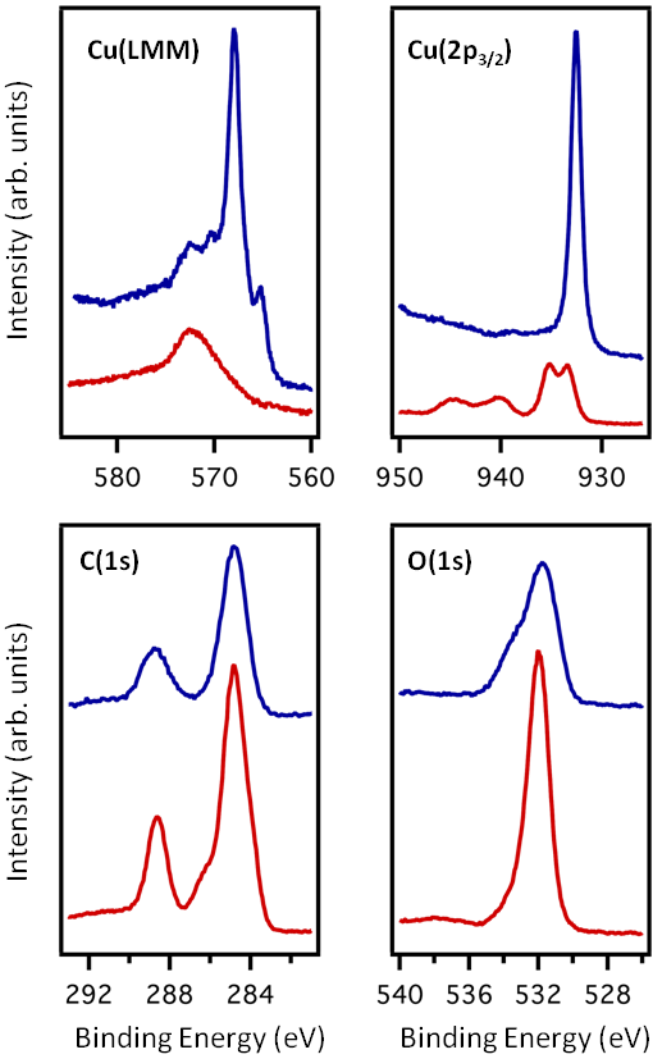

Figure C.5: XPS data for **1** pellet: as received (red); and after heating in flow of H_2 at 225 °C for 1 h (blue). The Cu(LMM) peak shape indicates that metallic Cu is formed after heating in H_2, and the Cu($2p_{3/2}$) peak at 932.6 eV is also consistent with metallic Cu. The C(1s) peak shape is not significantly changed after MOF reduction, whereas the 533.5 eV shoulder in the O(1s) spectrum suggests that another oxygen species is formed during reduction.

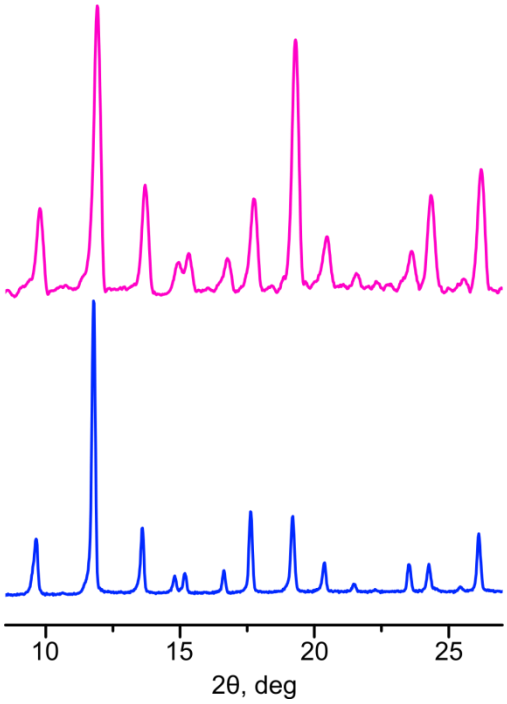

Figure C.6: The PXRD patterns of **1**: (*bottom*) as-synthesized and (*top*) after following successive treatments: heating in Ar at 225 °C for 14 h, exposing to O_2 at room temperature for 2 h, and heating in vacuum at 275 °C for 5 h.

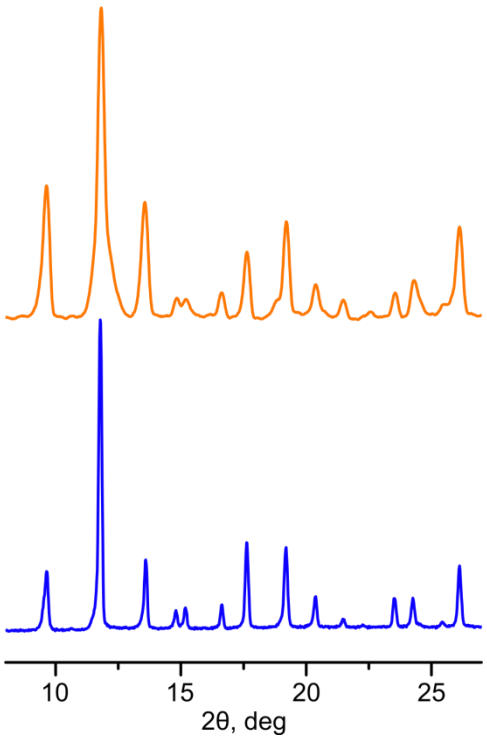

Figure C.7: The PXRD patterns of **1**: (*bottom*) as-synthesized and (*top*) after exposure to X-rays and the charge neutralizer for 110 min.

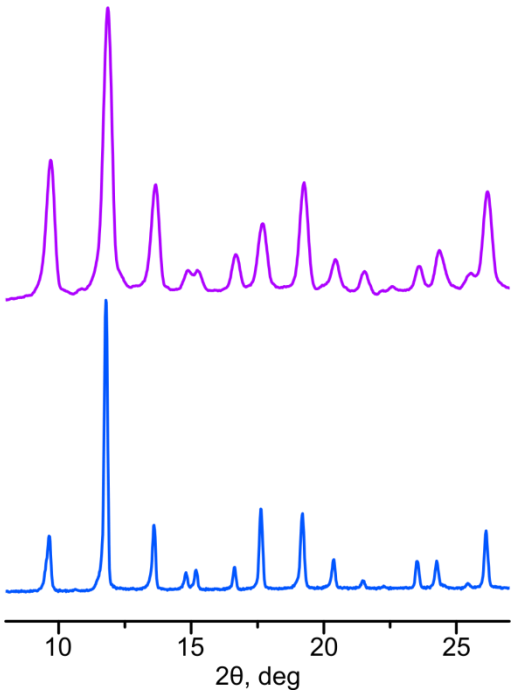

Figure C.8: The PXRD patterns of **1**: (*bottom*) as-synthesized and (*top*) after following successive treatments: heating in Ar at 225 °C for 14 h, exposure to CO at room temperature for 2 h, and heating in vacuum at 225 °C for 1 h.

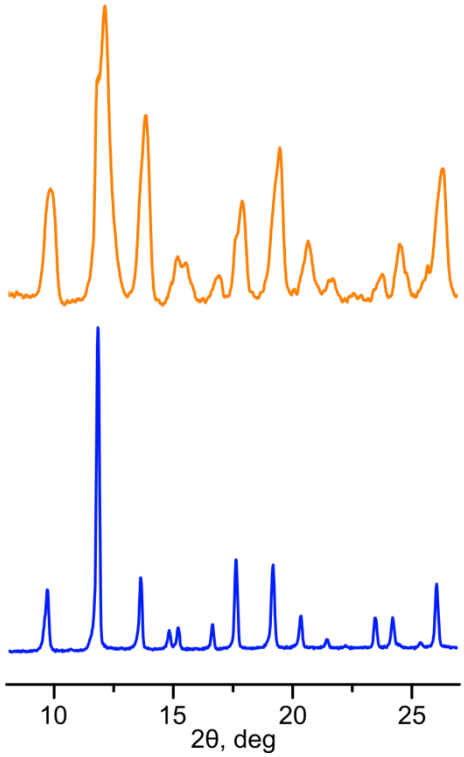

Figure C.9: The PXRD patterns of **1**: (*bottom*) as-synthesized and (*top*) after heating in Ar at 225 °C for 10 h, exposure to H_2 at 50 °C for 1 h, and exposure to H_2 at 100 °C for 2 h.

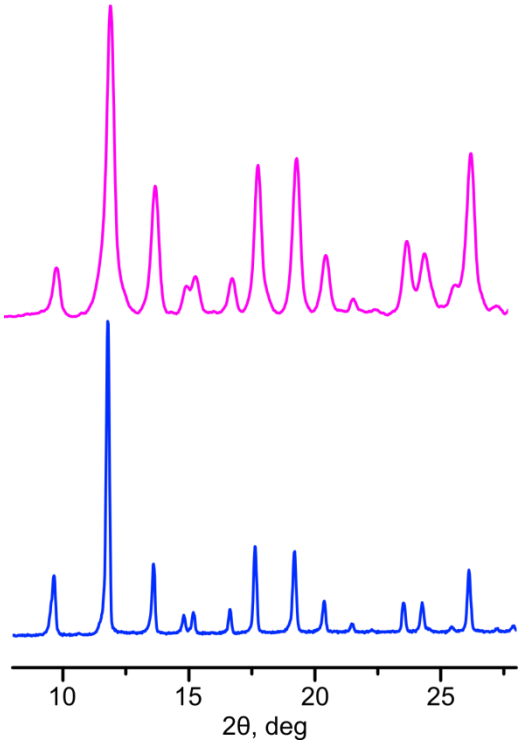

Figure C.10: The PXRD patterns of **1**: (*bottom*) as-synthesized and (*top*) after heating at 225 °C for 14 h, exposure to air at room temperature for 10–15 min, and heating in vacuum at 225 °C for 1 h.

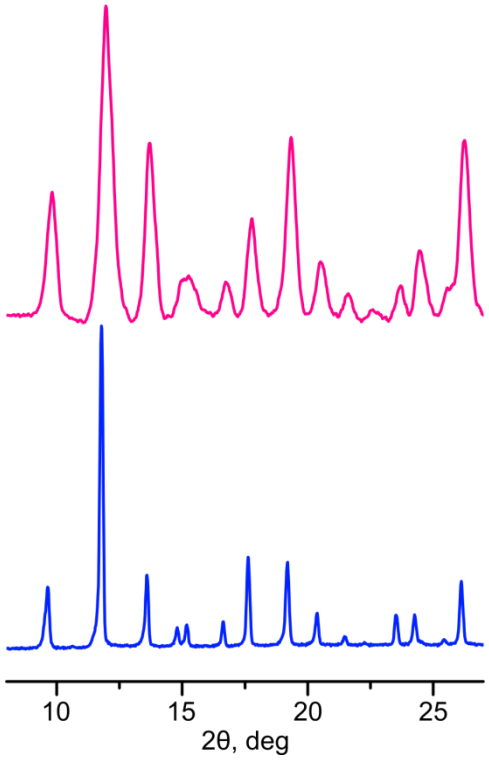

Figure C.11: The PXRD patterns of **1**: (*bottom*) as-synthesized and (*top*) after heating at 120 °C for 12 h and heating in vacuum at 225 °C for 35 h.

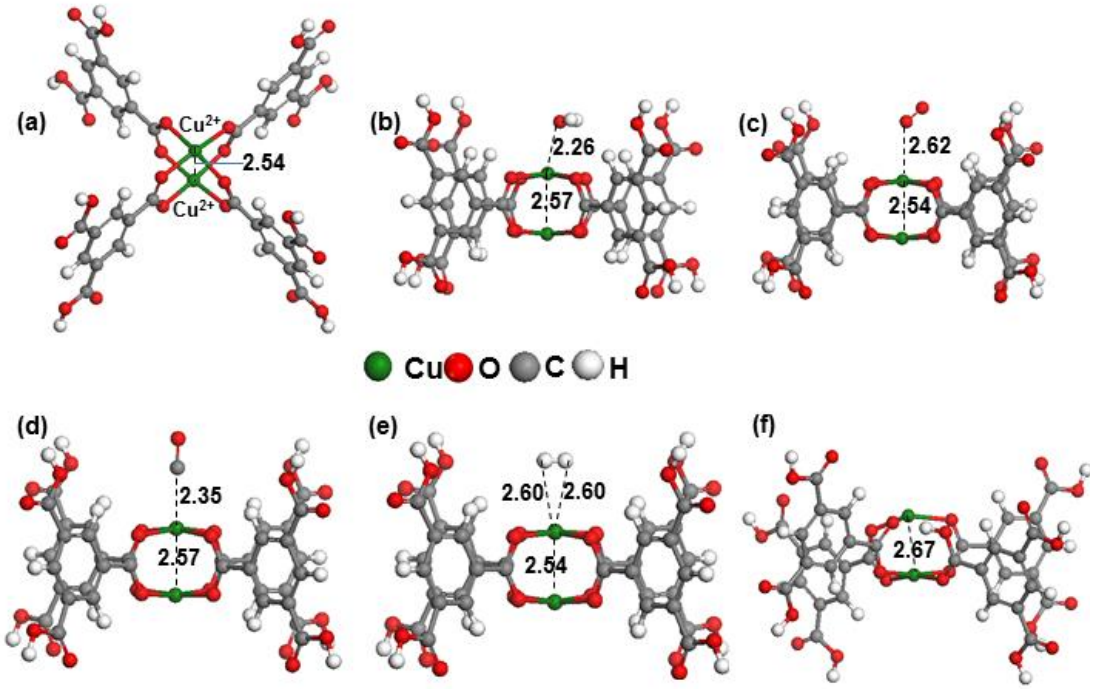

Figure C.12: (a) Optimized structure of neutral $Cu_2(BTC)_4$ cluster model. (b)-(e) Calculated minimum energy structures of H_2O (b), O_2 (c), CO (d), H_2 (e) adsorbed on the Cu^{2+} site of neutral $Cu_2(BTC)_4$ and H atom (f) adsorbed on the carboxylate oxygen. The bond distances are in Å.

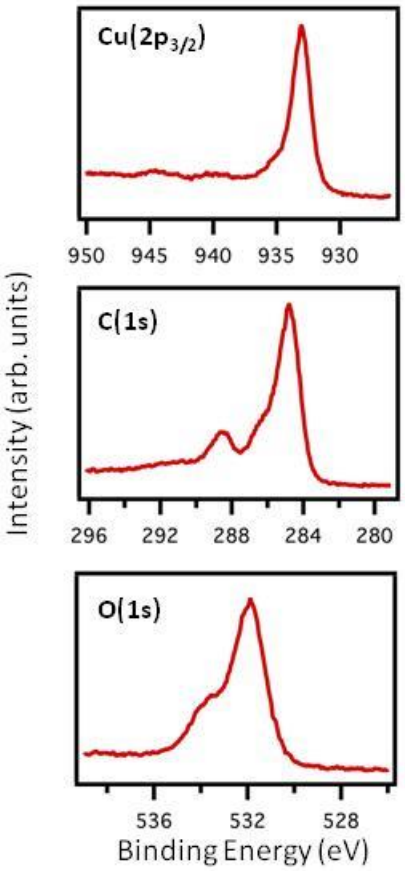

Figure C.13: XPS data for **1** powder heated in Ar in the catalysis cell for 35 h at 225 °C. The single Cu($2p_{3/2}$) peak at 933 eV demonstrates that only Cu^{+2} is present. The O(1s) shows a small shoulder at 533.5 eV that is associated with changes in the MOF during extensive heating, but PXRD studies on this sample indicate that the MOF is still crystalline. The ~286.5 eV shoulder in the C(1s) spectrum also appeared with heating but is sometimes observed on the as-received samples, as shown in Figure C.5 in red.

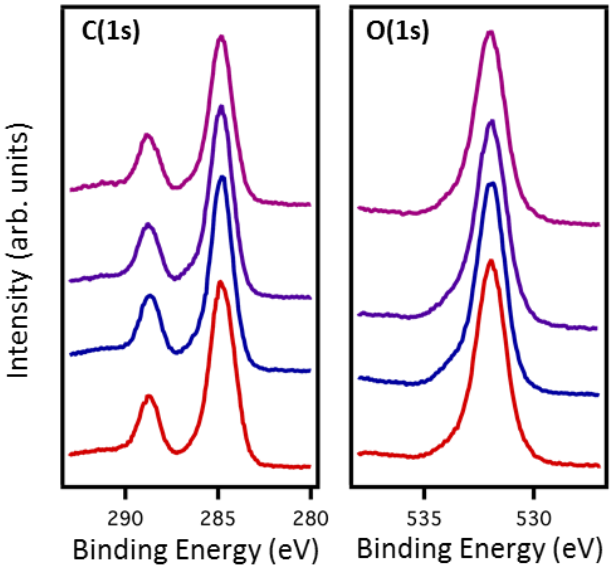

Figure C.14: XPS data for **1** powder: as received (red); after heating in Ar in the catalysis cell for 14 h at 225 °C (blue); after exposure to O_2 at room temperature for 2 h (purple); and after heating in vacuum at 275 °C for 5 h (pink).

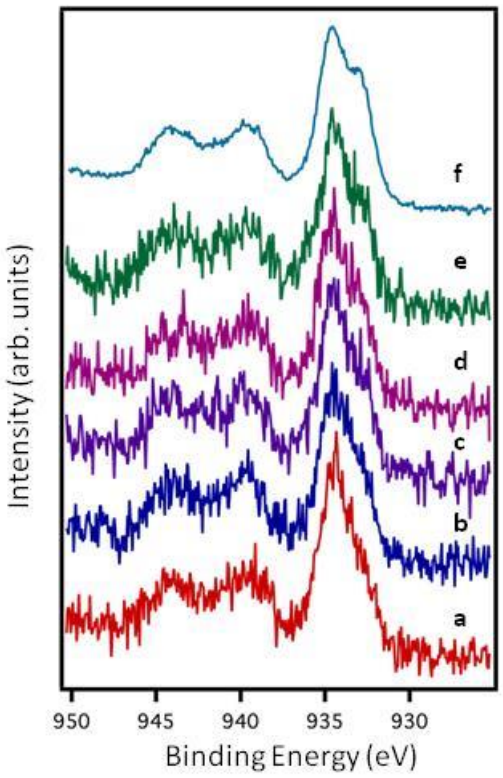

Figure C.15: XPS data for Cu($2p_{3/2}$) region for **1** in powder form after exposure to X-rays and the charge neutralizer for various times: a) 2 min; b) 3 min; c) 4 min; d) 5 min; e) 6 min; and f) 20 min. Scans (a–e) had 21 s acquisition times with 50 ms dwell times while scan (f) had a 10 min acquisition time with a 1600 ms dwell time.

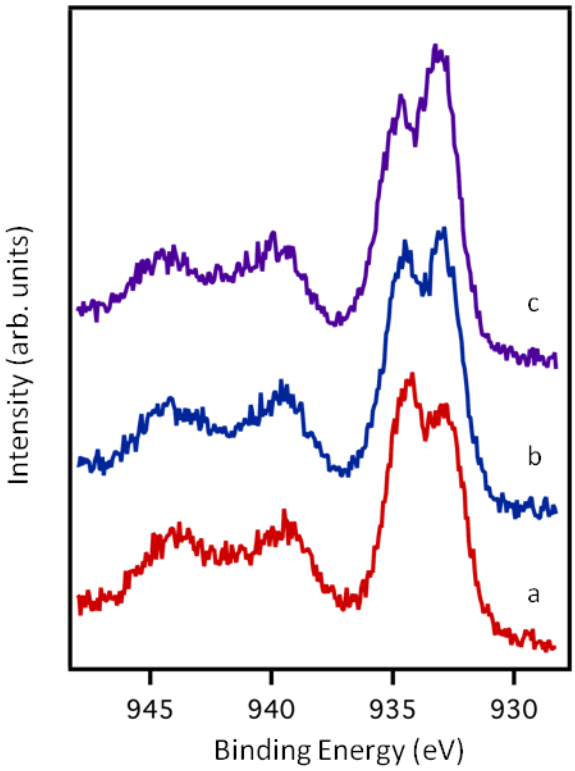

Figure C.16: XPS data for the Cu($2p_{3/2}$) region after the same **1** powder is successively exposed to the following: a) X-rays and the charge neutralizer for 45 min; b) the charge neutralizer only for 1 hour; and c) the charge neutralizer only for 1 h. The Cu^{+1}/Cu^{+2} ratio increased from 0.97 (a) to 1.18 (b) to 1.25 (c). Dwell times were 500 ms.

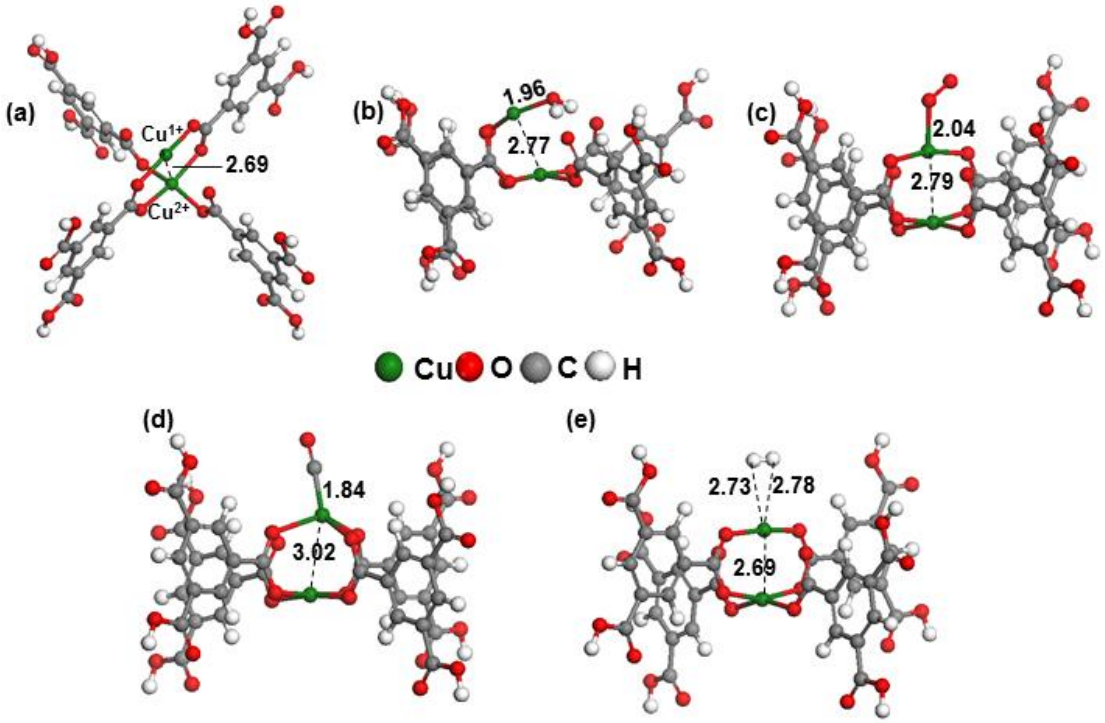

Figure C.17: (a) Optimized structure of negatively charged $Cu_2(BTC)_4$ cluster model. (b)-(e) Calculated minimum energy structures of H_2O (b), O_2 (c), CO (d), and H_2 (e) adsorbed on the Cu^{1+} site of negatively charged $Cu_2(BTC)_4$. The bond distances are in Å.

APPENDIX D

DESIGN FOR AN *IN SITU* IRAS SYSTEM

The primary function of the Leybold chamber is to perform experiments that bridge the "pressure gap" between UHV and ambient pressure. Model surfaces can be prepared and characterized via LEED, AES, and XPS before and after reaction in the atmospheric pressure microreactor coupled to the chamber without exposure to air. Recently, a second high pressure IR cell has been added to the chamber in order to conduct infrared reflection-absorption spectroscopy (IRAS) experiments on the same model surfaces for identifying reaction intermediates on the surface and for probing adsorbate binding sites. In this design, IRAS can be performed under UHV as a post-mortem for samples which have been treated in the microreactor, or the IR cell can be closed off to the rest of the UHV chamber and filled up to ~1 Torr of gas for performing IRAS *in situ*.

The IR cell

The IR cell highlighted by the red rectangle in Figure D.1 is a 6-port (4.5" CF (2); 2.75" CF (5)) stainless steel cube that connects the manipulator arm to the rest of the UHV chamber via the two 4.5" CF ports on either end. The top port of the cell must always be a viewport or window, enabling the user to inspect the sample position in the

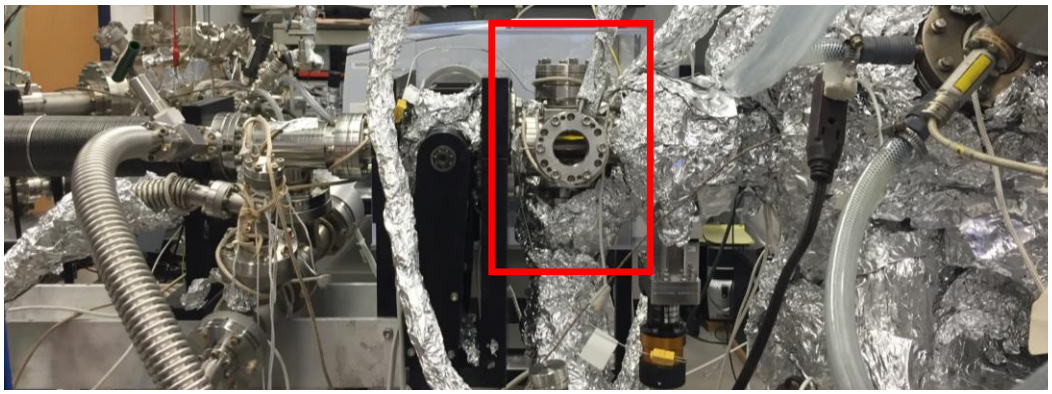

Figure D.1: IR cell.

cell visually. The two side ports of the cell are differentially-pumped BaF_2 windows, which have been described elsewhere, for allowing entrance and exit of the IR beam. The bottom port of the cell will be connected to a 2.75" CF 4-way cross, which will be connected at the horizontal ports to a 2.75" CF all-metal gate valve, which is connected to a turbo pump (Leybold Heraeus, TMP 150), and a 1.33" variable leak valve, which is connected to the chamber's gaslines. The bottom port of the 4-way cross will connect to a 5-way cross. One port of the 5-way cross will connect to a 2.75" CF nipple on which will be attached a nude ionization gauge (Agilent Technologies, UHV-24, 2.75" CF) for measuring pressures below 1 x 10^{-5} Torr. On the port directly opposite this gauge will be a digital capacitance diaphragm gauge (Inficon, CDG025D, 1.33" CF) for measuring pressures between 1 mTorr and 1 Torr. One or both of the two remaining ports on the 5-way cross can be connected to separate variable leak valves for introducing multiple gases to the cell.

The beam path

The infrared source comes from a Bruker Tensor 27 benchtop spectrometer equipped with a SiC globar for mid-infrared (MIR) measurements and a tungsten halogen lamp for extension into the near-infrared (NIR) range. The KBr beamsplitter also has an extended range for use in the NIR. The spectrometer is controlled remotely via the OPUS 6 software, and its status can be monitored through the software or by browsing for its physical IP address. Using the OPUS software, the user can operate the source through the spectrometer's sample compartment into the internal deuterated triglycine sulfate (DTGS) detector, but in order to perform IRAS experiments, the source must be directed through the right exit port of the spectrometer. Linus rails connect the exit port to a gold-

coated flat mirror, which deflects the IR beam at a 90° angle to a gold-coated parabolic mirror. The gold-coated parabolic mirror, which is used to direct the beam onto the sample in the IR cell, is connected via a separate set of Linus rails to a plastic disk as shown in Figure D.2. The plastic disk contains a set of 4 long screws which pass through it from the side with the parabolic mirror to the chamber side of the disk. These long screws are exactly the right length to pass through 4 holes in a photoelastic modulator (PEM) head, which contains a ZnSe crystal, before threading into an aluminum flange which should be pre-mounted to the outer stainless steel flange of the first of the two differentially-pumped BaF_2 windows. The beam reflects off the sample, which is rotated

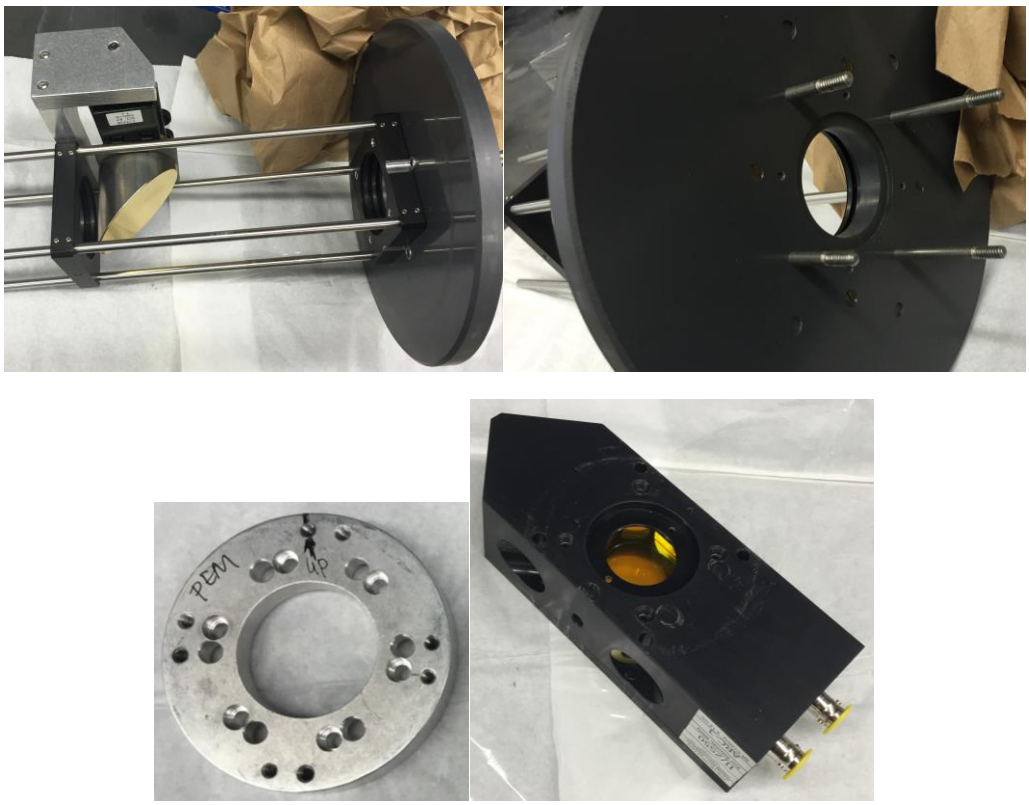

Figure D.2: Dark gray plastic disk for mounting parabolic mirror (Top left) to aluminum flange (Bottom left) on chamber with long screws (Top right) to accommodate PEM head (Bottom right).

~3° in the direction of the incident beam, and the reflected beam passes through the second of the two differentially-pumped BaF_2 windows. A second aluminum flange must be pre-bolted to the outer stainless steel flange of the second window in order to hold a third set of 4 Linus rails. On the Linus rails, a ZnSe focusing lens on a translation stage is placed after the aluminum flange to focus the reflected IR beam onto the chip in the liquid nitrogen cooled mercury cadmium tellurite (LN-MCT) detector, which is also secured in place on the Linus rails (Figure D.3).

The beam path and sample holder position were initially aligned using an infrared camera (FLIR) mounted on the outside of the second BaF_2 window to ensure the IR beam was properly focused onto and reflected off of a Pt(111) crystal in the sample holder. Then the IR camera was removed, and the focusing lens and LN-MCT assembly were mounted. The reflected IR beam was focused onto the detector element by adjusting the translation stage of the focusing lens to maximize the intensity of the signal centerburst in the OPUS software.

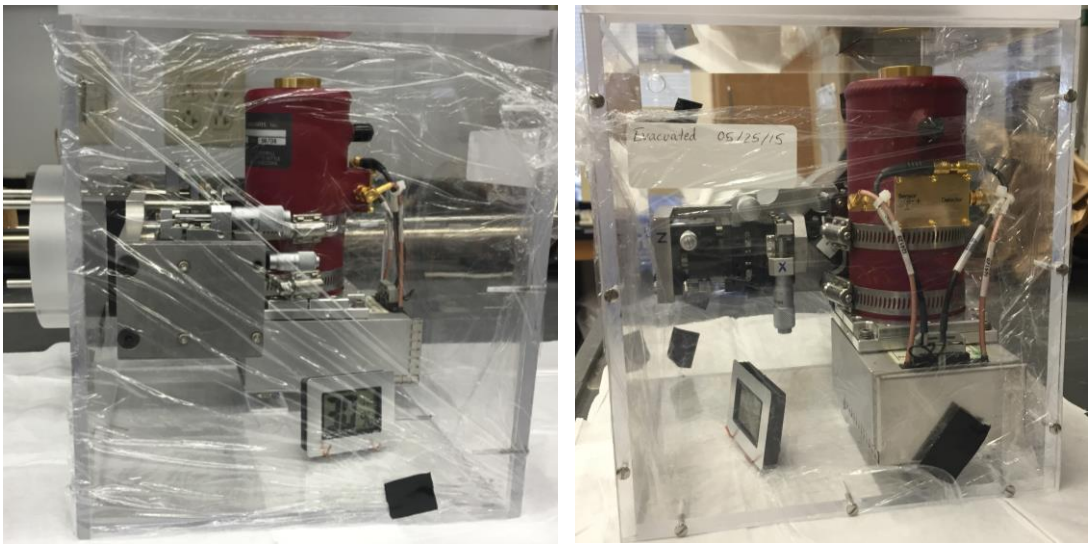

Figure D.3: LN-MCT detector assembly. Side view (Left); Rear view (Right)

Purging the beam path

The entire system is purged from an 80 psi supply of N_2(g) from liquid nitrogen boil-off. Since the spectrometer contains delicate equipment, the nitrogen is fed in via a ball valve which regulates the flow to 250 L/min into the spectrometer. The beam path is encased in two separate purge boxes, one on either side of the UHV chamber. Each box contains its own temperature and humidity sensor.

The beam path from the spectrometer to the first BaF_2 window is covered with 5 walls of a plexiglass box. The sixth wall is missing, and a sheet of plastic covers the gap between the box and the first BaF_2 window. Gaps in the box are filled with weatherstripping. The entire detector assembly was encased in a plexiglass purge box with small holes for the N_2 purge gas tube and detector power cable as well as a removable lid for adding liquid nitrogen to the LN-MCT at the start of an experiment (see Figure D.3). The openings in the box are completely covered with plastic wrap to improve the quality of the purge. The back of the detector purge box is attached by several small screws but is also removable so that the dewer of the LN-MCT can be pumped down periodically by the TMP 150. While the dewer was originally rated to hold vacuum for much longer, a crack in the BaF_2 window of the detector causes the dewer to leak air slowly over time. Celvaseal was applied to the outer edge of the window to minimize the leak, but it did not seal it completely. No further Celvaseal could be applied without compromising the transparence of the window.

High-pressure experiments

In its normal configuration, the IR cell is pumped by the main chamber turbo (Leybold Heraeus, TMP 360). In order to perform IRAS at pressures above 1 x 10^{-6} Torr,

the sample holder must be fully retracted into the IR cell and the gate valve between the cell and main chamber must be closed. While unpumped, the cell can then be backfilled with gas using one or more of the variable leak valves attached. Though the nude ionization gauge is rated by Agilent to measure pressures accurately up to 1 mTorr, this drastically reduces the lifetime of the filament, and therefore it is recommended that the ion gauge be shut off by 1 x 10^{-5} Torr

If desired, polarization-modulation IRAS (PM-IRAS) can be performed with a few more additions to the setup. A KRS-5 wire-grid polarizer (Figure D.4) can be mounted on a holder that allows it to be placed between the gold-coated parabolic mirror and the plastic disk described above. The PEM head with the ZnSe crystal can be connected to its corresponding PEM (Hinds Instruments) in order to switch back and forth between p- and s-polarization, and a lock-in amplifier allows the deconvolution of signals from the modulation.

At the end of experiments, the 2.75" CF all-metal gate valve can be slowly cracked open to the TMP 150 to pump out the cell before re-opening it to the rest of the UHV chamber.

Figure D.4: KRS-5 wire-grid polarizer.

APPENDIX E

PREPARATION OF CU-BTC THIN FILMS ON AL_2O_3/P-SI WAFERS

Figure E.1: Cu-BTC/Al_2O_3/p-Si. The thin film shown here is 40 cycles thick.

1. **Cut Al_2O_3/p-Si wafer into a ~10 x 10 mm^2 piece.** Rest wafer on a stack of 2-3 glass microscope slides so that a fragment of the desired size is hanging off the slide. Lay another glass microscope slide on top of the wafer and hold the whole stack firmly. Use a diamond scribe to score a line in the wafer, using the topmost glass slide as a straight-edge. Trace over the same line several times until the line becomes fairly deep. While holding the stack of slides firmly in one hand, use a finger to tap on the free part of the wafer until it breaks.

2. **Sonicate wafer in TCE for 30 min, acetone for 15 min, ethanol for 15 min.**

3. **Prepare 1 mM solution of copper acetate monohydrate ("CuAc").** Weigh out 0.019965 g of $Cu(CH_3COO)_2 \cdot H_2O$. Add to 100 mL volumetric flask and add enough ethanol to fill to 100 mL mark. Fill a 30 or 50 mL beaker with the solution. Fill a second 30 or 50 mL beaker with pure ethanol for rinsing.

4. **Prepare 1 mM solution of trimesic acid ("BTC").** Weigh out 0.021014 g of benzene-1,3,5-tricarboxylic acid. Add to 100 mL volumetric flask and add enough ethanol to fill to 100 mL mark. Fill a 30 or 50 mL beaker with the solution. Fill a second 30 or 50 mL beaker with pure ethanol for rinsing.

5. **Secure the wafer to a holder.** Use a pair of clean tweezers to grip just 1-2 mm of the edge of the wafer. Secure the tweezers by either locking them or, as I prefer, taping them in that position. If locking, make sure the tweezers don't apply too much pressure to the wafer or they will crack it. If taping, be sure the tape is high enough that it will NEVER see any of the solution. The tape reacts with the solution and turns yellow, and it seems it can affect the film growth.

6. **Grow the first layer.** Dip the wafer into the CuAc for exactly 1 minute. Remove. Dip in 1st beaker of pure ethanol and swish it around gently ~5 seconds to rinse the wafer. Use a stream of N_2 (I used the spigot under the hood) at medium pressure to dry the wafer thoroughly, front and back, ~15 seconds. Dip the wafer into the BTC for exactly 1 minute. Remove. Dip in the 2nd beaker of pure ethanol and swish it around gently ~5 seconds to rinse the wafer. Dry the wafer thoroughly, front and back, with N_2, ~15 seconds.

7. **Grow subsequent layers.** Repeat Step 6 for 39 more times for a total of 40 layers. A crystalline Cu-BTC MOF will appear as a blue-green holographic "fingerprint" covering some portion of the surface (See Figure E.1). If the entire surface turns dark blue, it's not a MOF.

N.B.: Al_2O_3/p-Si wafers were prepared by Dr. Jason Hattrick-Simpers' group in Chemical Engineering. The alumina film was estimated to be on the order of 100 nm thick.

Preparation method adapted from

(1) Nijem, N.; Fürsich, K.; Kelly, S. T.; Swain, C.; Leone, S. R.; Gilles, M. K. HKUST-1 Thin Film Layer-by-Layer Liquid Phase Epitaxial Growth: Film Properties and Stability Dependence on Layer Number. *Cryst. Growth Des.*, **2015**, *15*, 2948-2957.

(2) Summerfield, A.; Cebula, I.; Schröder, M.; Beton, P. H. Nucleation and Early Stages of Layer-by-Layer Growth of Metal Organic Frameworks on Surfaces. *J. Phys. Chem. C*, **2015**, *119*, 23544-23551.

(3) Stavila, V.; Volponi, J.; Katzenmeyer, A. M.; Dixon, M. C.; Allendorf, M. D. Kinetics and Mechanism of Metal-Organic Framework Thin Film Growth: Systematic Investigation of HKUST-1 Deposition on QCM Electrodes. *Chem. Sci.*, **2012**, *3*, 1531-1540.

(4) Zacher, D.; Baunemann, A.; Hermes, S.; Fischer, R. A. Deposition of Microcrystalline $[Cu_3(btc)_2]$ and $[Zn_2(bdc)_2(dabco)]$ at Alumina and Silica Surfaces Modified with Patterned Self Assembled Organic Monolayers: Evidence of Surface Selective and Oriented Growth. *J. Mater. Chem.*, **2007**, *17*, 2785-2792

APPENDIX F

PERMISSION TO REPRINT: CHAPTER 3

APPENDIX G

PERMISSION TO REPRINT: CHAPTER 4

APPENDIX H

PERMISSION TO REPRINT: CHAPTER 7